Yu Zhao
Yongfa Zhang
Pengfei He

Hydraulic Fracturing and Rock Mechanics

OPEN ACCESS

Springer

Hydraulic Fracturing and Rock Mechanics

Yu Zhao · Yongfa Zhang · Pengfei He

Hydraulic Fracturing and Rock Mechanics

Yu Zhao
College of Civil Engineering
Guizhou University
Guiyang, Guizhou, China

School of Civil Engineering
Chongqing University
Chongqing, China

Pengfei He
Department of Geotechnical Design
Shenzhen Geotechnical Investigation
and Surveying Institute Groups Co., Ltd.
Shenzhen, Guangdong, China

Yongfa Zhang
College of Civil Engineering
Guizhou University
Guiyang, Guizhou, China

School of Civil Engineering
Chongqing University
Chongqing, China

Preface

For over 50 years, hydraulic fracturing has been employed to stimulate unconventional reservoirs deep beneath the surface including shale gas, coalbed methane, geothermal energy, etc. During the fracturing treatment, the conductivity and permeability of reservoirs are significantly enhanced by injecting million gallons of fracturing fluid at high pressure into sealed subsurface formations to break up the rock and create interconnected and complex fracture networks. One of the important features needed in fracturing design is the ability to predict the geometry and the characteristics of the hydraulically induced fractures. To overcome the difficulty of predicting fracture behaviours conforming the formation of fracture networks, it is necessary to explore the multi-scale hydraulic fracturing process from fracture initiation to the formation of fracture networks in depth. However, current research efforts increasingly focus on modelling hydraulic fracture by assuming consistently constant internal fluid pressure along the crack surface, which is too simple to agree with the non-uniform fluid pressure in situations where variable injection rates are maintained in practical operations. This book is the first to consider the effect of non-uniform fluid pressure in hydraulic fractures and discusses the associated issues in the process of hydraulic fracture nucleation, growth, interaction and fracture network formation. Laboratory experiments and theoretical modelling are combined to elucidate the formation mechanism of complex fracture networks.

This book starts by introducing the theoretical background of *rock mechanics in hydraulic fracturing operations* and presented a hydraulic fracture model based on the Griffith's theory. Then, laboratory hydraulic fracturing of shale sampled from different formations is performed under *constant flow injection* and *constant pressure injection* modes, respectively. Based on the experimental results and considering non-uniform fluid pressure, a series of theoretical models involving *fracture initiation*, *fracture propagation* and *fracture interaction behaviours* are proposed and analysed. The final part reports the formation mechanism of complex fracture networks implied by the results of uniaxial and true triaxial hydraulic fracturing physical simulations.

This book is intended as a reference book for master/Ph.D. students, engineers and scientists in the field of rock engineering and earth sciences. The content presented in this book is based on many years of research of the three authors, which can

provide important reference for field treatment design and fracturing operations. During writing this book, we have made ample references to key publications in related fields and tried to tell the reader up-to-date research progress. Owing to the limitation of our knowledge, there must be mistakes and errors in the book. Your suggestions would be deeply appreciated.

Guiyang, China   Yu Zhao
January 2023   Yongfa Zhang
                                                                                      Pengfei He

Acknowledgements

Contents

Chapter 1
Introduction

1.1 Background

Compared with coal and oil, natural gas is clean and efficient, flexible in transportation and operation. Natural gas produces less dust, carbon dioxide and nitrogen oxides during combustion, which effectively reduces carbon emissions and mitigates the greenhouse effect [1, 2].

As an unconventional resource, shale gas exists in the shale reservoir [3, 4] as free or adsorbed. China is rich in shale gas reserves (close to 31.57 trillion cubic meters) [5, 6], mainly distributed in north China (including the Ordos and southern north China), northwest China (including Zhungeer basins) and southern China (including Sichuan Basin). At present, the Chinese industrial shale gas production area mainly includes in Weiyuan-Changning, Zhaotong and Fuling blocks [7]. The shale gas is affected by continental deposition and late transformation movement, geological conditions are complex in China. Natural gas is often detected in mountains or deserts. Earthquakes and shortages of water make the natural gas rich in the reservoir but difficult to extract, leading to high construction costs and great difficulty in exploitation [8, 9].

Hydraulic fracturing is one of the methods of mining shale gas reservoirs. During this process, high flow-rate and low viscosity fracturing fluid are injected into the strata through the wellbore, which can break down reservoir rock and facilitate migration and seepage of shale gas absorbed in the rock matrix. Due to the continuous injection of high-pressure fracturing fluid into the rock, hydraulic fractures will be created in the reservoir and will interact with preexisting interfaces in the formation, resulting in variable fracture propagation behavior (offset, arrest, crossing, branch, etc.) The propagation of subsequent fracture branches will also be disturbed by each other, which finally contributes to the formation of complex fracture networks [10, 11]. The current initial production rate of shale gas fields is only from 5 to 15% [12], far lower than expectation. Although the production has been improved by hydraulic fracturing, it is still not enough to exploit most of the shale gas. The main reason may be due to the insufficient understanding of the fracture initiation, propagation, intersection, and network formation mechanism. The current hydraulic fracture model

rarely considers the non-uniform fluid pressure effect caused by fluid viscosity and flow inside the fracture. No reliable analytical model has been established to predict the propagation path and ability of hydraulic fractures, which unfavorable fracturing efficiency of the reservoirs. Moreover, the injection of high-pressure water during the fracturing process may also reduce the effective stress in the formation, which may cause fault activation and seismic sliding. The fracture fluid flow via induced fractures easily invades and pollutes the groundwater source [13, 14]. Therefore, it is of great practical significance to study the process of hydraulic fracture initiation, propagation, intersection and network formation, to optimize the actual fracture path, intersection behavior and extension range during fracturing design and to improve the shale gas extraction rate.

1.2   Research Progress

1.2.1   Initiation and Propagation of Hydraulic Fracture in Shale Reservoirs

The initiation and propagation of hydraulic fracture are of great significance to the subsequent migration and exploitation of shale gas, especially the design and optimization of field construction schemes. In recent years, researchers have carried out extensive theoretical, experimental and numerical studies on the evolution of hydraulic fractures [15–17]. At present, it is mainly believed that the bonding strength and inclination of bedding planes, pore pressure, permeability, in-situ stresses, natural fracture properties, flow rate and viscosity of fracturing fluid are the main factors influencing the initiation direction, initiation pressure and propagation morphology of hydraulic fractures. The shale matrix is a tight material with ultra-low porosity (4–6%) and permeability (< 0.001 mD). Thus, fracturing fluid penetrating intact rock matrix is scarcely considered [15].
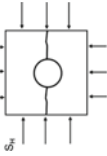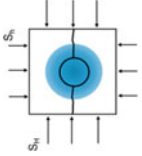
According to the linear elastic fracture mechanics, the initiation of the hydraulic fracture is consistent with the maximum principal stress direction in the homogeneous and isotropic rock. However, in shale reservoirs, the defects in shale such as bedding and microcracks are more likely distributed around the wellbore [18]. which makes a hydraulic fracture first nucleate and initiate. In 1981, Huang [19] proposed a critical criterion for predicting the vertical and horizontal initiation of hydraulic fracture. He argued that the formation of hydraulic fracture depended on the stress state around the wellbore and the hydraulic fracture propagated along the maximum stress regardless of the initial fracture direction. By analyzing the surface stress of horizontal wells of shale reservoir, Guo et al. [20] proposed three modes of perforation fracturing: rock cracking, shear failure along a bedding plane (or natural fracture) and tension failure along a bedding plane (or natural fracture). Sun et al. [21] found that the bedding inclination played a critical role in the initiation of hydraulic fractures. When the bedding strength is weak and the difference between vertical and horizontal stresses

is small, the hydraulic fracture mainly initiates along the bedding plane. Considering potential microcracks distribution in the axial direction of the wellbore, Bunger et al. [22] reported that if there were multiple defects in the wellbore axis after a hydraulic fracture cracks, the fluid pressure could continue to increase [23, 24] until the occurrence of multiple-fracture initiation. Zhou et al. [25], Rongved et al. [26], Zhu et al. [27] experimentally and numerically confirmed that multiple-fracture initiation will first start from the wellbore, and the initiation process is relatively independent. Kumar and Ghassemi [28] found that the stress shadow effect can limit multiple fracture initiation, promote fracture propagation in a mixed mode of type I and type II, and inhibit the growth of surrounding cracks. Zhang et al. [29] observed that the tight arrangement of perforation clusters will lead to uneven and asymmetric hydraulic fracture.

Hydraulic fracture initiation pressure refers to the critical fluid pressure when the fracture initiation. In most engineering practices, the hydraulic fracture initiation pressure is often equivalent to the rock breakdown pressure. Determination of the rock breakdown pressure determines the economy and safety of hydraulic fracturing operations, which is of crucial importance in the hydraulic fracturing process. The rock breakdown pressure model can better explain and distinguish the physical mechanism behind the hydraulic fracture initiation phenomenon, with which the breakdown pressure can be predicted based on measured parameters. In 1957, Hubbert and Willis [30] proposed a classical breakdown pressure model (H-W model) in the tectonic stress field, after ignoring the assumption of rock permeability (Table 1.1). In 1967, Haimon and Fairhurst [31] remodified the H-W model and proposed the H-F criterion by considering the effect of fluid leak-off on the rock breakdown process. Subsequently, more new breakdown pressure models emerge and are associated with multiple parameters such as pressurization rate, fracturing fluid properties and wellbore size, forming a variety of breakdown pressure models. According to the different critical breakdown conditions, the breakdown pressure model can be categorized into a tensile strength-based method, energy release rate-based method, stress intensity factor-based method and shear failure-based method. The hypotheses applicable range the different theoretical methods are summarized in Table 1.1.
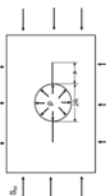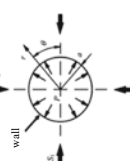
In addition to the hydraulic fracture models in Table 1.1, many models have been continuously developed and improved according to the practical fracturing treatments and prediction requirements. In 2017, Lu et al. [38] simulated the subcritical initiation and propagation of hydraulic fractures in impermeable homogeneous formations using open-hole fracturing. In 2019, Gunarathna and Silva [39] reported that vertical effective stress plays a major role in affecting the hydraulic fracture initiation pressure both for granite and shale strata. Through the analysis of the reservoir engineering data, they found that the hydraulic fracture initiation pressure increased with the vertical effective stress. In 2021, Chen et al. [40] considered the radially drilling fracturing construction and bedding orientation and established the radial drill fracture initiation pressure model of shale formation, which derived the fracture initiation pressure, the initiation direction and the location of the potential damage area. Michael and Gupta [41] compared the stress conditions in seven shale

Table 1.1 Hydraulic fracture initiation pressure models

Theory	Model	Authors (year)	Model overview and characteristics		Drawback
Maximum tensile stress criterion	H-W model	Hubbert and Willis (1957) [30]		Rock is homogeneous, line elastic, and isotropic Vertical stress is the minimum main stress (tectonic stress state)	The rock is impermeable Ignoring the fluid leak-off and injection rate effect
	H-F model	Haimon and Fairhurst (1967) [31]		Based on the H-W model, the rock is assumed as a porous elastic medium, and the Biot coefficient was introduced to consider the fracturing fluid leakage near the wellbore	Not applicable for rocks with low-permeability The Biot coefficient is assumed to be fixed during the fluid pressurization process

Table 1.1 (continued)

Theory	Model	Authors (year)	Model overview and characteristics	Drawback
	R-W model	Rumme and Winter (1983) [32]	Based on the H-F model, it assumes there is a pair of cracks near the wellbore with specific length a Fracking fluid filtration and wellbore size effects are considered Assuming that the damage occurs at the top of the characteristic crack when the maximum effective stress reaches the tensile strength	The length of the preexisting crack around the wellbore is difficult to determine
	Point stress model	Ito and Hayashi (1991) [33]	Consider the effect of the (constant) pressurization rate on the breakdown pressure based on the R-W model Stress component generated by stacking the gradient of the wellbore pressure	The mathematical solution process is very complicated, and the engineering application is limited
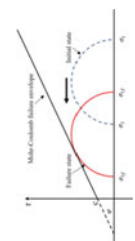
(continued)

Table 1.1 (continued)

Theory	Model	Authors (year)	Model overview and characteristics	Drawback
Griffith fracture criterion	P-K model	Perkins and Kern (1961) [34]	This method treats the wellbore as a circular crack pressurized by internal pressure and exposed to isotropic far-field stress. The model is based on the elasticity equation	The model is only suitable for analytical linear elastic materials, limited practical application due to the determination of multiple parameters
Based on the stress strength factor	Rummel model	Rummel (1987) [35]	2D isotropic rock. The critical fracture propagation follows the linear elastic assumption	Formation boundary conditions and fluid infiltration effects are ignored
	Cracking judgment	Zhang et al. (2017) [36]	Considering the properties of fracturing fluid and rock based on Rummel's model. The fracture toughness is assumed to vary with the initiation direction. The change of ambient pressure and Biot coefficient were considered. The prediction results are reliable	Complicated to be solved

Table 1.1 (continued)

Theory	Model	Authors (year)	Model overview and characteristics	Drawback
Mohr–Coulomb criterion	Morgenstern model	Morgenstern (1962) [37]	The fracture initiation pressure can be determined based on the known rock density, pore pressure, rock shear strength, and ambient pressure coefficient	Effective stress considerations based on bulk weight are not applicable in most fracturing processes, Natural fractures, reservoir anisotropy, wellbore size, and fracturing fluid properties are not considered

gas regions, proposed a semi-empirical method to determine the optimal perforation position and minimum ground stress, and evaluated the stress state and critical initiation conditions by using the correction factor. Among these numerous imitation pressure prediction models, current research and application are mostly based on the strength of the tension-based strength, but there is still a gap between the prediction results and the practical observation. Unknown parameters still limit engineering applications. Thus, comprehensive implementation of multiple methods should be used to obtain more reliable initiation pressure.

Fluid pressure distribution within the fracture is the internal cause that controls and affects the propagation morphology of hydraulic fracture. Fluid viscosity, flow rate and inter-joint temporary plugging can essentially affect the fluid fracture propagation state by changing the fluid pressure and its distribution form [42]. In recent decades, researchers have carried out detailed theoretical research on the resolving theoretical model of a fracture pressurized by internal fluid and obtained a series of analytical, semi-analytical, and numerical solutions, which have played a role in promoting the development of hydraulic fracturing theory to a certain extent. However, there are still gaps and deficiencies in these models compared with the real hydraulic fracturing process.

In 1921, Griffith [43] considered the effect of the fluid pressure in the fracture and obtained the stress field around a crack in a 2D infinite plane. However, the analytical solution and calculation process Griffith's is complicated. Subsequently, Sneddon et al. [44] proposed an alternative method and determined the stress field near the Griffith crack using the Westergaard stress function, but the results are still limited to the cases where the internal fluid pressure is constant. In 1997, Liu and Wu [45] adopted the Muskbelishvili complex function theory and presented an approximate analytical expression of crack opening degree (COD) (Fig. 1.1)

$$U(x', \alpha, \omega) = \frac{\sigma\omega}{E'}\left\{\frac{4}{\pi}\big[C_{1pl}x'F(\omega, x') + C_{2pl}F(\omega, x')\big] + C_{3pl}x' + C_{4pl}\right\} \quad (1.1)$$

where, C_{ipl} $(i = 1, 2, \ldots, 4)$ is the predetermined coefficient, and its expression is $C_{ipl} = \sum_{p=0}^{4}\left(\sum_{l=0}^{4} f_{ipl}\omega^l\right)\alpha^p$, $\omega = d/a$, $\alpha = a/W$ and $x' = X/a$.

The approximate treatment of the fracture width by Liu and Wu [45] significantly improves the accuracy and efficiency of the stress field near the crack tip. However, the segment and uniform pressure distribution is not sufficient to reflect the distribution state of fluid pressure along the fracture length.

To study the hydraulic fracture initiation, researchers have established different models of hydraulic fracture, as shown in Fig. 1.2, including PKN model, KGD model and Penny-shaped model. The PKN model assumes that each vertical section is an elliptical crack in a planar strain state and that the crack height along the propagation direction is constant [46]. The maximum crack width perpendicular to the vertical profile is determined by the local fluid pressure and the confining pressure stress. This model is to simulate the one-dimensional flow of the fluid along the crack. The KGD model is assumed in the horizontal cross-section and uses Poissuille's law to
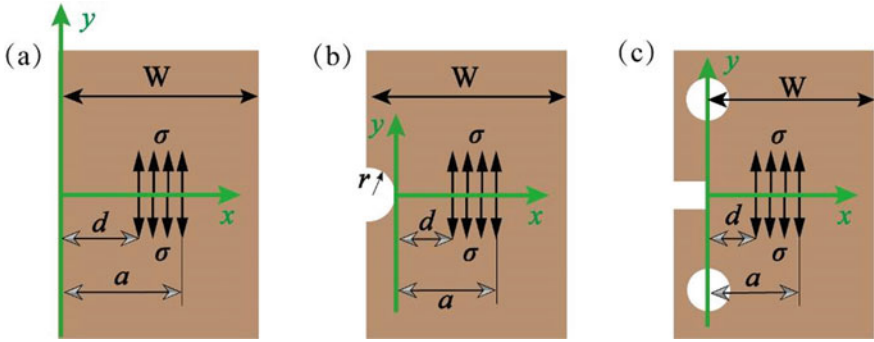
Fig. 1.1 Stress state of fracturing sample: **a** single side crack tensile sample, **b** single side band notch crack tensile sample, **c** compression tensile sample [45]

describe one-dimensional fluid flow within cracks, which describes the relationship between fluid pressure and fracture width [47]. The Penny-shaped hydraulic fracture model has a 3D axisymmetric shape extending radially around the wellbore [48]. In 2001, based on the KGD hydraulic fracture model (Fig. 1.2b), the research group of Detournay [49–52] established the relationship between the internal fluid pressure and the crack opening by coupling the fluid lubrication theory and the rock elasticity equation expressed as

$$p(x, t) = p_f(x, t) - \sigma_0 = -\frac{E'}{4\pi} \int_{-l}^{l} \frac{\partial w}{\partial s} \frac{ds}{s - x} \tag{1.2}$$

In addition, Detournay et al. [53] also defined two energy dissipation regimes (i.e., fluid viscosity-dominated and fracture toughness-dominated) based on different energy dissipation processes during the hydraulic fracturing process. The rock toughness response can be ignored when the viscous dissipation within the crack is dominated. In 2012, Garagash and Sarvaramini [54] categorized two types of hydraulic fracture propagation (Fig. 1.3). When the fracture length is less than the wellbore radius, hydraulic fractures are assumed as edge fractures. When the fracture is greater than the wellbore radius, the hydraulic fracture is assumed to be a Griffith crack. However, the works of Garagash and Sarvaramini [54] are only aimed at the fracture shape and critical propagation state, and the changes in the stress and displacement fields induced by non-uniform pressure fluid within the crack are not involved. In 2019, Zeng et al. [55] used the weight function and derived the analytical solution of the fracture initiation stress around the wellbore, and found that the initiation pressure subject to the nonuniform fluid pressure was higher than that under constant pressure. In 2020, Li et al. [56] divided the fluid pressure into a constant pressure section and a rapid pressure drop section based on the pressure form inside the hydraulic fracture. The approximate solution of the fracture opening under nonuniform fluid

(a) PKN model   (b) KGD model

(c) Penny shaped model
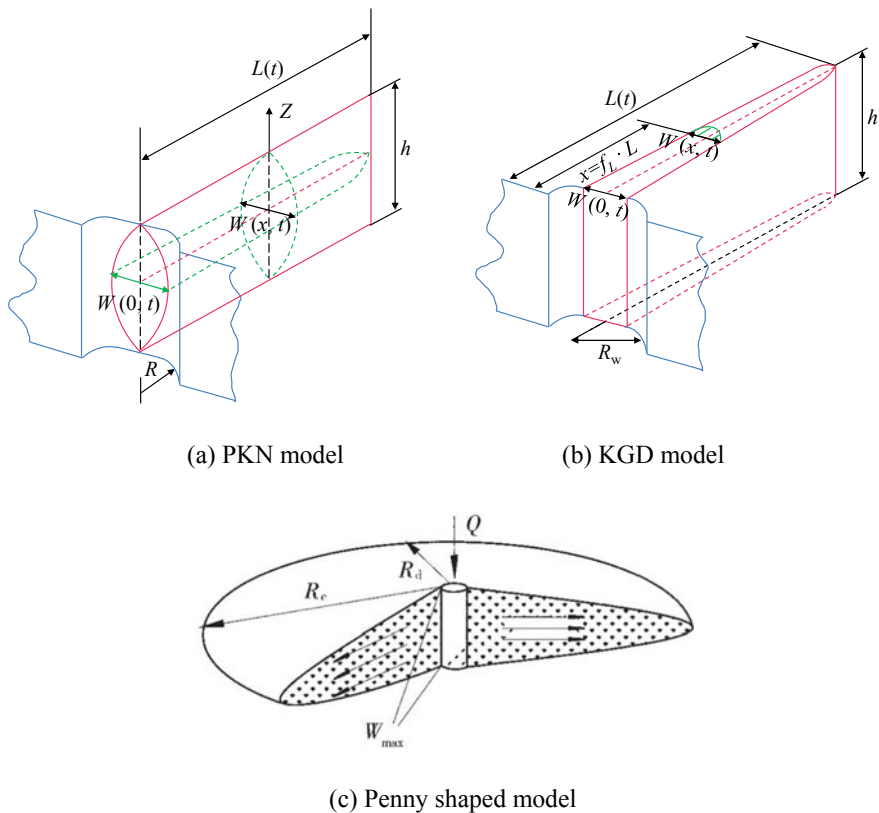
Fig. 1.2 Hydraulic fracture model in extending state

pressure is obtained by piecewise integration. The reliability of the solutions is verified by comparing the approximate solution to Sneddon's semi-analytical solution [44]. In 2022, Wrobel et al. [57] established a simplified model for the stress redistribution around the fracture tip and introduced a plasticity-related crack propagation condition. Wrobel et al. [57] considered the plastic deformation near the fracture tip. However, their model neglects the perturbation effect of the pressure gradient on the surrounding stress field. Previous hydraulic fracturing experiments, numerical simulations, and field studies have shown that the fluid pressure gradient in rock is nonlinear [58–60], especially in the disturbance of fluid viscosity and pumping parameters. In addition, numerous experimental and simulation studies [61, 62] have also shown that the nonuniform pressure form in the fracture has an important influence on the stable state of the initial fracture, new propagation direction, and final formation of an effective fracture network.

From this point of view, it is necessary to establish a model reflecting the influence of the nonuniform pressure inside the fracture on the propagation of hydraulic fracture. Sneddon [44] suggested using a general polynomial to characterize the internal
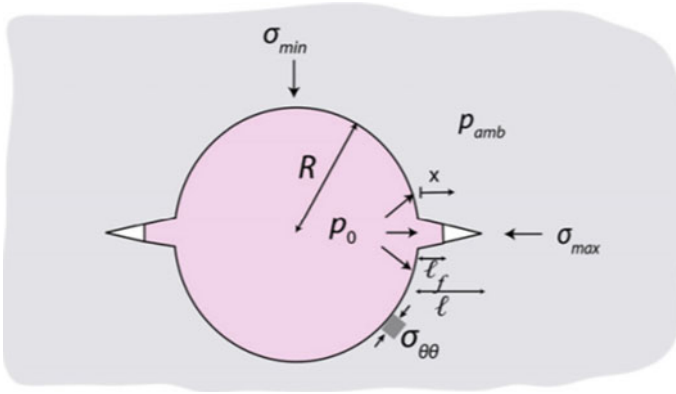
Fig. 1.3 Symmetrical crack distribution near the well bore [55]

fluid pressure e. Based on the integral transform of complex functions, the analytical form of the displacement induced by specified fluid pressure is derived. However, Sneddon [44] only gives the form solution of the displacement analytical equation and does not apply this analytical solution to determine the hydraulic fracture propagation, which has limitations in the practical engineering application. It is important to further investigate the perturbation effect of nonuniform fluid pressure on the propagation process of hydraulic fracture. The reliability of the analytical solution and its applicability to the actual fracture process can be further demonstrated by using experimental and engineering data.

1.2.2 Model of the Intersection of Hydraulic and Natural Fracture

Engineering experience [63, 64] shows that the interaction between hydraulic and natural fracture is an essential influencing factor in the formation of complex fracture networks and the intersection behaviour between fractures is the ultimate cause of high fracturing fluid filtration loss, early sand plugging, fracture propagation obstruction, fracture steering and high network pressure in the actual fracturing construction [65]. The intersection of hydraulic fracture and natural fracture involves complex effects such as flow-solid nonlinear coupling, fracture propagation, rock non-local fracture response and intersection disturbance, covering the two physical processes of hydraulic fracture gradually approaching natural fracture (extension approach) and fracture tip passivation (intersection passivation) when hydraulic fracture and natural fracture intersection. During the extended approximation process, the natural fracture stress state is disturbed by the gradually increasing fracture tip stress singularity; In the intersection passivation process, the fracture tip stress singularity has failed, and the subsequent fracture propagation is dominated by the dynamic flow

pressure of the fluid in the fracture [66]. Due to the singularity of fracture tip stress, the interaction between fractures and the extension path of fracture is different in different processes.

Some scholars have carried out a series of research based on the extended approximation process, mainly establishing the intersection criteria from the aspects of approximation perspective, critical stress state, fracture fluid pressure form, etc. In 1995, Renshaw and Pollard [67] proposed a model for the vertical intersection of hydraulic fracture and natural fracture (Fig. 1.4a): under the action of the stress field at the hydraulic fracture tip of the natural fracture, when a new fracture is produced on the other side of the natural fracture surface and the natural fracture surface does not slip, it is considered that the hydraulic fracture will pass through the natural fracture. This is an idealized either non-slip or pass-through compression crossing model, aiming at describing the perturbation effect of the fracture process region on the natural fracture, but this model is limited by the strict symmetrical vertical approximation angle, which does not show the propagation form of the inclined intersection. In 2013, Sarmadivaleh and Rasouli [68] extended the Renshaw and Pollard criteria to an arbitrary approximation angle (Fig. 1.4b) to obtain an analytical form of the compressed crossing criterion. In 2014, Zhang et al. [69] gave the calculation method for the turning Angle of hydraulic fracture through natural fractures based on Sarmadivaleh and Rasouli's works. They proposed a revised version of the intersection criterion (Fig. 1.4c) to determine the initial direction of subsequent compression through fracture propagation. The calculation results show that: when the approximate angle is constant, the horizontal principal stress ratio required for the hydraulic fracture to pass through the natural fracture is within limits. Neither too high nor too low principal stress ratios can make the hydraulic fracture pass through the natural fracture; In addition, under the large approximate angle and the horizontal principal stress ratio (maximum principal stress ratio, minimum principal stress), the hydraulic fracture tends to expand directly through the natural fracture; At the same approximation angle, the greater the horizontal primary stress ratio value, the piercing direction always tends to be close to the increased horizontal primary stress direction. Considering the matrix heterogeneity and rock mass seepage-stress-damage fracture characteristics, in 2016, Zhao et al. [70] studied the influence of natural structures of different scales. The results show that the tension damage between hydraulic fracture and nonclosed fracture directly led to penetration between fractures. If the intersection angle between the direction of the maximum principal stress and the bedding plane strike is small, the hydraulic fracture will propagate along the tectonic plane; While the direction of the maximum principal stress intersects the bedding plane at a large angle, the maximum principal compressive stress and the bedding plane simultaneously dominate the joint network propagation process. The study also confirmed that reservoir hydraulic fracture is a transient dynamic disturbance process within a local scope, but the study did not consider the disturbance effect of the stress field at the tip of the approximation process. In 2017, Llanos et al. [71] studied the influence of the hydraulic fracture vertical approach process on stability based on the change of constant fluid pressure, hydraulic fracture length, and approximation distance (Fig. 1.4d). The study shows that with the shortening of the approaching

(a) Renshaw and Pollard model [69]   (b) Sarmadivaleh modified model [70]

(c) Zhang Ran and Li Gensheng modified model [71]   (d) Llanos approximation model [73]
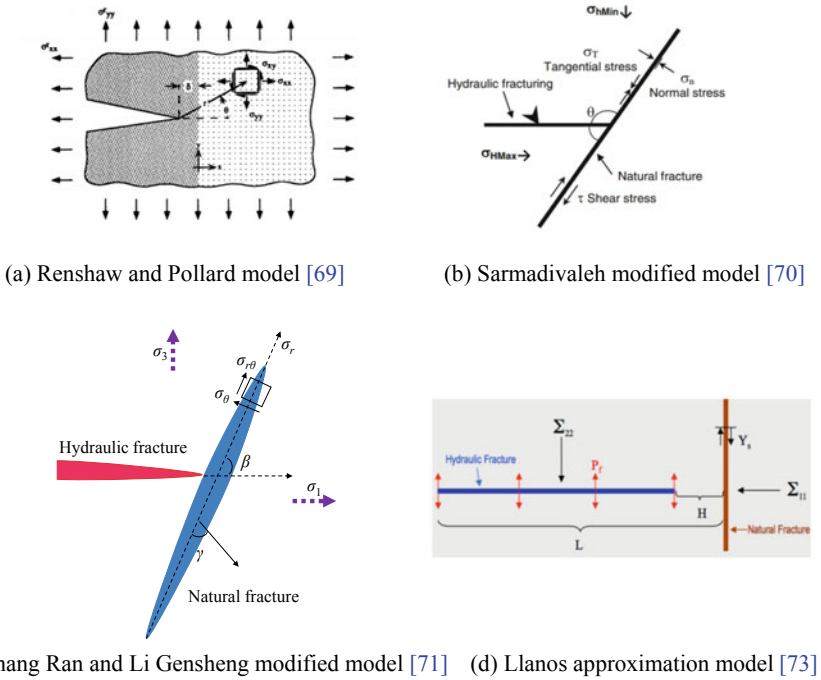
Fig. 1.4 Intersection model between a hydraulic fracture and a natural fracture based on the approaching process

distance, the stress state change on the natural fracture surface intensifies, and the natural fracture surface also tends to slip and initiate. However, Llanos' study only considers the orthogonal approximation of the two fractures, while the change in the actual approximation angle will also have different effects on the extension direction of the natural fracture [72].

In 2018, Zhao et al. [73] extended Llanos' approximation model to arbitrary approximation angles. They coupled it with the simultaneous fluid flow (lubrication equation) and rock elastic deformation (elastic equation), then proposed the intersection of toughness master hydraulic fracture (constant fluid pressure in the joint) and discontinuous friction interface, and clarified the disturbance law of the hydraulic fracture dynamic approach process to the stress state of any natural fracture surface. In 2019, Zhao et al. [74] introduced natural fracture critical opening conditions based on the crossing criteria and established a composite model of the dynamic approach of natural fracture in hydraulic fracture and predicting the three intersection behaviors (opening, crossing, and slip, shown in Fig. 1.5), to provide a theoretical basis for subsequent propagation behavior prediction. Janiszewski et al. [75] studied the interaction mechanism between hydraulic and natural fracture based on the fracture mechanics modeling code FRACOD simulation. They believed that a small approximation angle is beneficial to the hydraulic fracture angle and the activation

of natural fracture, which leads to the propagation of wing tensile fracture from the tip and forms a complex fracture network. Daneshy [76] established a 3D approach intersection model considering three types of natural fracture (open, closed unbound, closed bond) and found that the character of natural fractures directly affects the intersection behaviour and hydraulic fracture propagation state. In contrast, the ground stress, approach angle, and fracture fluid pressure are the main control factors leading to the activation of natural fracture. In 2020, Zeng et al. [77] proposed the criterion of type I/II mixed mode hydraulic fracture passing through the natural fracture based on the stress field around the hydraulic and the natural fracture and approached the zero simplified criterion through the composite degree (K_{II}/K_I) and applied it to the verification of the test results. In 2021, Zhu and Du [78] proposed a critical criterion for hydraulic fracture passing through natural fracture based on fracture tip T-stress. They found that T-stress always limits the direction change of hydraulic fracture when passing through the natural fractures interface. Zhao et al. [79] established a 3D intersection model of hydraulic and natural fracture and verified the prediction model combined with indoor experimental data. They also qualitatively summarized six types of intersection behaviors: crossing, sliding and initiation, initiation, sliding, sliding plus crossing and arrest. Unfortunately, only two kinds of crossing and slip were observed in Zhao's tests [79], and the test basis for the six types of intersection behaviors was not found. Also, the critical conditions and order for the occurrence of the six types of intersection behaviors were not given. There are only three independent intersection behaviors in the hydraulic approximation process theoretically (Fig. 1.5). Once the natural fracture slip, the stress state around the natural fracture will change, affecting the following propagation state of the fracture. In 2022, Zheng et al. [80] believed that the interaction of non-intersecting fracture in the propagation process could not be ignored. The inter-fracture interaction model was established based on the boundary element and rock fracture criteria and found that natural fracture could cause at least 22° deflection under appropriate conditions.

Most of the previous intersection standards based on the approximation process have ignored the effects of fluid viscosity and flow rate. The fluctuations in the fluid viscosity and the injection rate during the actual hydraulic fracturing process cause changes in the in-fracture fluid pressure with time and fracture length. The
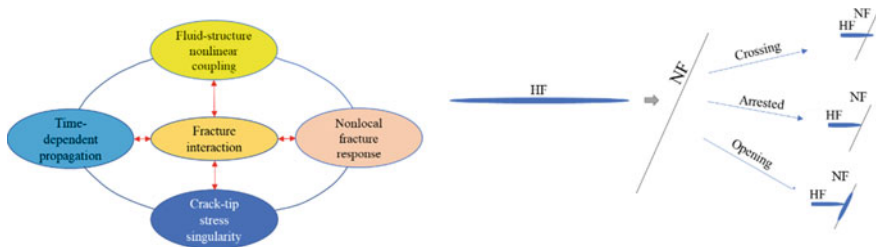
Fig. 1.5 Intersection behavior between a hydraulic fracture and a natural fracture

hypothetical fluid pressure is invalid, and the coordination criteria of the tough main control hydraulic fracture are no longer applicable.

The study of intersection criteria for intersection passivation processes goes from qualitative analysis to quantitative computation. In 1986, Blanton [82] simplified the forming of natural fracture shear stress distribution. Based on the critical fluid pressure conditions in the fracture after intersecting passivation, the culinary stress component of the rock resistance and geological stress component was qualitative. However, the judgment only considers the critical condition of fracture crossing and ignores the disturbance effect of the propagation state fracture induction. In 1987, Warpinski and Teufel [83] superimposed the stress field and supplemented the critical stress conditions of natural and hydraulic fracture after passivation and intercourse. However, it is still limited to the interaction of the fracture tip and the grounding force field. The fluid pressure effect, natural fracture penetration, and the position and direction of the new fracture after passivation is not considered. In 2014, Chuprakov et al. [81] established a fracture tip passivation model considering the influence of rock fracture toughness, hydraulic fracture length, natural fracture permeability, and the effect of injection rate (Open T model, shown in Fig. 1.6a). It described the partition characteristics of the natural fracture opening and sliding segments of the fracture tip passivation zone, determined the orientation of the new nucleation fracture, and described the natural fracture activation problem quantitatively. Considering the type of T-type passivation contact form, in 2015, Chuprakov and Prioul [84] established the friction sticky interface of natural fractures on fracture high control effects (FRACT models) and applied the criteria to the 3D bedding rock stream coupling model simulation, and analyze the high control mechanism of natural fracture on hydraulic fracture. In 2019, Xu [85] considered hydraulic fracture fluid lag area effect and fracture tip passivation using analytical and numerical (noncontinuous deformation analysis) way to establish the hydraulic and natural fracture intersection model which mainly predicts the fracture tip to natural fracture and fluid front did not contact with natural fracture, hydraulic fracture crossing the natural fracture. It was found that hydraulic fracture is easier to cross natural fracture under large crustal stress, approximation angle, interface friction, injection rate, and fracturing fluid viscosity. In 2020, Zhao et al. [86] investigated the intersection mechanism of hydraulic and natural fracture with different shear strengths based on the 3D lattice-spring method. The results show that the tensile strength of the intact fracture and the shear strength of the joint play a dominant role in the intersection behavior between the two fractures. However, the intersection criteria and models of the fracture intersection passivation process described above ignore the perturbation effect of the hydraulic fracture tip stress singularity, which is particularly significant in the two-fracture propagation approximation process.

In general, the intersection process of hydraulic fractures and natural fractures is affected by rock mechanical properties (elastic modulus, fracture toughness, tensile strength, etc.), natural fracture mechanical properties (shear strength, interface friction coefficient, cohesion, etc.), fracturing fluid flow and viscosity, approach angle, crustal stress difference, etc. The approximation process of the intercourse is rarely involved in the non-average pressure flow effect of the fracture caused by fluid
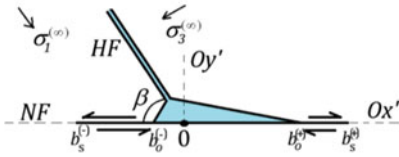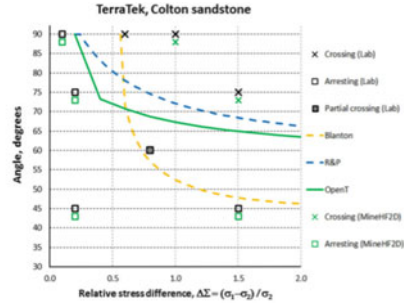
(a) Open-T model   (b) The behavior predicted by the model

Fig. 1.6 Open-T model and its predicted fracture behavior [81]

viscosity and flow velocity changes. Therefore, it is not considered that the distur-
bance of the stress field of dynamic changes around the surrounding dynamic changes
in the actual hydraulic fracture. Monitoring data deviations are large. To further
enhance the reliability of the prediction results of the interchange standards, a reason-
able change in fluid pressure conditions needs to be introduced within the standard,
and the dynamic propagation of hydraulic fracture and dynamic propagation of the
natural fracture process of new fracture, propagation, and interchange stress thresh-
olds. The stability change rule of the natural fracture surface is revealed to predict
the subsequent intersection behavior.

1.2.3   Formation Mechanism of the Complicated Crack Network of Shale

Shale is formed by clay mineral dehydration, cement and later deposition, rich in
apparent thin sheet bedding and natural microcracks [87, 88]. The combinations of
different productive bedding, microcracks and other matrix defects form discrete
crack systems in shale reservoirs. In the hydraulic fracturing of fractured shale
reservoirs, high-pressure fluid-driven hydraulic fracture connected with the reser-
voir anisotropy and randomly distributed fracture clusters, branch fracture in the
rock body breakdown with all kinds of fracture overlap and extension, forming a
complex 3D fracture network (Fig. 1.7). Influenced by the bedding direction and the
random distribution of natural fracture, the shale hydraulic pressure fracture network
is diverse and discrete characteristics [89, 90]. Establishing a large-scale and inter-
connected complex fracture network is the key to realizing the effective extraction
and commercial development of shale gas reservoirs.

Indoor hydraulic fracturing test plays a vital role in understanding the fracture
propagation mechanism, studying the formation of the complex fracture networks,
and simulating the field fracturing process. Based on physical model experiments and
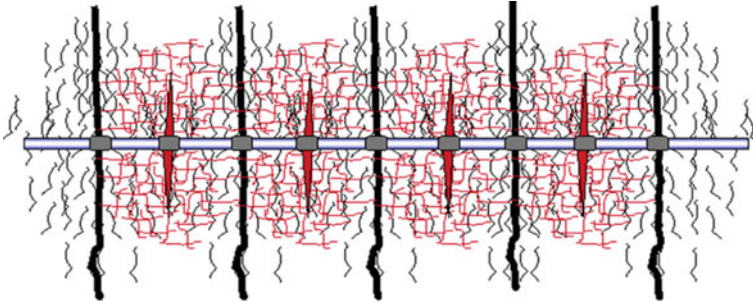
Fig. 1.7 Schematic diagram of a complex fracture network (multistage fracturing) [91]

dynamic acoustic monitoring technology, scholars have carried out some research work in fracture pattern characteristics and fracturing modification [92], focusing on the analysis of the influence of stress state, fluid viscosity, pump injection flow, formation lithology, occurrence and distribution of fractures (including bedding and primary microfractures), fracturing technology, etc. on hydraulic fracture propagation path and fracture pattern.

The model experiment of studying the complex fracture mesh in shale reservoirs has undergone a transition process from rock-like materials to rock materials, prefabricated cracks to natural fractures, and visual observation to acoustic wave dynamic scanning and monitoring. Considering the influence of 3D production and ground stress in natural fractures comprehensively, in 2005, de Pater et al. [93] studied the influence of fluid properties on fracture intersection behavior with the help of fracture intersection model experiments and numerical simulation. It was found that the high-flow and high-viscosity fracturing fluid produces multiple hydraulic fractures, while the low-flow fracturing fluid tends to open the natural fractures. In 2015, Dehghan et al. [91] studied the influence of natural fracture yield and horizontal stress difference on fracture propagation with the help of the true three-axial hydraulic fracture. The experimental results show that under the condition of small horizontal stress difference, the strike and dip angle of natural fractures play a controlling role in the propagation law of hydraulic fractures. Improving the horizontal stress difference or increasing the strike and dip angle of natural fractures on the experimental scale can inhibit the poor development of hydraulic fractures. Considering the influence of the shale lamination effect, Tan et al. [94] used horizontally laminated shale test samples to carry out the true triaxial hydraulic fracturing experiment in 2017. They studied the effects of ground stress, laminar surface, injection rate, fracturing fluid viscosity, and other factors on fracture vertical propagation behavior and fracture morphology, and summarized four typical propagation modes of vertical production of laminar shale fracture (Fig. 1.8): Single fracture, fish-bone fracture, fish-bone fracture with bedding opening, and multi boundary fish-bone fracture network. Differences in the physical and mechanical properties of natural fractures are limited by changes in the sedimentary environment. In 2018, focusing on the influence of the sedimentary environment

and natural bedding on fracturing morphology, Zhao et al. [95] compared the differences in hydraulic fracturing forms of Marine shale and continental shale and gave the relationship between section roughness and stress state based with the experimental results. In 2019, Chong et al. [96] studied the effect of shale reservoir anisotropy on pressure fracture networks based on hydraulic fracturing experiments with different initial stress states and injection rates. Based on a CT scan, they explained the impact of shale anisotropy inclination on hydraulic fracture. According to the analysis of CT images and results of 3D reconstructed hydraulic fracturing samples, Jiang et al. [97] believed that the key to shale fracturing volume change was the complexity of fracture formation and the fracture propagation distance generated by fracturing, and the stress difference played a significant role in controlling the formation of the complex fracture network. Considering the effect of fluid properties, Wang et al. [98] studied the influence of fluid viscosity and flow on the fracturing effect based on the true three-axial hydraulic fracturing test of bedding shale and found that the fracturing fluid with high injection rate and viscosity mainly forms a single main crack form. In contrast, the fracturing fluid with low viscosity and low injection rate promotes the formation of a complex fracture network. Hou et al. [99] conducted an experimental study on the effect of slippery water/guar glue fusion injection on fracture initiation and propagation in deep shale gas reservoirs. The study found that guar gum tends to open transverse fractures in deep shale reservoirs. In contrast, slippery water tends to activate the surface under the temporary blocking of guar glue combined with the fracture propagation morphology, a large and complex fracture network was injected alternately with different viscous fracturing fluids.

It is of great significance to understand the initiation and geometric properties of hydraulic fractures for optimizing hydraulic fracturing design and improving the final production of shale reservoirs. In 2019, Wu et al. [100] applied the shear tensioning fracture model to the data analysis of the triaxial hydraulic fracturing acoustic emission of stratified shale and evaluated the cumulative change pattern of the test sample tensioning and shear fracture in the hydraulic fracture process, and used the average fracture inclination and initiation width index to identify the fracture morphological characteristics quantitatively. In 2020, Chen et al. [101] used the true three-axial fracturing test system to simulate the influence of the ground stratification, ground stress difference, the hydraulic fracture initiation and propagation process. They found that the hydraulic fracture is easy to extend along the bedding direction with weak cementation, and the high ground stress difference promotes the formation of a single fracture form, while the viscous fracturing fluid and temporary plugging in the front are conducive to the formation of the complex fracture network. Dehghan [102] performed a series of true three-axis hydraulic fracturing tests based on large synthetic rock samples of preformed natural fracture on the laboratory scale and studied the extended behavior and length change characteristics of hydraulic fracture in natural fracture reservoirs. They believed that ground stress is the dominant factor in disturbing fracture intersection behavior and controlling fracture propagation length. Zhang and Sheng [103] considered the influence of the power-law distribution form and spacing of natural fracture and obtained the optimal fracture

Fig. 1.8 Schematic diagram of hydraulic fracture propagation morphology in vertical plane of shale reservoirs [94]
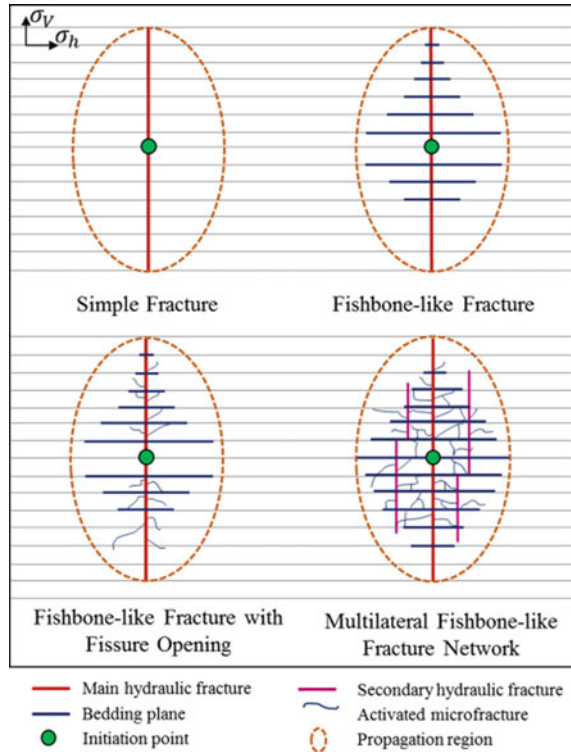
mesh layout method of complex natural fracture reservoirs by the simulation and optimization of various complex fracture network layout methods.

In 2021, Wu et al. [104] established an evaluation model of fracture network connectivity based on acoustic emission data. Combined with the triaxial hydraulic fracturing experiment, the correlation between the microcrack onset position and the fracture pull-shear characteristics in the formation process of the hydraulic fracturing-induced fracture network was discussed entirely, which can effectively estimate the hydraulic fracturing effect. Zhang [105] conducted a volume fracture simulation study of a deep shale fracturing fracture network based on a 3D Wiremesh model. The results show that increasing construction time, improving construction displacement, and reducing fracturing fluid viscosity are conducive to increasing the volume of the fracturing fracture network and improving fracturing efficiency. Based on physical experiments and simulations, Abe et al. [106] found that the inter-fracture stress shadow effect is the main reason for affecting the effective fracture extension and the formation of a large-scale fracture network.

In sum, the above scholars have analyzed the influence of ground stress conditions, fracturing fluid properties, natural fracture properties, construction schemes, and other factors on the fracture mesh form through hydraulic fracturing experiments. Hydraulic injection fluid-driven hydraulic fracture formation joint mesh is

a dynamic and cyclic multi-scale process [107], which needs to comprehensively consider the influence of bore layout, ground stress, injection rate, reservoir medium properties, and other factors. In addition, to maximize the exploitation of reservoir resources, the best effect of hydraulic fracturing should be to form a complex fracture network system dominated by effective length hydraulic fracture [65]. In addition, to maximize the exploitation of reservoir resources, the best effect of hydraulic fracturing should be to form a complex fracture network system dominated by effective length hydraulic fracture. However, the actual engineering of hydraulic fracture-induced fracture network production is mainly based on experience and the lack of reliable fracturing theory based on the in-depth study of shale reservoir hydraulic fracturing fracture propagation and the formation mechanism of the complex fracture network. It is necessary to start the influence of confining pressure, water pressure, and physical and mechanical response characteristics of rock materials on the fracture network form, with the real-time monitoring and positioning of the deformation and acoustic emission signals on the rock through dynamic monitoring technologies such as high-precision displacement sensor and acoustic emission. By analyzing the characteristics of the time and frequency evolution of acoustic transmission signals, the microscopic (tension or shear) fracture response law of the process of hydraulic fracturing, combined with microscope observation and CT 3D reconstruction, the dynamic process of fracture network initiation, intersection propagation, and fracture network formation is finely characterized and the formation mechanism of complex fracture network is explained.

1.2.4   Existing Problems

According to the above research, scholars have carried out lots of detailed studies on the theory, experiment, and numerical simulation of the process of hydraulic fracture initiation, propagation, intersection and network formation involved in hydraulic fracture. The disturbance effect of the fracture network by fracturing parameters has also been discussed, but the current research work still faces the following problems:

(i)   The fracturing mechanism and model of the reservoir rock are mainly studied under constant pressurization rate or constant current injection conditions, while the breakdown process of rock under the perturbation of constant pressure and static fatigue in the fracture is relatively scarce. During the hydraulic fracturing segment construction, the hydraulic injection operation often needs to be repeated, and the inner wall of the wellbore will inevitably withstand the fatigue disturbance caused by continuous pressurization. Moreover, many physical experiments [22, 108, 109] have confirmed that when the fluid is applied to the rock for a long time at constant high pressure (60–95% Pb), the rock eventually breaks up and produces a relatively tortuous hydraulic fracture form. Studying the constant pressure fatigue fracture mechanism in the fracture

is helpful to deeply understand the internal mechanism of rock hydraulic fracturing and improve the rock hydraulic fracture theory. The fracturing pressure of reservoir rock can be effectively reduced by adjusting the constant flow and pressure injection methods, and the fracturing operation cost can be saved.

(ii) In the actual hydraulic fracture process, especially for pulse hydraulic fracture and fatigue hydraulic fracture, fluid pressure in the cracks is always fluctuating [110, 111]. However, the existing hydraulic fracturing theory does not consider the dynamic change of heterogeneous cloth fluid pressure effect caused by viscous flow and flow decay, which is limited by engineering applications [112, 113]. The heterogeneous distribution effect of the fluid pressure in the joint can better reflect the dynamic propagation law of the hydraulic fracture in the actual fracturing process.

(iii) At present, some progress has been made in studying the crack intersection mechanism of hydraulic approximation and fracture tip passivation, but the cognition of the critical transition state of the two processes is still not clear enough, and the predicted results of the criteria deviate significantly from the actual indoor experiments and engineering monitoring data [72, 114]; Considering the influence of fluid pressure, rock material, and mechanical properties of natural fracture, the composite criterion reflects the critical state of hydraulic and natural fracture, which is of great significance in analyzing the intersection of multiple fractures and predicting the formation of a complex fracture network.

(vi) High-pressure fluid-driven hydraulic fracture to form fracture mesh is a dynamic, cyclic multiscale process [107]. The current research on complex fracture mesh focuses on reflecting the fracturing effect and the characteristics of reservoir breakdown through the macroscopic fracture morphology while less considering the fracture evolution law of the hydraulic loading process and the fracture characteristics after the breakdown. In in-depth exploring the formation mechanism of complex sewing nets, it is necessary to consider the effects of well-laying tube layout, geographical stress direction, stress shadow effect of cracks, and changes like reservoir medium on the evolution of complex fracturing networks and morphological characteristics. To further explore the formation mechanism of complex fracturing nets, it is necessary to consider the effects of well-laying tube layout, geographical stress direction, stress shadow effect of fracture, and changes like reservoir medium on the evolution of complex fracturing networks and morphological characteristics [115,116].

References

1. Jiang TiX, Gu CG, Wang HY (2017) Shale gas horizontal well SRV fracturing technology. Science Press, Beijing. (in Chinese)
2. Ma X, Wang H, Zhou S et al (2021) Deep shale gas in China: geological characteristics and development strategies. Energy Rep 7(6):1903–1914

3. Zeng YJ, Yang CH, Zhang BP (2017) The theory and practice in shale gas development engineering. Science Press, Beijing. (in Chinese)
4. Yin PF (2020) Study on mechanical behavior and hydraulic fracturing mechanism of Longmaxi formation shale in Southern Sichuan Basin. China University of Mining and Technology
5. Zhao W, Jia A, Wei Y, Wang J, Zhu H (2020) Progress in shale gas exploration in China and prospects for future development. China Petrol Explor 25(01):31–44
6. Zhong D (2019) Numerical simulation research on the performance of fracturing horizontal well in shale gas reservoir. Southwest Petroleum University
7. He Z, Nie H, Hu D, Jiang T, Wang R, Zhang Y, Zhang G, Lu Z (2020) Geological problems in the effective development of deep shale gas: a case study of Upper Ordovician Wufeng-Lower Silurian Longmaxi formations in Sichuan Basin and its periphery. Shiyou Xuebao/Acta Pet Sin 41(04):379–391. https://doi.org/10.7623/syxb202004001
8. Ma Y, Cai X, Zhao P (2018) China's shale gas exploration and development: understanding and practice. Pet Explor Dev 45(04):561–574. https://doi.org/10.1016/S1876-3804(18)300 65-X
9. Zhao J, Ren L, Jiang T, Hu D, Wu L, Wu J, Yin C, Li Y, Hu Y, Lin R, Li X, Peng Y, Shen C, Chen X, Yin Q, Jia C, Song Y, Wang H, Li Y, Wu J, Zeng B, Du L (2021) Ten years of gas shale fracturing in China: review and prospect. Nat Gas Ind 41(08):121–142
10. Pan L, Zhang Y, Cheng L, Lu Z, Kang Y, He P, Dong B (2018) Migration and distribution of complex fracture proppant in shale reservoir volume fracturing. Nat Gas Ind B. 38(05):61–70. https://doi.org/10.1016/j.ngib.2018.11.009
11.]Jiao F (2019) Theoretical insights, core technologies and practices concerning "volume development" of shale gas in China. Nat Gas Ind B 39(05):1–14. https://doi.org/10.1016/ j.ngib.2019.05.001
12. Liu Z, Wang T, Gao Y, Zeng Q, Zhuang Z, Huang KC (2016) The key mechanical problems on hydraulic fracture in shale. Guti Lixue Xuebao/Acta Mech Solida Sin 37(1):34–49
13. Lee KS, Kim TH (2016) Integrative understanding of shale gas reservoirs. Springer, Heidelberg
14. Wang X, Wang P, Li Y, Lv M, Wei Y (2021) Research on the relationship between fracture volume density and shale gas productivity. Geophys Prospect Pet 60(05):826–833. https:// doi.org/10.3969/j.issn.1000-1441.2021.05.013
15. Jia Y, Song C, Wang J, Gan Q (2021) The breakdown process of low-permeable shale and high-permeable sandstone rocks due to non-aqueous fracturing: the role of fluid infiltration. J Nat Gas Sci Eng. 89(4):103873. https://doi.org/10.1016/j.jngse.103873
16. Wang XL (2017) Numerical simulation of hydraulic fracturing in shale gas reservoirs based on the extended finite element method. University of Science and Technology of China
17. Sampath K, Perera M, Ranjith PG (2018) Theoretical overview of hydraulic fracturing break-down pressure. J Nat Gas Sci Eng 58:251–265
18. Dou F, Wang JG, Leung CF, Ma Z (2021) The alterations of critical pore water pressure and micro-cracking morphology with near-wellbore fractures in hydraulic fracturing of shale reservoirs. Eng Fract Mech 242:107481. https://doi.org/10.1016/j.engfracmech.2020.107481
19. Huang RZ (1981) Initiation and propagation of hydraulically fractured fractures. Petrol Explor Dev 1981(05):62–74
20. Guo T, Zhang S, Liu W, Lai W (2013) Initiation pressure of multi-stage fracking for perforated horizontal wells of shale gas reservoirs. Nat Gas Ind 33(12):87–93. https://doi.org/10.3787/j. issn.1000-0976.2013.12.013
21. Sun K, Zhang S, Xin L (2016) Impacts of bedding directions of shale gas reservoirs on hydraulically induced crack propagation. Nat Gas Ind B 36(2):45–51. https://doi.org/10.1016/ j.ngib.2016.03.008
22. Bunger AP, Lu G (2015) Time-dependent initiation of multiple hydraulic fractures in a formation with varying stresses and strength. SPE J 20(6):1317–1325
23. Bunger AP, Gordeliy E, Detournay E (2013) Comparison between laboratory experiments and coupled simulations of saucer-shaped hydraulic fractures in homogeneous brittle-elastic solids. J Mech Phys Solids 61(7):1636–1654. https://doi.org/10.1016/j.jmps.2013.01.005

24. Ma L, Fauchille AL, Chandler MR, Dowey P, Taylor KG, Mecklenburgh J, Lee PD (2021) In-situ synchrotron characterisation of fracture initiation and propagation in shales during indentation. Energy 215. https://doi.org/10.1016/j.energy.2020.119161

25. Le ZZ, Zhang GQ, Xing YK, Fan ZY, Zhang X, Kasperczyk D (2019) A laboratory study of multiple fracture initiation from perforation clusters by cyclic pumping. Rock Mech Rock Eng 52(3):827–840. https://doi.org/10.1007/s00603-018-1636-5

26. Rongved M, Holt RM, Larsen I (2019) The effect of heterogeneity on multiple fracture interaction and on the effect of a non-uniform perforation cluster distribution. Geomech Geophys Geo-Energ Geo-Resour 5:315–332

27. Zhu Y, Zhang H, Pan D, Zhai L, Gao S, Zhang Y, Chen C (2020) A case study on the optimal design of the horizontal wellbore trajectory for hydraulic fracturing in Nong'an oil shale. Energies 13(1):286. https://doi.org/10.3390/en13010286

28. Kumar D, Ghassemi A (2018) Three-dimensional poroelastic modeling of multiple hydraulic fracture propagation from horizontal wells. Int J Rock Mech Min Sci 2018:S1365160917310316. https://doi.org/10.1016/j.ijrmms.2018.01.010

29. Zhang Z, Zhang S, Zou Y, Ma X, Li N, Liu L (2021) Experimental investigation into simultaneous and sequential propagation of multiple closely spaced fractures in a horizontal well. J Pet Sci Eng 202(1):108531. https://doi.org/10.1016/j.petrol.2021.108531

30. Hubbert M, Willis D (1957) Mechanics of hydraulic fracturing. Transp Soc Petrol Eng AIME 210:153–168

31. Haimson B, Fairhurst C (1976) Initiation and extension of hydraulic fractures in rocks. Soc Petrol Eng J 7(03):310–318

32. Rummel F, Winter RB (1983) Application of laboratory fracture mechanics data to hydraulic fracturing feld tests. In: Nemat-Nasser S, Abé H, Hirakawa S (eds) Hydraulic fracturing and geothermal energy. Mechanics of elastic and inelastic solids, 5. Springer, Dordrecht

33. Ito T, Hayashi K (1991) Physical background to the breakdown pressure in hydraulic fracturing tectonic stress measurements. Int J Rock Mech Min Sci 28(4):285–293. https://doi.org/10.1016/0148-9062(91)90595-D

34. Perkins TK, Kern LR (1961) Widths of hydraulic fractures. J Pet Technol 222(9):937–949. https://doi.org/10.2118/89-pa

35. Rummel F (1987) Fracture mechanics approach to hydraulic fracturing stress measurements. In: Atkinson BK (ed) Fracture mechanics of rock. Academic Press, London, pp 217–239

36. Zhang X, Wang JG, Gao F, Ju Y (2017) Impact of water, nitrogen and CO_2 fracturing fluids on fracturing initiation pressure and flow pattern in anisotropic shale reservoirs. J Nat Gas Sci Eng 45:291–306. https://doi.org/10.1016/j.jngse.2017.06.002

37. Morgenstern N (1962) A relation between hydraulic breakdown pressures and tectonic stresses. Geofisica pura e applicate 52(1):104–111

38. Lu G, Gordeliy E, Prioul R, Bunger A (2017) Modeling initiation and propagation of a hydraulic fracture under subcritical conditions. Comput Methods Appl Mech Eng 318:61–91. https://doi.org/10.1016/j.cma.2017.01.018

39. Gunarathna G, da Silva BG (2019) Influence of the effective vertical stresses on hydraulic fracture initiation pressures in shale and engineered geothermal systems explorations. Rock Mechan Rock Eng 52(11):4835–4853

40. Chen Y, Ding Y, Liang C, Bai Y, Zhu D, Zou C (2021) An analytical model for fracture initiation of radial drilling-fracturing in shale formations. Lithosphere 1:3387123. https://doi.org/10.2113/2021/3387123

41. Michael A, Gupta I (2021) A comparative study of oriented perforating and fracture initiation in seven shale gas plays. J Nat Gas Sci Eng 88(4–5):103801

42. Fu Y (2019) The study on the rule of slick-water fracturing fluid flow in plugging of main fracture during the fracture of hydraulic fracturing. Xi'an Shiyou University

43. Griffith AA (1902) The phenomena of rupture and flow in solids. Philosop Trans R Soc Math Phys Eng Sci A221(4):163–198

44. Sneddon IN, Elliot HA (1946) The opening of a Griffith crack under internal pressure. Q Appl Math 4(3):262–267

45. Liu JZ, Wu XR (1997) Analytical expressions for crack opening displacements of edge cracked specimens under a segment of uniform crack face pressure. Eng Fract Mech 58(1):107–119

46. Hai TN, Lee JH, Elraies KA (2020) A review of PKN-type modeling of hydraulic fractures. J Petrol Sci Eng:107607

47. Wu Z, Cui C, Jia P, Wang Z, Sui Y (2021) Advances and challenges in hydraulic fracturing of tight reservoirs: a critical review. Energy Geosci. https://doi.org/10.1016/j.engeos.2021.08.002

48. Khalil MA, Susi AO (2020) Hydraulic fracture geometry modeling techniques for extracting unconventional reservoirs. J Eng Res Rep 5:1–5

49. Napier JAL, Detournay E (2019) Simulation of buoyancy-driven fracture propagation using the displacement discontinuity boundary element method. In: Advances in engineering materials, structures and systems: innovations, mechanics and applications, 525–530

50. Detournay E (2004) Propagation regimes of fluid-driven fractures in impermeable rocks. Int J Geomech 4(1):35–45

51. Detournay E, Hakobyan Y (2022) Hydraulic fracturing of weak rock during waterflooding. Int J Numer Anal Meth Geomech 46(2):416–435

52. Gao Y, Detournay E (2021) Hydraulic fracture induced by water injection in weak rock. J Fluid Mechan 927

53. Detournay E, Peirce AP, Bunger AP (2007) Viscosity-dominated hydraulic fractures. American Rock Mechanics Association

54. Garagash DI, Sarvaramini E (2012) Equilibrium of a pressurized plastic fluid in a wellbore crack. Int J Solids Struct 49(1):197–212

55. Zeng Y, Jin X, Ding S, Zhang B, Bian X, Shah S, McLennan J, Roegiers JC (2019) Breakdown pressure prediction with weight function method and experimental verification. Eng Fract Mech 214:62–78. https://doi.org/10.1016/j.engfracmech.2019.04.016

56. Li K, Smirnov NN, Pestov DA, Qi C, Kiselev AB (2020) An approximate analytical solution for hydraulic fracture opening under non-uniform internal pressure. Mater Phys Mech 44(3):288–305. https://doi.org/10.18720/MPM.4432020_2

57. Wrobel M, Papanastasiou P, Peck D (2022) A simplified modelling of hydraulic fractures in elasto-plastic materials. Int J Fract. https://doi.org/10.1007/s10704-021-00608-w

58. Ji Y, Wanniarachchi WAM, Wu W (2020) Effect of fluid pressure heterogeneity on injection-induced fracture activation. Comput Geotech 123:103589. https://doi.org/10.1016/j.compgeo.2020.103589

59. Ji Y, Yoon JS, Zang A, Wu W (2021) Mitigation of injection-induced seismicity on undrained faults in granite using cyclic fluid injection: a laboratory study. Int J Rock Mech Min Sci 146. https://doi.org/10.1016/j.ijrmms.2021.104881

60. Li Z, Elsworth D, Wang C (2021) Constraining maximum event magnitude during injection-triggered seismicity. Nat Commun. https://doi.org/10.1038/s41467-020-20700-4

61. Fang Z, Wu W (2022) Laboratory friction-permeability response of rock fractures: a review and new insights. Geomechan Geophys Geo-Energ Geo-Resour 8(1)

62. Wei M, Dai F, Ji Y et al (2021) Effect of fluid pressure gradient on the factor of safety in rock stability analysis. Eng Geol 12:106346. https://doi.org/10.1016/j.enggeo.2021.106346

63. Shrivastava K, Hwang J, Sharma M (2018) Formation of complex fracture networks in the Wolfcamp Shale: calibrating model predictions with core measurements from the hydraulic fracturing test site. In: SPE annual technical conference and exhibition

64. Zhao J, Ren L, Shen C, Li Y (2018) Latest research progresses in network fracturing theories and technologies for shale gas reservoirs. Nat Gas Ind B 38(03):1–14. https://doi.org/10.1016/j.ngib.2018.03.007

65. Wang G, Yang D, Kang Z, Zhao J, Lv Y (2019) Numerical investigation of the in-situ oil shale pyrolysis process by superheated steam considering the anisotropy of the thermal, hydraulic, and mechanical characteristics of oil shale. Energy Fuels 33(12):12236–12250. https://doi.org/10.1021/acs.energyfuels.9b02883

66. Gao Y, Detournay E (2020) A poroelastic model for laboratory hydraulic fracturing of weak permeable rock. J Mechan Phys Solids 143

67. Renshaw CE, Pollard DD (1995) An experimentally verified criterion for propagation across unbounded frictional interfaces in brittle, linear elastic-materials. Int J Rock Mechan Min Sci Geo-Mechan Abstr 32(3):237–249

68. Sarmadivaleh M, Rasouli V (2013) Modified Renshaw and pollard criteria for a non-orthogonal cohesive natural interface intersected by an induced fracture. Rock Mech Rock Eng 47(6):2107–2115

69. Zhang R, Li GS, Zhao ZH, Sheng M, Fan X, Chi HP (2014) New criteria for hydraulic fracture crossing natural fractures. Yantu Gongcheng Xuebao/Chinese J Geotech Eng 2014(3):585–588. https://doi.org/10.11779/CJGE201403024

70. Zhao HJ, Ma FS, Liu G, Guo J, Feng XL (2016) Influence of different scales of structural planes on propagation mechanism of hydraulic fracturing. J Eng Geol

71. Llanos EM, Jeffrey RG, Hillis R, Zhang X (2017) Hydraulic fracture propagation through an orthogonal discontinuity: a laboratory, analytical and numerical study. Rock Mech Rock Eng 50(8):2101–2118. https://doi.org/10.1007/s00603-017-1213-3

72. Yao Y, Wang W, Keer LM (2018) An energy based analytical method to predict the influence of natural fractures on hydraulic fracture propagation. Eng Fract Mech 189(2018):232–245

73. Zhao Y, He P, Zhang Y, Wang C (2019) A new criterion for a toughness-dominated hydraulic fracture crossing a natural frictional interface. Rock Mech Rock Eng 2018:1–13. https://doi.org/10.1007/s00603-018-1683-y

74. Zhao Y, Zhang YF, He PF (2019) A composite criterion to predict subsequent intersection behavior between a hydraulic fracture and a natural fracture. Eng Fract Mech 209:61–78. https://doi.org/10.1016/j.engfracmech.2019.01.015

75. Janiszewski M, Shen BT, Rinne M (2019) Simulation of the interactions between hydraulic and natural fractures using a fracture mechanics approach. J Rock Mechan Geotech Eng 11(6):1138–1150

76. Daneshy A (2019) Three-dimensional analysis of interactions between hydraulic and natural fractures. In: Society of petroleum engineers—SPE hydraulic fracturing technology conference and exhibition 2019, HFTC 2019

77. Zeng Y, Cheng W, Zhang X, Xiao B (2020) A criterion for identifying a mixed-mode I/II hydraulic fracture crossing a natural fracture in the subsurface. Energy Explor Exploit 38(6):2507–2520. https://doi.org/10.1177/0144598720923781

78. Zhu D, Du W (2022) A criterion for a hydraulic fracture crossing a frictional interface considering T-stress. J Pet Sci Eng 209. https://doi.org/10.1016/j.petrol.2021.109824

79. Zhao Z, Zhao Y, Jiang Z, Guo J, Zhang R (2021) Investigation of fracture intersection behaviors in three-dimensional space based on CT scanning experiments. Rock Mech Rock Eng 54(11):5703–5713. https://doi.org/10.1007/s00603-021-02587-9

80. Zheng P, Xia Y, Yao T, Jiang X, Xiao P, He Z, Zhou D (2022) Formation mechanisms of hydraulic fracture network based on fracture interaction. Energy 243:123057. https://doi.org/10.1016/j.energy.2021.123057

81. Chuprakov D, Melchaeva O, Prioul R (2014) Injection-sensitive mechanics of hydraulic fracture interaction with discontinuities. Rock Mech Rock Eng 47(5):1625–1640. https://doi.org/10.1007/s00603-014-0596-7

82. Blanton TL (1986) Propagation of hydraulically and dynamically induced fractures in naturally fractured reservoirs. In: Society of petroleum engineers—SPE unconventional gas technology symposium, UGT 1986

83. Warpinski NR, Teufel LW (1987) Influence of geologic discontinuities on hydraulic fracture propagation. JPT J Pet Technol 39(2). https://doi.org/10.2118/13224-pa

84. Chuprakov D, Prioul R (2015) Hydraulic fracture height containment by weak horizontal interfaces. In: SPE hydraulic fracturing technology conference, the Woodlands, Texas, USA

85. Xu W, Zhao J, Rahman SS, Li Y, Yuan Y (2019) A comprehensive model of a hydraulic fracture interacting with a natural fracture: analytical and numerical solution. Rock Mech Rock Eng 52:1095–1113. https://doi.org/10.1007/s00603-018-1608-9

86. Zhao K, Stead D, Kang H, Damjanac B, Donati D, Gao F (2020) Investigating the interaction of hydraulic fracture with pre-existing joints based on lattice spring modeling. Comput Geotech 122:103534. https://doi.org/10.1016/j.compgeo.2020.103534

87. Fu L, Shen R, Pang F, Yang H, Chen K (2019) Experiments on friction and non-steady slip for shale. Diqiu Kexue - Zhongguo Dizhi Daxue Xuebao/Earth Sci J China Univ Geosci 44(11):3783–3793. https://doi.org/10.3799/dqkx.2019.189

88. Wang R, Hu Z, Zhou T, Bao H, Wu J, Du W, He J, Wang P, Chen Q (2021) Characteristics of fractures and their significance for reservoirs in Wufeng-Longmaxi shale, Sichuan Basin and its periphery. Oil Gas Geol 42(06):1295–1306. https://doi.org/10.11743/ogg20210605

89. Jinzhou Z, Yongming L, Song W, Youshi J, Liehui Z (2014) Simulation of complex fracture networks influenced by natural fractures in shale gas reservoir. Nat Gas Ind B 34(01):68–73. https://doi.org/10.1016/j.ngib.2014.10.012

90. Zeng FH, Zhang T, Ma L, Guo JC, Zeng B (2021) Dynamic permeability model of volume fracturing network in deep shale gas reservoir and its application. Nat Gas Geosci 32(07):941–949. https://doi.org/10.11764/j.issn.1672-1926.2021.04.001

91. Dehghan AN, Goshtasbi K, Ahangari K, Jin Y (2015) Experimental investigation of hydraulic fracture propagation in fractured blocks. Bull Eng Geol Environ 74(3):887–895. https://doi.org/10.1007/s10064-014-0665-x

92. Sheng GL, Huang LY, Zhao H, Rao X, Ma JL (2021) Fracture network propagation and gas flow in shale gas reservoirs. J Southwest Petrol Univ (Sci Technol Edn) 43(05):84–96

93. de Pater CJ, Beugelsdijk LJL (2005) Experiments and numerical simulation of hydraulic fracturing in naturally fractured rock. In: American rock mechanics association—40th US rock mechanics symposium, ALASKA ROCKS 2005: rock mechanics for energy, mineral and infrastructure development in the northern regions

94. Tan P, Jin Y, Han K, Hou B, Guo X, Gao J, Wang T (2017) Analysis of hydraulic fracture initiation and vertical propagation behavior in laminated shale formation. Fuel 206:482–493.https://doi.org/10.1016/j.fuel.2017.05.033

95. Zhao Z, Li X, He J, Mao T, Li G, Zheng B (2018) Investigation of fracture propagation characteristics caused by hydraulic fracturing in naturally fractured continental shale. J Nat Gas Sci Eng 53:276–283. https://doi.org/10.1016/j.jngse.2018.02.022

96. Chong Z, Yao Q, Li X (2019) Experimental investigation of fracture propagation behavior induced by hydraulic fracturing in anisotropic shale cores. Energies 12(976):1–16. https://doi.org/10.3390/en12060976

97. Jiang C, Niu B, Yin G, Zhang D, Yu T, Wang P (2019) CT-based 3D reconstruction of the geometry and propagation of hydraulic fracturing in shale. J Pet Sci Eng 179:899–911. https://doi.org/10.1016/j.petrol.2019.04.103

98. Wang J, Guo Y, Zhang K, Ren G, Ni J (2019) Experimental investigation on hydraulic fractures in the layered shale formation. Geofluids 4621038

99. Hou B, Chang Z, Fu W, Muhadasi Y, Chen M (2019) Fracture initiation and propagation in a deep shale gas reservoir subject to an alternating-fluid-injection hydraulic-fracturing treatment. SPE J 24(4). https://doi.org/10.2118/195571-PA

100. Wu S, Li T, Ge H, Wang X, Li N, Zou Y (2019) Shear-tensile fractures in hydraulic fracturing network of layered shale. J Pet Sci Eng 183:106428. https://doi.org/10.1016/j.petrol.2019.106428

101. Chen Z, Li SM, Chen Z, Wang HT (2020) Hydraulic fracture initiation and extending tests in deep shale gas formations and fracturing design optimization. Petrol Drilling Tech 48(3):7

102. Dehghan AN (2020) An experimental investigation into the influence of pre-existing natural fracture on the behavior and length of propagating hydraulic fracture. Eng Fract Mech. https://doi.org/10.1016/j.engfracmech.2020.107330

103. Zhang H, Sheng JJ (2020) Numerical simulation and optimization study of the complex fracture network in naturally fractured reservoirs. J Pet Sci Eng. https://doi.org/10.1016/j.petrol.2020.107726

104. Wu S, Ge H, Wang X, Li T, Gao K (2021) Characterization and quantitative evaluation of hydraulic fracture network based on acoustic emission monitoring. In: 55th U.S. rock mechanics/geomechanics symposium 2021

105. Zhang W (2021) Deep shale hydraulic fracture network volume model and its application. Oil Drill Product Technol 43(01):97–103

106. Abe A, Kim TW, Horne RN (2021) Laboratory hydraulic stimulation experiments to investigate the interaction between newly formed and preexisting fractures. Int J Rock Mech Min Sci 141:104665. https://doi.org/10.1016/j.ijrmms.2021.104665

107. Li S, Li Y, Yang C, Zheng X, Wang Q, Wang Y, Li D, Hu W (2019) Experimental and numerical investigation of the influence of roughness and turbulence on LUT airfoil performance. Acta Mech Sin Xuebao 35(6):1178–1190. https://doi.org/10.1007/s10409-019-00898-3

108. Zhao Y, Zhang Y, Yang H, Liu Q, Tian G (2022) Experimental study on relationship between fracture propagation and pumping parameters under constant pressure injection conditions. Fuel 307. https://doi.org/10.1016/j.fuel.2021.121789

109. Zeng B, Lu D, Zou Y, Zhou J, Li S, Li N, Cao Z (2020) Experimental study of the simultaneous initiation of multiple hydraulic fractures driven by static fatigue and pressure shock. Rock Mech Rock Eng 53(11):5051–5067. https://doi.org/10.1007/s00603-020-02190-4

110. Zang A, Zimmermann G, Hofmann H, Niemz P, Kim KY, Diaz M, Zhuang L, Yoon JS (2021) Relaxation damage control via fatigue-hydraulic fracturing in granitic rock as inferred from laboratory-, mine-, and field-scale experiments. Sci Rep 11(1):6780. https://doi.org/10.1038/s41598-021-86094-5

111. Li Q, Wu X, Zhai C, Hu Q, Ni G, Yan F, Xu J, Zhang Y (2021) Effect of frequency and flow rate of pulsating hydraulic fracturing on fracture evolution. Zhongguo Kuangye Daxue Xuebao/J China Univ Min Technol 50(06):1067–1076

112. Jin W, Arson C (2020) Fluid-driven transition from damage to fracture in anisotropic porous media: a multi-scale XFEM approach. Acta Geotech 15:113–144. https://doi.org/10.1007/s11440-019-00813-x

113. Zheng H, Pu C, Sun C (2020) Numerical investigation on the hydraulic fracture propagation based on combined finite-discrete element method. J Struct Geol 130:1–8. https://doi.org/10.1016/j.jsg.2019.103926

114. Zhao Y, Zhang YF, Tian G, Wang CL, Bi J (2022) A new model for predicting hydraulic fracture penetration or termination at an orthogonal interface between dissimilar formations. Pet Sci 19(6):2810–2829. https://doi.org/10.1016/j.petsci.2022.08.002

115. Zhao J, Ren L, Hu Y (2013) Controlling factors of hydraulic fractures extending into network in shale formations. Xinan Shiyou Daxue Xuebao/J Southwest Pet Univ 35(01):1–9. https://doi.org/10.3863/j.issn.1674-5086.2013.01.001

116. Zhang Y, Long A, Zhao Y, Zang A, Wang C (2023) Mutual impact of true triaxial stress, borehole orientation and bedding inclination on laboratory hydraulic fracturing of Lushan shale. J Rock Mech Geotech Eng. https://doi.org/10.1016/j.jrmge.2023.02.015

Part I
Theoretical Background

Chapter 2
Rock Mechanics in Hydraulic Fracturing Operations

Rock, fracture and fluid mechanics are crucial elements in understanding and engineering design of hydraulic fracture treatments. The combination of rock, fracture and fluid mechanics creates the study of fracture propagation, interaction and sensitivity caused by different treatment variables. The formation to be fractured and the resulting hydraulic fracture morphology is of paramount significance for hydrocarbon migration and extraction.

2.1 Stress

Mechanical stress is usually quantified as second-order tensor invariants. This tensor (N/m^2 or Pa) represents the force acting on a unit area of a surface or a unit volume of the material, which can be expressed by

$$\boldsymbol{\sigma} = \lim_{\Delta A \to 0} \left(\frac{\Delta \boldsymbol{F}}{\Delta A} \right) \tag{2.1}$$

where $\boldsymbol{\sigma}$ is the stress vector, $\boldsymbol{F}$ is the force (traction) vector and A is the contact area of $\boldsymbol{F}$.

The stress has both magnitude and direction. Since the area A of the contact surface is assumed close to zero, the stress reflects a point property. Note that there are some practical limitations in reducing the contact area of the force to zero. For easy calculation, the stress magnitude in experiments and fields is directly determined by dividing $|\boldsymbol{F}|$ by A. Stresses normal to the contact surface can be tensile or compression, while those parallel to the surface are called shear. In the Cartesian coordinate system, there are 9 stress components (σ_{xx}, σ_{yy}, σ_{zz}, σ_{xy}, σ_{yx}, σ_{xz}, σ_{zy}, σ_{yz} and σ_{zx}) in terms of the stress in different directions, of which only 6 (σ_{xx}, σ_{yy}, σ_{zz}, σ_{xy}, σ_{yz} and σ_{zx}) are independent for $\tau_{xy} = \tau_{yx}$, $\tau_{xz} = \tau_{zx}$, $\tau_{yz} = \tau_{zy}$. If there

is no shear stress applied on the surface, the normal stresses become the principal stress, and the stress vector can be written as

$$\boldsymbol{\sigma} = \begin{bmatrix} \sigma_{xx} & \tau_{xy} & \tau_{xz} \\ \tau_{yx} & \sigma_{yy} & \tau_{yz} \\ \tau_{zx} & \tau_{zy} & \sigma_{zz} \end{bmatrix} = \begin{bmatrix} \sigma_1 \\ \sigma_2 \\ \sigma_3 \end{bmatrix} \tag{2.2}$$

The three stress components are perpendicular to each other. In geologic applications, one of the principal stresses is often assumed in the vertical direction, and the other two are horizontally specified by default.

2.2 Stain

Strain represents the relative deformation between material points. If the original distance between the two points is l, after a period of action by force $\boldsymbol{F}$, the distance becomes $l + \Delta l$. The engineering stain is defined by

$$\varepsilon = \frac{\Delta l}{l} \tag{2.3}$$

The strains caused by tensile force correspond to extension whereas those under compressive force correspond to contraction. A shear strain is associated with surfaces sliding over each other. In the Cartesian coordinate system, each direction should have a corresponding strain component consistent with the stress. So, the strain can be expressed by

$$\boldsymbol{\varepsilon} = \begin{bmatrix} \varepsilon_{xx} & \gamma_{xy} & \gamma_{xz} \\ \gamma_{yx} & \varepsilon_{yy} & \gamma_{yz} \\ \gamma_{zx} & \gamma_{zy} & \varepsilon_{zz} \end{bmatrix} \tag{2.4}$$

Similar to stress, six independent components (ε_{xx}, ε_{yy}, ε_{zz}, ε_{xy}, ε_{yz} and ε_{zx}) should also be specified to give the state of strain at a given point.

2.3 Linear Elastic Material and Its Failure

For a linear elastic material, the stress varies linear with the strain, which can be described by Hoek's law under uniaxial stress, i.e.,

$$\sigma_{xx} = E_{xx}\varepsilon_{xx} \tag{2.5}$$

where E_{xx} is the elastic modulus in the x-axis direction. In fact, the deformations in the normal direction (e.g., ε_{xx}, ε_{yy} and ε_{zz}) can affect each other. For instance, the relation between ε_{xx} and ε_{yy} in the x–y plane can be given by

$$\varepsilon_{yy} = -v\frac{\sigma_{xx}}{E} \tag{2.6}$$

where v is the Poisson's ratio ($0 < v < 0.5$).

In the Cartesian coordinate system, the complete relationship between stress and strain is reflected by the so-called elastic constitutive equation

$$\varepsilon_{xx} = \frac{1}{E}\big(\sigma_{xx} - v(\sigma_{yy} + \sigma_{zz})\big)$$

$$\varepsilon_{yy} = \frac{1}{E}\big(\sigma_{yy} - v(\sigma_{xx} + \sigma_{zz})\big)$$

$$\varepsilon_{zz} = \frac{1}{E}\big(\sigma_{zz} - v(\sigma_{xx} + \sigma_{yy})\big)$$

$$\gamma_{xy} = \frac{1}{G}\tau_{xy}, \ \gamma_{yz} = \frac{1}{G}\tau_{yz}, \ \gamma_{xz} = \frac{1}{G}\tau_{xz} \tag{2.7}$$

where G is the shear modulus, a function of elastic modulus and Poisson's ratio, i.e.,

$$G = \frac{E}{2(1 + 2v)} \tag{2.8}$$

When stresses exceed rock strength, the rock fractures and fails. A fracture criterion specifies the critical conditions for which failure occurs in a material. According to different failure mode and scales, the fracture criterion can be constructed by phenomenological theories (Mohr–Coulomb or Hoek–Brown) and mechanistic theories (Griffith, fracture mechanics models) [1].

For shear failure, Mohr–Coulomb criterion is often used, given by

$$\tau = \mu\sigma + C \tag{2.9}$$

where μ is the friction coefficient, C is the cohesion strength. This criterion is applicable for closely compacted rock without appreciable open cracks.

Hoek–Brown criterion is an empirical law obtained from a variety range of triaxial tests on intact rock samples. It is fitted with three parameters (A, B and C) and its expression is

$$\tau = A(\sigma_N + B)^C \tag{2.10}$$

In 1921, Griffith proposed a criterion for tensile failure in brittle materials initiating at the tips of defects (flat elliptical cracks). It is suitable for quasi-static single tensile crack growth based on specific surface energy. For rock failure with a certain tensile strength T_0 later extended by [2], it can be written as.

$$\begin{array}{ll} (\sigma_1 - \sigma_3)^2 - 8T_0(\sigma_1 + \sigma_3) = 0 & \text{if} \quad \sigma_1 > -3\sigma_3 \\ \sigma_3 = -T_0 & \sigma_1 < -3\sigma_3 \end{array} \tag{2.11}$$

Among the above rock failure criteria, Mohr–Coulomb and Griffith are more frequently used in hydraulic fracturing operations as the critical conditions for the initiation of hydraulic fracture. Plain strain is a reasonable approximation in a simplified description of hydraulic fracturing. On this basis, a KGD hydraulic fracture is introduced in the horizontal plane, and a PKN hydraulic fracture model is proposed in the vertical plane (normal to the fracture propagation. For a short fracture (a few meters of length) with considerable height (tens of meters) and small width (millimeters), one can assume the state of plain strain in every horizontal plane (KGD fracture). For a long fracture with the length of hundreds of meters, a limited height of tens of meters and small width in millimeters, one can assume the plane strain in every vertical plane orthogonal to the length direction (PKN fracture). In this book, only KGD model is used for theoretical analysis (see Chaps. 7 and 8).

2.4 Pressurized Crack

Linear elasticity deals with static equilibrium issues. If the fracture propagates stably or at a constant velocity, a "snapshot" of this fractured state can be considered quasistatic, and such a state of equilibrium will be introduced in the following part.

In an infinite plane, there is a hollow two-dimensional "crack" without any appreciable opening and is completely pressurized by internal fluid. The stress state around the fracture should be analyzed if its propagation state needs to be determined. For simplicity, the plane is assumed in the x–y axial plane, and the fracture is propagating in a direction aligned with the x-axis with its center as the origin (Fig. 2.1). The boundary condition of this problem is

$$\begin{array}{ll} \sigma_{yy}(x,0) = -P(x), & 0 \leq x \leq l \\ u_y(x,0) = 0, & x \geq l \\ \tau_{xy}(x,0) = 0, & x \geq 0 \end{array} \tag{2.12}$$

Muskhelishvili [3] has accomplished the pioneering work of the above mathematical model by solving integral equations or applying the integral transformation. This method starts with a function $g(\xi)$ constructed by

$$g(\xi) = \int_0^{\xi} \frac{P(x)dx}{(\xi^2 - x^2)^{1/2}}, \; 0 < \xi < l \tag{2.13}$$
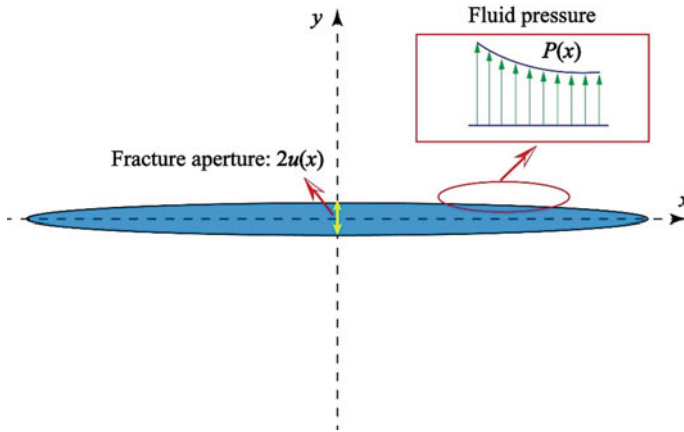
Fig. 2.1 Fracture pressurized by internal fluid

where $g(\xi)$ is modified fluid pressure summing up the fluid effect along the fracture length of l. With known $g(\xi)$, the fracture aperture can be calculated by twice of the normal displacement of any point on the upper side of the crack [4], given by

$$u_y(x, 0) = -\frac{4}{\pi E'} \int_x^l \frac{\xi g(\xi) d\xi}{(x^2 - \xi^2)^{1/2}}, \ x \leq \xi \leq l \tag{2.14}$$

where E' is the plain strain elastic modulus and can be expressed by $\frac{E}{1-v^2}$.

To solve this problem, $g(\xi)$ needs to be differentiable and the fluid pressure should be a function of the location inside the crack. For specific fluid pressure distribution along the crack, the above integrals can be solved in closed form (see Chap. 7).

References

1. Zang A, Stephansson O (2013) Stress field of the earth's crust
2. Griffith AA (1924) Proceedings of the 1st international congress on applied mechanics. Delft, The Netherlands, pp 55–63
3. Muskhelishvili NI (1953) Some basic problems of the mathematical theory of elasticity. Noordhoff, Groningen
4. Griffith AA (1921) Philosop Trans R Soc Lond (Ser A) 221(2):163–198

Part II
Laboratory Observation

Chapter 3
Reservoir Characteristics

3.1 Introduction

Organic matter-rich Marine shale is mostly gray-black stone-containing carbon or silica-rich rock phase. Due to the change of reservoir formation environment, plate extrusion and uneven deposition, the thin layered structure is developed, showing obvious anisotropy characteristics. Researchers have studied the hydraulic fracturing characteristics of shale reservoirs based on indoor tests. However, due to the different reservoir formation conditions, shale properties, and stress environment, the hydraulic fracture morphology and fracture propagation law of shale also show obvious anisotropic characteristics. In this chapter, the Longmaxi Formation shale obtained from Sichuan Basin is taken as the research object. The mineral components, the distribution characteristics of pores and fissures, and the mechanical properties of shale are detected and analyzed by means of XRD, nuclear magnetic resonance (NMR), microscope, scanning electron microscope (SEM), and basic mechanical experiments. On this basis, by comparing the indoor hydraulic fracturing tests of Longmaxi shale and Lushan shale, the hydraulic fracturing characteristics of shale reservoirs under different reservoir formation conditions and stress environments are studied.

3.2 Sample Preparation

3.2.1 Sampling Location

To compare the effects of the Marine sedimentary environment differences on the material properties and fracturing characteristics of shale, the shale specimens obtained from Changning County, Sichuan Province, and the Lushan Mine, Jiangxi Province are taken as test materials (Fig. 3.1). The Longmaxi shale, as the main experimental group, is used to study the hydraulic fracturing characteristics of shale

reservoirs. This kind of shale located at the southern edge of the Sichuan Basin belongs to the Longmaxi Formation of the Silurian system (hereinafter referred to as Longmaxi shale). Affected by the multi-stage tectonic evolution of Changning anticline (deep burial in the early stage, and strong uplift in the later stage) and the deep-water shelf facies sedimentary environment, the Longmaxi shale is characterized by dark mud debris sediment. Its burial depth is generally 2000–4500 m [1, 2], which belongs to the same stratum (about 285 km apart) as Longmaxi Shale in Fuling District, China's main shale gas production area. The Lushan shale, as a comparison group, is mainly used to analyze the disturbance of the hydraulic fracturing effectiveness caused by the difference of rock properties caused by the reservoir formation environment. This kind of shale with a buried depth of 1000–4000 m [3, 4] belongs to the Upper Sinian of the Lower Paleozoic, mainly located in the Jiujiang depression structural block. Due to the tectonic compression and slippage in the later period, local shale has fragmented silification and decarbonization, but the overall content remains stable, that is, the main component is mainly gray-black siliceous shale.

According to the processing and test procedure shown in Fig. 3.2, the regolith outcrop shale is stripped by mechanical cutting first and then cut off the complete rock block. With reference to the sample specifications and standards of the International Society for Rock Mechanics (ISRM), cylindrical (φ50 mm $\times$ 100 mm) and cubic (200 mm $\times$ 200 mm) samples with flatness deviation less than 0.1 mm were prepared by mechanical processing and core drilling sampling methods for uniaxial and true triaxial fracturing tests.
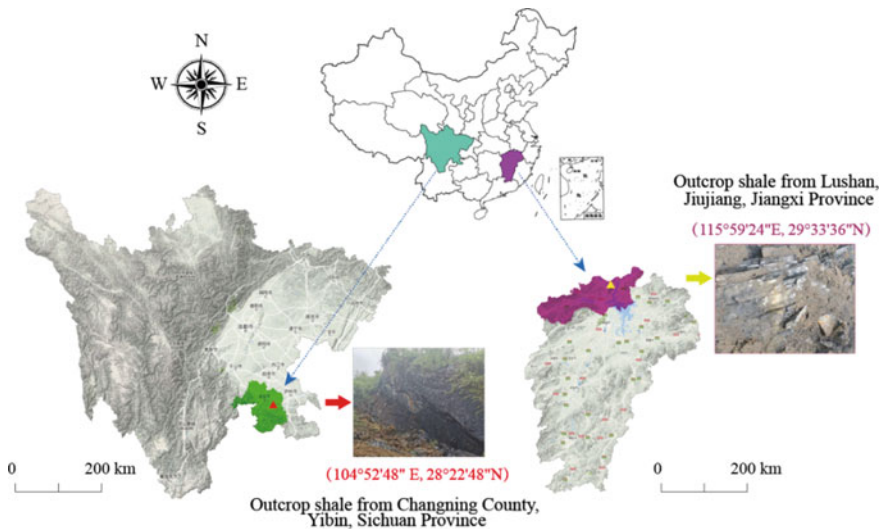
Fig. 3.1 Schematic diagram of shale sampling location
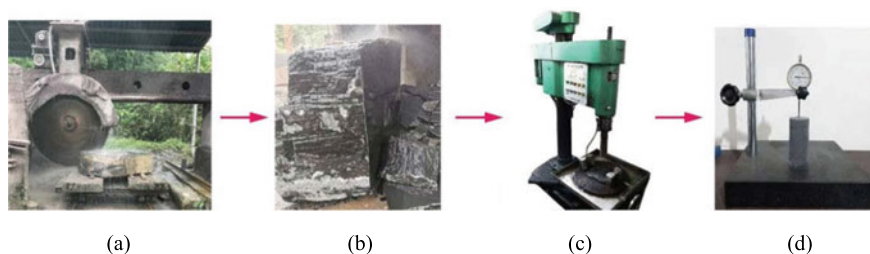
Fig. 3.2 Processing and preparation of rock samples. **a** Open rock block cutting, **b** complete rock block, **c** drill core sampling, **d** end-surface flatness detection

3.2.2 Mineral Composition Characteristics

Small shale pieces were ground to powder with an average particle size of ~ 70 μm. The Brooke D8 Advanced X-ray diffractometer was used to carry out a conventional XRD diffraction test of shale minerals, with a diffraction angle range of 5–90° and a scanning rate of 8°/min. Figure 3.3 shows the X-ray diffraction patterns of two kinds of shale. Based on the whole pattern fitting (WPF) and the Rietveld refined quantitative analysis, the main mineral compositions and relative contents of the two kinds of shale can be determined by using the unique X-ray atlas of each shale component mineral. The relevant results are summarized in Table 3.1.

From Table 3.1, we can see that Longmaxi shale contains 5 types of minerals, mainly quartz and dolomite, where the two types of minerals are similar in content, and the sum is more than 70% of the total content; Lushan shale contains 7 kinds of
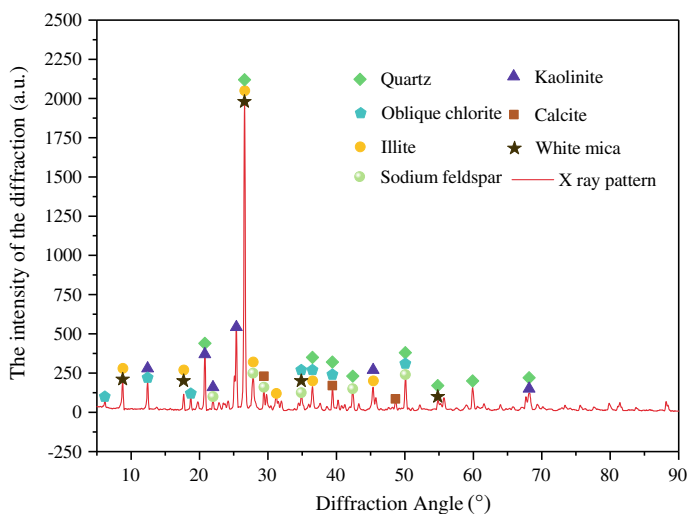
Fig. 3.3 X-ray diffraction pattern of powder shale sample

Table 3.1 Summary of relative mineral content of Longmaxi and Lushan shale

Shale	Ingredient					
	Quartz (%)	Albite (%)	Carbonate minerals (%)	Clay mineral (%)	Clinochlore (%)	Talc (%)
Longmaxi Shale	36.3	–	Calcite 15.3 Dolomite 34	Illite 13.7 Kaolinite 0.7	–	–
Lushan shale	25.4	8.7	Calcite 2.5	Illite 40.7 Kaolinite 1	15.1	6.6

minerals, among which illite accounts for the largest proportion, followed by quartz. Compared with the Longmaxi shale, the Lushan shale has a more complex mineral composition, including quartz, carbonate and clay minerals, sodium feldspar, chlorite and dolomite. According to the calculation method of rock mineral brittleness index (the ratio of quartz content to brittle mineral content), the brittleness indexes of the two shales are 36.3 and 36.5, respectively, indicating that the brittleness of the two types of shale is good and their properties are similar and are prone to produce induced fractures during hydraulic fracturing, forming a complex fracturing network. In addition, the content of clay minerals in Lushan shale is 41.7%, which is approximately three times that of Longmaxi shale, which shows that Lushan shale is dominated by clay minerals. The difference in mineral composition and relative content of the two types of shale reflects the difference in their brittleness and sedimentary environments, which ultimately leads to the difference in shale's physical and mechanical properties.

3.2.3   Microstructural Characteristics

Shale is a fine-grained sedimentary rock with ultra-low permeability and porosity composed of a matrix, pores, and microcracks. Pores and microcracks are the main places and transmission channels for shale gas free or adsorption and their structure, spatial distribution and connectivity determine the reservoir performance of shale reservoirs. According to the International Federation of Pure and Applied Chemistry (IUPAC) classification standards, shale pores can be divided into micropores, mesopores and macropores on the basis of their pore size (as shown in Fig. 3.4). Microcracks are generally considered that width observed in the perspective of millimeter level is generally less than 1 mm, not limited by the distribution of shale particles, and can be manifested as transgranular crack or intergranular crack [5, 6]. Qualitative description and quantitative characterization of shale microstructural features are important in optimizing hydraulic fracturing design and evaluating reservoir rock properties.

Laboratory visualization of rock microstructural features is mainly achieved by means of CT scanning, microscope observation and scanning electron microscope (SEM). However, as shown in Fig. 3.4, these detection methods can vary due to the
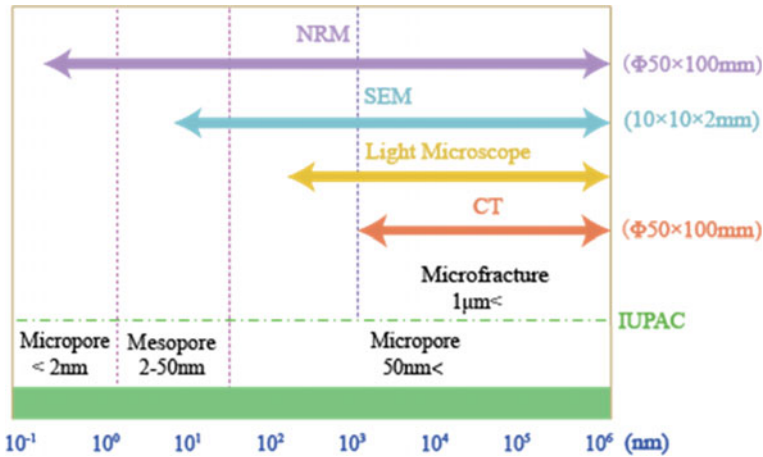
Fig. 3.4 Multiscale pore-fracture characterization techniques

limitation of the sample size or the scanning accuracy. In detail, CT scanning can characterize the internal structural characteristics of rocks, but its accuracy is limited to the micromillimeter scale. Although the microscope and SEM can show the micro and nano rock scale structure, they can only observe the rock surface morphology and require a small sample size. Under high pore pressure stress, shale pores and cracks show strong capillary force, which affects the mechanical properties of rocks and misleads the analysis results. Herein, it is necessary to observe and describe the structural characteristics of shale pores and fissures by comprehensively using microscopy, CT scanning, and SEM at different scales.

(i) Microscopic examination

Under natural light (non-polarized light) irradiation, the surface defects and their distribution of shale samples are directly observed with a microscope. As shown in Fig. 3.5a, it can be observed that the two types of shale are mainly composed of a brownish matrix and bright white phenocrysts. Longmaxi shale particles are evenly distributed, without fracture holes, and local bright white sheet-distributed calcite and dolomite debris (Fig. 3.5b). Compared with Longmaxi shale, Lushan shale is mainly composed of a light gray matrix, with locally developed pores whose aperture change range is larger (10–600 µm) (Fig. 3.5c in red dotted line). The locally developed pores are formed by the complex uneven cementation between white muscovite (light green dotted line), yellow-green chlorite (blue dotted line) and shale matrix (brown material), which is conducive to the transmission and adsorption of reservoir resources.

(ii) CT scan imaging

In the CT test, the three-dimension micro focal industry CT analyzer was used to scan the complete cylindrical sample with Φ 50 mm × 100 mm. As shown in Fig. 3.6, the
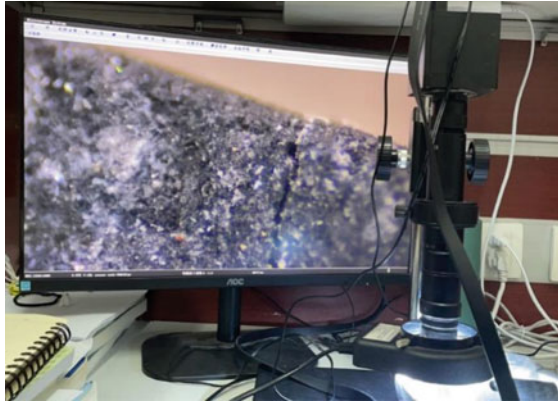
(a) LED natural light microscopy interface
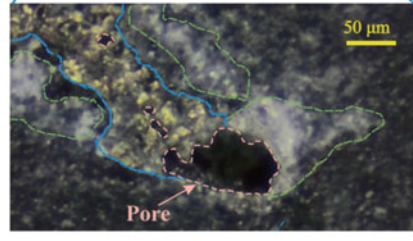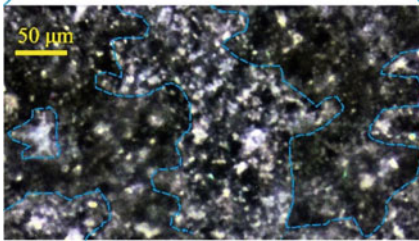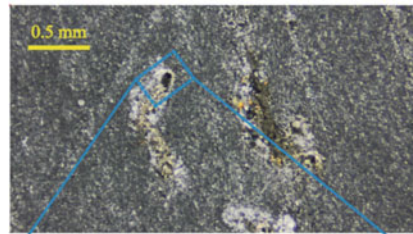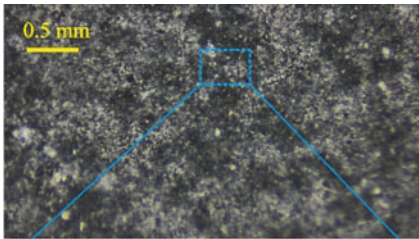
(b) Longmaxi Shale   (c) Lushan shale

Fig. 3.5 Results of microscopic observation of shale surface under natural light

CT scanner is CD-130BX/CT series, with a spatial resolution of 5–10 μm, and can accommodate a sample with a maximum diameter of 130 mm and a maximum mass of 50 kg. The CT scanner with integrated protective structure design, convenient installation, good safety, and strong environmental adaptability can quickly, high-resolution, and directly 3D scan, which meets the precision requirements of micro millimeter scale structure detection of shale pores and fissures.

As shown in Fig. 3.7, the gray material represents a rock matrix with high density. The Longmaxi shale matrix is gray-white, while the Lushan shale matrix is dark-gray. This difference is related to the radiation intensity of the X-ray source and
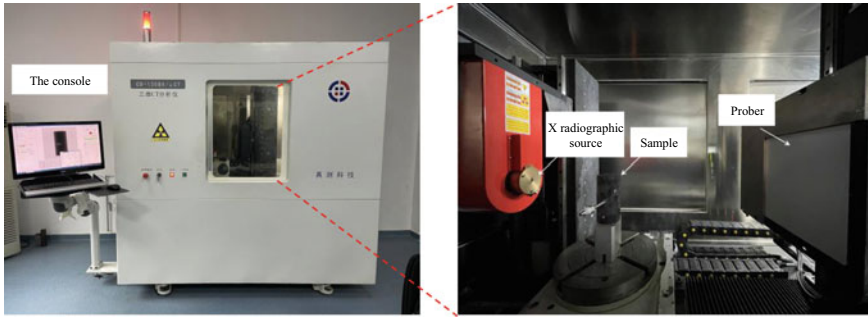
Fig. 3.6 Microfocus 3D industrial CT detector

does not represent the difference between the actual materials. Both types of shales contain light white spotted impurities (blue circles) and sheet-like distributed bedding (dotted ellipses), which may be caused by the legacy of plant fossils or weak interlayer accumulation during diagenetic deposition. In contrast, Longmaxi shale has good homogeneity, while Lushan shale, with more granular impurities and schistose beddings, has poor homogeneity. Combined with the XRD analysis results, it is speculated that the main components of this heterogeneity are inadequately cemented illite clay minerals. On the whole, there are no obvious microcracks and holes in the two types of shale, indicating that the two samples are complete and of good quality. However, their internal structures have some differences, indicating the importance of the subsequent comparison of different types of shale on the test results.

(iii) SEM observation

As shown in Fig. 3.8, the sheet shale sample was sprayed with gold to eliminate the electronic charging effect on the surface of the material and enhance the electrical conductivity of the rock material. Subsequently, the microstructural morphology of the pores and fissures of the sample was observed under the JEOL JSM-7800F field emission scanning electron microscope in Chongqing University. In general, according to the geological genetic differences, shale pores can be divided into organic matter pores, intergranular pores and intergranular pores [7, 8], and microcracks can be divided into matrix companion cracks, diagenetic shrinkage cracks, tectonic stress cracks (bedding cracks and angle cracks) and other cracks [9]. The EDS energy spectrometer was used to analyze the X-ray characteristics of the mineral elements under the specified scale of the sample, and the pore and microcrack types in the sample can finally be determined according to the XRD analysis results.

Figure 3.9 shows the observation results of shale pore structure under the microscope. It can be seen that the pore morphology of the two types of shale is dominated by intragranular pores (yellow arrow points) and intergranular pores (light blue arrow points). The intragranular pore usually refers to the pore formed inside the particle. The intragranular pores with irregular shapes and pore sizes between 0.5 and 3 μm observed in Longmaxi shale are mainly developed in the calcite. Such intragranular
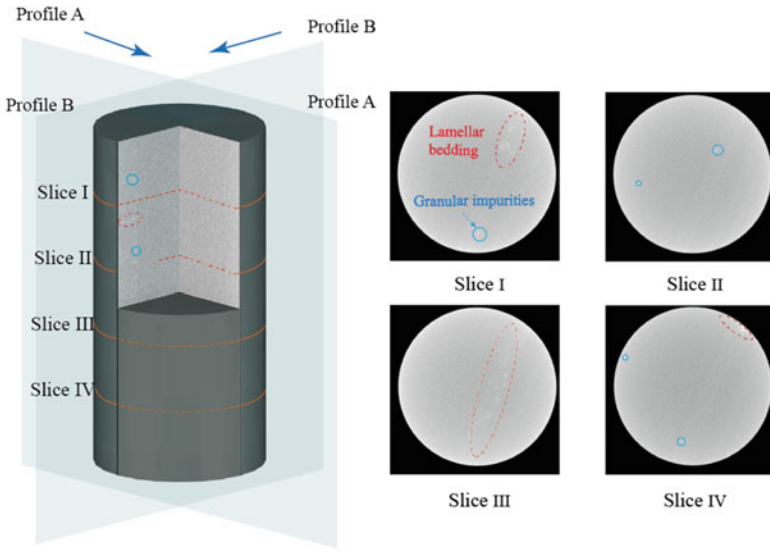
(a) Longmaxi Shale
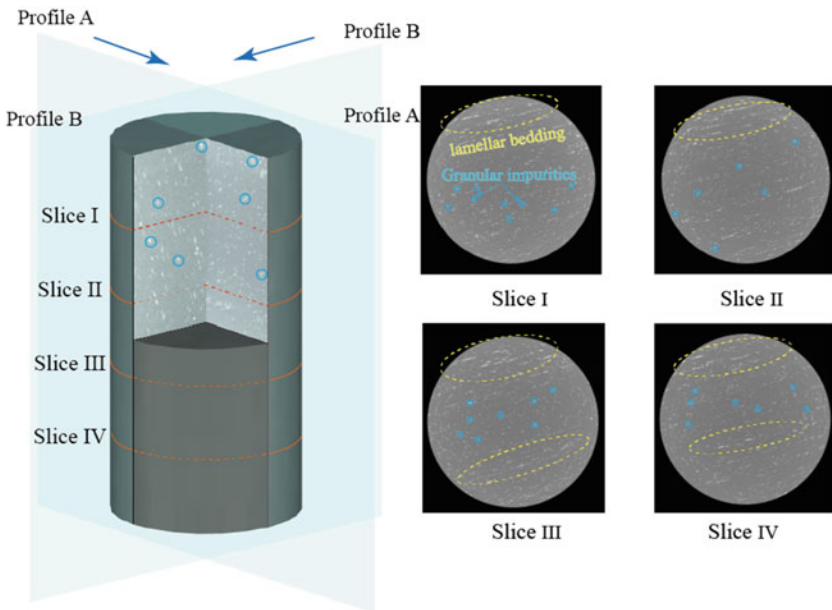
(b) Lushan Shale

Fig. 3.7 Comparison of CT sections of intact specimens between Longmaxi shale and Lushan shale
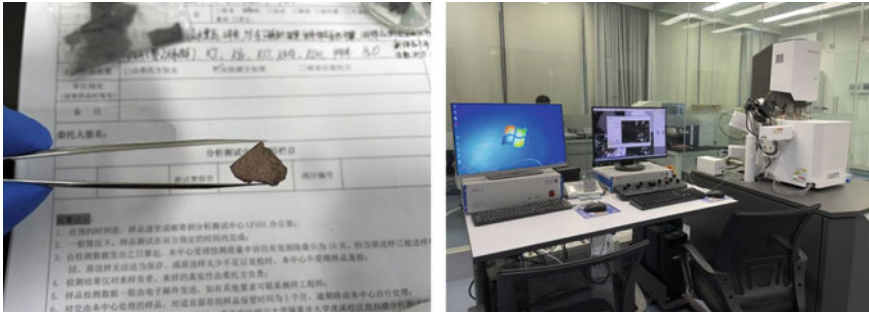
Fig. 3.8 Photographs of the shale sample after gold spraying and the scanning electron microscope

pores are mostly formed by the dissolution of carbonate or alkane organic acid [10], which vary greatly in depth. In addition to the intragranular pore formed by carbonate dissolution, the intergranular pore developed between thin layered illite and other clay minerals (Fig. 3.9b), with a width between 0.2 and 1 μm, is also observed in Lushan shale. The intergranular pore appears in a slit shape and is mostly formed by a series of tectonic geological effects such as diagenetic evolution and biochemical transformation [11]. Intergranular pores are formed between different mineral particles or between minerals and organic matter. Both types of shale have more interparticle pores, which are mostly found in the contact cementing zone between different mineral particles like quartz, illite, calcite, etc. The pore shape is irregular, mainly depending on the shape of pore particles; the variation range of pore size is large, between 1 and 10 μm, affected by the joint influence of formation into rock transformation and interparticle cementing. Compared with the isolated intergranular pores, the intergranular pores have a larger pore size and better connectivity. When the content of intergranular pores in the selected shale is large, it is conducive to forming an effective pore network and promoting the migration and precipitation of alkanes.

Micro-nano scale crack structure of shale is the key to connecting matrix pores and forming a complex fracture network in reservoir stimulation. As shown in Fig. 3.10, both types of shale develop effective microcracks ranging from nano-scale to micrometers-scale, which are specifically manifested as bedding cracks, transgranular cracks and intergranular cracks. The bedding crack develops at a scale of several hundred micrometers (Fig. 3.10a, c), and its contour is basically the same as the lamellar edge. Such microcracks are usually formed by the accumulation of sheet clay mineral matrix in the process of sedimentation. Clastic minerals or organic matter with weak cohesive force filled between lamellas are easy to flake off along mineral bedding under external force [12]. In Fig. 3.10b, d, grain inner cracks and grain margin cracks are distributed at tens of micron scales of shale samples, extending along the particle profile and penetrating matrix, respectively [13]. This kind of crack is usually long, narrow, and tortuous, with no filling minerals, and its opening varies with the propagation path at the range of 2–9 μm, and its length is mostly less than 50 μm.

(a) Longmaxi shale sample

(b) Lushan shale sample
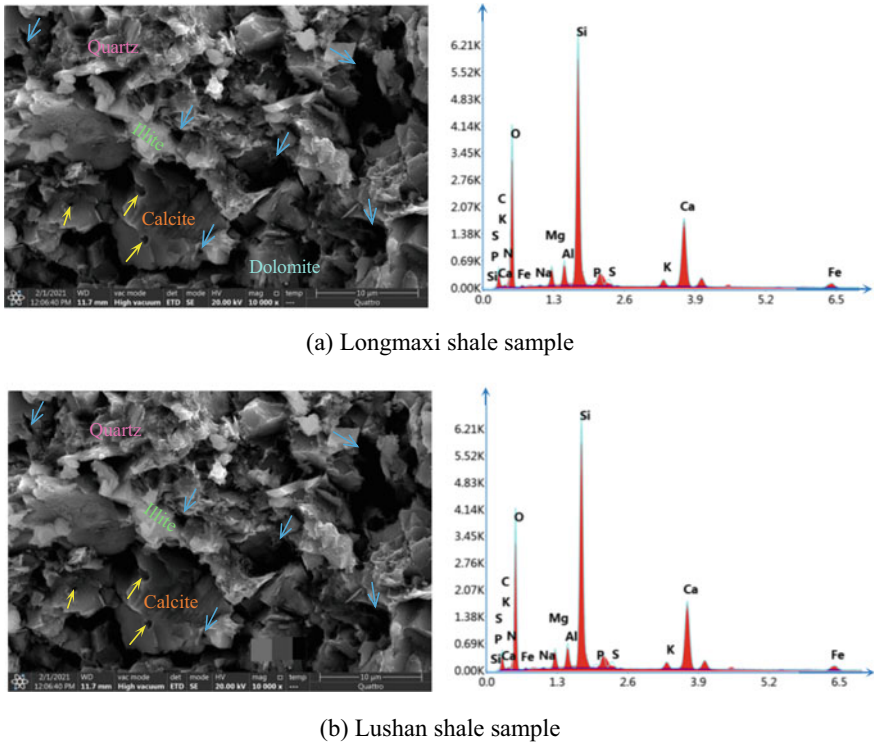
Fig. 3.9   Shale pore types, mineral distribution and X-ray energy spectrum

In addition, grain inner cracks and grain margin cracks do not always occur independently. For example, in Fig. 3.10d, microcracks are respectively grain margin crack, grain inner crack, and grain margin crack from top to bottom. The opening of grain margin crack is the largest, which is related to the uneven external forces caused by thermal expansion, dehydration shrinkage, or tectonic evolution of shale matrix during the formation of microcracks. On the whole, the microcracks of two types of shale are developed, but the size and length of the local microcracks are limited, and the macro crack structures are not formed in a large range. This type of crack structure of reservoir is conducive to effectively communicating the organic matter pores in the matrix in reservoir stimulation, forming migration channels of shale gas, which accelerates the precipitation and migration of alkane resources and improves the shale gas extraction rate.

Through the above comparison, it can be found that the environmental conditions of reservoirs directly affect the mineral composition of rock and the structural morphology of the matrix. Therefore, even if the same construction parameters are selected in the fracturing process, the hydraulic fracturing results of shale will still be significantly different. The different hydraulic fracturing effectiveness resulting

(a) Bedding crack in Longmaxi shale

(b) Intergranular crack in Longmaxi shale

(c) Bedding crack in Lushan Shale

(d) Intergranular and transgranular cracks in Lushan Shale
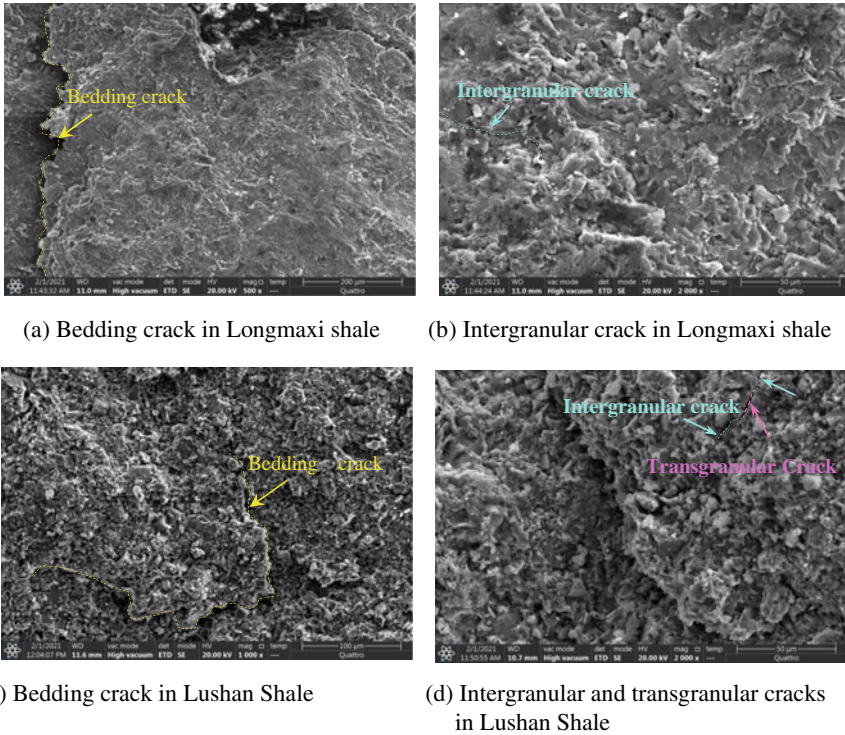
Fig. 3.10 Characteristic of the microcracks in shale samples

from differences in the reservoir environment are discussed in detail in Sect. 3.4.3 of this chapter.

3.3   Determination of the Physical and Mechanical Parameters of Shale

The basic physical parameters of Lushan shale as the comparative group have been discussed in detail by Shang et al. [14]. Therefore, the basic physical properties of Longmaxi shale as the research object are tested and analyzed as follows. Strictly speaking, the physical and mechanical parameters of the rocks should reflect the high temperature and high-pressure characteristics of the in-situ reservoir, so as to have a reference value for the actual construction of the project. However, considering the difficulty of in-situ sampling and test instruments, we focus on fracture propagation form and ignore the influence of high temperature and high pressure, therefore the following physical and mechanical parameters of shale (such as porosity, permeability, uniaxial compressive strength, cohesion, internal friction angle, etc.) are based

on laboratory conditions under the room temperature and pressure. Although the indoor conditions are quite different from the actual shale occurrence environment, the test results can still provide a reference for the subsequent design of the indoor hydraulic fracturing scheme [14–16].

3.3.1 Porosity

Porosity is an important indicator to measure the degree of rock pore structure development, which affects the storage and adsorption of shale gas and the strength and permeability of shale. Therefore, the porosity and permeability of the shale specimen should be clarified before hydraulic fracturing. To ensure the reliability of the measurement results, the porosity was measured by the gaseous method and the saturated mass method, respectively.

Nitrogen gas is selected as the measuring medium. The used shale sample is cylindrical with 50 mm in diameter and 100 mm in height. Before the test, the sample was placed in a 105 °C constant temperature drying incubator for 24 h, and then the shale porosity test was conducted on the BRS-II pulse tester. The BRS-II type pulse tester can automatically measure the porosity of shale specimens in the Hassler Holder based on the Boyle law. Figure 3.11 shows a schematic diagram of the porosity measurement. A total of five sets of porosity tests were conducted, and the porosity results are summarized in Table 3.2. From Table 3.2, the average pore volume is 4.73 mL, and the average porosity is 2.39% with a standard deviation of 0.843%, indicating that the test results are less discrete.

The saturated mass method is to calculate the pore volume in the shale specimen by using the definition of density. The calculation formula is

$$n = \frac{m_w - m_s}{\rho V_s} \tag{3.1}$$
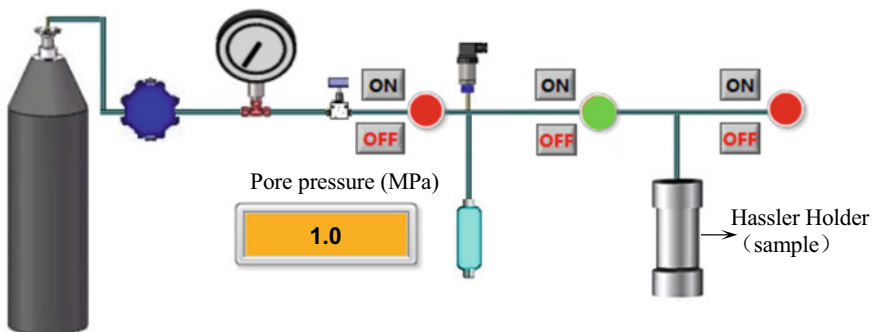
Fig. 3.11 Schematic diagram of the porosity measurement of shale cores

Table 3.2   Results of porosity measurement by gaseous method

No.	H/mm	D/mm	Pore volume/mL	Prosity/%
PG-1	100.12	50.05	4.6	2.33
PG-2	100.22	50.01	4.1	2.08
PG-3	100.26	50.02	5.4	2.74
PG-4	100.13	50.12	7.3	3.69
PG-5	100.19	50.20	2.2	1.11
Average	100.184	50.08	4.72	2.39
Standard deviation	0.053	0.071	1.66	0.843

Table 3.3   Results of porosity measurement by mass fraction method

NO	H/mm	D/mm	Dry sample mass m_s/g	Mass after saturation m_w/g	Porosity/%
PM-1	100.04	50.08	514.752	520.547	2.898
PM-2	100.11	50.16	519.518	525.420	2.977
PM-3	100.01	50.11	517.364	522.955	2.835
Average	100.053	50.117	517.211	522.974	2.903
Standard deviation	0.042	0.033	1.949	1.989	0.058

where, m_w is the mass of the saturated specimen, m_s is the mass of the specimen treated at 105°C for 24 h before saturation, ρ is the density of water at normal temperature and pressure, which takes 1 g/cm^3, and V_s is the sample volume. After calculation, the average porosity of the rock is 2.903%, which is similar to the gas measurement result (2.39%), so the selected shale is a dense rock with low porosity (Table 3.3).

To further analyze the pore size of Longmaxi shale, the NMR technology was used to measure the relative distribution of Longmaxi shale pores. Based on the relationship between the transverse relaxation time of hydrogen nuclei (^{1}H) of the fluid inside the rock pores and the pore radius, the pore size distribution of different pores can be indirectly obtained by using NMR, realizing the analysis of rock microstructure [14]. NMR techniques can characterize pores at a sub-micron scale and offer unique advantages in analyzing small, complex pore structures [15, 16]. Before the test, the samples were placed in a saturator under a vacuum for 24 h to saturate them with water. and then the MRI test was carried out in the MacroMR12-150H-I nuclear magnet core analysis instrument (Fig. 3.12) produced by Suzhou Numai Technology Company. The magnetic field strength was 0.3 T, with the dominant frequency of 12 MHz, and an RF delay time of 0.02 ms.

The wave peak number, distribution form, continuity, and trend of the T$_2$ spectrum reflect the development characteristics of pores at all levels in the sample. Figure 3.13 shows the signal intensity of the nuclear magnetic T$_2$ spectrum with of shale specimens changing with transverse relaxation time. The T$_2$ spectrum of two specimens
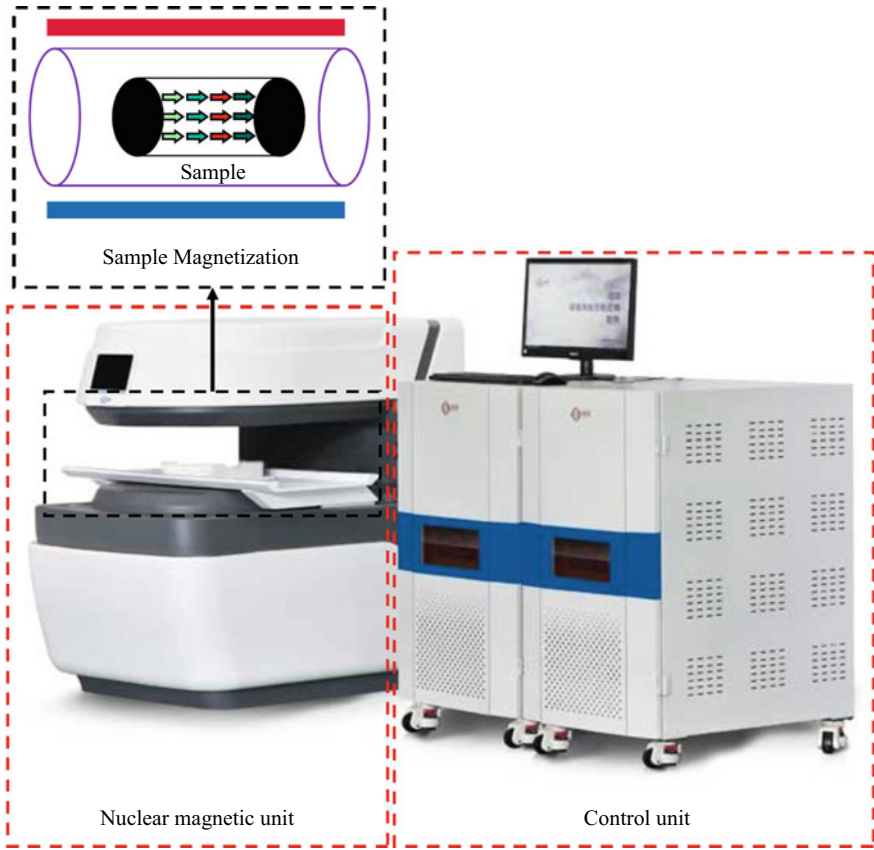
Fig. 3.12 Schematic diagram of nuclear magnetic resonance system

is mainly in the asymmetric discontinuous bimodal form. The signal intensity of the right peak is far less than that of the left peak. The relaxation time range of the left peak is 0.1–10 ms, the relaxation time range of the right peak is 10–100 ms, and the spectral peak area of the left peak accounts for nearly 98.7% of the total area. From the trend of the T_2 spectrum curve, there should be mainly two types of pores divided by the range of pore size in the sample, and the connectivity of the two pores is poor.

Based on the signal intensity parameters of the T_2 spectrum, the ratio relationship between the pore radius and the signal intensity is used to convert the T_2 spectrum curve into the pore throat distribution curve to further analyze the scale size of the pore structure. Its conversion relationship is as follows:

$$r = CT_2 \tag{3.2}$$

where, C is the conversion coefficient, r is the pore radius, and T_2 is relation time.
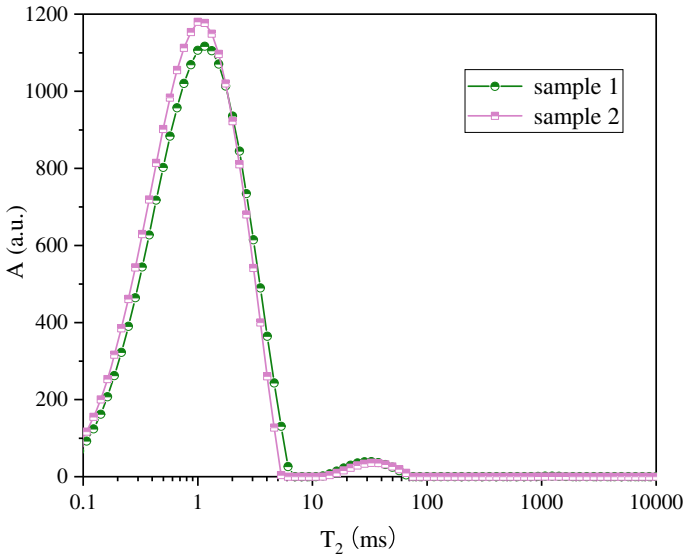
Fig. 3.13 Nuclear magnetic resonance T_2 spectrum of shale specimens

As shown in Fig. 3.14a, b, comparing the pore throat radius distribution of two samples, it can be seen that the pore throat of shale specimens is concentrated at the radius of 0.001–0.01 μm. Based on the definition of IUPAC on micropores (< 2 nm), medium pores (2–50 nm), and macro pores (> 50 nm), the pore radius distribution of two shale specimens can be counted to obtain the percentage of different types of pores in the total pore volume. As shown in Fig. 3.14c, the pores in the sample are dominated by medium pores, followed by micropores, with the minimum proportion of macropores. Combined with the T_2 spectrum curve characteristics, it is continuous in the range of micropores and medium pores, indicating that the connectivity between micro and medium pores is good, while the macropore distribution is relatively independent, demonstrating that macropores have poor connectivity with other types of pores.

3.3.2 Permeability

Permeability, an important indicator to measure the permeability of the rock and evaluate the conductivity of reservoir rocks, is an indirect reflection of the distribution state of rock pore structure, which has been widely used in deep energy exploitation, infrastructure engineering and nuclear waste storage and other fields.

The transient pressure pulse method (referred to as the transient method) is a common method to determine the low permeability rock (< 10^{-19} m^2 [17]), whose testing principle is shown in Fig. 3.15. The rock specimen dried in a 105 °C for
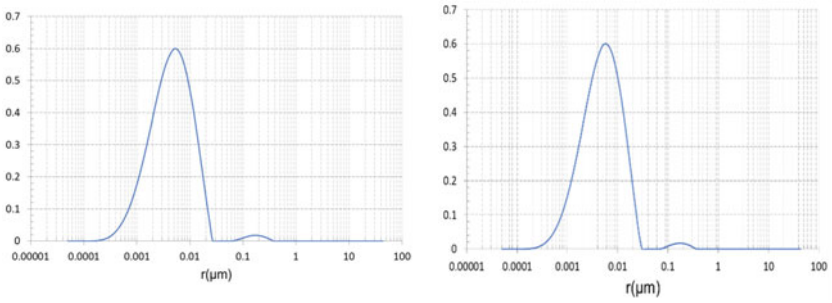
(a) Pore throat radius distribution of sample 1   (b) Pore throat radius distribution of sample 2
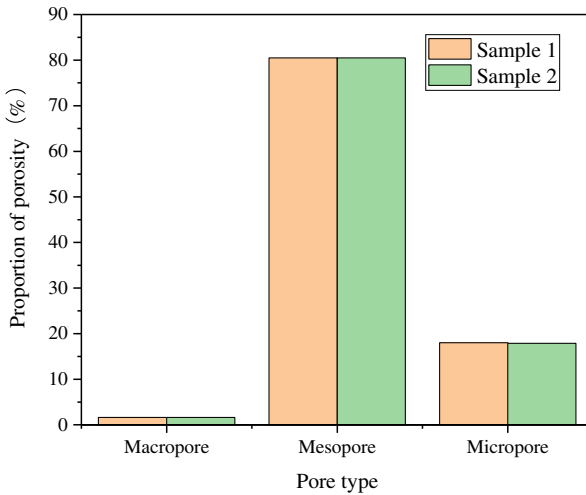
(c) Proportion of different porosity

Fig. 3.14 Pore throat radius distribution and relative content of different pore types of shale specimens

24 h is put into a holder, and a certain amount of initial fluid pressure is injected at both ends of the specimen to balance the upstream and downstream pressure. After the upstream and downstream pressures are stabilized, the constant pulse pressure is applied to the upstream end of the sample. The permeability of the rock is calculated by recording the upstream and downstream pressure changes of the sample using the following equation [18].

$$K = \frac{\alpha \mu \beta L}{\left(\frac{1}{V_u} + \frac{1}{V_d}\right) A} \tag{3.3}$$
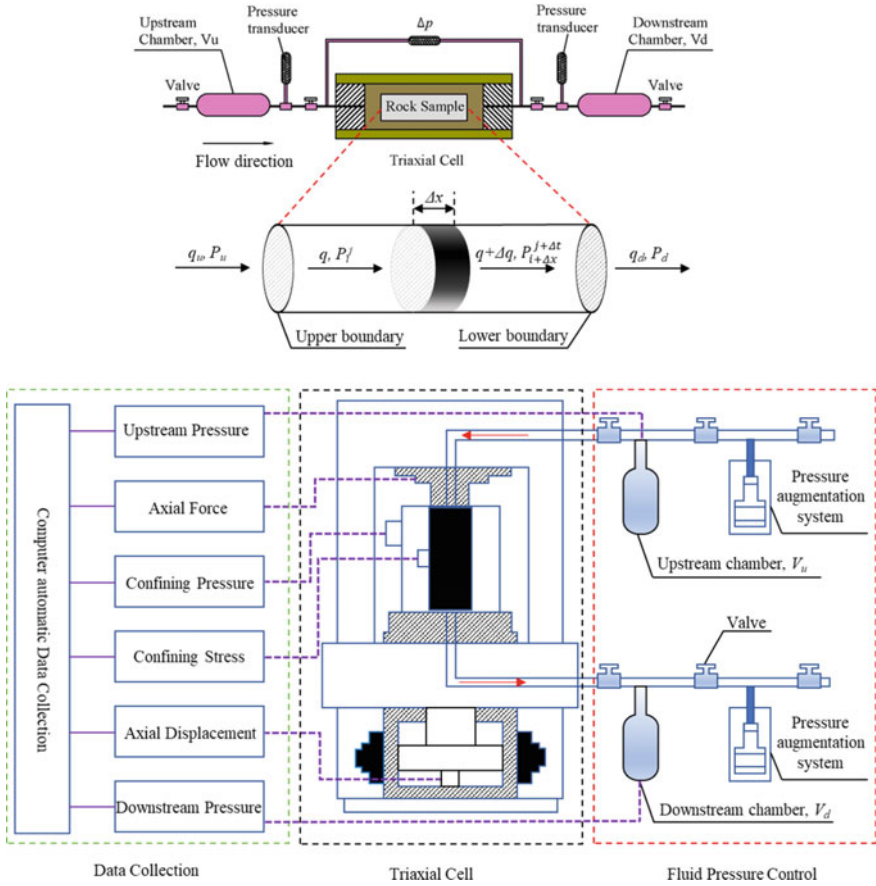
Fig. 3.15 Schematic diagram of the permeability measurement of shale cores

where, K is the rock permeability (permeability coefficient), μ is the gas dynamic viscosity, β is the fluid compression coefficient, L is the sample length, V_u and V_d are the upstream and downstream gas chamber volumes, whose value is 2.199×10^{-5} m^{-3} and 2.102×10^{-5} m^{-3}, respectively, A is the sample's cross-sectional area, α is the attenuation coefficient, which can be calculated by upstream and downstream pressure difference [19], and its calculation formula is expressed as

$$\alpha = -\frac{1}{t} \ln \frac{P_u(t) - P_d(t)}{P_u(0) - P_d(0)} = -\frac{1}{t} \ln \frac{\Delta P(t)}{\Delta P(0)} \tag{3.4}$$

where t is the fluid permeability time, $P_u(t)$ and $P_d(t)$ correspond to the upstream and downstream pressure values at time t (t = 0 corresponds to the initial time), and the upstream and downstream pressure differences at different times are $\Delta P(t)$ and $\Delta P(0)$, respectively.

Table 3.4 Results of permeability measurement by pulse-test method

H/mm	D/mm	$\Delta P(0)$/MPa	$\Delta P(t)$/MPa	t/s	μ/μPa·s	$\beta/10^{-4}$ MPa	$K/10^{-22}$ m^2
99.91	50.07	0.27	0.08	44,794	17.975	4.642	1.172
100.07	50.10	0.33	0.12	61,524	17.996	4.398	2.556
100.03	50.03	0.58	0.28	21,380	18.136	4.329	1.551
Average permeability							1.76
Standard deviation of permeability							0.583

Table 3.4 makes statistics on the upstream and downstream pressure decay trend, the gas permeability time, the dynamic viscosity of the gas, and the compression coefficient. According to Eqs. (3.3) and (3.4), the average permeability of the shale specimens is 1.76×10^{-22} m^2 with a standard deviation of 0.583×10^{-22} m^2.

To sum up, the rocks of the Longmaxi shale gas reservoirs in the Changning area are dense in structure, characterized by an ultra-low porosity whose average value is 2.903% and an ultra-low permeability whose average value of 1.76×10^{-22} m^2.

3.3.3   Basic Mechanical Properties of Longmaxi Shale

The basic mechanical properties of the rock, such as uniaxial compressive strength, elastic modulus, Poisson ratio, splitting tensile strength, cohesion and internal friction angle, are the macroscopic characterization of the bonding effect of microscopic mineral and the stress evolution of the pore throat structure. Mastering the basic mechanical properties of the reservoir rocks is the basis for the subsequent analysis of the hydrofracturing mechanism and the dynamic process of the initiation, propagation, and intersection of hydraulic fracture, which can provide an important reference for the subsequent theoretical calculation of the hydrofracturing and the calibration of simulation parameters of rock fracture evolution.

The basic mechanical properties of shale were tested on the DSZ-1000 rock mechanics test machine as shown in Fig. 3.16. The DSZ-1000 type rock mechanics test machine is composed of hydraulic power system, servo control system, data monitoring and acquisition system, test platform and operating platform, which can perform mechanical tests such as uniaxial compression, triaxial compression, rock rheology, cyclic loading and unloading, etc. The maximum axial pressure is 1000 kN, whose adjustable loading rate range is 0.1–100 mm/min, the maximum circumferential confining pressure is 60 MPa, whose loading rate range is 0.1–60 MPa/min, and the measurement accuracy range of pressure and displacement is $\leq \pm 0.5\%$ FS. The rigidity of the testing machine is 5 GN/m. The LVDT circumferential and axial strain gauges with an accuracy of 0.25% FS are installed, and they can withstand up to 60 MPa hydrostatic pressure, meeting the technical requirements for testing the basic mechanical parameters of rocks.
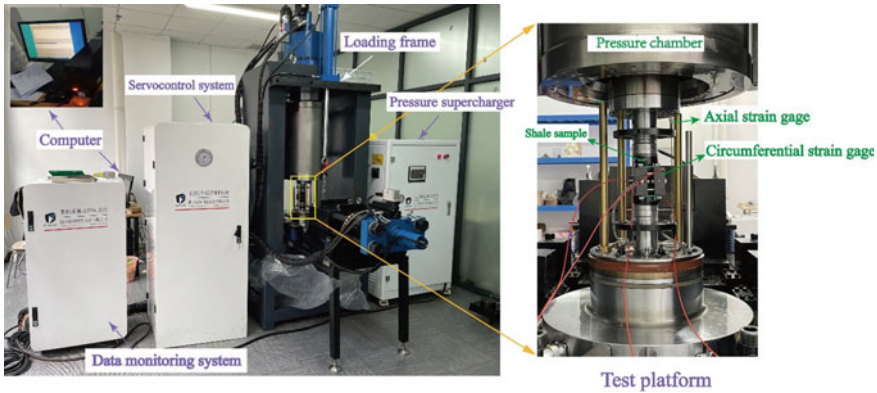
Fig. 3.16 DSZ-1000 rock mechanics test system

(i)   Uniaxial compressive strength, elastic modulus, and Poisson ratio

With reference to the methods recommended by the International Society for Rock Mechanics (ISRM), cylindrical samples with a diameter of 50 mm and a height of 100 mm are selected for uniaxial compressive strength, elastic modulus and Poisson ratio tests of shale. To reduce the discrete error of sampling, three sets of uniaxial compression tests were performed successively, and the sample numbers were UC-1, UC-2 and UC-3. Displacement mode with a loading rate of 0.1 mm/min was used to control the loading process. The sample is sheathed with a heat-shrinkable tube to prevent the splashing of fragments when the rock sample is damaged, causing accidental injury to the tester and damaging the instruments and equipment.

Figure 3.17 shows the stress–strain curve of uniaxial compression. Compared with the uniaxial compression stress–strain curve of conventional rock (such as sandstone) [20], the curvature of initial axial strain of Longmaxi shale is low, and its circumferential strain increases slowly. The overall change of curve in the compaction process is not obvious, indicating that the deformation caused by pore compaction is small, the shale matrix is dense, and the structure of pore microcracks in the sample is not developed. In terms of the rock deformation response, the deformation in the linear elastic stage of the rock accounts for a large proportion. With the increase of axial strain, the growth rate of circumferential strain increases, and the number of microcracks in the rock increases. Subsequently, the rock was almost fractured directly beyond the yield stage, accompanied by a significant splitting sound, and no residual strength appeared after the peak, showing obvious brittle characteristics. In terms of the fracture morphology of intact shale (Fig. 3.18), the tensile failure is dominant in three samples, and -3 specimens UC-2 and UC have a single inclined plane shear failure. The shear plane is generally short, which may be related to the orientation of potential bedding in the specimen. The vein-like secondary fractures are attached around the main fracture. The obvious compression fragmentation and flake exfoliation can be seen after removing the heat shrinkage tube (Fig. 3.18d). The thickness of the fragments is less than 10 mm, and the fragments whose length is less
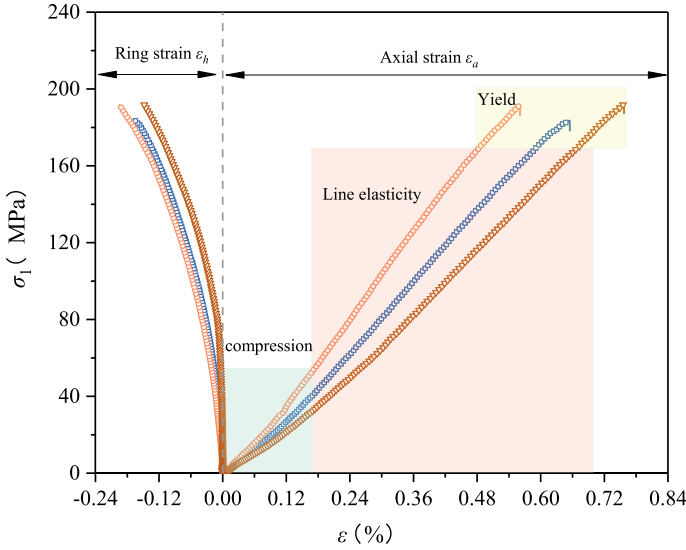
Fig. 3.17 Curves of stress versus strain during the process of uniaxial compression

than 60 mm account for 94% of the total, indicating that the degree of compression crushing is relatively high.

The geometry dimensions and the measured mechanical parameters of the uniaxial compression of the specimen are summarized in Table 3.5. ρ is the density of the specimen, σ_p is the uniaxial compressive strength of the rock, E is the elastic modulus of the rock, E_{50} is the secant slope of the stress–strain curve at 50% axial stress, v is the Poisson ratio, $\varepsilon_{a\text{-max}}$ is the peak of axial strain, $\varepsilon_{h\text{-max}}$ is the peak of circumferential strain. From the standard deviation calculated from the three sets of test data, the shape and density of the selected specimens are consistent. The standard deviation of the measured mechanical parameters is within a reasonable range, indicating that the shale specimens have a uniform texture and stable properties, which can be used for the subsequent study on the change of external factors in the shale hydraulic fracturing process. As can be seen from Table 3.5, the average uniaxial compressive strength of shale samples is 189.25 MPa, the average elastic modulus is 31.29 GPa, and the average Poisson ratio is 0.119.

(ii)   Splitting tensile strength

The Brazilian splitting method is commonly used to indirectly measure the tensile strength through the lateral tension of rock caused by vertical compression. The shale disc sample with a diameter of 50 mm and a thickness of 25 mm can be subjected to the Brazilian splitting test on the DSZ-1000 rock mechanics testing machine by using the fixture shown in Fig. 3.19a. The fixture is made of solid steel, with strong rigidity, small deformation, and low storage elastic energy. It is embedded groove and equipped with a filler strip with a diameter of 1 mm to ensure that the specimen

(a) UC-1   (b) UC-2

(c) UC-3   (d) The sample fragmentation form after
                                removing the thermal tube
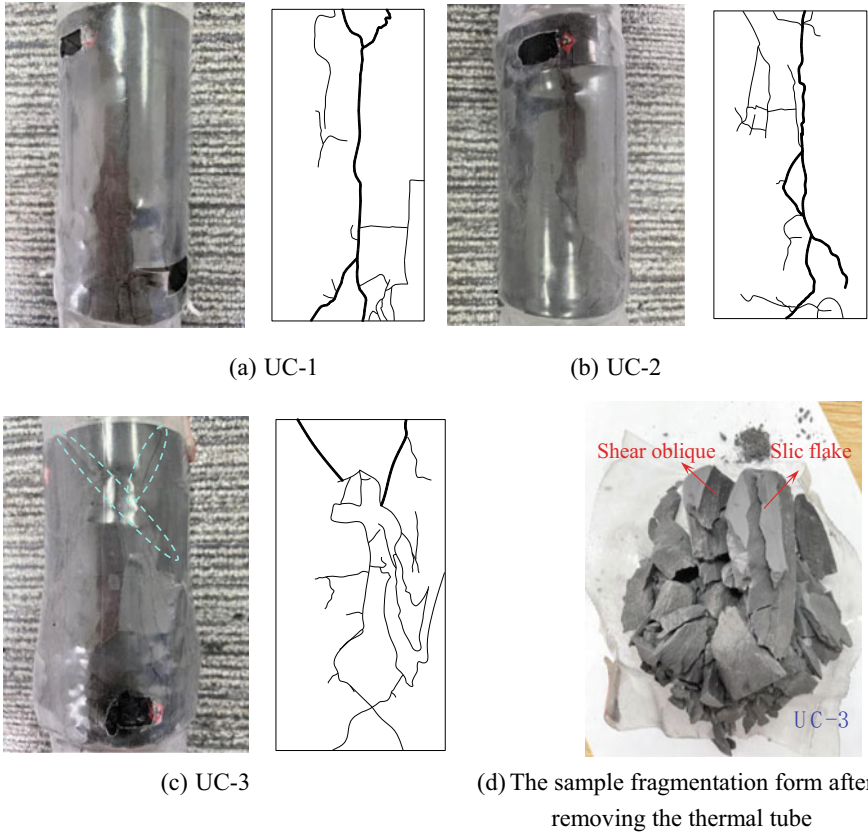
Fig. 3.18 Fracture morphology of shale samples under uniaxial compression state

cracks along the centerline. During the test, the initial pressure of 100 N is loaded
to fix the specimen. Then, the specimen is loaded at a rate of 0.05 mm/min in a
displacement-controlled manner until the specimen is broken.

The specimen bears the line load in the thickness direction, and the tensile strength
calculation formula is

$$\sigma_t = \frac{2P}{\pi DT} \tag{3.5}$$

where P is the maximum axial load, D is the specimen diameter, and T is the specimen
thickness.

The splitting failure effect of the disc specimen is shown in Fig. 3.19b. It can be
found that the four groups of specimens are basically subject to symmetrical tensile
failure along the loading direction, and the specimen is divided by the fracture along
the loading direction, forming a relatively regular linear fracture. Except for a small
amount of flaking fragments at the loading point, no fragments and rock debris

Table 3.5 Summary of shale mechanical parameters from uniaxial compression tests

No.	H/mm	Φ/mm	ρ/g·cm^{-3}	σ_p/MPa	E/GPa	E_{50}/GPa	ν	$\varepsilon_{a\text{-max}}$ (10^{-3})	$\varepsilon_{h\text{-max}}$ (10^{-3})
UC-1	100.31	50.15	2.642	183.76	30.61	27.35	0.120	6.54	1.69
UC-2	100.26	50.24	2.634	191.54	34.93	34.15	0.185	5.61	1.96
UC-3	100.33	50.08	2.631	192.46	28.34	23.46	0.052	7.57	1.49
Average	100.3	50.16	2.636	189.25	31.29	28.32	0.119	6.57	1.71
Standard deviation	0.029	0.065	0.005	3.902	2.733	4.418	0.054	0.801	0.193
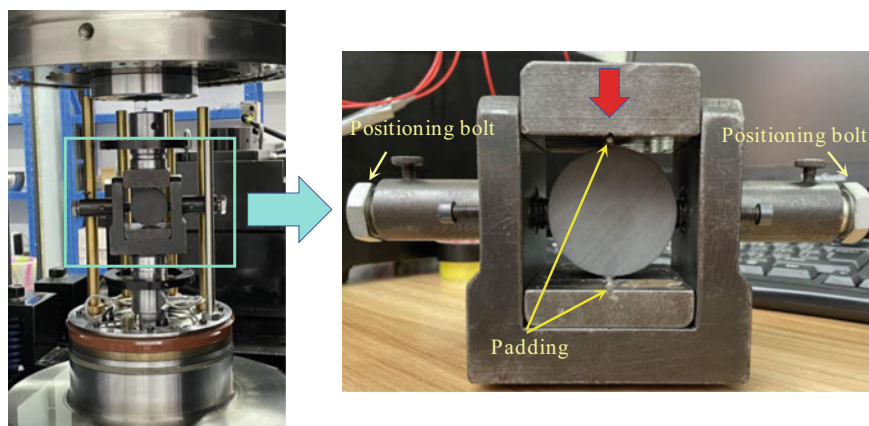
(a) Brazilian splitting test device
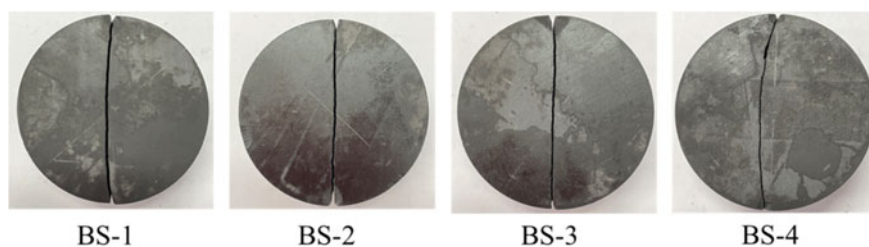
(b) Broken form

Fig. 3.19 Brazilian splitting test of shale disks

occurred elsewhere, indicating that the damage to the specimen is a typical tensile failure. Using Eq. (3.5) and Table 3.6, the average split tensile strength of shale samples is 6.71 MPa and its standard deviation is 1.147.

Table 3.6 Results of Brazil splitting tests

No.	Diameter Φ/mm	Thickness T/mm	Peak load P/kN	Splitting tensile strength σ_t/MPa
BS-1	50.12	24.99	13.40	6.81
BS-2	50.04	24.97	13.18	6.72
BS-3	50.08	25.03	9.91	5.03
BS-4	50.22	24.96	16.28	8.27
Average	50.12	24.99	13.19	6.71
Standard deviation	0.067	0.027	2.256	1.147

(iii)   Cohesion and internal friction angle

Based on the triaxial compression loading module of the rock mechanical test system shown in Fig. 3.16, the conventional triaxial compression test of shale is carried out to obtain the cohesion and internal friction angle of shale. Three sets of shale cylinder specimens (Φ 50 $\times$ 100 mm) marked TC-1, TC-2, and TC-3, respectively, were taken, corresponding to the confining pressure (σ_{3c}) of 5, 10, and 20 MPa [20]. The confining pressures of different gradients were set to calculate cohesion and internal friction angle using the Mohr strength envelope theorem. The stress control mode with a loading rate of1 MPa/min was used to control the confining pressure. It remained constant when the confining pressure increased to the target value. Then, the displacement control mode with a loading rate of 0.1 mm/min was used to increase the axial pressure until the specimen was damaged. The strength and deformation parameters of the rock were recorded in the loading process, and the fracture morphology of the rock was observed.

Figure 3.20a shows the stress–strain curve of shale specimens under different triaxial stress states. Compared with the uniaxial compression curve, the curve shown in Fig. 3.20a almost has no the compression stage and directly reaches the linear elasticity stage, which shows that the different stress and strain test curves in the initial compression stage coincide because the pores in the sample have been compacted by the confining pressure before the application of deviatoric stress. With the increase of the confining pressure, the rock elastic modulus increases, and the peak of axial stress also correspondingly increases. The rock volume strain is positive and increases with the confining pressure, indicating that the increase of confining pressure has a positive effect on the increase of rock deformation. Figure 3.20b shows the fracture morphology of the shale specimen after the test. Under the action of confining pressure, only a single oblique main fracture with a small number of secondary fractures was observed in the specimen. After removing the heat shrinkage pipe, the specimens can still maintain strong integrity which differs from the almost complete fracture morphology under uniaxial compression.

The cohesion and internal friction angle are calculated by the Mohr strength envelope theorem [21] based on the statistics of the peak value of axial pressure of each group of samples and the results of the uniaxial compression test (mean value). The calculation equations are as follows:

$$c = \frac{B}{2\sqrt{K}} \tag{3.6}$$

$$\varphi = \tan^{-1}\frac{K-1}{2\sqrt{K}} \tag{3.7}$$

where c is the cohesion and φ is the internal friction angle, K is the slope of the linear fitting curve of the measured data points in the coordinate space between the peak value of axial stress σ_{1p} (longitudinal axis) and the confining pressure σ_{3c} (transverse axis), and B is the intercept of the fitting curve on the longitudinal axis
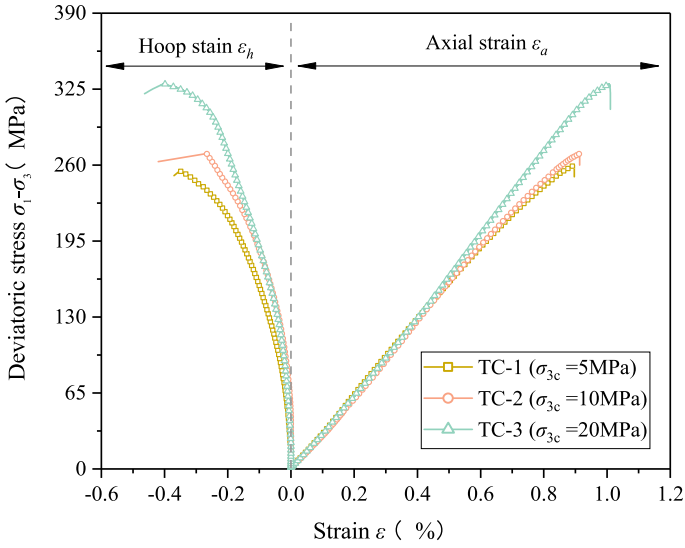
(a) Stress- strain curves

TC-1   TC-2   TC-3

(b) fracture morphology

Fig. 3.20 Curves of stress versus strain and fracture morphology of shale specimens under different confining pressures

which actually represents the uniaxial compressive strength value estimated by the triaxial compression test parameters.

Figure 3.21 shows the linear fitting results of the peak value of the axial stress under different confining pressure conditions. By calculation, K is 7.259, B is 208.603, and the fitting accuracy is 0.949, indicating a strong linear correlation between the
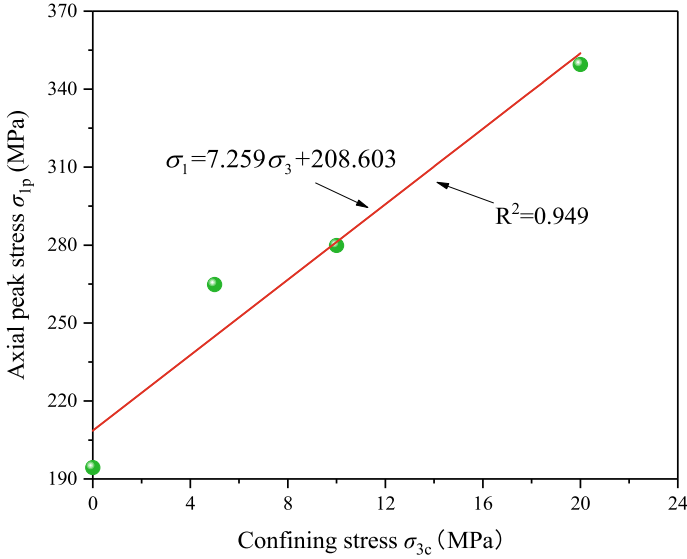
Fig. 3.21 Peak values of axial stress under different confining pressures

confining pressure and the peak of axial stress. Substituting K and B into Eqs. (3.6) and (3.7), the cohesion is 38.71 MPa and the internal friction angle is 49.27. The geometric dimensions, strength, and deformation parameters of shale specimens are summarized in Table 3.7.

3.4   Uniaxial Hydraulic Fracturing Characteristics

Under the uniaxial stress conditions, due to the relevant variables being better controlled, the evolution mechanism of initiation and propagation of hydraulic fracture was mainly studied to clarify the formation process and micromorphology characteristics of fracture under different conditions [22]. Before the simulation of the true hydraulic fracturing process in the laboratory, hydraulic fracturing tests under simple and ideal stress conditions are often carried out to eliminate the disturbance effect of different stress states on hydraulic fracturing characteristics [23–26], which directly reflects the mechanical response characteristics of the specimen under external hydraulic injection [23]. Therefore, in this section, the shale hydraulic fracturing tests under the ideal uniaxial stress state were carried out to explore the hydraulic fracture characteristics and fracture propagation law without the confining pressure.

To facilitate fluid injection, a central hole with a 6 mm diameter and 55 mm depth was drilled on one end face of the shale specimen to model the injection hole, as shown in Fig. 3.22. In this injection mode, as the fluid accumulates in the hole, the

Table 3.7 Size and parameters of strength and deformation of shale specimens used for conventional triaxial compression experiments

No.	Φ/mm	H/mm	Density/g/cm^3	σ_{3c}/MPa	σ_{1p}/MPa	E_t/GPa	$\varepsilon_{t a\text{-max}}$ (10^{-3})	$\varepsilon_{\text{th-max}}$ (10^{-3})	$\varepsilon_{\text{v-max}}$ (10^{-3})
TC-1	50.14	100.11	2.644	5	264.79	31.14	8.96	3.53	1.9
TC-2	50.13	100.07	2.642	10	279.83	32.96	9.14	2.67	3.8
TC-3	50.07	99.98	2.664	20	349.49	35.57	12.07	4.04	3.99
Cohesive c/MPa						38.71			
Internal friction angle φ/°						49.27			

Fig. 3.22 Conventional fracturing method by injecting water from one specimen end face

stress concentration is prone to generate near the fluid outlet, prompting the fracture to initiate at the bottom of the specimen (near the water outlet), rather than the bottom of the drilling hole. Then, as the fluid flows out along the fracture, the subsequent propagation of the fracture cannot be maintained, resulting in incomplete fracturing of the specimen, as shown in Fig. 3.23. In addition, in this injection mode, the entire inner wall of the borehole is in direct contact with the fluid. Under the action of internal high pressure, fluid can penetrate into the rock matrix, which will disturb the subsequent breakdown pressure and fracture morphology of the shale specimen, leading to the experimental results do not truly reflect the hydraulic fracturing performance of the sample. Based on this, the author independently designed the inlet tube seal pipe valve to carry out the uniaxial hydraulic fracturing test by lateral injection. This lateral injection mode can truly reflect the actual (through the bore) hydraulic fracturing process, easy to observe the sample surface fracture propagation morphology in the hydraulic injection process, and can avoid incomplete fracturing phenomenon.

3.4.1 Experimental Set-Up

(i) Design of the inlet pipe seal pipe valve parts

To ensure the sealing effect, a set of injection pipe sealing pipe valve devices was designed (Fig. 3.24). The device is installed with two-way nut (1), positioning ferrule
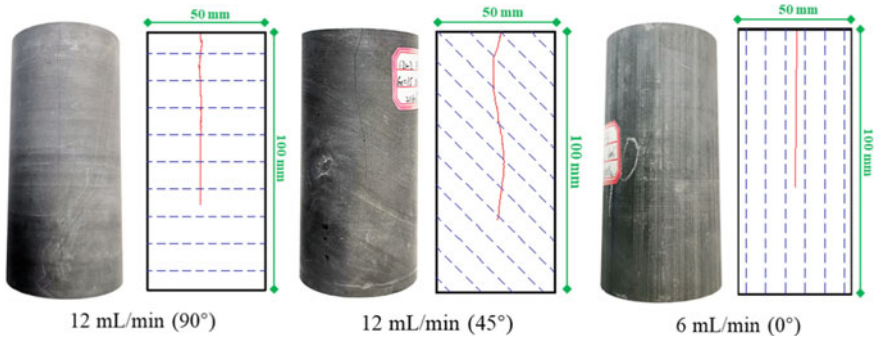
Fig. 3.23 Incomplete fracturing of specimens under condition of injecting water from sample end

(2), hexagonal hollow bolt (3) and incident steel pipe (4). The two-way nut, locating ferrule, hexagon hollow bolt and steel pipe are installed along the same axis. The assembly combination effect and principle are shown in Fig. 3.24.

The advantages of the device are shown as follows:

Positioning sleeve (2): the middle part of the outer wall is the arc wall, the diameter of the upper and lower edges of the positioning sleeve outer wall is less than the maximum diameter of the arc wall, and the part of the positioning sleeve outer wall near the two end is the inclined wall, the arc wall and the inner wall of the double pass nut (6) seal, to prevent the leakage of the injected fluid. By setting the outer wall of the positioning sleeve to the inclined wall and arc wall combination structure, in the positioning sleeve into the double nut and taking out from the double nut, so that the inclined wall to take out and put easier, the arc wall to ensure that the positioning sleeve and the double nut inner wall sealing, effectively avoid water through the outer

1-Two way nut
2-Positioning ferrule
3-Hexagon hollow bolt
4-Incident steel pipe
5-Threaded section
6-Incident pipeline interface

Fig. 3.24 Schematic diagram of sealing device of injection tube

wall along the incident steel pipe, greatly improve the sealing of the incident device. Injection steel pipe (4): the outer wall under the hexagonal hollow bolt with rough thread Sect. 3.5, the thread can effectively increase the contact area of the outer wall of the incident steel pipe and sealant, at the same time and increase the sealant and the incident steel pipe wall friction, avoid sealant sliding on the incident steel pipe wall, ensure the seal viscosity maximization, prevent liquid leakage along the wall, which can greatly improve the sealing effect of fluid injection. The smooth inner wall of the incident steel pipe can effectively reduce the resistance of the fluid when passing through the incident steel pipe, avoid the impact of the fluid fluctuations on the test results, reduce the load of the water pressure pump, and improve the stability of the device.
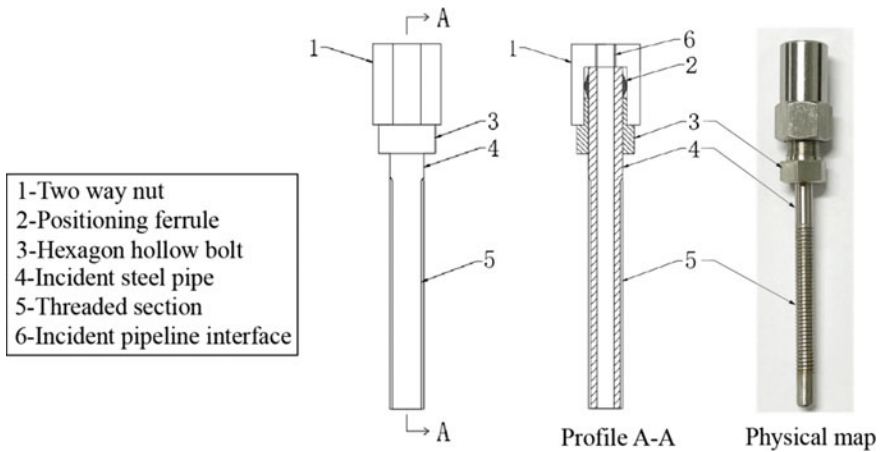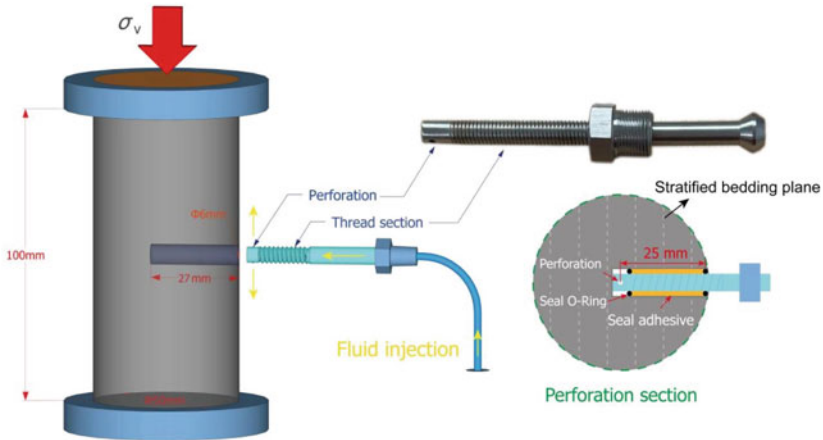
(ii)   Sample preparation

As shown in Fig. 3.25a, an injection hole (Φ 6 $\times$ 27 mm) perpendicular to the specimen's longitudinal direction was drilled at the center of each cylindrical specimen. The specimens were shaped so that the orientations of bedding planes were aligned with the axial loading directions, causing the injection holes orthogonal to the bedding planes. Using epoxy AB adhesive, a 75-mm long 316 L steel tube with a sealed bottom and two perforations (Φ 1 mm) was fixed to the eyehole to simulate the wellbore, leaving an isolated, pressurized open hole section (~ 4 mm long) for fluid accumulation around the perforations, as depicted in Fig. 3.25b, c [27]. The specimens are then placed in a 260 °C oven for 24 h to achieve the optimal sealing effect.

(iii)   Experiment apparatus

Laboratory experiments were conducted using a hydraulic fracturing system constituted by a TC-260L syringe pump and an axial loading device of the MTS 815 rock testing system. The syringe pump, manufactured by Jiangsu Tuochuang Scientific Research Instruments Co. Ltd., provides a total capacity of 266 mL, owns a maximum working pressure (P_{inj}) of 100 MPa, and can adjust the fluid flow (V_{inj}) from 0.01 to 120 mL/min. The injection mode of this pump can be maintained at either constant pressure or constant flow. Herein, the constant pressure injection mode was mainly adopted to initiate and sustain hydraulic fractures in shale specimens. Under this treatment, the fluid pressure is pumped stably by a constant pressure valve with feedback loop control (Fig. 3.26b), and the injection fluid will no longer maintain a constant flow rate but fluctuate with the fracture behavior [28, 29]. To capture real-time changes in pressure and flow rate during the fracturing process, we additionally installed pressure transducers and flow valves at the inlet of the wellbore, as shown in Fig. 3.26b [30].

(iv)   Acoustic emission equipment

In the uniaxial hydraulic fracturing process, the Micro-Express Acoustic Emission detection system (hereinafter referred to as the AE system) developed by the American Physical Acoustic Corporation (PAC) is used to dynamically monitor the evolution law of fracture initiation and propagation in hydraulic fracturing. The AE monitoring system is mainly composed of three parts: PCI-Express 8 data acquisition

(a) 3D sample and perforation section view
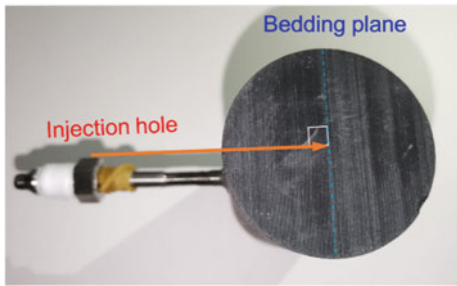
(b) Relative position of injection tube and bedding plane

(c) Specimen assembly drawing

Fig. 3.25 Shale specimen preparation

system, NANO-30 AE probe and preamplifier. Each part is connected by a special data line to realize the dynamic acquisition, conversion and transmission of acoustic signals to electrical signals. A Acoustic emission characteristic parameters acquisition, waveform acquisition and analysis can be carried out at the same time. The AE acquisition system is equipped with an eight-channel AE graphics card, which can provide up to eight AE channels simultaneously to ensure that the sample fracture development process determines the real-time linear location, surface location, and spatial location and performs image display and storage simultaneously.

In this test, the AE system bandwidth is set as 1 kHz–1.2 MHz, the preset threshold value is 40 dB, the preamplifier is set as 40 dB, and other related acquisition parameters are shown in Table 3.8. Where, the system sampling frequency is 1 MSPS, representing 1 trillion samples being collected per second, equivalent to one sample being collected per microsecond. The PDT defines the peak time (Peak definition
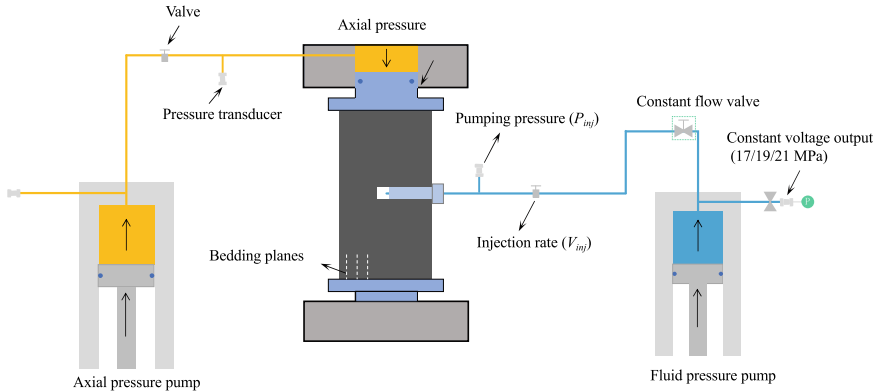
(a) Schematic diagram of the test principle
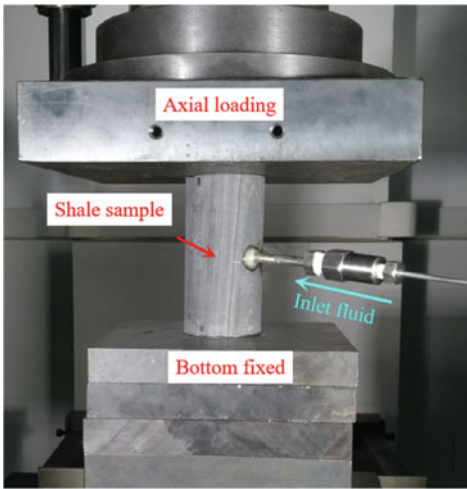
(b) Axial pressure device   (c) TC-260 L injection pump
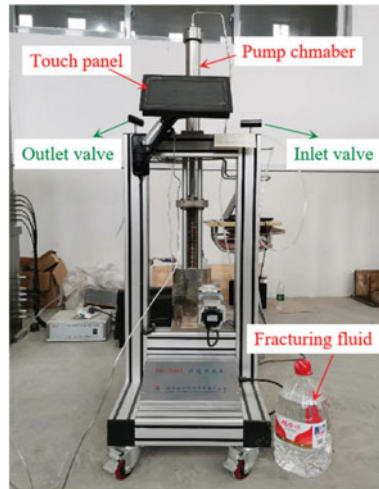
Fig. 3.26   Uniaxial hydraulic fracturing test system

time, in microseconds), and the setting of the PDT will affect the rise time and the peak amplitude of the identification signal peak. The HDT is the impact definition time (Hit definition time), and the HDT setting ensures that the AE signal detected in the structure is only a single impact when reflected into the system. HLT is the impact cloth layout time (Hit layout time), HLT avoids the non-true detection noise when the AE signal attenuation, and also improves the data acquisition speed.

Four NANO-30 probes were used in these tests to monitor the evolution of rock breakdown. As shown in Fig. 3.27, it is installed in four positions before and after the sample (mutual). Before installing the AE probe, apply agent to the probe end to ensure full contact with the specimen. After the probe is installed, the lead break

Table 3.8 The acquisition parameter of AE system

Rate/MSPS	Signal threshold/dB	PDT/μs	HDT/μs	HLT/μs	Probe resonance frequency/kHZ
1 (1 MHz)	40 dB	200	800	1000	300
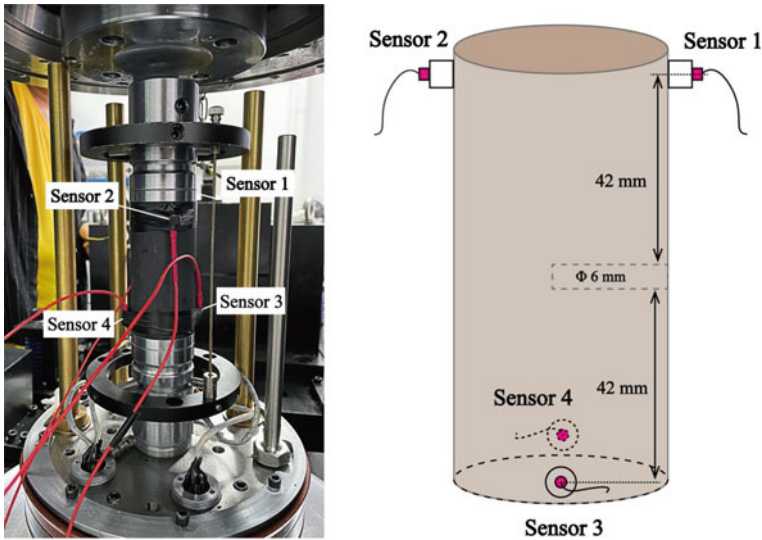
Fig. 3.27 Schematic diagram of the layout of AE sensors

test is required to monitor the coupling quality of the probe and the sample and the positioning accuracy of the acoustic emission event. The specific operation method is to use a 0.5 mm HB automatic pencil with the test sample plane, and check the silent emission signal and the degree of consistency with the lead break position.

3.4.2 Experimental Procedures

Under the uniaxial stress state, the constant flow hydraulic fracturing test, the constant pressure hydraulic fracturing test and the shale anisotropic hydraulic fracturing test were conducted by changing pumping conditions and shale sample types. Constant flow hydraulic fracturing is to apply fluid pressure on the specimen at a constant injection rate (flow rate) until hydraulic fracturing occurs. Constant pressure hydraulic fracturing is the hydraulic fracturing of the sample due to static fatigue damage caused by constant fluid pressure acting on the sample [31]. In the anisotropic shale hydraulic fracturing test, the effect of shale bedding orientation (relative to the horizontal plane) is mainly considered when fracturing shale samples at a constant injection rate. In

this respect, the difference in fracturing effect between the conventional constant flow hydraulic fracturing test mainly depends on the initial axial stress, flow rate and bedding angle.

(i)   Constant flow hydraulic fracturing test

Lin et al. [28] carried out a conventional triaxial hydraulic fracturing test using the Longmaxi shale, and analyzed the impact of in-situ stress difference and injection rate on the hydraulic fracturing effectiveness. However, there are few reports on the hydraulic fracturing effectiveness of Longmaxi shale without confining pressure. In order to compare the disturbance of the confining pressure on the breakdown pressure, circumferential deformation state and fracture propagation mode with reference to the test parameters of Lin et al. [28], the axial pressures of 5, 15 and 25 MPa were taken in turn to explore the impact of initial axial stress on hydraulic fracture effectiveness. At the same time, the injection rates of 6, 9 and 12 mL/min were selected to explore the disturbance effect of the injection rate of hydraulic fracturing. Meanwhile, test groups with incident conditions of 3 and 30 mL/min are added to further evaluate the change rule and evolution trend of fracture parameters at different injection rates. The specific test parameters are shown in Table 3.9.

(ii)   Constant pressure hydraulic fracturing test

Based on the above specimens and apparatus, the specific experimental procedure is designed as follows: first, initial axial stress (σ_v) is applied until the required experimental conditions are established at $\sigma_v = 5$ MPa, which is approximately 5% of the uniaxial compression strength (UCS) of the selected shale. The reason for applying 5 MPa axial stress is to avert unintentional loading deviation of shale specimens during fluid injection and synchronously to make sure that no fractures are induced in the sample under this elastic compaction state. Then, the experiment commences when fracturing fluid (distilled water) is injected under the control of constant low and constant pressure modes, respectively; see Table 3.10. For convenience, the

Table 3.9 Grouping parameters of hydraulic fracturing tests under constant flow injection conditions

No.	Sample	Bedding angle $\beta/°$	Axial pressure σ_1/MPa	Injection rate Q_{inj}/mL/min
CI-90-3	Longmaxi shale	90	5	3
CI-90-6	Longmaxi shale	90	5	6
CI-90-12(CA-90-5)	Longmaxi shale	90	5	12
CI-90-18	Longmaxi shale	90	5	18
CI-90-30	Longmaxi shale	90	5	30
CA-90-15	Longmaxi shale	90	15	12
CA-90-25	Longmaxi shale	90	25	12
LV-90-12	Lushan shale	90	5	12

Table 3.10 Grouping parameters of hydraulic fracturing tests under constant pressure injection condition

No.	Axial pressure σ_1/MPa	Bedding plane β/°	Injection rate Q_{inj}/mL/min	Constant pressure P_{con}/MPa	Remark
V-5	5	–	12	–	P_b
P-17	5	–	–	21	94% P_b
P-19	5	–	–	19	85% P_b
P-21	5	–	–	17	76% P_b
V-25	25	–	12	–	–

injection rate of the constant flow rate tests is fixed at 12 mL/min in line with Lin et al. [32] who performed flow-controlled triaxial hydraulic fracturing experiments using samples from the same shale formations. A constant flow test design (V-5) was first performed to attain the sample's instantaneous breakdown pressure ($P_b = 22.35$ MPa) which serves as the upper limit for setting the subsequent output pressure reading on the constant pressure valve (i.e., $P_{con} = 17$, 19, and 21 MPa). Additionally, another constant flow trial (V-25) was conducted under higher axial stress ($\sigma_v = 25$ MPa), which is consistent with the axial restriction of a triaxial fracturing case ($\sigma_v = 25$ MPa and $\sigma_c = 20$ MPa) carried out by Lin et al. in the laboratory scale [32]. Through fracturing specimen V-25 and comparing its results to Lin et al. [32], we can appropriately evaluate and analyze the influence of the confining pressure on the breakdown pressure and the fracture morphology, with which the reliability of the uniaxial fracturing results under constant flow rate conditions can also be verified.

(iii) Anisotropic Shale hydraulic fracture

The Longmaxi shale specimens with bedding angles of 0°, 45°, and 90° (Fig. 3.28) were taken to conduct hydraulic fracture tests under a constant flow injection mode. Referring to Lin's test [28], the injection rate of 12 mL/min was also selected. In addition, due to the characteristics of the anisotropic difference caused by changes in the reservoir environment, constant flow fracturing tests were carried out for Lushan shale with 0°, 45° and 90° bedding angles. The test parameters are shown in Table 3.11.

Based on the above test devices and methods (Figs. 3.24, 3.25 and 3.26) and the test parameters (Tables 3.9, 3.10 and 3.11), the uniaxial hydraulic fracture tests were conducted. The specific test steps are as follows:

(1) Fracturing fluid: For better observation of the fracture geometry, a water-based fluorescent substance is added to the fracturing fluid before experiments. This substance can dissolve in water and hardly change the viscosity of the injected fluid. Under ultraviolet light, the mixed fracturing fluid shows bright yellow-green color, which will help identify whether fracturing fluid is leaking out during the fracturing process.

(2) Sample installation and stress loading: Vaseline was spread evenly on the end face of the shale sample embedded incident tube and acoustic emission probe
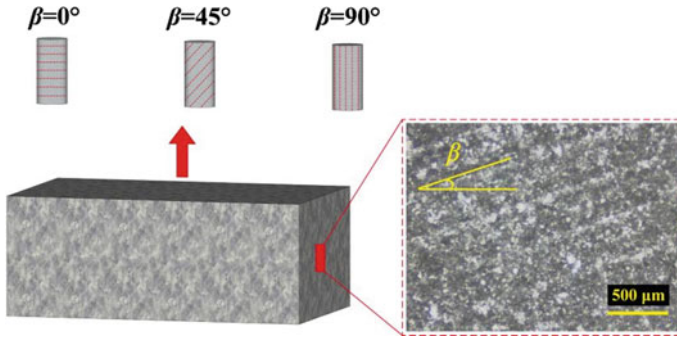
Fig. 3.28 Schematic diagram of shale samples with anisotropic bedding planes

Table 3.11 Grouping parameters of hydraulic fracturing tests adopting shale samples with anisotropic bedding planes

No.	Sample	Bedding angle $\beta/°$	Axial pressure σ_1/MPa	Injection rate Q_{inj}/mL/min
CV-0-12	Longmaxi shale	0	5	12
CV-45-12	Longmaxi shale	45	5	12
CV-90-12	Longmaxi shale	90	5	12
LV-0-12	Lushan shale	0	5	12
LV-45-12	Lushan shale	45	5	12
LV-90-12	Lushan shale	90	5	12

to reduce friction. The stress control mode with a loading rate of 0.5 MPa/min was used to load the axial pressure to the target value, and the acoustic emission system started data acquisition simultaneously.

(3) Fluid pressurization and fracturing: Before fluid injection, flow back into the pump pipeline for about 5 min to remove the possible residual air in the pipeline, and then connect the sample with the incident pipeline. Before starting the test, keep the constant voltage output mode of 0.5 MPa to check the pipeline for water leakage, then change the constant speed or keep the constant voltage mode, and set the preset constant current or constant voltage value. Acoustic emission accumulation time is recorded simultaneously with the fluid injection to distinguish the acoustic emission signals induced by fluid injection. The fluid pressure and the injection rate of the injection sample are measured by the pressure sensor (P_{inj}) and the flow valve (V_{inj}) near the wellhead, respectively, and the data is output in real-time by connecting to the computer. When a steep drop in fluid pressure or a steep increase in the injection rate is observed, hydraulic splitting damage occurred in the sample. After the sample breakdown, the injection continues for a period of time until the fluid pressure reaches balance and then the injection pump is turned off to ensure complete fracturing

of the sample. While closing the pump, the acoustic emission system and the axial pressure loading system to ensure the consistency of the data acquisition time scale;

(4) Observation of fracture morphology: After experiments, microscope observation, industrial CT scanning (0.2 mm voxel resolution), and 3D laser scanning were jointly conducted to investigate fracture morphology characteristics under different injection modes. The high-definition LEICA M205A microscope enables us to obtain the microscopic details of the trajectory of hydraulic fractures on the surfaces of the fractured specimens. The CT scanning system (CD-130 BX/μCT, manufactured by Chongqing Zhence Science and Technology Co. Ltd.) has a maximum resolution of 0.005 mm and can accommodate a sample with a full size of 130 mm in diameter and 50 kg in weight, which is sufficient to identify whether there are hydraulic fractures induced in the shale specimens after the long duration pressurization. The 3D laser scanner was used to scan the fracture surface to visualize the extension distribution characteristics of the specimen in the 3Dimensional space.

3.4.3 Experiment Results and Analysis

(i) Constant flow hydraulic fracturing

Unstable crack propagation leading to a macroscopic failure (a crack reaching the rock surface and splitting the specimen into two parts) is accompanied by a simultaneous drop of fluid pressure in the wellbore [33]. To quantitatively analyze the relationship between fluid pressure and crack propagation, we introduced a pressure decay rate (v_{decay}) inside the wellbore following Gehne et al. [34], which can be expressed as

$$v_{\text{decay}} = \frac{P(t) - P(t + \Delta t)}{\Delta t} \tag{3.8}$$

where $P(t)$ refers to the wellbore pressure at a certain time t, and Δt denotes an increment of time. According to Song et al. [35], Hu et al. [36], when ignoring the friction flow of fracturing fluid inside the wellbore, the wellbore pressure ($P(t)$) can be considered the pumping (or wellhead) pressure (P_{inj}) which is automatically monitored in real-time by a pressure transducer near the injection hole. Thus, Eq. (3.7) was rewritten as

$$v_{\text{decay}} = \frac{P_{inj}(t) - P_{inj}(t + \Delta t)}{\Delta t} \tag{3.9}$$

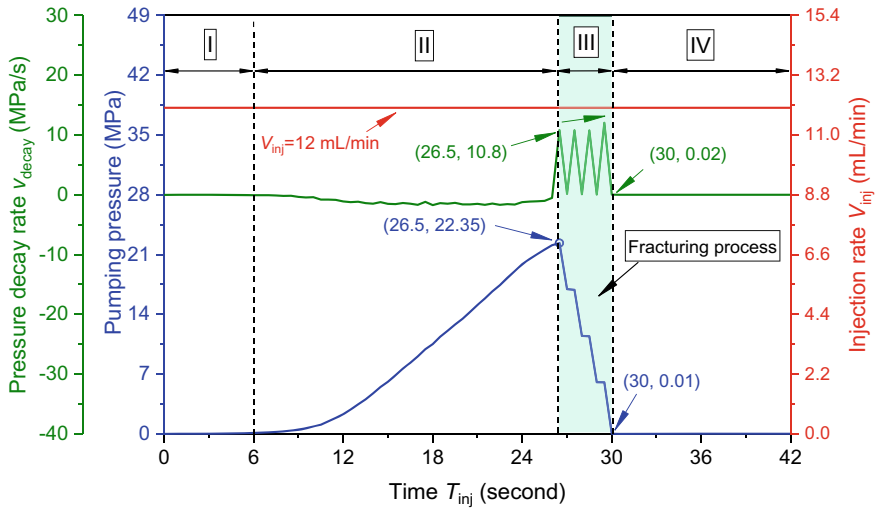(1) Typical curves of pumping pressure and injection rate versus time

Fig. 3.29 Curves of pumping pressure, injection rate, and pressure decay rate versus time

Similar to previous observations regarding conventional triaxial hydraulic fracturing [37, 38], in Fig. 3.29, the pumping pressure curves of the constant flow test (V-5) presented a trend of first increasing and then decreasing, which was characterized as four typical stages: initial pressurization stage (I), rapid pressurization stage (II), pressure drop stage (III) and post-peak stable pressure stage (IV).

(2)   Hydraulic fracture morphology

The fracture morphology of the specimen VC-5 surface before and after the test is shown in Fig. 3.30a–d. It is easy to see that there is no visible fracture on the sample surface before the test. After the pumping pressure reaches the breakdown pressure, the sample cracks and the fracture extends along the axial pressure direction as a whole. Once the specimen is completely cracked, the subsequently injected fluid will leak through the existing fractures (Fig. 3.30b). Figure 3.30d shows the 3D fracture morphology obtained by 3D laser scanning. The fracture surface is vertically straight and smooth, without bifurcation and convex surface, indicating that the sample has been completely broken. Figure 3.31 shows the microscopic fracture morphology of sample V-5. It can be seen that the hydraulic fracture morphology is not affected by its propagation direction. Even at the scale of 500 µm, the hydraulic fracture is still straight and smooth, without branching and secondary fracture. The fracture width is evenly distributed along the length direction and is about 350 µm.

(ii)   Disturbance of reservoir environment to hydraulic fracturing

According to the analysis of Sect. 3.2, the difference in the reservoir environment will directly affect the mineral composition and microstructure distribution of shale, and then affect the hydraulic fracturing and the fracture propagation law. To highlight
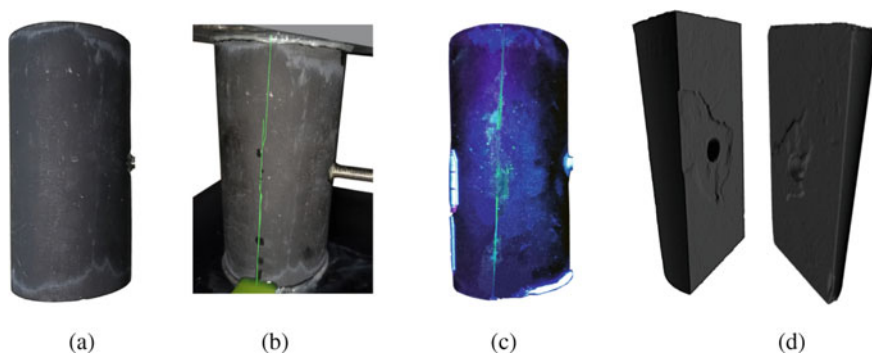
Fig. 3.30 Fracture morphology of specimen VC-1 sourced from Longmaxi shale reservoirs **a** before experiment, **b** during experiment, **c** after experiment, **d** 3D view of fractured surface
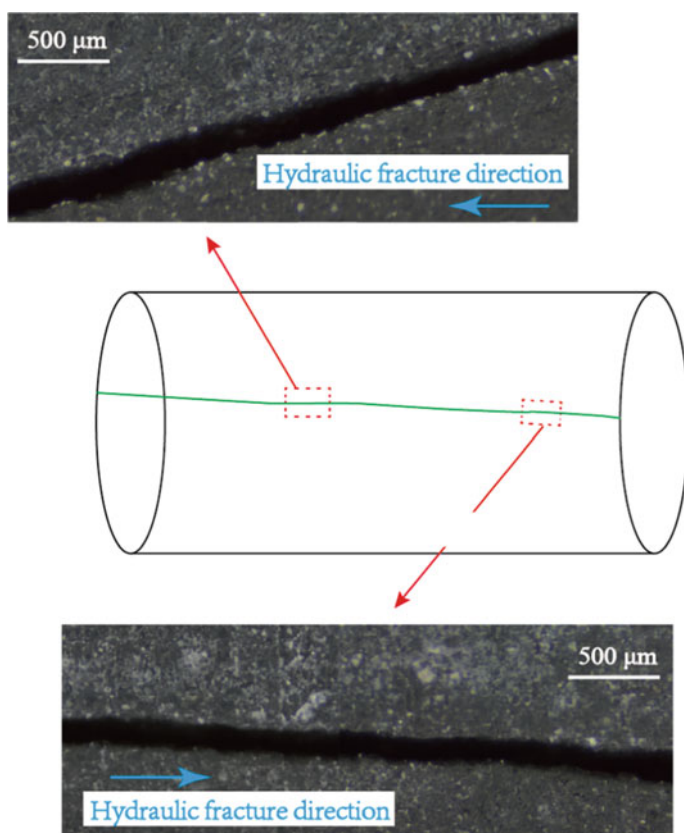

Fig. 3.31 Micrograph showing some details of the hydraulic fracture morphology of specimen V-5
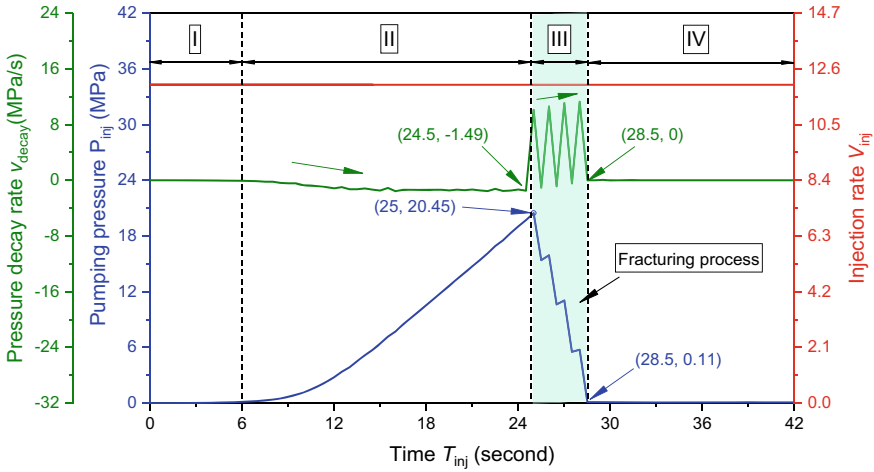
Fig. 3.32 Curves of pumping pressure versus time of specimen LV-90-12 sourced in Lushan Mine

the unique characteristics of hydraulic fracturing of Longmaxi shale, a constant flow hydraulic fracturing test was also conducted for the Lushan shale samples. Here, the sample LV-90-12 is taken as an example, and its hydraulic fracturing is analyzed.

The pump pressure–time curve of the sample LV-90-12 is shown in Fig. 3.32. Overall, under the same axial pressure and injection rate conditions, the evolution trend of pump pressure, injection rate and pump pressure decay rate of Lushan shale in the hydraulic fracturing process is consistent with those of Longmaxi shale. However, compared with Longmaxi shale, the breakdown pressure, injection time and peak decay rate of Lushan shale are significantly reduced. This is because there are many primary defects such as pores and microcracks in the Lushan shale (see Sect. 3.2.3 of this chapter), which makes it easier to induce fracture initiation and propagation when constant flow pressurization occurs.

Figure 3.33 shows the hydraulic fracture morphology of Lushan shale. The hydraulic fractures of Longmaxi shale mainly propagate along the bedding plane, and the fracture surface is relatively smooth. Due to the influence of internal micro fractures and uneven distribution of clay minerals, the fracture surface of Lushan shale is relatively rough, and the concave-convex surface fluctuates significantly (Fig. 3.32).

To further analyze the disturbance of rock structure difference to the hydraulic fracture propagation law, the fracture morphology of Lushan shale was observed with a stereomicroscope at the same magnification (500 μm), and the results are shown in Fig. 3.34. Comparing Figs. 3.31 and 3.34, it can be found that although the hydraulic fracture of Lushan shale with significant heterogeneity propagates along the axial direction of the specimen, its opening decreases significantly and changes unevenly, making it difficult to observe the fracture morphology directly. Compared with the smooth and straight fracture morphology of Longmaxi shale, the main hydraulic fracture of Lushan shale branches into secondary fractures, and its fracture

(a)   (b)   (c)   (d)
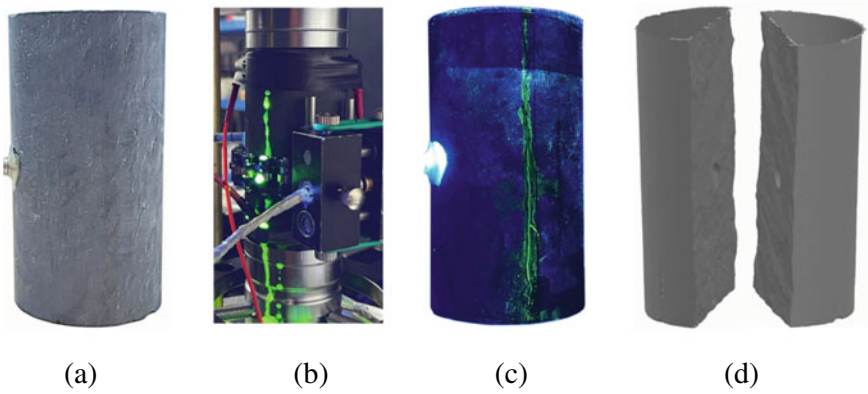
Fig. 3.33 Surface fracture morphology of specimen LV-90-12 sourced in Lushan Mine. **a** Before experiment. **b** During experiment. **c** After experiment. **d** 3D view of fractured surface

morphology is tortuous and complex. This is because Lushan shale contains many micro defects and holes, which leads to the hydraulic fracture tends to crack along the direction of the weakest mechanical properties of the rock matrix, leading to the main fracture morphology becoming more torturous.
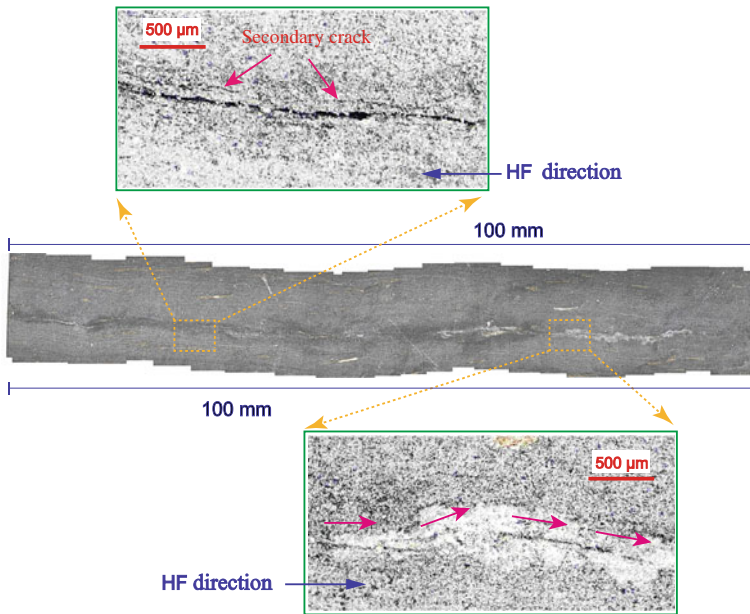
Fig. 3.34 Microscopic fracture morphology of specimen LV-90-12 sourced in Lushan Mine

3.5 Characteristics of True Triaxial Hydraulic Fracture

During the hydraulic fracturing construction process on the site, the deep rock bears the anisotropic and true triaxial pressure (Fig. 3.35). The physical model test of true triaxial hydraulic fracturing was carried out to simulate the pressure environment conditions of the underground rock. Three mutually perpendicular servo-hydraulic independent control flat jacks were applied to the sample's triaxial unequal pressure stress. In combination with the pump pressure–time curve, the rock fracture process was qualitatively analyzed, the expansion form of hydraulic fractures under true triaxial stress was described, and the morphological characteristics of the true triaxial hydraulic fracturing network were analyzed.

3.5.1 Sample Preparation and Test Equipment

(i) True three-axis hydraulic fracking test system

Figure 3.36 shows the true triaxial hydraulic fracturing physical model testing machine and working diagram. The true three-axis hydraulic fracturing test system consists of three parts: the true three-axis loading system (including the true three-axis pressure chamber, the operating computer and the hydraulic control system), the pump pressure injection system (the hydraulic injection pump), and the data acquisition system. The true three-axis loading system adopts the servo motor control (power 400 W), which can realize the accurate servo control of displacement and pressure. The true three-axis pressure chamber cylinder block is made of high-strength 2507 duplex stainless steel, the pressure cavity roof is fixed, the other five sides

Fig. 3.35 On-site true triaxial stress environment in situ reservoir
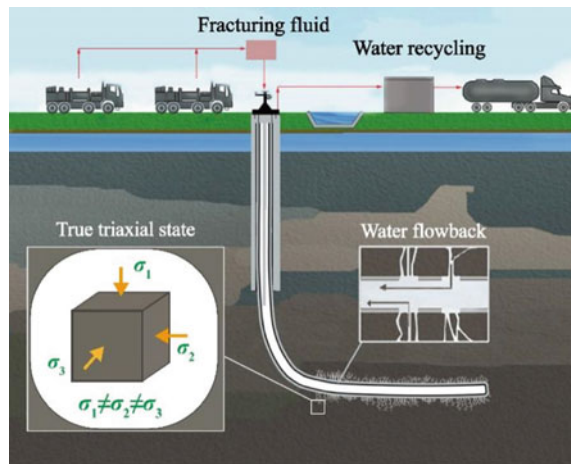
are equipped with hydraulic pistons (maximum stroke 10 mm), and the axial pressure shall be applied independently to the three directions of the sample XYZ. The true three-axis load system can output a maximum output pressure of 50 MPa, and a unique hydraulic mechanism is designed to recover the main hydraulic cylinder to facilitate the rapid removal of the sample. The pump pressure injection system is equipped with a model TC-100D injection pump. The pump is a double with cylinder layout, cylinder A discharging simultaneously as cylinder B suction to ensure continuous and constant flow rate without pulse liquid injection sample injection. Injection pumps can provide real-time monitoring of internal flow pressure and flow signal. The technical parameters are: the working pressure is 70 MPa, the flow adjustment range is 0.01–30 mL/min, the effective volume of the pump body is 100 mL, and the pressure accuracy is 0.1% FS.

(a) Hydraulic fracturing test system
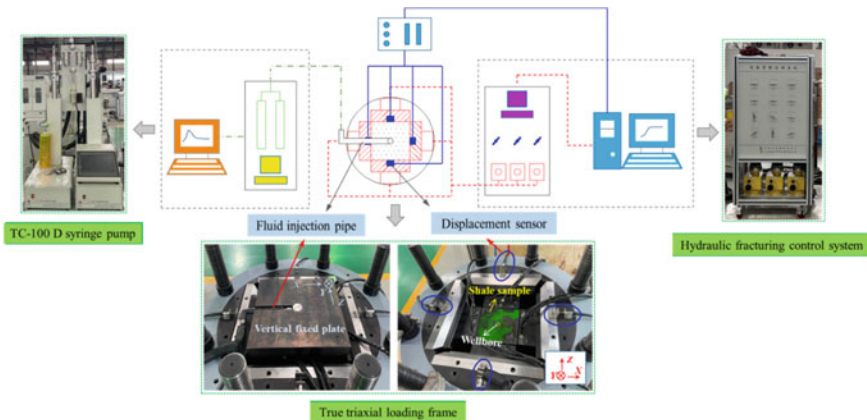
(b) Schematic diagram of the hydraulic fracturing system

Fig. 3.36 True triaxial hydraulic fracturing test system

(ii)   Sample preparation

The rocks used in the test were taken from the outcrop shale reservoir of Longmaxi Formation, Sichuan Basin, as described in Sect. 3.2. Based on the allowable sample size of the test machine, bedding inclination, relative orientation of wellbore and bedding, fracture expansion path, mutual disturbance between seams, change of fluid pressure in the seam and the difficulty of sampling, transportation, loading and unloading. The length of the cubic sample specification used in the true three-axis hydraulic fracture are 400 mm [29], 300 mm [39], 200 mm [40], 100 mm [41] and 50 mm [42]. Considering the size of the confining pressure cavity and the difficulty of installation and disassembly, the specification is $200 \times 200 \times 200$ mm shale test sample. Considering the size of the confining pressure chamber and the difficulty of installation and disassembly, the true triaxial hydraulic fracture shale sample carried out in this paper is $200 \times 200 \times 200$ mm, taking into account the difference of bedding dip anisotropy($\beta = 0°$, 45° and 90°), the appearance of the sample is shown in Fig. 3.37. The sample appearance is shown in Fig. 3.37. The centre size of the sample is $\Phi\ 25 \times 110$ mm round hole, with 90°, 45° and 0° angles between drilling and shale bedding.

(iii)   Fracture design

In this test, the high-strength steel pipe with a length of 100, 15 mm outer diameter, and 10 mm internal diameter is used. The schematic diagram and physical objects are shown in Fig. 3.38. The ring groove of the steel pipe outer wall is 5 mm apart to increase the friction resistance of the steel pipe outer wall. Welding circular steel rings at the bottom near the outlet prevent colloidal infiltration and sealing of the outlet when filling the sealant.
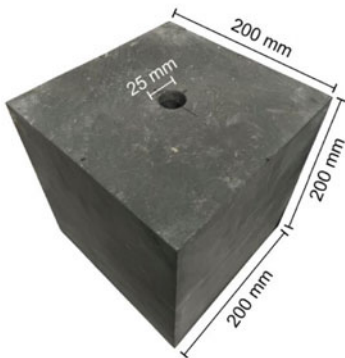

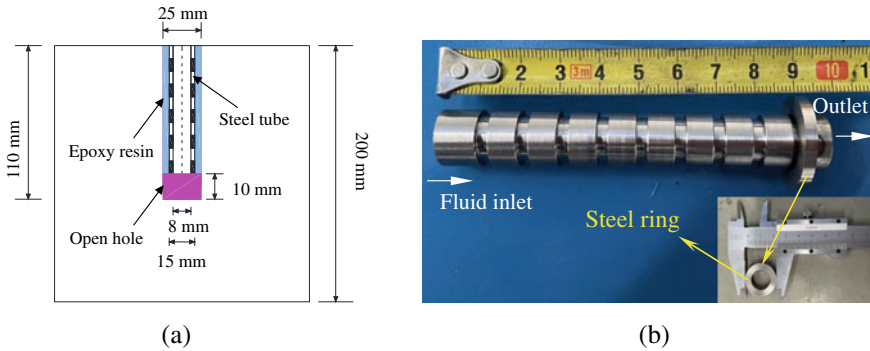**Fig. 3.37**   Shale specimen for triaxial hydraulic fracturing tests

Fig. 3.38 Schematic diagram (**a**) and photographic image (**b**) of fracturing wellbore

3.5.2   Fracturing Scheme

Shale is a typical sedimentary rock, which forms a certain inclination angle level in the diagenesis stage. Due to the differences in the stress environment and diagenesis history, the direction of the shale reservoir level has prominent anisotropic characteristics. In this case, the bore will no longer be parallel or orthogonal to the group but at an angle α to the bedding. To clarify the conventional horizontal well and vertical shaft wellbore layout of the traditional design (0° or 90° Fig. 3.39a) and the wellbore and bedding surface into a specific inclination particular case (45°, Fig. 3.39b) between the hydraulic fracturing effect difference, based on the different ground stress conditions and level direction, prepared six shale samples for hydraulic fracturing test. As shown in Table 3.12, BP refers to the natural bedding surface. Assuming that the ground stress ratio in the main direction of the sample is consistent with the Japanese Minami-Nagaoka natural gas field (max: med: min = 4:3:2 [43]), the test maximum, middle, and minimum principal stresses are 12, 9, and 6 MPa, respectively. This assumption scales the stress state of the in situ reservoir to a certain extent, which can prevent the direct use of the in situ stress to cause the original fracture due to the uneven stress difference in the loading process, which is conducive to reducing the disturbance of the preloading process to the subsequent hydraulic fracturing process. Reugelsdijk et al. [44] and Zhou et al. [45] also proposed similar assumed conditions and parameter arrangements in the true three-axis hydraulic fracturing simulation. The influence of the ground stress direction is mainly considered here (maximum, middle and minimum principal stress size fixed, principal stress difference $\Delta\sigma = 3$ MPa), fixed flow $Q_{inj} = 20$ mL/min injection, simulating the fracturing situation shown in Fig. 3.39.

   To explore the fracturing mechanism of complex fracture networks and the hydraulic fracturing process of characteristic rock strata. The scheme and related parameters grouping are shown in Table 3.12 and Fig. 3.40. It should be noted that the vertical stress v directions of samples 5 # and 6 # in Table 3.12 are not aligned with the Y-axis direction in Fig. 3.40 but in the Z-axis direction. This is because

(a) General case   (b) Special case
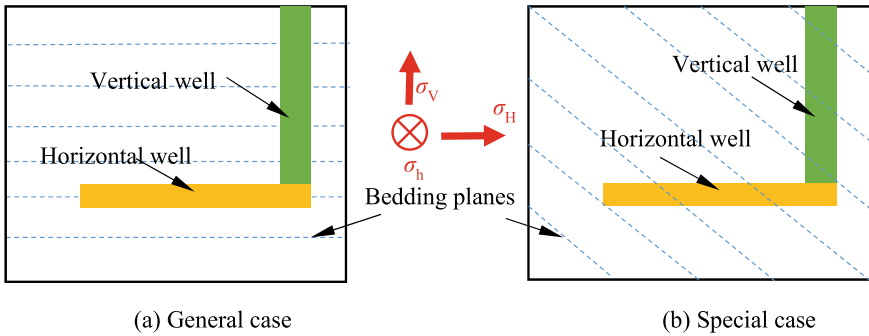
Fig. 3.39 Schematic diagram of the intersecting relationship between the wellbore and the shale formations

Table 3.12 Hydraulic fracturing schemes under true triaxial stress state

No.	σ_v/MPa	σ_H/MPa	σ_h/MPa	Bedding angle (relative to the horizontal plane BP)/°	Type of shaft arrangement
1#	12 (σ_{max})	9 (σ_{med})	6 (σ_{min})	0	Vertical wellbore
2#	9 (σ_{med})	12 (σ_{max})	6 (σ_{min})	0	Vertical wellbore
3#	12 (σ_{max})	9 (σ_{med})	6 (σ_{min})	45	Inclinde wellbore
4#	6 (σ_{min})	12 (σ_{max})	9 (σ_{med})	45	Inclinde wellbore
5#	12 (σ_{max})	9 (σ_{med})	6 (σ_{min})	90	Horizontal wellbore
6#	9 (σ_{med})	12 (σ_{max})	6 (σ_{min})	90	Horizontal wellbore

only the top cap is movable in the true triaxial circumference pressure cavity. To realize the sample stress state during horizontal wellbore construction (the wellbore direction is consistent with the minimum ground stress direction), assume that the Z-axis direction is the direction of vertical stress applied here. Therefore, 5 # and 6 # samples simulate the positive fault stress state (normal-faulting stress regime) and tectonic stress state (tectonic stress regime), respectively, 3 # sample is the positive fault stress state, and 4 # sample is the reverse fault stress state (reverse faulting stress regime).

3.5.3   Analysis of Fracturing Results

(i)   Analysis of pump pressure time curve

Taking 5# as an example, the change curve of the true three-axial hydraulic fracturing pump is analyzed. As can be seen from Fig. 3.41, under the true triaxial stress state,
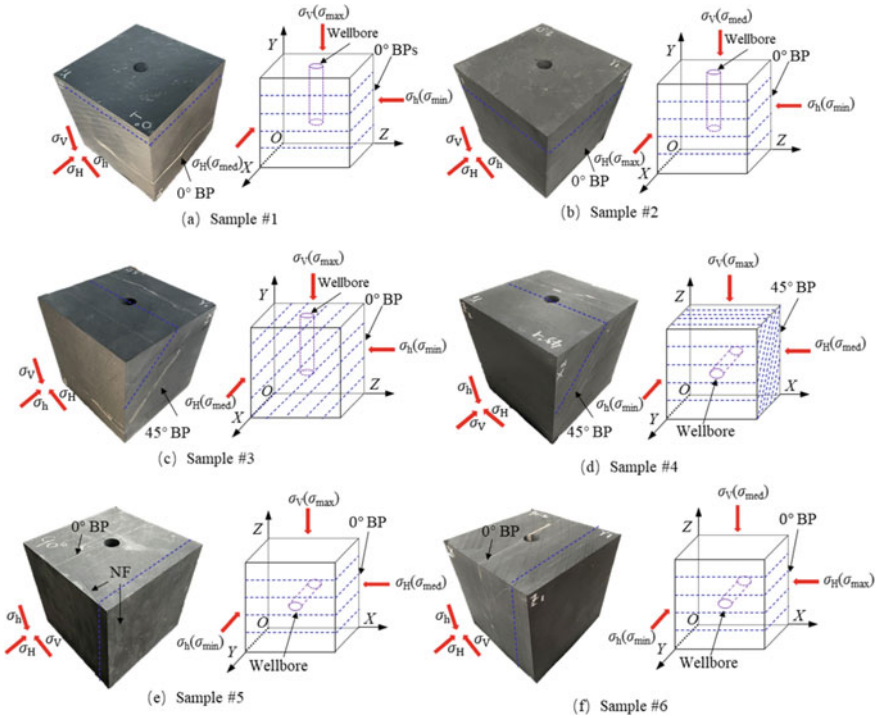
Fig. 3.40 Hydraulic fracturing test scheme of complex fracture network

the pump pressure–time curve is similar to the uniaxial state, which can still be divided into four stages: initial compression stage (I), rapid compression stage (II), post-peak pressure drops stage (III), and post-peak pressure stabilization stage (IV). The changing trend of the curve in the first three (I–III) phases and its corresponding physical processes are similar to the uniaxial stress state. In stage IV, the pump pressure curve does not steep to 0 as in the uniaxial state. This phenomenon is because, under the action of the lateral confining pressure, the hydraulic force induces the fracture to gradually close, and the newly injected fracturing fluid accumulates in the fracture, resulting in pressure to suppress, and the fluid pressure gradually increases. When the internal fluid pressure is greater than the fracture closure pressure, the fracture will be initiated, and the excess fluid will drive the hydraulic fracture to be further propagated. When a new fracture appears, the fluid pressure accumulated in the fracture is released and the pumping fluid pressure decreases. Therefore, in the process of unstable expansion, the pump pressure maintains the fluctuation state. This process corresponds to phase IV under the triaxial stress state. According to Fig. 3.41, the breakdown pressure P_b of the 5# sample is 17.69 MPa, and the lowest post-peak pump pressure (P_{lowest}) is 8.79 MPa. The pressure suppression again causes the fracture starting pressure (P_p) to be 10 MPa.

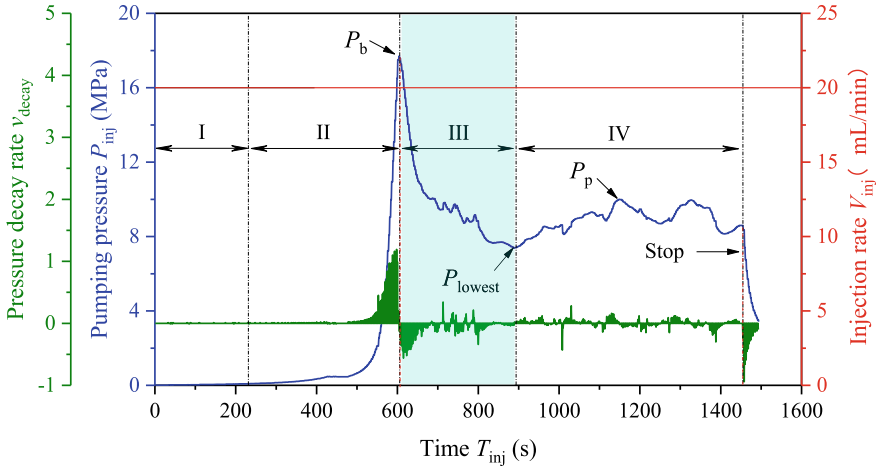**Fig. 3.41** Pumping pressure curve versus time under true triaxial stress state

(ii)   Morphological characterization of hydraulic fracture

Figure 3.42 shows the fracture form of the hydraulic fracturing end surface of shale samples in the true triaxial state. It can be seen that three approximately parallel extended hydraulic fractures (H_1, H_2, H_3, and H_4) are induced near the wellbore, with the fracture direction consistent with the middle and principal stress σ_{med}. Different hydraulic fractures show different fracture expansion behavior when intersecting with the weakly cemented level (M_1) and natural fracture (N_1) in the rock. The closer distance of the hydraulic fracture H_1 and H_2 passes directly through the natural discontinuous surface M_1 and N_1, and run through to the outer surface of the sample. In contrast, the hydraulic fracture H_3 and H_4 are directly overlapped with the natural discontinuous surface, and the fracturing fluid enters the activated natural fracture, resulting in a deflection in the extending direction of the hydraulic fracture mode. Engineering practice and physical simulation experimental data show that the intersection behaviors such as fracture crossing [46], slip, and branches are easy to disturb the expansion direction of hydraulic fracture, leading to complex fracture mesh patterns in the reservoir hydraulic fracturing process.

Shale reservoirs also differ due to different buried environments, rock properties, and stress conditions. Based on this background, this chapter takes the Longmaxi shale in Sichuan province as the primary research object and the Lushan shale as the comparison object. Studies of the mineral composition and microstructure of two types of shale have been carried on. Based on the plugging device independently designed by the author, the hydraulic fracturing test under the single axis and true three-axis stress state was conducted to explore the influence of the shale reservoir rock properties and stress conditions (single axis or true three-axis) on the reservoir rock fracture pressure and fracture expansion law.
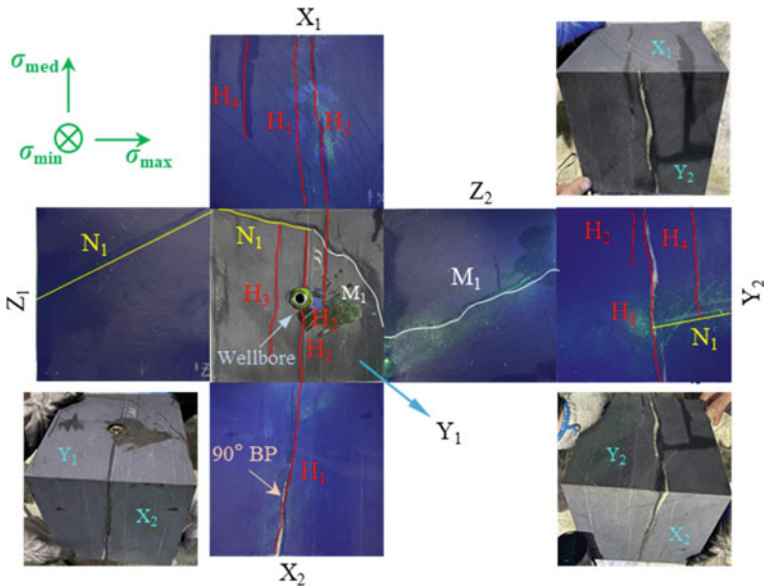
Fig. 3.42 Fracture propagation morphology of fractured specimens

References

1. Ma XH, Xie J, Yong R, Zhu YQ (2020) Geological characteristics and high production control factors of shale gas reservoirs in Silurian Longmaxi formation, southern Sichuan Basin, SW China. Petrol Explor Dev 47(05):841–855
2. Si X, Wang Z, Wang W (2016) Study on the high performance water-based drilling fluid in Longmaxi shale gas formation. Energy Chem Industr 37(05):41–46
3. Li W (2015) Petrological characteristics and shale gas enrichment of organic matter-rich shale in Jiangxi province. China University of Mining and Technology Xuzhou
4. Zhang XJ (2020) Flow mechanism and productivity model for heat-gas-fluid-solid interactions on permeability enhancement in heterogeneous shale volume fracturing. Chinese doctoral dissertations full-text database. China University of Mining and Technology Xuzhou
5. Liu SX (2015) Research on microscopic characteristics of carboniferous shale reservoir in Eastern Qaidamu Basin. China University of Petroleum (East China)
6. Li A, Ding WL, Zhang GL, Zhang MG, Zhang ZX, Yan BZ, Zhou CX, Chen ZZ, Bai P (2016) Reservoir characteristics of marine shale in the Malong block of eastern Yunnan Province and comparison analysis. Earth Sci Front 23(02):176–189
7. Feng YX, Zhang Y, Zhang YW (2020) Physical properties of shale gas reservoir in Xinkailing formation of Northwestern Jiangxi. Jiangxi Coal Sci Technol 2020(03):1–3+7
8. Loucks RG, Reed RM, Ruppel SC, Hammes U (2012) Spectrum of pore types and networks in mudrocks and a descriptive classification for matrix-related mudrock pores. Am Assoc Pet Geol Bull 96(6):1071–1098. https://doi.org/10.1306/08171111061
9. He X, Wu J, Yong R, Zhao SX, Zhou XJ (2021) Accumulation conditions and key exploration and development technologies of marine shale gas field in Changning-Weiyuan block, Sichuan Basin. Acta Petrolei Sinica 42(02):259–272
10. Liu HY, Tian ZY, Liu B, Guo R, Shi KB (2019) Classification and prediction of giant thick strongly heterogeneous carbonate reservoirs in the Middle East area: a case study of Mid-Cretaceous Mishrif Formation in the W oilfield of Iraq. Acta Petrolei Sinica 40(06):677–691

11. Zeng FH, Zhang Q, Chen SY, Guo JC, Fan Y (2020) Dynamic characterization of microscopic pore structures of shale under the effect of hydration: a case study of Longmaxi formation shale in the Changning area of the Sichuan Basin. Nat Gas Ind 40(10):66–75
12. Zhang S, Liu HM, Wang YS, Zhang SP, Zhang KH (2019) Diagenetic event of Paleogene shale and its influence on development characteristics of shale pore space in Dongying Sag. Petrol Geol Recov Efficiency 26(01):109–118
13. Zhao LQ, Feng JW (2018) Interrelationship study between rock mechanical stratigraphy and structural fracture development. J Shandong Univ Sci Technol (Nat Sci) 37(01):35–46
14. Yao Y, Liu D, Che Y, Tang D, Tang S, Huang W (2010) Petrophysical characterization of coals by low-field nuclear magnetic resonance (NMR). Fuel 89(7):1371–1380. https://doi.org/10.1016/j.fuel.2009.11.005
15. Liu Z, Liu D, Cai Y, Yao Y, Pan Z, Zhou Y (2020) Application of nuclear magnetic resonance (NMR) in coalbed methane and shale reservoirs: a review. Int J Coal Geol
16. Ēriks K, Lucio F, Andrew GW, Yong JRJ, Tim DWC (2021) Parallel nuclear magnetic resonance spectroscopy. Nat Rev Methods Primers 27
17. Liu JF, Skoczylas F, Talandier J, Pu H (2016) Dismantling of the EB experiment: experimental research on the retrieved GBM and bentonite blocks. Nucl Eng Des 300:297–307. https://doi.org/10.1016/j.nucengdes.2016.01.023
18. Liu JF, Ni HY, Pu H, Huang BX, Yao QL (2021) Test theory, method and device of gas permeability of porous media and the application. Chin J Rock Mech Eng 300:297–307
19. Wu ZS, Feng ZJ, Shi XD, Hui Z (2020) Study on permeability of granite under different confining pressures and its permeability sensitivity. Min Res Dev 40(10):46–50
20. Cai MF, He MC, Liu DY (2002) Rock mechanics and engineering. Science Press, Beijing
21. Yang T, Xu C, Wang BX, Zhang L, Liao GH (2007) The cohesive strength and the friction angle in rock-soil triaxial rests. China Min Mag 16(12):104–107
22. Tan J, Xie J, Li L, Lyu Q, Han J, Zhao Z (2020) Multifractal analysis of acoustic emissions during hydraulic fracturing experiments under uniaxial loading conditions: a niutitang shale example. Geofluids. https://doi.org/10.1155/2020/8845292
23. Wan XL, He JM, Zheng B (2017) Effect of bedding orientation on hydraulic fracture propagation in shale under uniaxial compression. J Eng Geol 25(01):88–94
24. Chitrala Y, Moreno C, Sondergeld C, Rai C (2011) Microseismic and microscopic analysis of laboratory induced hydraulic fractures. In: Society of petroleum engineers—Canadian unconventional resources conference 2011, CURC 2011
25. He J, Zhang Y, Li X, Wan X (2019) Experimental investigation on the fractures induced by hydraulic fracturing using freshwater and supercritical CO_2 in shale under uniaxial stress. Rock Mech Rock Eng 52(10):3585–3596. https://doi.org/10.1007/s00603-019-01820-w
26. Zhao Y, Zhang Y, Wang C, Liu Q (2022) Hydraulic fracturing characteristics and evaluation of fracturing effectiveness under different anisotropic angles and injection rates: an experimental investigation in absence of confining pressure. J Nat Gas Sci Eng. 97:104343. https://doi.org/10.1016/j.jngse.2021.104343
27. Li Q, Wu X, Zhai C, Hu Q, Ni G, Yan F, Xu J, Zhang Y (2021) Effect of frequency and flow rate of pulsating hydraulic fracturing on fracture evolution. Zhongguo Kuangye Daxue Xuebao/J China Univ Min Technol 50(06):1067–1076
28. Lin C, He J, Li X, Wan X, Zheng B (2017) An experimental investigation into the effects of the anisotropy of shale on hydraulic fracture propagation. Rock Mech Rock Eng 50(3):543–554. https://doi.org/10.1007/s00603-016-1136-4
29. Tan P, Jin Y, Han K, Zheng X, Hou B, Gao J, Chen M, Zhang Y (2017) Vertical propagation behavior of hydraulic fractures in coal measure strata based on true triaxial experiment. J Pet Sci Eng 158:398–407. https://doi.org/10.1016/j.petrol.2017.08.076
30. Jin W, Arson C (2020) Fluid-driven transition from damage to fracture in anisotropic porous media: a multi-scale XFEM approach. Acta Geotech 15:113–144. https://doi.org/10.1007/s11440-019-00813-x
31. Zhou JW (2019) Investigation into the initiation behavior of hydraulic fractures in a tight sandstone formation driven by abnormal borehole pressure. China University of Petroleum, Beijing

32. Lu G, Gordeliy E, Prioul R, Bunger A (2017) Modeling initiation and propagation of a hydraulic fracture under subcritical conditions. Comput Methods Appl Mech Eng. 318:61–91. https://doi.org/10.1016/j.cma.2017.01.018

33. Gunarathna G, da Silva BG (2019) Influence of the effective vertical stresses on hydraulic fracture initiation pressures in shale and engineered geothermal systems explorations. Rock Mechan Rock Eng 52(11):4835–4853

34. Gehne S, Benson PM, Koor N, Dobson KJ, Enfeld M, Barber A (2019) Seismo-mechanical response of anisotropic rocks under hydraulic fracture conditions: new experimental insights. J Geophys Res Solid Earth 124(9):9562–79. https://doi.org/10.1029/2019JB017342

35. Song C, Lu Y, Tang H, Jia Y (2016) A method for hydrofracture propagation control based on nonuniform pore pressure feld. J Nat Gas Sci Eng 33:287–95. https://doi.org/10.1016/j.jngse.2016.05.029

36. Hu Q, Liu L, Li Q, Wu Y, Wang X, Jiang Z et al (2020) Experimental investigation on crack competitive extension during hydraulic fracturing in coal measures strata. Fuel 2020. https://doi.org/10.1016/j.fuel.2019.117003

37. Michael A, Gupta I (2021) A comparative study of oriented perforating and fracture initiation in seven shale gas plays. J Nat Gas Sci Eng 88(4–5):103801

38. Fu Y (2019) The study on the rule of slick-water fracturing fluid flow in plugging of main fracture during the fracture of hydraulic fracturing. Xi'an Shiyou University

39. Guo T, Zhang S, Qu Z, Zhou T, Xiao Y, Gao J (2014) Experimental study of hydraulic fracturing for shale by stimulated reservoir volume. Fuel 128:373–380. https://doi.org/10.1016/j.fuel.2014.03.029

40. Zhang F, Ma G, Liu X et al (2018) Experimental analysis of multiple factors on hydraulic fracturing in coalbed methane reservoirs. Plos One 13(4)

41. Wu S, Li T, Ge H, Wang X, Li N, Zou Y (2019) Shear-tensile fractures in hydraulic fracturing network of layered shale. J Pet Sci Eng 183:106428. https://doi.org/10.1016/j.petrol.2019.106428

42. Minaeian V, Dewhurst DN, Rasouli V (2020) An investigation on failure behavior of a porous sandstone using single-stage and multi-stage true triaxial stress tests. Rock Mech Rock Eng 53(8):3543–3562

43. Sato K, Wright C, Ichikawa M (1999) Post-frac analyses indicating multiple fractures created in a volcanic formation. SPE Prod Facil 14(4):61–63

44. Beugelsdijk LJL, Pater C, Sato K (2000) Experimental hydraulic fracture propagation in a multi-fractured medium. In: SPE Asia pacific conference on integrated modelling for asset management

45. Zhou J, Chen M, Yan J et al (2008) Analysis of fracture propagation behavior and fracture geometry using a tri-axial fracturing system in naturally fractured reservoirs. Int J Rock Mech Min Sci 45(7):1143–1152

46. Fisher K, Warpinski N (2012) Hydraulic-fracture-height growth: real data. SPE Prod Oper 27(1):8–19

Chapter 4
Constant Flow Injection

4.1 Introduction

The hydro-mechanical coupling is one of the research hotspots in the fields of petroleum, mining and tunneling engineering. The hydro-mechanical coupling issues encountered in hydraulic fracturing process can be mainly reflected in two aspects: (1) shales are fractured by the constant flow. The breakdown of rock in this process is mainly manifested as instantaneous breakdown. The time to breakdown is usually less than 30 s [1]. (2) When constant high fluid pressure is applied for a long duration, the microcracks in the sample grow in a subcritical way. The macroscopic evolution of a hydraulic fracture is time-dependent, which is named "delayed initiation" [2]. In terms of the fluid pressure distribution in the fracture, the fluid pressure in the two hydraulic fracturing processes corresponds to the "non-uniform" and "constant" states, respectively. Different injection conditions cause the rock to deform and fracture in different mechanisms. The effects of fluid pressure on stress state, fracture propagation, and softening of rock matrix also differ significantly.

In the process of engineering practice, conventional hydraulic fracturing construction still prefers constant flow conditions (fracturing at a constant injection rate). The continuous increase of fluid pressure induces the instantaneous breakdown of rock, which promotes the intersection of hydraulic fractures with discontinuities (such as natural fractures, and beddings) to form a complex fracture network, thus creating a flow channel for subsequent alkane and thermal energy exploitation. Although many works have been focused on hydraulic fracture propagation under constant flow injection conditions, few efforts have paid attention to the microcrack evolution (acoustic emission events) before the breakdown occurs. In the following part, we will fracture shale with constant flow mode in the laboratory and investigate the fracture propagation under different axial stresses and injection rates.

Y. Zhao et al., *Hydraulic Fracturing and Rock Mechanics*,

4.2 Instantaneous Fracturing Mechanism of Constant Flow Pressurization

Under the constant flow injection mode, before the hydraulic fracture starts to initiate, its length is 0, and the fluid pressure in the wellbore is constant at a certain time, as shown in Fig. 4.1(i) (the darker the color of the mineral, the greater its rigidity is). The fluid pressure in the wellbore gradually increases with time increases. The high-pressure fluid induces a high-stress area around the wellbore. The mineral particles near the wellbore have different deformation due to their different stiffness, which forms stress concentration in local areas, resulting in the primary weak surface cracking and generating hydraulic fractures, as shown in Fig. 4.1(ii) [3]. The high-pressure fluid accumulated in the wellbore immediately diffuses into the fracture to drive the hydraulic fracture's further propagation, causing the sample's instantaneous breakdown. In this process, due to the fluid flow in the main fracture, the fluid pressure presents a gradient distribution of non-uniform pressure from the injection point to the fracture tip [4]. Since the pump pressure curve and fracture morphology characteristics of shale constant flow hydraulic fracturing under a uniaxial stress state have been described in detail in Chap. 3, this section will focus on the analysis of the disturbance effect of axial stress (5, 15 and 25 MPa) and injection rate (3, 6, 12, 18 and 30 mL/min) on the shale instantaneous fracturing process.
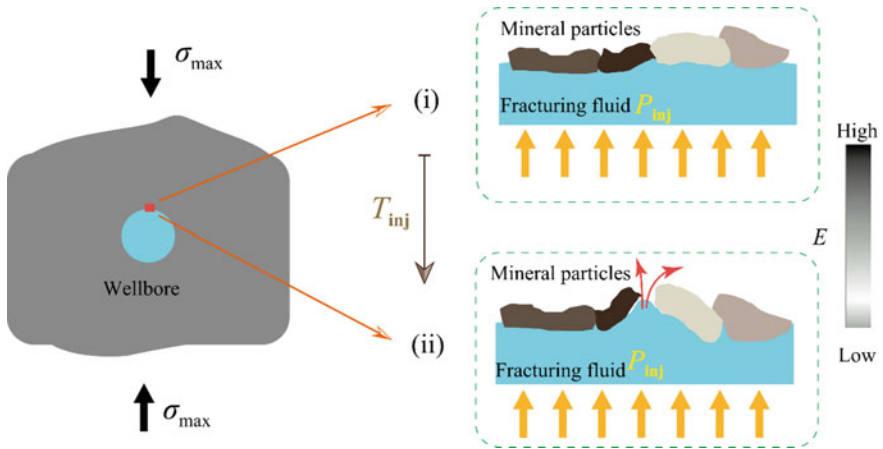

Fig. 4.1 Schematic of hydraulic fracture initiation around the wellbore under the constant flow injection condition

4.2.1 Impact of Axial Load

Under the uniaxial stress state, the axial stress is taken as the maximum principal stress (σ_{max}) that acts on the sample, so the disturbance of external stress to the hydraulic fracture is mainly reflected by the axial stress. According to the test scheme in Sect. 3.4.2 of Chap. 3 the sample is limited by axial stress in the whole hydraulic fracturing test process, including the preloading and hydraulic pressurization stages. Therefore, the disturbance effect of axial stress in the two stages is analyzed.
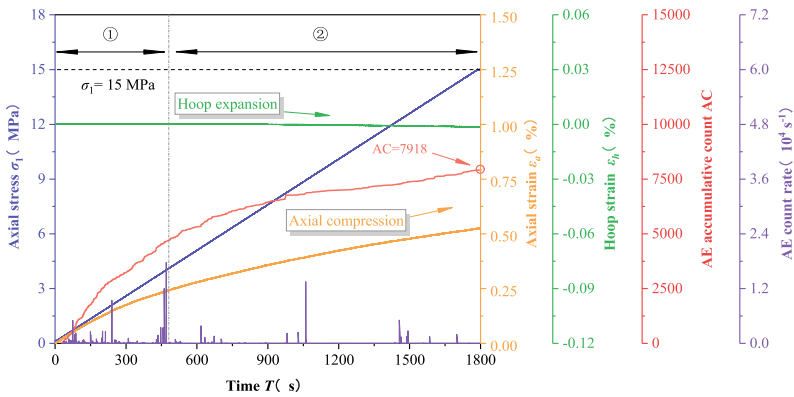
① **Preloading stage**

Referring to the experimental scheme of Lin et al. [5], the axial stress is preset as 5, 15 and 25 MPa. The axial stress, strain and AE characteristics during preloading are shown in Fig. 4.2. The axial loading rate is 0.5 MPa/min. With time elapsing, the axial strain (ε_a), circumferential strain (ε_h) and AE cumulative counts (AC) show a non-linear increasing trend, while the AE count rate presents an obvious segmentation characteristic. Combined with the axial stress variation, the preloading process can be further divided into two stages: (a) the micropore and fissure compaction stage; (b) the damage stable accumulation stage. The stage ① in Fig. 4.2a–c corresponds to the pores and fissures compaction stage. Under the initial axial load, the pores and fissures in the sample are closed or partially opened, resulting in the increase of axial and circumferential strains (in magnitude). Specifically, the sample is compacted in the axial direction and slightly expanded in the circumferential direction. Rapid closing or opening of micro pores and fissures will generate intense AE activities. According to Jiang et al. [6], the AE cumulative counts reflect the degree of damage in the rock. Therefore, the rapidly increasing AE cumulative counts imply the state of rapid accumulation of damage during the compaction stage. The stage ② in Fig. 4.2a–c corresponds to damage stable accumulation in the linear loading stage. With increasing axial strain, the circumferential strain increases continuously, which suggests that the sample still is in the radial expansion state in the linear elastic stage. Then, the AE cumulative counts began to increase progressively and steadily, indicating that the internal damage of the sample also cumulates correspondingly in the elastic loading stage. It is worth noting that even at the damage stable accumulation stage, the AE count rate still varies unstably with sudden jumps. This phenomenon may be explained by the growth of microcracks induced by the accumulation and/or release of the strain energy in the sample.

Figure 4.2d shows the relative changes of the axial strain, circumferential strain and AE cumulative counts in the compaction stage and the damage stable accumulation stage subject to different axial stresses. Overall, the axial strain in the compaction stage is greater than that in the damage stable accumulation stage. By comparison, the circumferential strain and AE cumulative counts are more likely to be affected by the axial stress. When the axial stress is relatively low (<5 MPa), the circumferential strain and AE activities are concentrated in the compaction stage. With the increase of the axial stress, the circumferential propagation deformation and AE cumulative counts in the linear elastic stage start to increase, indicating that higher axial stress can induce more damage in the sample.

The rock fracture process is often accompanied by unstable emission of AE signals [7, 8]. One single AE signal can be detected by multiple probes and output in the form of elastic waves of different frequency bands. Numerous studies have proven that [9–11], AE waveform signals contain information that can reflect the properties of AE sources, such as failure mode, crack coalescence pattern, and spatial scale of fractures. To reveal the microfracture mechanism of samples under different axial stress, this section will further carry out statistical analysis on the dominant frequency characteristics of AE waveforms. As shown in Fig. 4.3, the
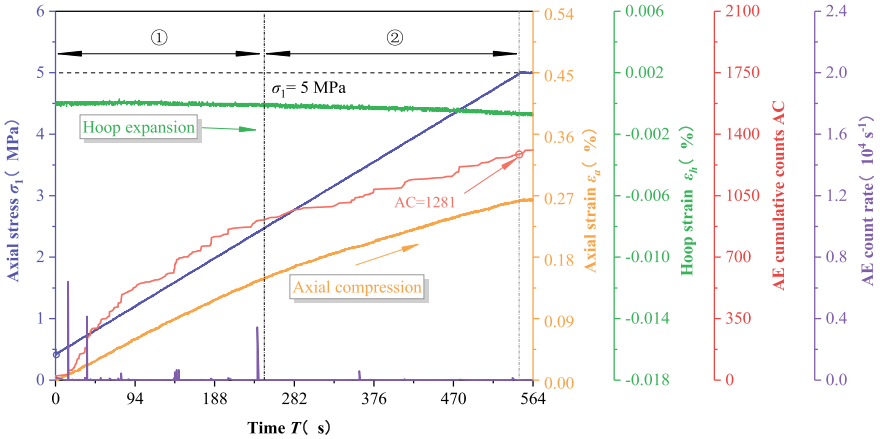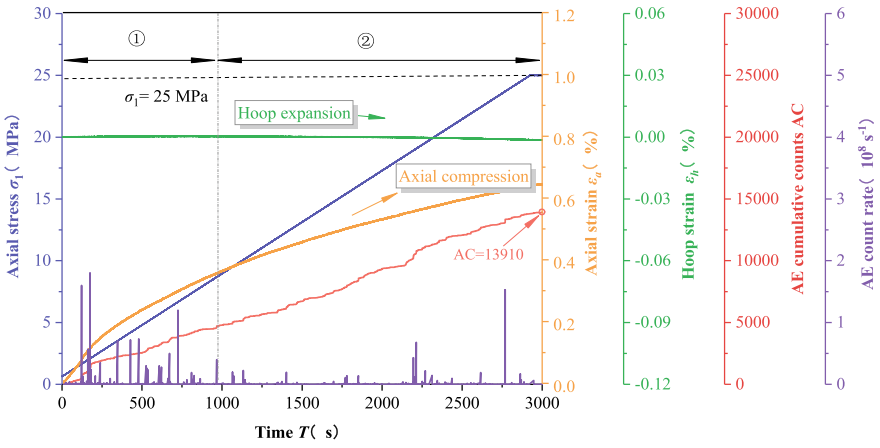

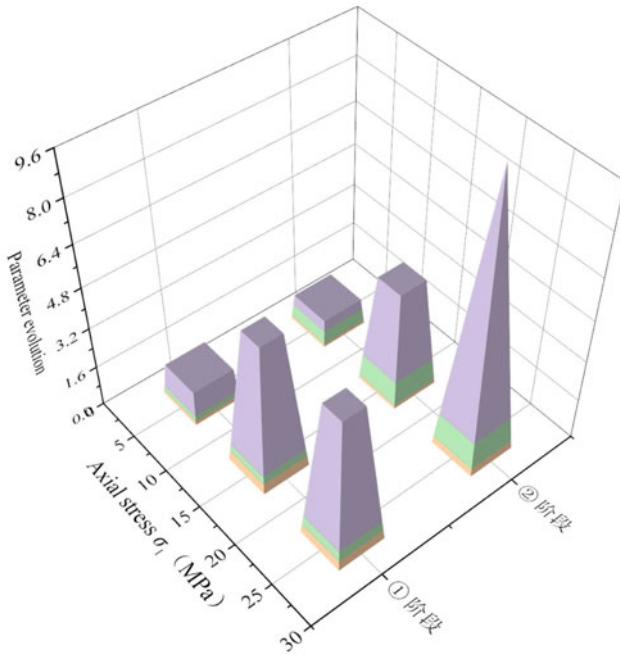(a) Axial stress 5 MPa (Sample CA-90-5)

(b) Axial stress 15 MPa (Sample CA-90-15)

Fig. 4.2 Characteristics of sample deformation and AE during the preloading stage

(c) Axial stress 25 MPa (Sample CA-90-25)

(d) Relative variation of deformation and AE parameters in different stages
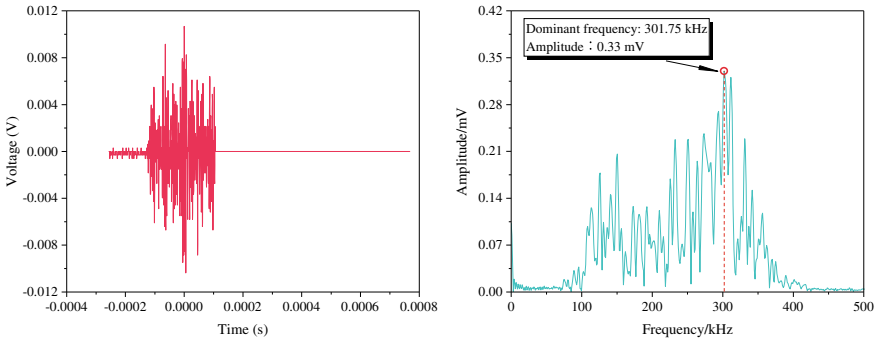
Fig. 4.2   (continued)

Fig. 4.3 An example of the dominant frequency extraction process

discrete time-domain waveform signals are transformed into continuous frequency-domain waveform signals utilizing the fast Fourier transform (FFT). The frequency corresponding to the maximum amplitude in the frequency domain spectrum is the dominant frequency of the AE waveform signal. Based on this principle, the time-varying dominant frequency characteristics of AE during preloading are explored by processing with MATLAB software and extracting the dominant frequency.

The mesoscopic fracture process of rock is characterized by different frequency response characteristics [12–14]. A lot of research has been carried out on the fracturing mechanism of rock using the first motion polarity method and moment tensor method, which reported that the rock fracture process presents obvious characteristics of two dominant frequency bands. Specifically, the tensile fracture in the rock generates the waveform signals with a low dominant frequency band, while the shear fracture produces a high dominant frequency band. However, the division of the dominant frequency band of AE has not formed a unified standard. Referring to the research ideas of Lei et al. [15], the AE signal during preloading is divided into three dominant frequency bands, namely, the low frequency band (0 ~ 140 kHz), medium frequency band (140 ~ 210 kHz) and high frequency band (210 ~ 350 kHz). Considering interference of the environmental noise, the actual value range of the low frequency band starts from 20 to 140 kHz. According to the frequency band characteristics of AE signals, the types of microcracks are classified, and the micro fracturing mechanism of rock during preloading is analyzed.

The time-varying evolution characteristics of AE signals in the frequency domain under different preload disturbances are shown in Fig. 4.4. It can be seen that the AE signal presents obvious dual dominant frequency band (high-low) characteristics. In addition, AE signals with low dominant frequency and low amplitude are mainly generated during the preloading process, which accounts for over 85%, indicating that the tensile fractures are mainly generated at the initial preloading stage. The medium dominant frequency signal appears in all axial loading processes, indicating that the mixed tensile-shear fractures occur in both of the compaction and the linear loading stages. In contrast, the high dominant frequency signal is more sensitive to the magnitude of the axial load. With the increase of axial load, the high frequency

signal in the sample begins to increase, implying that the increase of axial load will also induce more shear fractures.

① **Fluid injection process**

Figure 4.5 is the evolution curves of deformation, pump pressure and AE signal induced by fluid injection under different stress conditions. The hydraulic fracturing curves under constant injection rate (Q_{inj} = 12 mL/min) condition show the morphological characteristics of instantaneous change. At the initial pressurization stage (0 ~ 13 s), the sample's strain and AE signal change slightly. With the increase of pump pressure, the AE signal increases gradually accompanied by the axial and circumferential strains. When the pump pressure exceeds 80% of the breakdown pressure (P_b), the AE signal surges and the sample is hydraulically fractured followed by the subsequent sudden change of axial and circumferential deformation and steep drop of pump pressure. Afterward, the pump pressure declines to zero, the AE signal falls synchronously, and the axial and circumferential strains remain at an approximately constant level.

Under different axial stress conditions, the evolution of deformation and AE induced by fluid injection is also different. Comparing Fig. 4.5a–c, it can be found that when the initial axial stress is low (≤5 MPa), the AE ring counting rate with an increasing rate from slow to fast will be generated in the pressurization and energy storage stage before fracturing. This indicates that the closing, initiation or reconnection of micro-cracks becomes more frequent, promoting the nonlinear increase of circumferential strain (Fig. 4.5a). With the increase of the initial axial stress, the axial restraint on the sample increases. Compared with the axial stress of 5 MPa, when the axial stress is 15 MPa, the activity and spanning time of AE before breakdown are significantly reduced, indicating that the micro-cracks in the sample are in a slow growth state where the cracks are instantaneously initiated or closed, which leads to a stepwise increase in the circumferential strain (Fig. 4.5b). When the axial stress is further increased to 25 MPa, it can be seen from Fig. 4.5c that there is almost no AE counting signals before the hydraulic breakdown, implying that the hydraulic fracturing process is featured by instantaneous breakdown under high-stress conditions. The circumferential strain is positive and increases gradually, indicating that the sample has a certain degree of shrinkage deformation in the radial direction during the injection process. This implies that the continuously increasing pump pressure under high axial stress (25 MPa) induces the opposite effect of the axial stress (compression and expansion). At lower axial stress, the pumping injection causes lateral expansion of the sample (ε_h < 0), which is beneficial to the axial compression and expansion. Under low axial stress (5 MPa and 15 MPa), the axial strain remains approximately constant. On the other hand, under the axial stress of 25 MPa, the axial strain shows a slowly increasing trend, indicating that under the action of high axial stress, the hydraulic pressurization causes the compressive deformation of the sample in the axial direction. These phenomena may be because the low axial stress is not enough to close the micro defects completely, so the pump pressure facilitates the main fractures to develop or close, thus contributing to the radial expansion of the sample. However, under high axial stress, the sample is in a
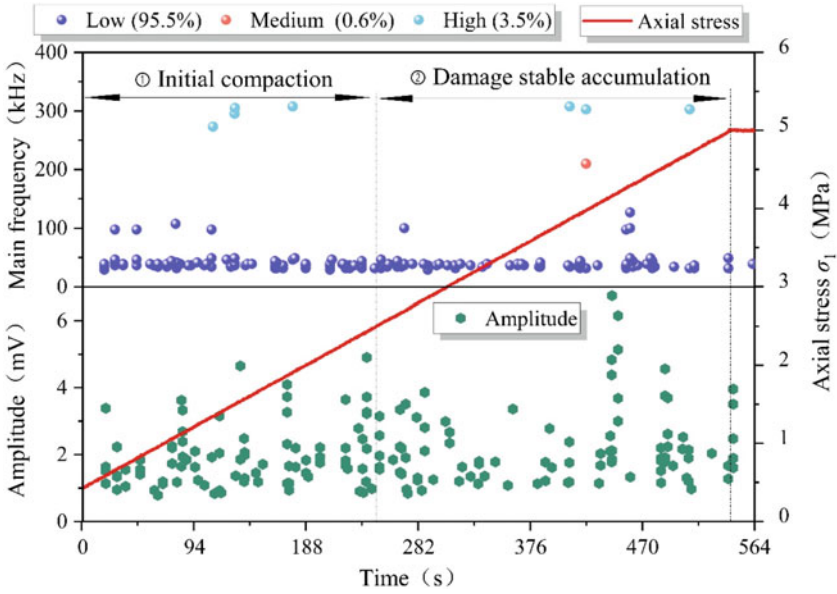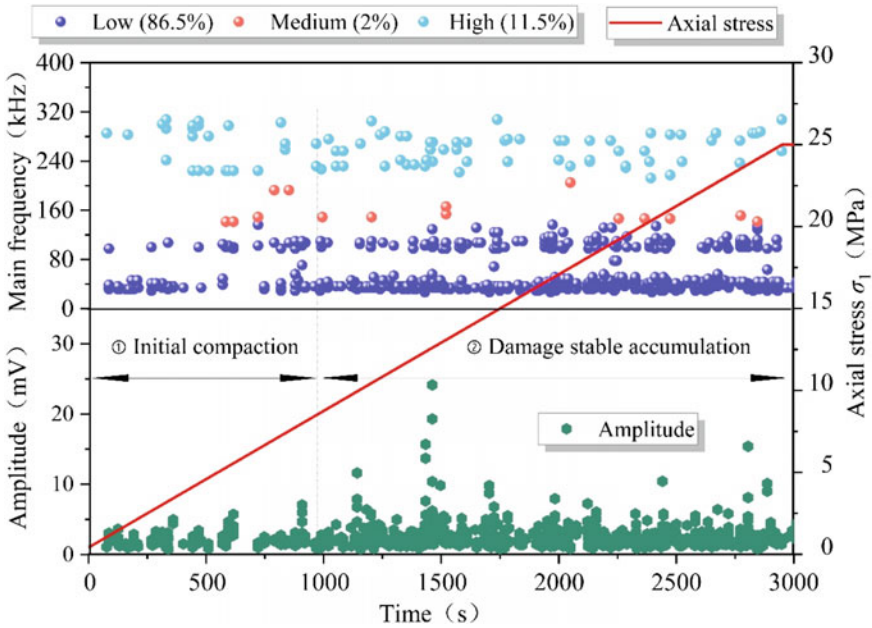
(a) Axial stress of 5 MPa (Sample CA-90-5)
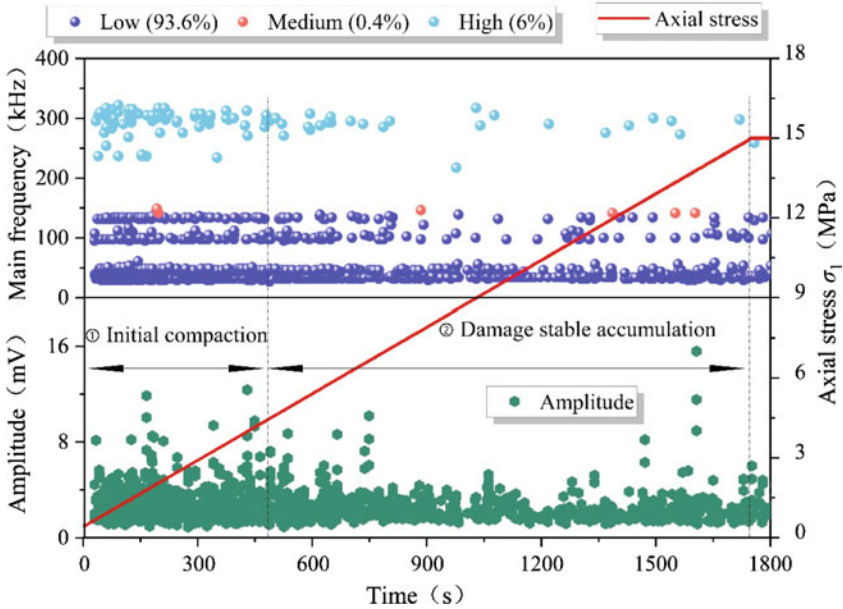
(b) Axial stress of 15 MPa (Sample CA-90-15)

Fig. 4.4 The time-varying characteristics of AE frequency domain during preloading process

(c) Axial stress of 25 MPa (Sample CA-90-25)

Fig. 4.4 (continued)

completely compact state, and the pump pressure enlarges the pore pressure around the wellbore, resulting in shrinkage in both radial and axial directions.

Table 4.1 shows the comparison of breakdown pressure, instantaneous strain increment and AE signal characteristic parameters during hydraulic fracturing under different axial stresses. Where AC represents an AE cumulative (ringing) count, $\Delta\varepsilon_h$ and $\Delta\varepsilon_a$ is the circumferential and axial instantaneous strain increment, respectively. It can be seen from Table 4.1 that the breakdown pressure of rock decreases with the increase of Axial stress. The initial damage in the sample before the injection is small (Fig. 4.4), and the axial limit of the sample is small under the condition of low Axial stress. In the process of hydraulic injection, the micro-cracks close, crack and connect frequently. The energy accumulated by hydraulic pressurization can be released to a certain extent by opening or closing these defects, so higher pump pressure is required to crack the rock. On the contrary, compared with the low Axial stress, the samples with high Axial stress have more initial damage, and the pressure drop and energy consumed by the closure and communication of micro-fractures are small, which makes it possible to maintain effective pump pressure in the borehole and facilitate the induction of hydraulic fracturing under low pump pressure. In terms of rock deformation, with the increase of initial Axial stress, the instantaneous increment of circumferential strain increases gradually while the instantaneous increment of axial strain decreases gradually. It is shown that different axial stresses also have

different degrees of restraint (or promotion) on the deformation of the samples at the moment of fracturing, mainly showing that increasing the initial axial stress will promote radial expansion and inhibit axial compression. In addition, the cumulative counts and peak count rate of AE are negatively correlated with the change of axial
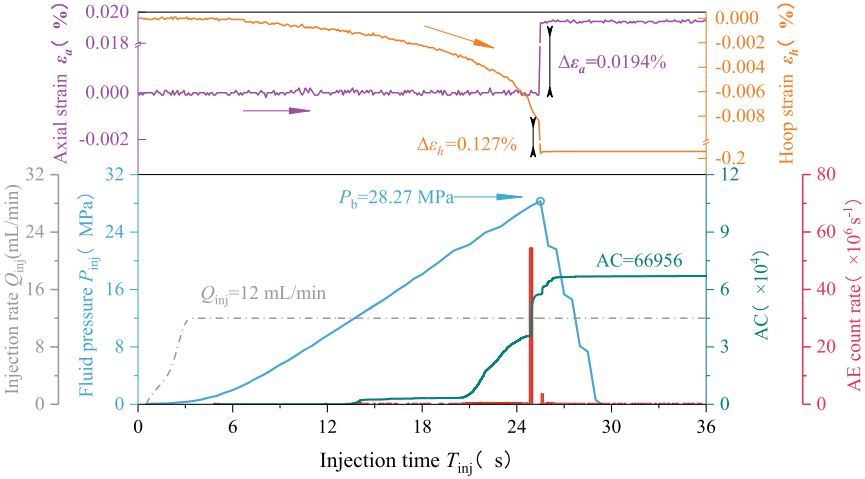
(a)   Axial stress of 5 MPa (Sample CA-90-5)
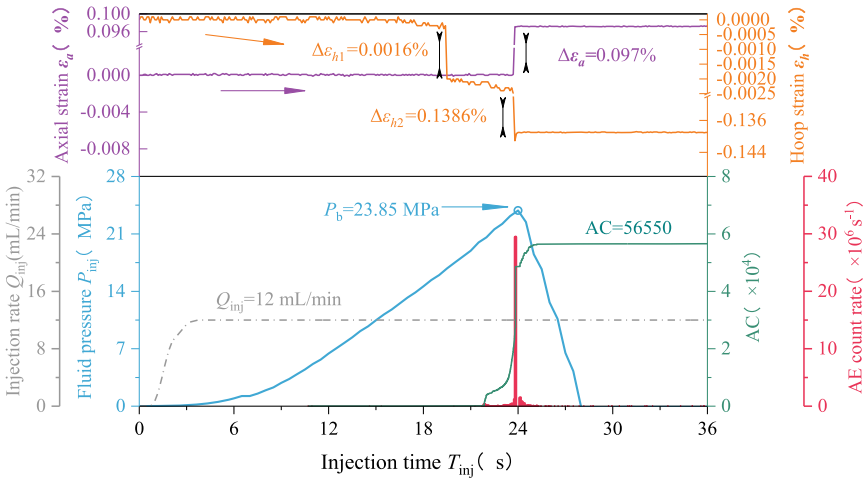
(b)   Axial stress of 15 MPa (Sample CA-90-15)

Fig. 4.5   Evolution curves of pump pressure, rock deformation and AE under different axial stress states
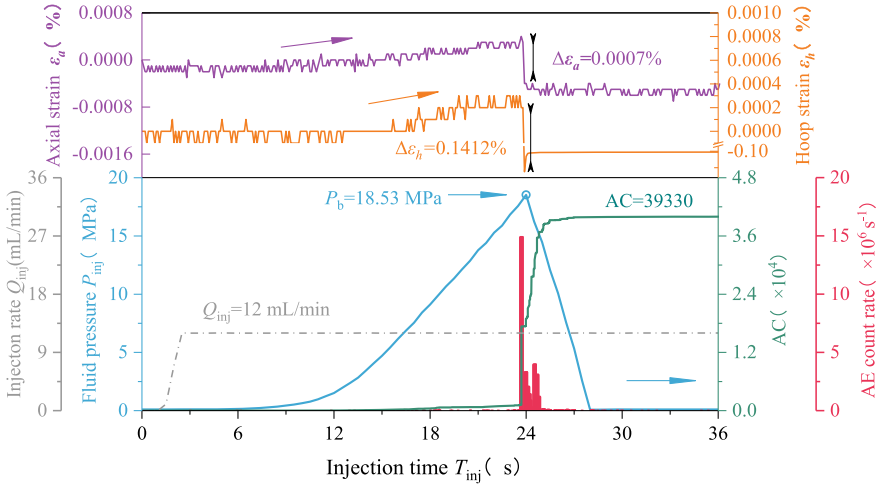
(c) Axial stress of 25 MPa (Sample CA-90-25)

Fig. 4.5 (continued)

stress, indicating that the AE activity decreases with the increase of initial axial stress during hydraulic fracturing.

The time-domain evolution of the dominant frequency and amplitude of AE during hydraulic fracturing is shown in Fig. 4.6. Similar to the preloading process, the low-frequency and low amplitude AE signals are produced in the hydraulic injection process. The low-frequency signals under different axial stress account for more than 87%, indicating that the tensile micro-cracks are mainly produced in hydraulic fracturing.

According to the time-domain distribution characteristics of the dominant frequency and amplitude of AE, the hydraulic fracturing process can be divided into three stages:

(1) Sporadic distribution stage of low frequency and low amplitude signals (stage i). This stage corresponds to the nonlinear pressure rise and energy storage process of the fluid in the borehole. The pump pressure transits from the initial slow

Table 4.1 Hydraulic fracturing parameters of shale samples under different axial stresses

Axial stress/MPa	Breakdown pressure P_b/MPa	Instantaneous strain increment /%		AE characteristic parameters	
		Circumferential $\Delta\varepsilon_h$	Axial $\Delta\varepsilon_a$	AC	Peak count rate (s^{-1})
5	28.27	0.127	0.0194	66,956	5.4×10^7
15	23.85	0.1386	0.0097	56,550	2.9×10^7
25	18.53	0.1412	−0.0007	39,330	1.5×10^7
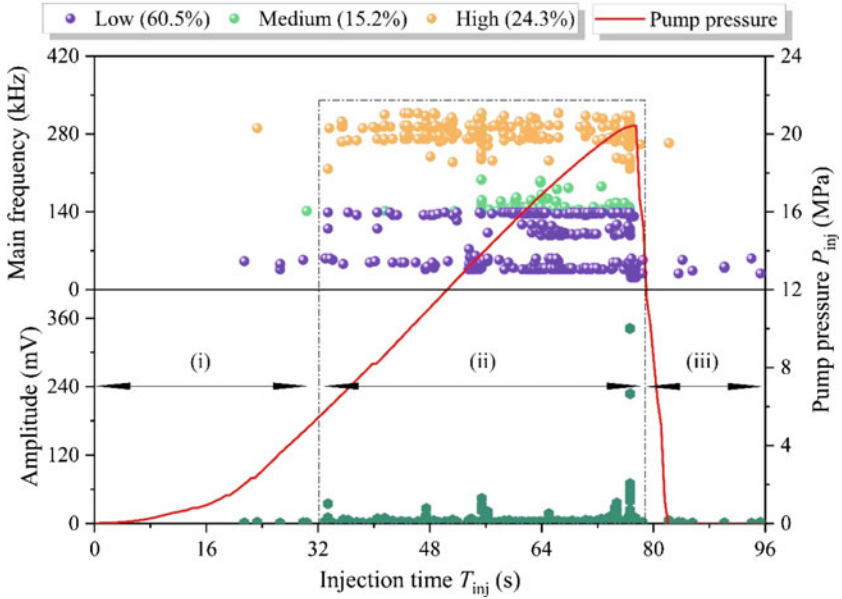
(a) Axial stress 5 MPa (Sample CA-90-5)
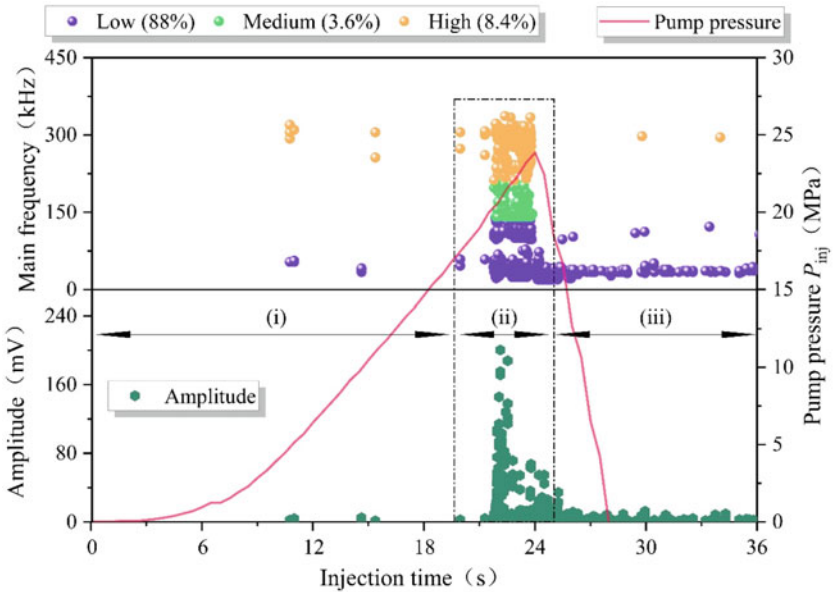
(b) Axial stress 15 MPa (Sample CA-90-15)

Fig. 4.6 Time–frequency characteristics of hydraulic injection process under different axial stresses
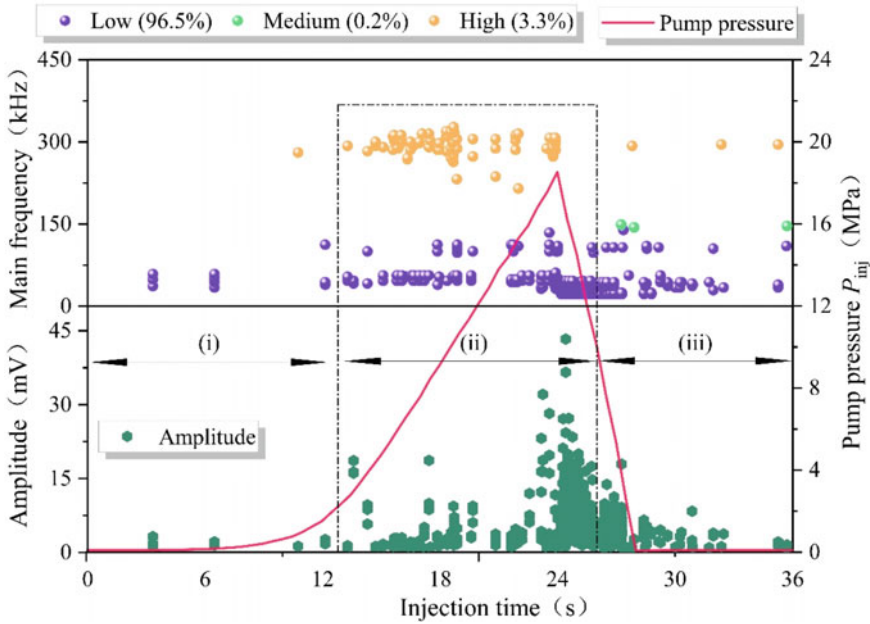
(c) Axial stress 25 MPa (Sample CA-90-25)

Fig. 4.6 (continued)

increase to the rapid and stable increase, and a small amount of high-frequency and low amplitude signals are generated during the injection process, indicating that the shear fracture could occur during the initial injection process.

(2) Intensive concentration stage of dominant frequency amplitude (stage ii). At this stage, the pump pressure keeps increasing rapidly and steadily until the breakdown pressure is reached. The sharply increased low and high-frequency double band high amplitude signals and medium frequency low amplitude signals appear at this stage and are densely distributed near the breakdown pressure, indicating that various types of micro-fractures are cracked, developed and connected before the breakdown of the sample, and the hydraulic fracturing process is accompanied by obvious high amplitude events.

(3) Stable extension stage of low frequency and low amplitude signals (stage iii). This stage corresponds to the pressure drop stage. The hydraulic fracture generated by fracturing provides a stable seepage channel for the fracturing fluid in the hole. Under the action of internal pressure, the fracturing fluid overflows along the hydraulic fracture, resulting in the rapid attenuation of pump pressure. When the overflow flow is equal to the injection flow, the pressure in the sample remains constant (0 MPa). Since then, the low-frequency and low amplitude AE signals monitored are mainly generated by the flow of fracturing fluid on the fracture and sample surface, which indicates that the constant flow of fluid

in the fracture may also generate low-frequency and low amplitude AE signals during hydraulic fracturing.

According to Fig. 4.6, when the axial stress is 5 MPa, the proportions of the high, medium, and low dominant frequency bands are 87.5%, 10%, and 2.5%, respectively; When the axial stress is 15 MPa, the high, medium and low dominant frequency bands are 88%, 3.6%, and 8.4%, respectively; When the axial stress is 25 MPa, the high, medium and low dominant frequency bands are 96.5%, 0.2%, and 3.3%, respectively. Comparing the proportions of various frequency bands under different Axial stress, it can be found that with the increase of axial stress, the proportion of low-frequency signals in the sample gradually increases, and the intermediate frequency signals gradually decrease, indicating that hydraulic fracturing under high axial stress promotes the generation of tensile micro fractures, and restrains the generation of shear fractures, especially tensile-shear mixed fractures.

To sum up, in the process of hydraulic fracturing, high local stress is generated around the borehole through constant flow pressurization, which promotes the radial expansion of the sample. When the pump pressure in the hole increases to the ultimate strength in a certain direction, the strain energy is released instantaneously, and the sample is fractured. When the axial stress is larger, the compaction effect of micro-cracks and pores in the sample is more obvious, and the breakdown pressure of the rock is lower. In addition, the increase of axial stress will promote tensile microfracture and inhibit the growth of tensile-shear mixed microfracture. It should be noted that the pressure corresponding to the high axial stress mentioned in this paper is less than 30% of the uniaxial compressive strength of the sample, that is, the axial stress applied will not generate macro-cracks in the sample. In addition, it is also noted that the pump pressure curve fluctuates obviously after the pump pressure reaches the breakdown pressure (such as sample CA-90-5). The reason is that the fluid pressure will be released with the fracture's propagation, and the fracturing fluid in the fracture will leak along the existing fracture, resulting in the closure of the fracture tip or even fracture arrest. Only by continuously increasing the pump pressure can the continuous crack initiation and propagation be maintained, thus causing the pump pressure to fluctuate.

② **Hydraulic fracture morphology**

(1) **Surface fracture morphology**

The fracture morphology on the sample surface under different axial stress is shown in Fig. 4.7. By referring to Ishida et al. [16] and Hou et al. [17], the fracture propagation path and morphology are depicted based on direct observation. In addition, the hydraulic fracture morphology is quantitatively characterized by the tortuosity [18], whose expression is

$$\tau = \frac{L}{l} \tag{4.1}$$
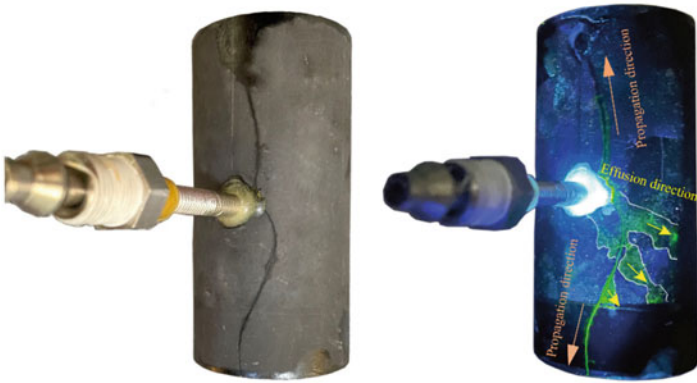
(a) Axial stress of 5 MPa (Sample CA-90-5)
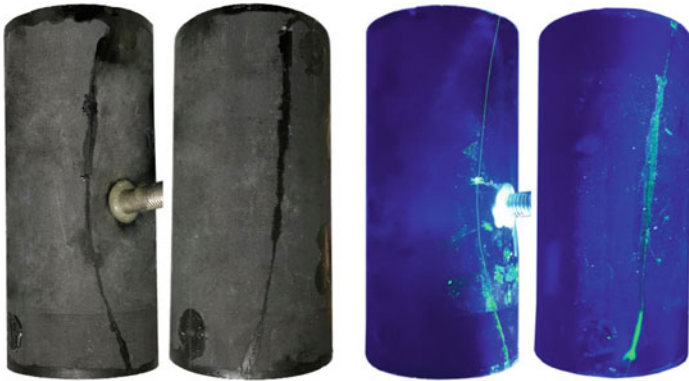
(b) Axial stress 15 MPa (Sample CA-90-15)
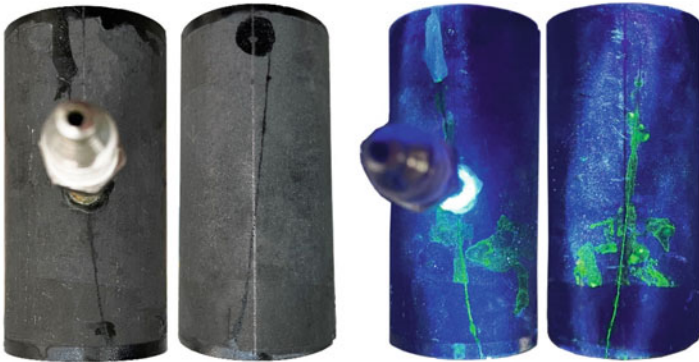
(c) Axial stress 25 MPa (Sample CA-90-25)

Fig. 4.7 Fracture morphology induced by hydraulic fracturing under different axial stresses (Left: natural light observation; Right: Ultraviolet light observation)

Table 4.2 Fracturing
parameters under different
axial stresses

Sample number	Axial stress σ_1/MPa	Injection rate Q_{inj}/mL/min	Tortuosity τ
CA-90-5	5	12	1.050
CA-90-15	15		1.028
CA-90-25	25		1.007

where τ represents the tortuosity, L is the actual length of the hydraulic fracture, and l is the distance between the two ends of the hydraulic fracture. The calculated tortuosity under different axial stresses is shown in Table 4.2. It should be noted that the tortuosity mentioned in this chapter is only for the main hydraulic fracture.

On the whole, no matter how the axial stress varies, the hydraulic fracture shows a bi-wing vertical propagation mode along both sides of the borehole. The axial stress has a certain disturbance on the fracture morphology of the sample surface. When the axial stress is 5 MPa, the hydraulic fracture initiates from the asymmetric position of the wellbore and then deflects in the direction of axial stress, and its morphology is tortuous ($\tau = 1.05$). With the increase of axial stress, the hydraulic fracture tends to be smooth gradually. When the axial stress increases from 5 to 15 MPa, the hydraulic fracture tortuosity decreases from 1.05 to 1.028, decreasing by 2.1%; When the axial stress continues to increase from 15 to 25 MPa, the tortuosity of the main fracture decreases from 1.028 to 1.007, decreased by 2%. This phenomenon shows that fracture tortuosity generally decreases with the increase of axial stress.

(2)   **Roughness of fracture surface**

The roughness of the fracture surface is very important to evaluate the fluid flow and proppant migration in hydraulic fractures. The three-dimensional space coordinates x, y, and z (Fig. 4.8) of each point on the fracture surface can be acquired by the three-dimensional laser scanner and stored and output in text format so that the roughness parameters of the fracture surface can be calculated. The parameters used to quantitatively characterize roughness mainly include: the standard deviation of fracture surface height (SD) [19, 20], mean three-dimensional angle θ_s [21], and surface roughness coefficient R_s [22]. Three parameters have a certain correlation in their length scale, but they independently correspond to different physical meanings, which can characterize the morphological characteristics of rough fracture surfaces from different perspectives.

The standard deviation of fracture surface height (SD) refers to the standard deviation of the vertical height (i.e. z coordinate value) of each point on the fractured surface. SD is often used in geography to describe the topographic elevation degree. Here, it represents the fluctuation deviation degree of the concave-convex topography of the fracture surface. Its calculation formula is:

$$SD = \sqrt{\frac{\sum_{i=1}^{N} (z_i - \bar{z})^2}{N - 1}} \tag{4.2}$$

(a) – Assembly of elementary surfaces

(b) – An elementary surface
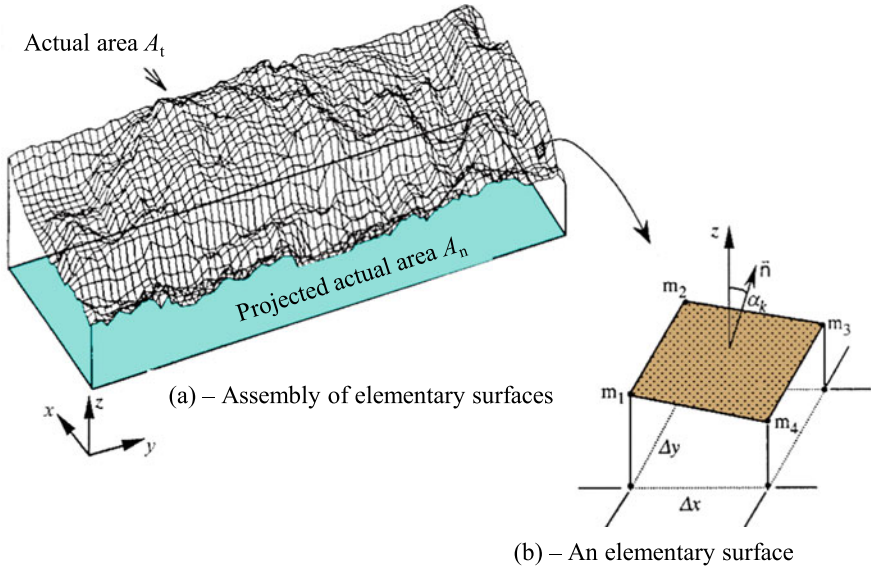
Fig. 4.8 Illustration of the calculating method of fracture toughness [22]

where N is the number of all coordinate points obtained from the fracture surface; Z_i is the Z coordinate value of the i_{th} coordinate point and $\overline{Z}$ the average value of the Z coordinates of all points.

Figure 4.9 is the standard deviation of fracture height and isoline cloud diagram of the main hydraulic fracture under different axial stress. It can be seen that SD decreases with increasing axial stress. When the axial stress is 5 MPa, the fracture surface is the roughest (SD = 2.79), with the highest height of 15.59 mm and the lowest height of −0.42 mm. When the axial stress increases to 15 MPa, the fracture surface is relatively flat, and the maximum and minimum heights of the fracture surface are 10.89 mm and 0.11 mm, respectively. When the axial stress reaches 25 MPa, the roughness of the fracture surface is the lowest, and the height of the fracture surface varies from 3.73 mm to 8.31 mm. These laws further show that increasing axial stress is beneficial for forming a straight hydraulic fracture.

The mean three-dimensional angle θ_s was first proposed by Belem et al. [21] and applied to evaluate the angular shape of the fracture surface. The calculation of θ_s should meet certain assumptions: the fracture surface is composed of a series of basic unit planes determined by the coordinate points on the fracture surface, as shown in Fig. 4.8. In Fig. 4.8, α_k refers to the angle between the normal vector of the basic unit plane and the Z coordinate axis. The θ_s is the arithmetic average of all α_k, and its calculation formula is:

$$\theta_s = \frac{1}{m} \sum_{i=1}^{m} (\alpha_k)_i \tag{4.3}$$

Fig. 4.9 Contour maps of
vertical hydraulic fractures
in shale samples under
different axial stresses
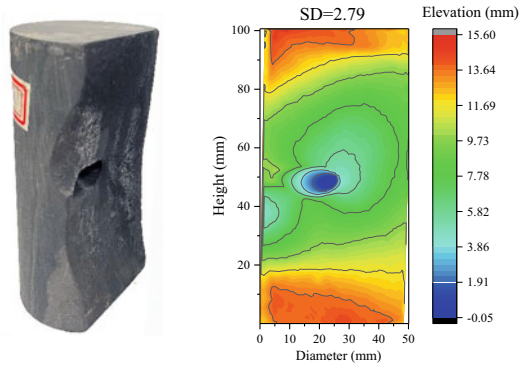
(a) Axial stress of 5 MPa (Sample CA-90-5)
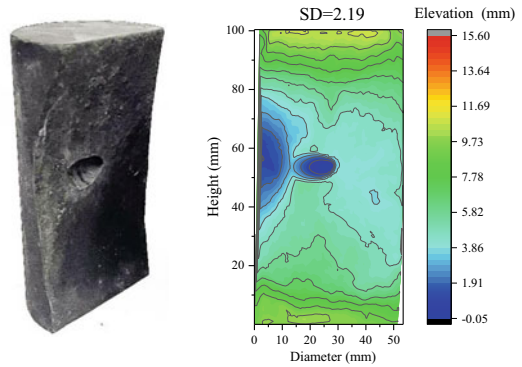
(b) Axial stress of 15 MPa (Sample CA-90-15)
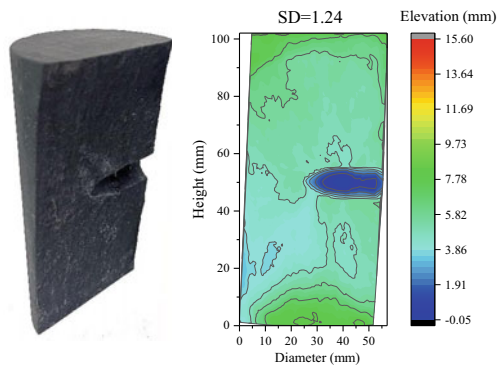
(c) Axial stress of 25 MPa (Sample CA-90-25)

where m represents the number of basic element planes in the fracture surface.

The surface roughness coefficient R_s represents the roughness of the fracture surface, which is defined as the ratio of the true area of the fracture surface (A_t) to its normal projection area (A_n) (≥ 1). The calculation formula is:

$$R_s = \frac{A_t}{A_n} \tag{4.4}$$

According to Belem et al. [21], the true area of fracture surface (A_t) can be approximately calculated by the following formula:

$$A_t \approx (\Delta x \Delta y) \sum_{i=1}^{N_x - 1} \sum_{j=1}^{N_y - 1} \sqrt{1 + \left(\frac{z_{i+1,j} - z_{i,j}}{\Delta x}\right)^2 + \left(\frac{z_{i,j+1} - z_{i,j}}{\Delta y}\right)^2} \tag{4.5}$$

where Δx and Δy are constant calculation steps of the x-axis and the y-axis, respectively. According to the definition of R_s, the larger R_s corresponds to the larger the actual area of the fracture surface and the rougher fracture surface.

The mean three-dimensional angle and surface roughness coefficient of the fracture surface can be calculated by Eqs. (4.3) and (4.4), and the calculation results are shown in Fig. 4.10. It is easy to see that as the axial stress increases, θ_s and R_s are gradually decreased, indicating that the degree of angular undulation of the fracture surface is decreased and its flatness is increased. This law further confirms that increasing axial stress will promote the propagation of hydraulic fracture along the direction of maximum principal stress, and form a flat fracture with low roughness.

4.2.2 Effect of Injection Rate

The process of hydraulic fracturing in constant flow mode has obvious injection rate effect. Chitrala et al. [23] simulated the hydraulic fracturing process of Lyons sandstone reservoir through laboratory tests and found that a high injection rate induces high breakdown pressure. However, Zeng [24] thought that the high injection rate will reduce the breakdown pressure of the sample based on the hydraulic fracturing test of Jackfork sandstone and theoretical derivation and proposed a breakdown pressure model reflecting this relationship based on linear elastic fracture mechanics. Shao et al. [25] studied the effect of injection rate on breakdown pressure and pressurization rate by conducting true triaxial hydraulic fracturing tests. The results show that with the injection rate increase, breakdown pressure increases nonlinearly, but the increase rate decreases gradually. In addition, it is also found that the injection rate has a linear positive correlation with the hydraulic pressurization rate in the stable pressurization stage. On the premise of considering the anisotropy of granite and ignoring the confining pressure disturbance, Zhuang et al. [26] carried out uniaxial hydraulic fracturing tests with the aid of AE and CT scanning. It is found that the
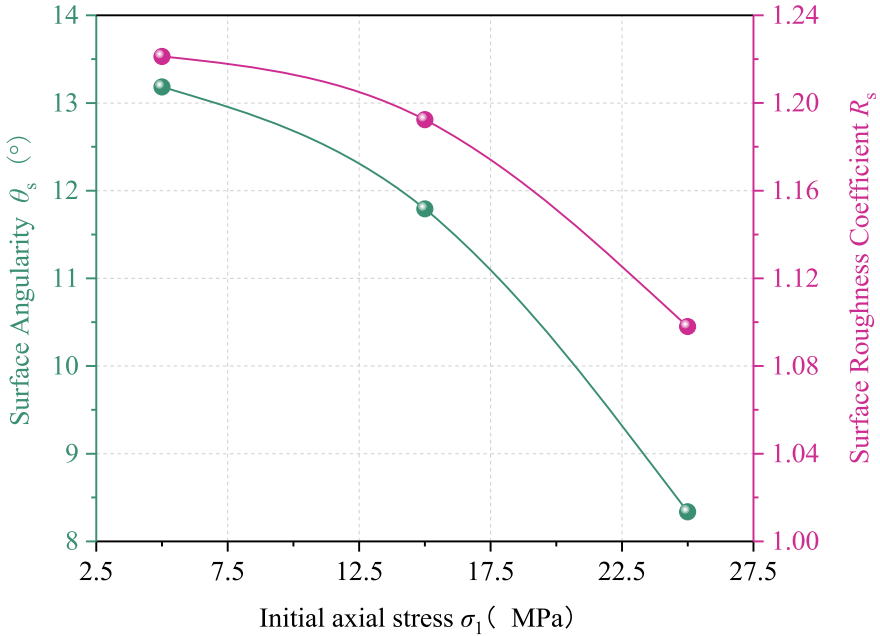
Fig. 4.10 Evolution of mean three-dimensional angle and roughness coefficient of fracture surfaces under different axial stresses

effect of injection rate on the hydraulic fracturing process has the characteristics of stage threshold. When the injection rate is lower than the critical threshold, the hydraulic pressure in the hole increases slowly, and the water permeates into the rock matrix, resulting in the sample finally reaching the fully saturated state without being fractured. When the injection rate is greater than the critical threshold, the pump pressure in the hole increases rapidly until hydraulic fracturing occurs, and the critical breakdown pressure increases with the increase of the injection rate.

According to the above research status, the disturbance of injection rate on the hydraulic fracturing process is mainly reflected in the following two aspects: (1) the effect of injection rate on the change of pressurization rate. Generally speaking, a high injection rate will produce a high pressurization rate and induce a strain rate effect, leading to a rapid increase of pore pressure gradient around the borehole during hydraulic pressurization and promoting rock fracture. (2) The injection rate is closely related to the hydraulic infiltration process. At a low injection rate, the hydraulic pressurization process takes a long time, and the fluid permeates into the rock matrix, which is mainly affected by the permeability of the sample and the pressurization time; On the other hand, when the injection rate is high, the pressure increases rapidly, resulting in hydraulic fracturing of the sample before infiltration.

However, previous studies have not analyzed and discussed the evolution law of microfracture during hydraulic fracturing under different injection rates, so there is a lack of explanation of the mechanism of injection rate on microfracture during

hydraulic fracturing. In this section, combined with AE and strain, the hydraulic fracturing results at injection rates of 3, 6, 12, 18 and 30 mL/min are mainly analyzed to explore the disturbance mechanism of different injection rates on the microfracture process of rocks.

① **Evolution of pump pressure, deformation and AE**

The evolution law of the pump pressure, deformation and AE of the sample under different injection rates is shown in Fig. 4.11. Comparing Fig. 4.11a–e, it can be seen that under different injection rates, the evolution trends of pump pressure, deformation and AE are relatively consistent, that is, with the continuous increase of pump pressure, the change of circumferential strain (in numerical value) of each sample shows a nonlinear increase, while the axial strain basically does not change. At the same time, the signal accumulation rate of AE counting is gradually accelerated. When the pump pressure is close to the breakdown pressure, the AE counting rate reaches the peak first. After about 0.1 ~ 0.3 s, the circumferential strain increases sharply, the axial strain decreases abruptly, and the pump pressure decays rapidly to zero.

Comparing the curves under five injection rates, it can be found that with the increase of injection rate, the time for hydraulic fracturing of the sample is shortened and the breakdown pressure (P_b) is increased, which is consistent with the test results of Haimson [27], Zoback [28] and Solberg [29].

In addition, different injection rates have different effects on the deformation of the samples during hydraulic fracturing. When the injection rate is low (Q_{inj} = 3 mL/min), the axial and circumferential strains of the sample increase slowly during the injection pressurization process. Until the sample is broken, the axial and circumferential strains are almost constant, and the volume strain increment at the critical failure is 0.0881% (Fig. 4.11a). However, for the sample with Q_{inj} = 6 mL/min, when the pump pressure increases to 10 MPa, the circumferential strain increases abnormally ($\Delta\varepsilon_{h1} = 0.0009\%$), which may be caused by the sudden release of high pump pressure accumulated in the borehole due to local fracture in the sample (Fig. 4.11b).

Unlike the experimental results with an injection rate of 3 mL/min, the circumferential strain of the sample with an injection rate of 6 mL/min keeps a stable decreasing trend before fracturing, and at the moment of fracturing, the instantaneous volume strain increment of the sample reaches 0.1275%. When the injection rate is 12 mL/min, the circumferential strain of the sample will show an obvious nonlinear downward trend with the pump pressure increase, and the volumetric strain at the time of failure is 0.2734%, as shown in Fig. 4.11c. When the injection rate is 18 mL/min or 30 mL/min, the axial strain of the sample is basically constant during the hydraulic pressurization process, and the circumferential strain shows a significant increasing trend (obvious lateral expansion). At the moment of fracturing, the volume strain increment of the two injection rates is 2.0951% and 2.938%, respectively. Overall, the injection rate's effect on the sample's deformation process is mainly reflected in the initial pressurization and instantaneous fracturing stages. The deformation of the sample after complete fracturing is no longer disturbed by the injection rate.
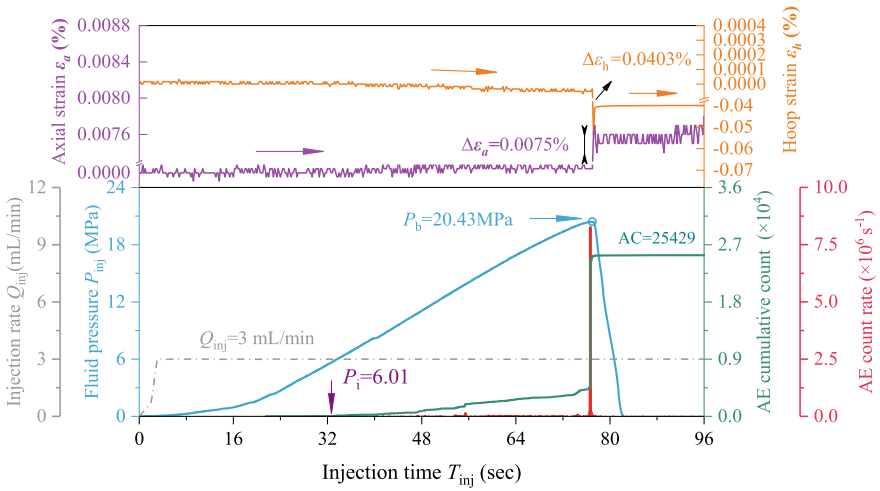
(a) Q_{inj} = 3 mL/min (Sample CI-90-3)
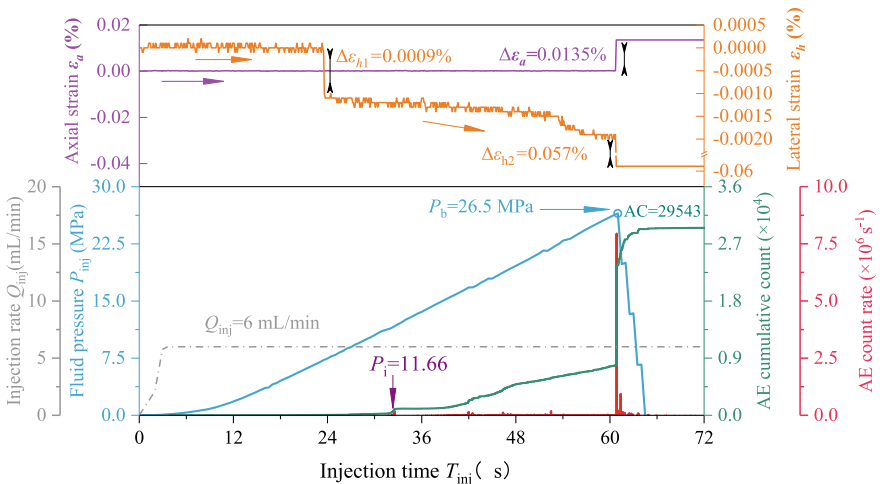
(b) Q_{inj} = 6 mL/min (Sample CI-90-6)

Fig. 4.11 Evolution curves of pump pressure, rock deformation and AE under different injection rates

In the process of hydraulic pressurization, with the increase of injection rate, the radial expansion deformation of samples before fracturing tends to be more obvious. At the moment of fracturing, the volume strain at critical failure also gradually increases with the injection rate increase. This phenomenon can be explained from the perspective of energy, that is, a high injection rate will accumulate higher strain
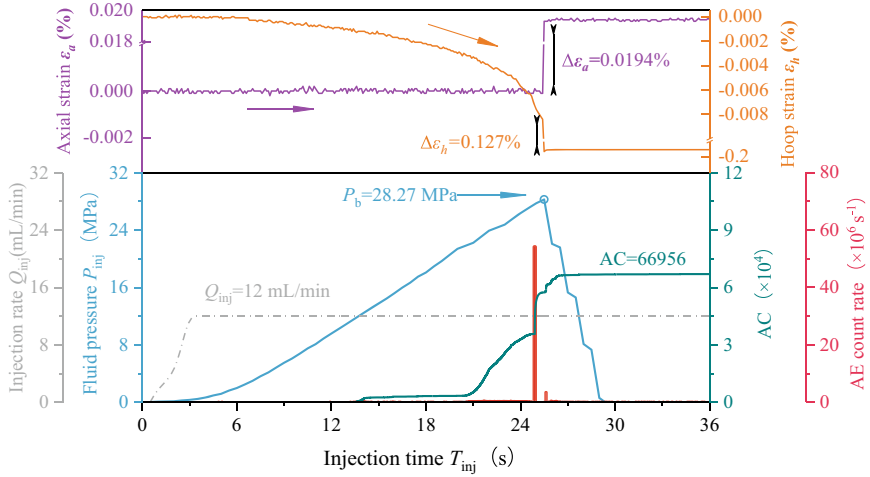
(c) Q_{inj} = 12 mL/min (Sample CA-90-12)
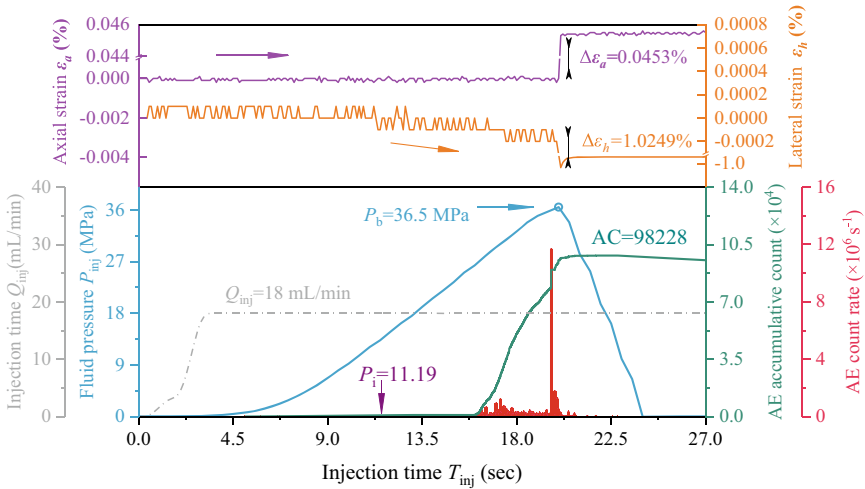
(d) Q_{inj} =18 mL/min (Sample CI-90-18)

Fig. 4.11   (continued)

energy, resulting in the release of more energy during fracturing, which induces the sample to produce greater volume strain. This conclusion is further confirmed by the increase of AE cumulative counts with the injection rate increase during fracturing, as shown in Fig. 4.11a–e.

There are also differences in damage accumulation and fracture mode evolution under different injection rates. Comparing Fig. 4.11a–e, it can be found that with the
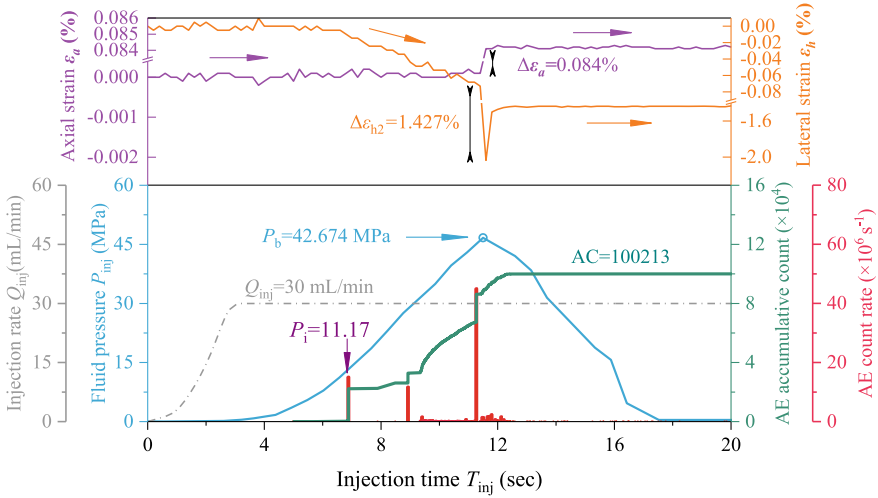
(e) $Q_{inj} = 30$ mL/min (Sample CI-90-30)

Fig. 4.11 (continued)

increase of injection rate, the growth rate of AE cumulative counts gradually accelerates. Specifically, when the injection rate is low, the AE count generally shows a changing trend of slowly increasing at first and then rapidly increasing. The accumulation of AE signals has a transient change, as shown in Fig. 4.11a–c. With the increase of injection rate ($Q_{inj} \geq 18$ mL/min), the slow growth section of AE cumulative counts is significantly shortened. The count signal increases rapidly in the preloading stage before critical failure. In contrast, the AE count released during fracturing is relatively small, indicating that a high injection rate will aggravate the development of microfracture and promote the propagation and penetration process of microfracture. In addition, the AE count rate gradually fluctuates significantly in the hydraulic pressurization stage. Especially when the injection rate is 30 mL/min, there are two independent peaks in the count rate before fracturing, indicating that there are two fractures cracking in the sample. The initiation of a new fracture may lead to pressure loss at the crack tip, so it is necessary to further increase the pump pressure, which will eventually lead to the unstable propagation of the fracture, resulting in a higher breakdown pressure [28].

Table 4.3 records the breakdown pressure, deformation and AE characteristic parameters at different injection rates. It can be seen that the instantaneous strain, AE cumulative counts and peak count rate of the sample are positively correlated with the injection rate. It should be noted that the peak count rate does not strictly increase with the injection rate, which may be due to the difference of individual physical properties of the sample or the uneven distribution of micro cracks, resulting in the difference of the cracking degree of the sample.

Table 4.3 Fracturing results at different injection rates

Injection rate (mL/min)	Breakdown pressure P_b (MPa)	Instantaneous strain increment /%		AE characteristic parameters	
		Circumferential $\Delta\varepsilon_h$	Axial $\Delta\varepsilon_a$	Accumulative AC	Peak count rate (s^{-1})
3	20.43	0.0403	0.0075	25,429	0.82×10^7
6	26.5	0.057	0.0135	29,543	0.74×10^7
12	28.27	0.127	0.0194	66,956	5.4×10^7
18	36.5	1.0249	0.0453	98,228	1.17×10^7
30	42.674	1.427	0.084	100,213	4.51×10^7

Microfracture initiation pressure refers to the pump pressure corresponding to the time when the AE activity starts to change significantly during hydraulic fracturing [28]. The fracture initiation pressure of the sample under different injection rates has been marked in Fig. 4.11, and its magnitude relative to the breakdown pressure and its variation with the injection rate is shown in Fig. 4.12. Compared with the breakdown pressure, the fracture initiation pressure is smaller. When the injection rate is greater than 6 mL/min, the fracture initiation pressure is no longer sensitive to the change of the injection rate. The difference between the two pressures increases with the increase of the injection rate.

Fig. 4.12 Breakdown pressure and fracture initiation pressure under different injection rates

Figure 4.13 shows the time–frequency evolution of AE during hydraulic injection at different injection rates. Comparing Fig. 4.13a–e, it can be seen that the proportion of low-frequency AE signals generated by hydraul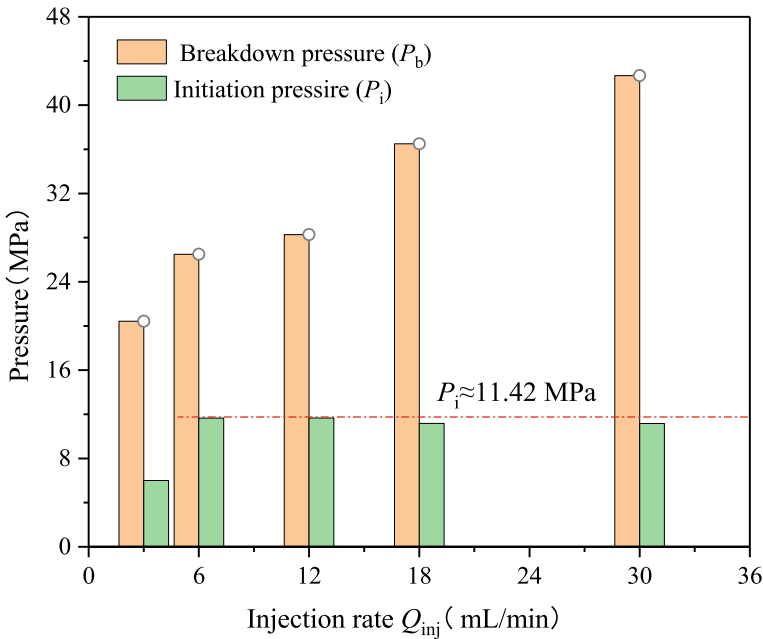ic fracturing at each injection rate is more than 60%, indicating that the hydraulic fracturing process mainly produces tensile micro-fractures, which is less affected by the injection rate. In contrast, the ratio of shear type (high-frequency band) AE signal is more sensitive to the change of injection rate. When the injection rate is low (3 and 6 mL/min), the high-frequency signals of shear fracture produced by hydraulic pressurization account for 24.3% and 17.9%, respectively. With the increase of injection rate (12, 18, and 30 mL/min), the shear type high-frequency band signal is gradually decreasing (2.5%, 3.6%, and 3.3%, respectively), indicating that a high injection rate is more prone to produce tensile microcracks and a low injection rate promote the generation of shear micro-cracks. The influence of injection rate on the time-domain distribution of dominant frequency amplitude is mainly reflected in the dense concentration section (ii). It is easy to see that with the increase of the injection rate, the dominant frequency time domain gradually presents a zonal characteristic, that is, the dominant frequency is concentrated at the beginning and end of the dense concentration section (ii), while the AE signal is less at the middle position. The above phenomenon is because this period corresponds to the linear pressurization process, and the sample is approximately in the elastic stage, so the micro crack initiation and penetration activities are less.

Overall, the higher the injection rate, the more low-frequency and high amplitude signals are induced, and the more tensile micro fractures are generated. In addition, for Longmaxi shale with low permeability and high brittleness, the change of injection rate will not affect the overall fracture type of rock. In other words, no matter how the injection rate changes, the microfractures induced by hydraulic fracturing are still mainly tensile fractures, which account for more than 60%. However, Chitrala et al. [30] found in the tests that shear failure induced by hydraulic fracturing usually occurs at low and medium injection rates (0.5–5 mL/min), while tensile fracture occurs at a high injection rate. This conclusion seems to contradict the current experimental results. However, it should be noted that there are essential differences between the two test materials. Chitrala et al. [30] explored the injection rate effect based on Lyons sandstone samples, with a permeability of 10 μD, which is almost 100 times of permeability of the rock used in this experiment. Therefore, in the hydraulic fracturing test with low and medium injection rates, the influence of local leakage of Lyons sandstone is obviously greater than that of the current shale. When the fluid infiltrates into the sandstone matrix, the pore pressure around the wellbore increases, and the effective stress decreases significantly, which is more likely to promote the local sliding of micro fractures and produce shear fractures. On the other hand, it is also found in the current test that when the injection rate is low, the high-frequency shear signal generated in the fracturing process is significantly increased, indicating that a low injection rate will be conducive to generating micro shear fracture in the sample. However, whether the shear fracture finally occurs in the sample still depends on the physical and mechanical properties of the rock. Moreover, in-situ stress, temperature, fluid viscosity, et al., may have complex effects on rock fracture
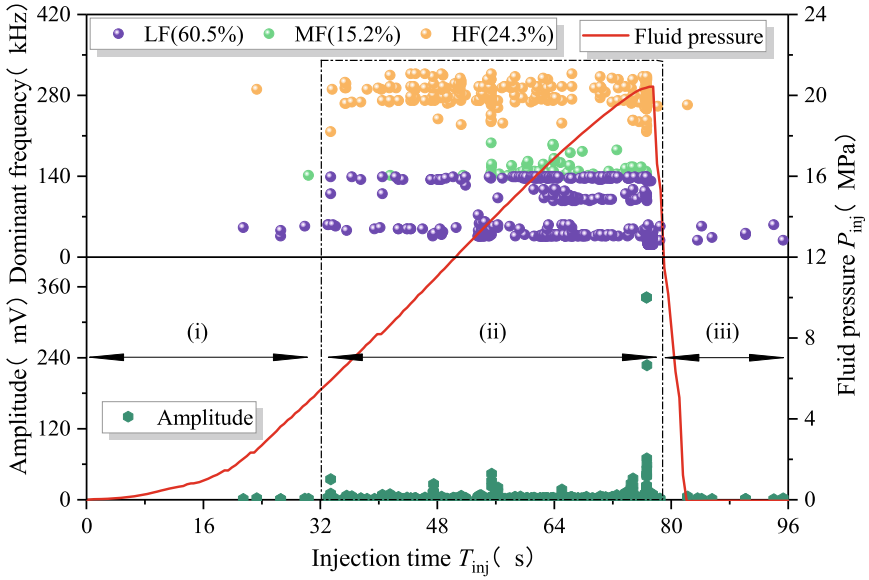
(a) Q_{inj}=3 mL/min (Sample CI-90-3)
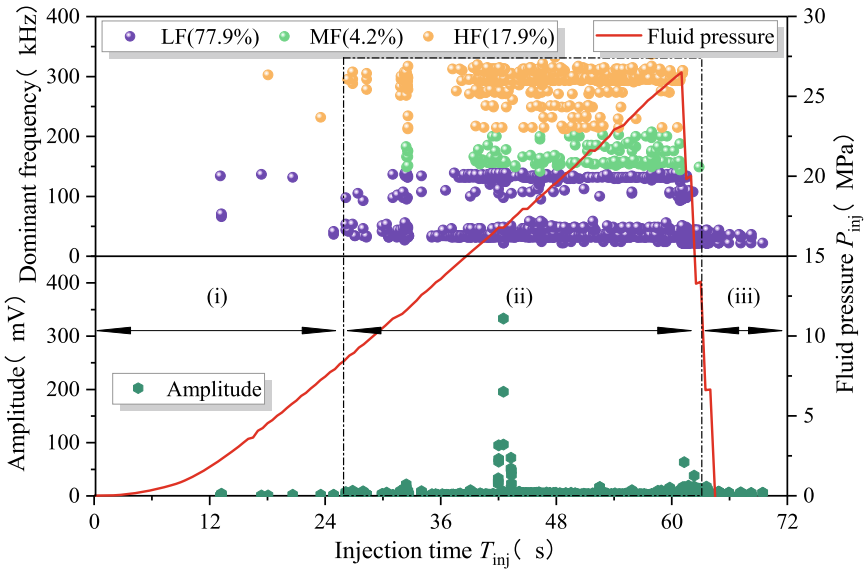
(b) Q_{inj}=6 mL/min (Sample CI-90-6)

Fig. 4.13 Time–frequency characteristics of hydraulic injection process under different injection rates

(c) Q_{inj}=12 mL/min (Sample CI-90-12)

(d) Q_{inj}=18 mL/min (Sample CI-90-18)
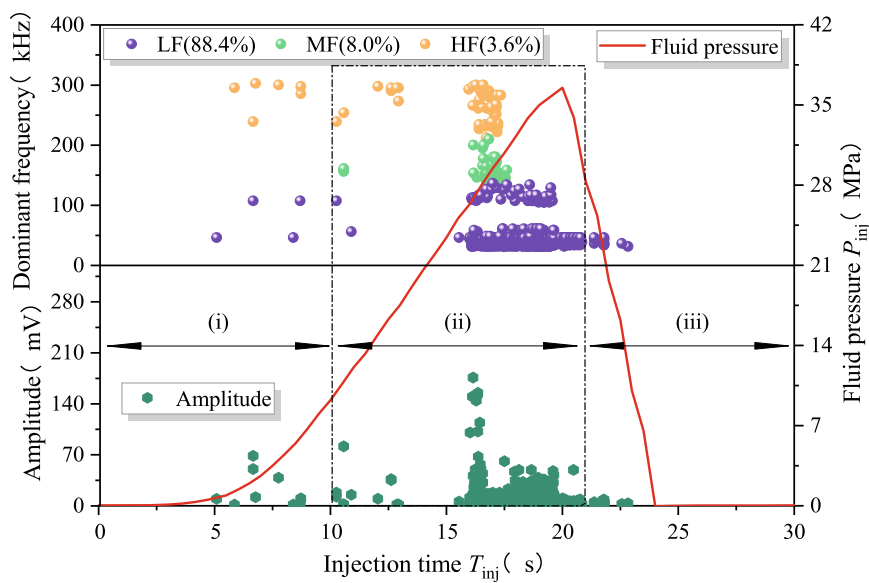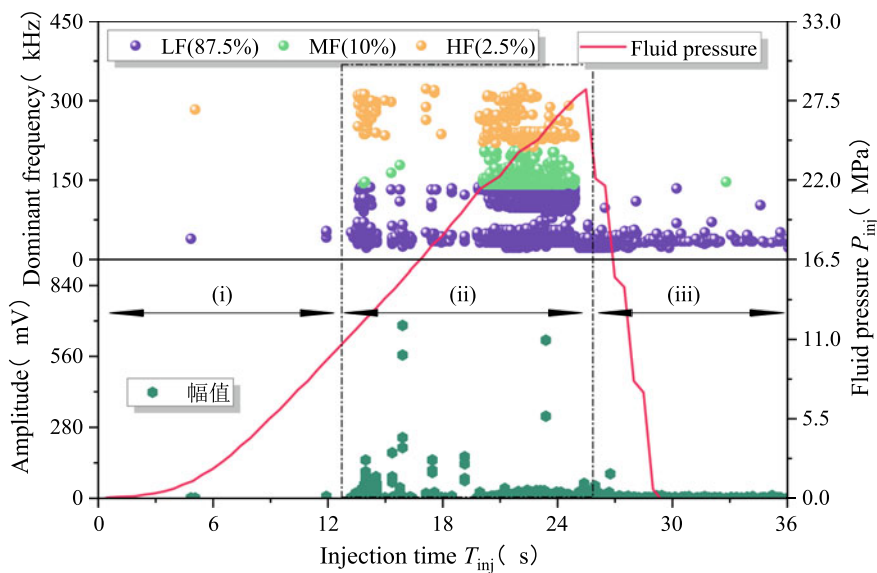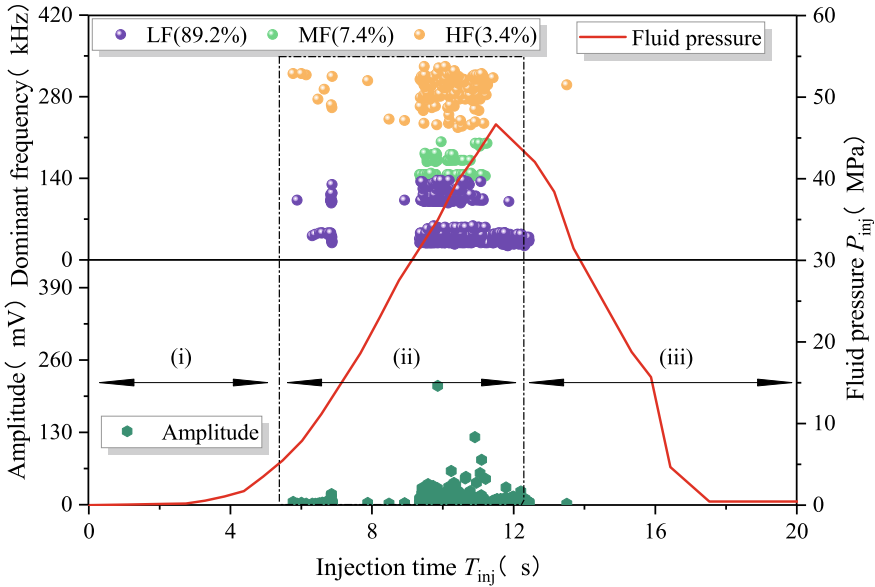
Fig. 4.13   (continued)

(e) Q_{inj}=30 mL/min (Sample CI-90-30)

Fig. 4.13   (continued)

mode, and these factors are still worth further discussion. Nevertheless, the current test results can still provide some reference for directional control of fractures and evaluation of fracture morphology through injection rate in actual fracturing design.

② **Evolution of pressurization rate**

Pressurization rate refers to the increase rate of pump pressure per unit of time, which is mainly related to sample size, wellbore size and injection rate [1]. As we all know, the larger the injection rate, the faster the fluid pressurization, and the more intense the evolution of the pressurization rate. Under the premise of ignoring permeability, this parameter is a physical quantity to measure the speed of hydraulic pressurization in the wellbore.

   Figure 4.14 is the time-varying curve of the pressurization rate during hydraulic fracturing before fracturing under different injection rates. The abscissa of the symbol at the end of the curve corresponds to the time of the fracturing moment. It can be seen from Fig. 4.14a that the evolution trend of the pressurization rate with time is similar under different rates. Taking sample CI-90–12 as an example (see Fig. 4.14b), the pressurization rate goes through three stages in total. The pressurization rate increases monotonously at the beginning (stage A), then remains constant (stage B), and gradually decreases near the breakdown pressure (stage C). The pressurization rate at different rates has a maximum value in stage B. However, the difference is that when the rate is low (Q_{inj} = 3 and 6 mL/min), the evolution process of the pressurization rate before fracturing is relatively gentle. At the same time, for the

high injection rate ($Q_{\text{inj}} = 12 \sim 30$ mL/min), the pressurization rate increases rapidly in stage A, then keeps fluctuating in stage B, and drops quickly in critical fracturing. These phenomena become more obvious with the increase of the injection rate.

To evaluate the relationship between injection rate and pressurization rate, the average value of pressurization rate in stage B is used to reflect the pressurization effect of injection rate. It can be calculated from Fig. 4.14 that when the injection rate is 3, 6, 12, 18, and 30 mL/min, the corresponding stable pressurization rate is 0.353, 0.74, 1.458, 2.392, and 6.412 MPa/s, respectively, indicating that the pressurization rate increases with the increase of the injection rate. However, from the change law of the stable pressurization rate relative to the injection rate (Fig. 4.15), different from the previous test results [25–31], the stable pressurization rate and the injection rate do not maintain a strict linear relationship but are in the form of a quadratic polynomial ($R^2 = 0.997$). The nonlinear relationship between stable pressurization rate and injection rate was also verified in the experiment of Chitrala et al. [30]. As shown in Fig. 4.15, it can be found by fitting that the quadratic polynomial relationship is also suitable for Chitrala's test results ($R^2 = 0.998$). The reason why the stable pressurization rate does not maintain a strictly linear relationship with the injection rate may be that the fluid is compressed to a certain extent during the hydraulic pressurization process and may also be related to the wellbore size, permeability of reservoir rock, fracture distribution, temperature, in-situ stress [32, 33]. It should be noted that because the Lyons sandstone is selected as the research object in the test of Chitrala et al. [30], and the Longmaxi shale is selected as the research object in the current test, the relationship between the pressurization rate and the injection rate does not meet the same binomial formula. Nevertheless, considering the compressibility of liquid and the permeability of rock, this nonlinear relationship is more suitable for the actual hydraulic fracturing process.

③ **Fracture morphology**

(1) **Fracture surface morphology**

Figure 4.16 shows the fracture morphology of shale samples under different injection rates. By comparing the calculation results of fracture morphology under different injection rates (see Table 4.4), it can be found that with the increase in injection rate, the fracture morphology on the surface of the sample gradually changes from a branched and twisted fracture to a single bi-wing fracture. This phenomenon is caused by the fact that under the low injection rate ($Q_{\text{inj}} = 3 \sim 6$ mL/min), the fluid is more likely to penetrate the weak bedding plane, resulting in the increase of pore pressure and the decrease of effective stress, which makes it easier to slip or activate secondary fractures. Under the continuous action of the pump pressure, the fluid will have sufficient time to penetrate into the secondary fractures, thus leading to the propagation and penetration of the fractures at all levels, forming a tortuous and complex fracture morphology. When the injection rate is high ($Q_{\text{inj}} = 12 \sim 24$ mL/min), the pump pressure increases rapidly, and the fluid cannot fully penetrate into the primary defects and structural planes. When the local fracture cracks, the high pressure accumulated in the wellbore will be directly released through the
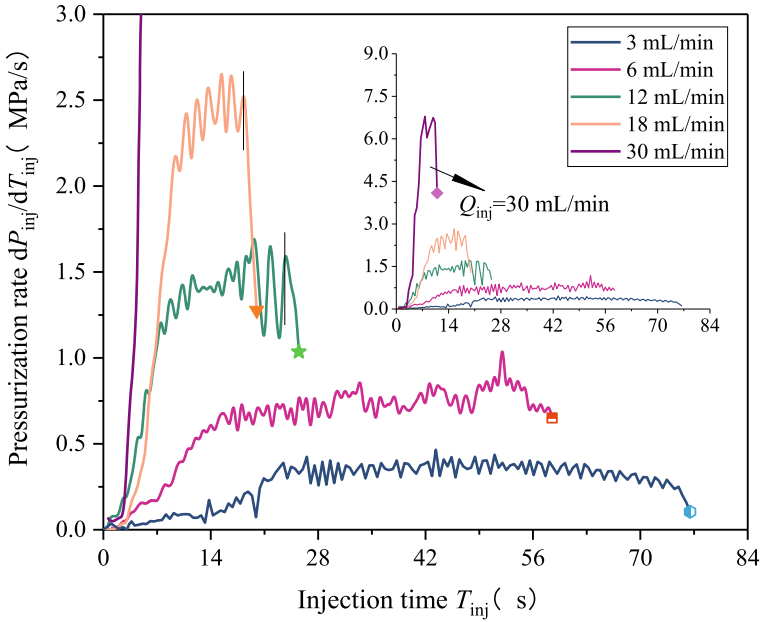
(a) Comparison of pressurization rate under different injection rates
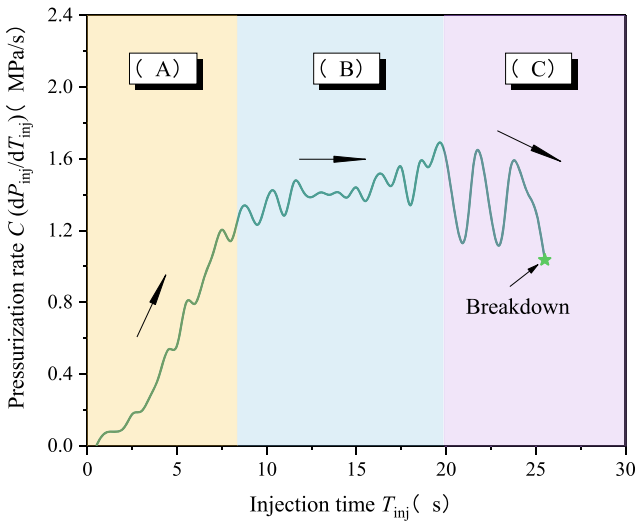
(b) Sample CI-90-12 (Q_{inj}=12 mL/min)

Fig. 4.14 Curves of pressurization rate versus time (the signs at the end of the curves represents the time when the breakdown occurs)
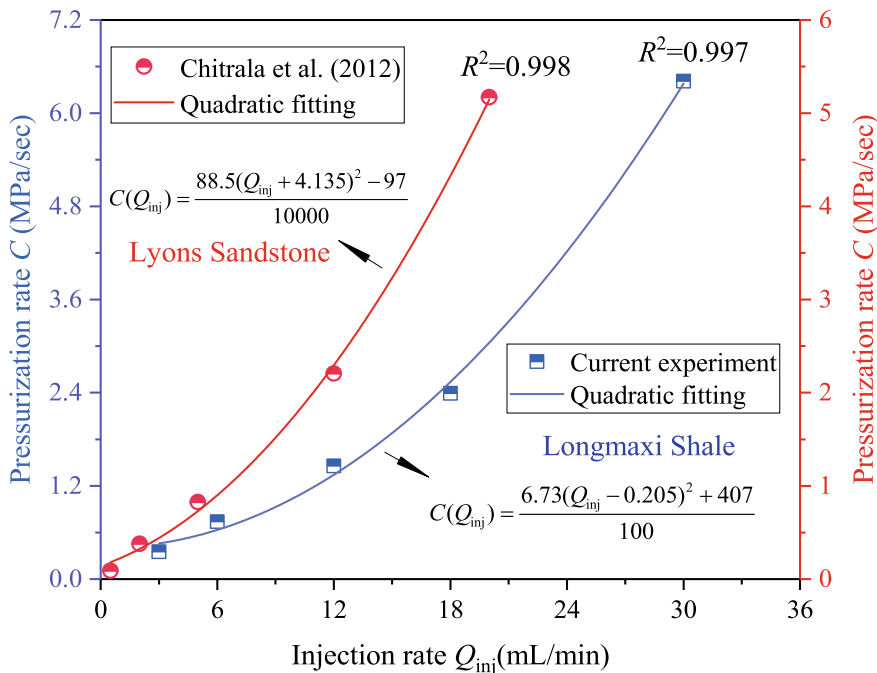
Fig. 4.15 Relationship between pressurization rate and injection rate

fracture, which induces the hydraulic fracture to propagate along its mechanically preferable direction (i.e., the direction of the maximum principal stress), forming a simple fracture. In addition, it can also be found that when the injection rate is lower than 6 mL/min, the angle between the hydraulic fracture and the bedding plane is approximately 60°, indicating that a low injection rate is conducive to inducing tortuous hydraulic fractures. This phenomenon may be due to the fact the axial preloading and fluid injection process produce more shear micro-fractures in the sample. At a low injection rate, the fracturing fluid has more time to infiltrate into the micro-fractures of the matrix, resulting in local shear along the original defects and disturbing the main hydraulic fracture to deviate from the initial fracture initiation direction, forming a tortuous fracture.

A stereomicroscope was used to observe the local fracture propagation morphology and measure the fracture width to further study the detailed characteristics of hydraulic fracture propagation under different injection rates. Taking the samples with an injection rate of 3 mL/min and 30 mL/min as examples, the results are shown in Fig. 4.17. It can be seen that in hydraulic fracturing with a low injection rate, the main fracture produces two branch fractures. One branch fracture (branch 1) still propagates along the initial direction, but the fracture width gradually decreases. The other branch fracture generates local shear (green arrow position), leading to a

(a) Q_{inj}=3 mL/min (Sample CI-90-3)

(b) Q_{inj}=6 mL/min (Sample CI-90-6)

(c) Q_{inj}=12 mL/min (Sample CI-90-12)
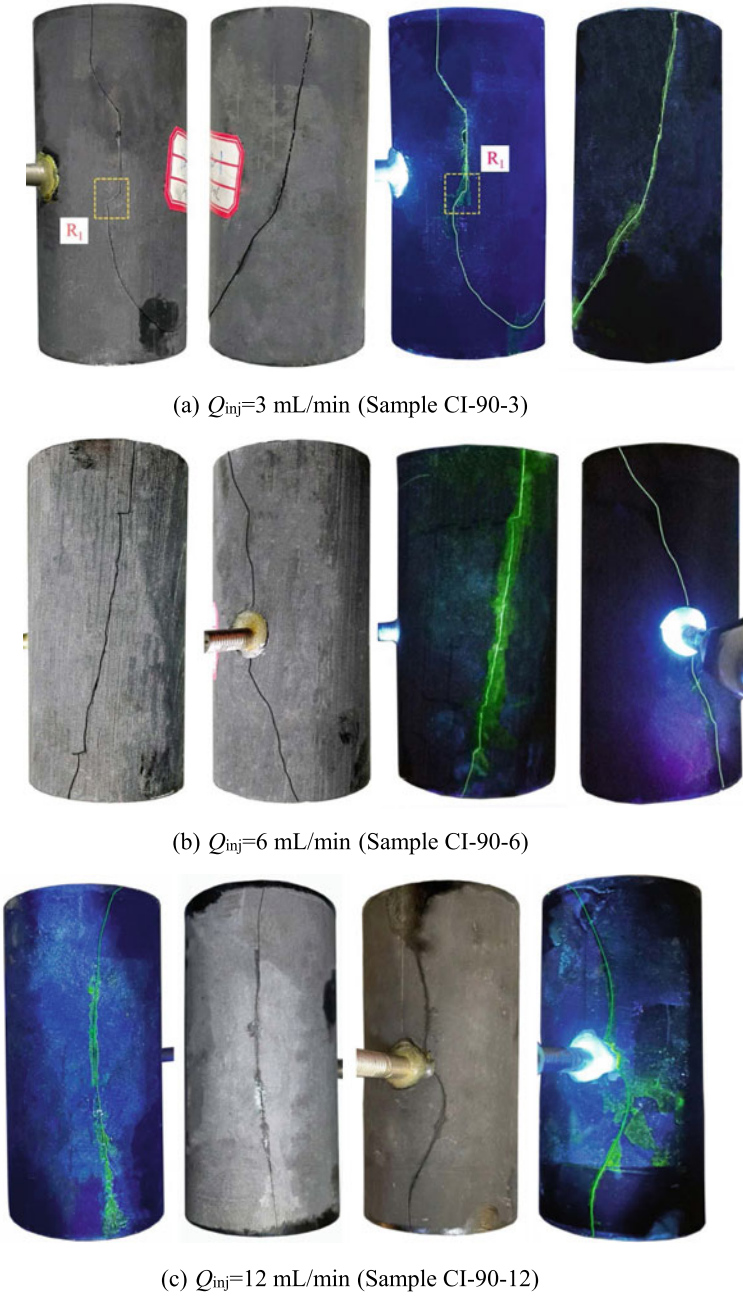
Fig. 4.16 Surface fracture morphology under different injection rates
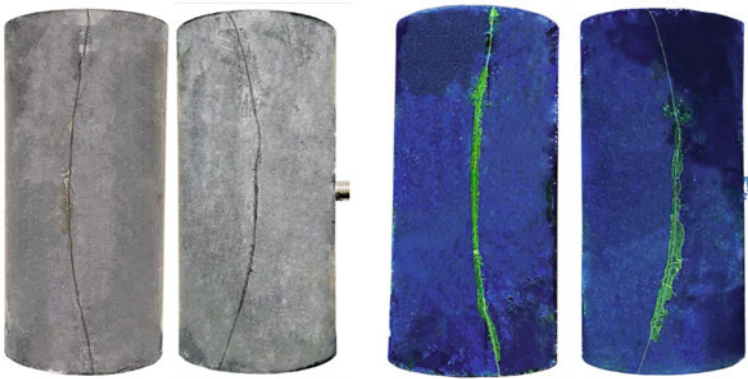
(d) Q_{inj}=18 mL/min (Sample CI-90-18)
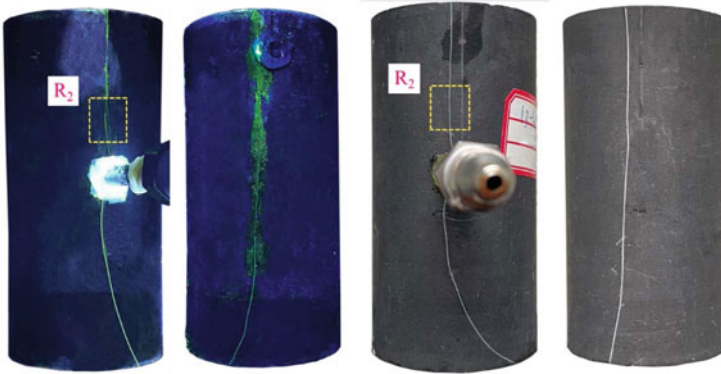
(e) Q_{inj}=30 mL/min (Sample CI-90-30)

Fig. 4.16 (continued)

Table 4.4 Fracture tortuosity under different injection rates

Sample	σ_1/MPa	Injection rate Q_{inj}/mL/min	Tortuosity τ
CI-90-3	5	3	1.231
CI-90-6		6	1.112
CI-90-12		12	1.028
CI-90-18		18	1.023
CI-90-30		30	1.016

certain degree of deflection in the main fracture path. However, the final propagation direction of the main fracture is still consistent with the main fracture direction before shear slip (i.e., along the direction of the maximum principal stress), further confirming the previous inference that a low injection rate is conducive to inducing microfracture and shear slip. It should be noted that although the residual fracture

width after the test may differ from the fracture width under dynamic loading of stress and pump pressure, the evolution of the fracture width can still provide some reference for analyzing the fracture propagation process [34]. Comparing the change of fracture width before and after the fracture branching, it can be found that the total width of the fracture after branching is reduced. The above phenomenon is because after the local shear slip occurs, the concave and convex bodies on the two staggered sections support each other, which forms the residual pore diameter to provide a channel for the internal fluid overflow [35], promoting the local injection energy loss, and reducing the fracture cracking effectiveness. In addition, after the slip, branch 2 gradually evolves into the main crack and continues to propagate, while the opening of branch 1 decreases until it stops propagating, which indicates that the local slip behavior of branch 2 impedes the subsequent propagation of branch 1. Similar conclusions can also be found in the experimental study of Zhao et al. [36]. With the increase of injection rate, the morphology of hydraulic fracture tends to be single and straight, the direction of fracture propagation coincides with the direction of maximum principal stress, and the width of fracture keeps approximately the same.

(2) **Three-dimensional fracture morphology**

Figure 4.18 shows fracture morphology and standard deviation of fracture elevation after hydraulic fracturing under different injection rates. From the fracture surface morphology of the sample, it can be seen that with the increase of the injection rate, the fracture surface gradually changes from a shear slip surface propagating obliquely to a tensile fracture surface propagating vertically, which further confirms that the low injection rate is conducive to inducing shear cracks in the sample. In addition, when the injection rate is increased from 3 mL/min to 30 mL/min, the standard deviation of fracture surface elevation is reduced from 4.63 to 2.38, indicating that with the increase of injection rate, the lower the standard deviation of fracture surface elevation is, the rougher the fracture surface is. In fact, the relationship between the standard deviation of surface elevation and injection rate is nonlinear. For example, when the injection rate is 6 mL/min, the maximum and minimum elevations of the fracture surface are 18.03 mm and 2.15 mm respectively, and the elevation contrast of the fracture surface is 4.06, which is 12.3% lower than that of 3 mL/min. When the injection rate is 12 mL/min, the maximum and minimum elevations of the fracture surface are 15.59 and −0.04 mm. Compared with 6 mL/min, the maximum and minimum elevations of 12 mL/min are reduced, and the standard deviation is 2.79, which is 31.3% lower than that of 6 mL/min. When the injection rate increased to 18 mL/min, the maximum and minimum elevations of the fracture surface became 15.45 mm and 0.01 mm, while the standard deviation of surface elevation decreased to 2.57, which decreased by 7.9% compared with the injection rate of 12 mL/min. When the injection rate is further increased to 30 mL/min, the maximum elevation of the fracture surface of the sample is 11.59 mm, the minimum elevation is 1.29 mm, and the standard deviation of elevation is 2.38, which is only 7.4% lower than that at an injection rate of 18 mL/min. These laws indicate that the disturbance effect of injection rate on fracture surface morphology is limited. Within the limited injection
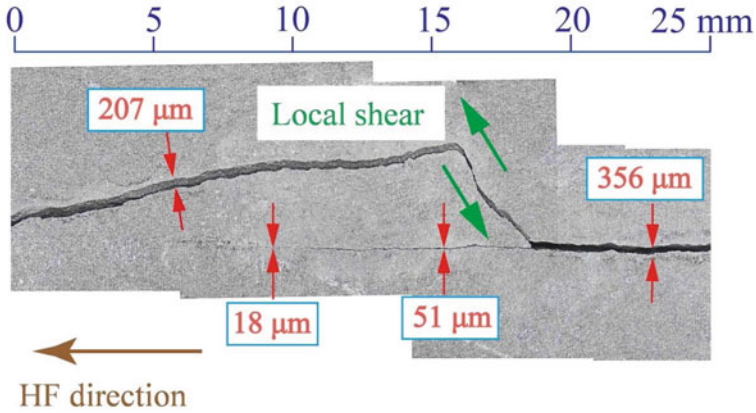
(a) Q_{inj}=3 mL/min，Sample CI-90-3 (corresponding to details at R_1 in Fig. 4.16 (a))
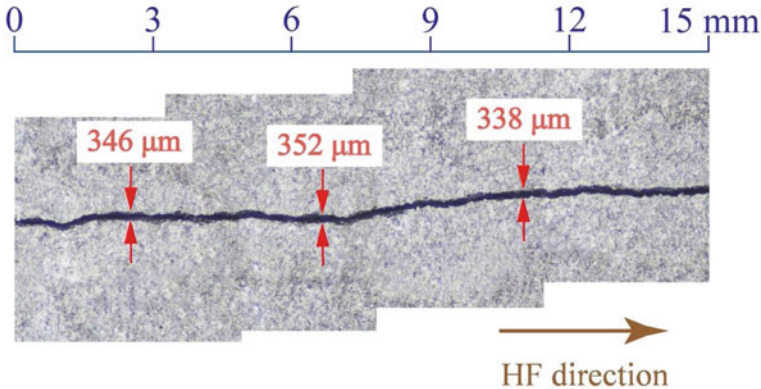
(b) Q_{inj}=30 mL/min，Sample CI-90-30 (corresponding to details in R_2 in Fig. 3.16 (e))

Fig. 4.17 Local growth path and width evolution of hydraulic fractures under different injection rates

rate range ($\leq$12 mL/min), the injection rate has a significant effect on the standard deviation of section elevation. On the contrary, when the injection rate is greater than 12 mL/min, the disturbance effect of the injection rate on the fracture roughness is weakened. In general, SD decreased with the increase in injection rate, but the decrease of SD decreased gradually. When the injection rate exceeds the critical threshold (approximately 12 mL/min), the standard deviation of the fracture surface elevation tends to be constant.

To further quantify and characterize the relationship between the injection rate and the roughness morphology, the three-dimensional average inclination angle and

(a) Q_{inj}=3 mL/min，Sample CI-90-3

(d) Q_{inj}=18 mL/min，Sample CI-90-18

(b) Q_{inj}=6 mL/min, Sample CI-90-6

(e) Q_{inj}=30 mL/min，Sample CI-90-30

(c) Q_{inj}=12 mL/min, Sample CI-90-12
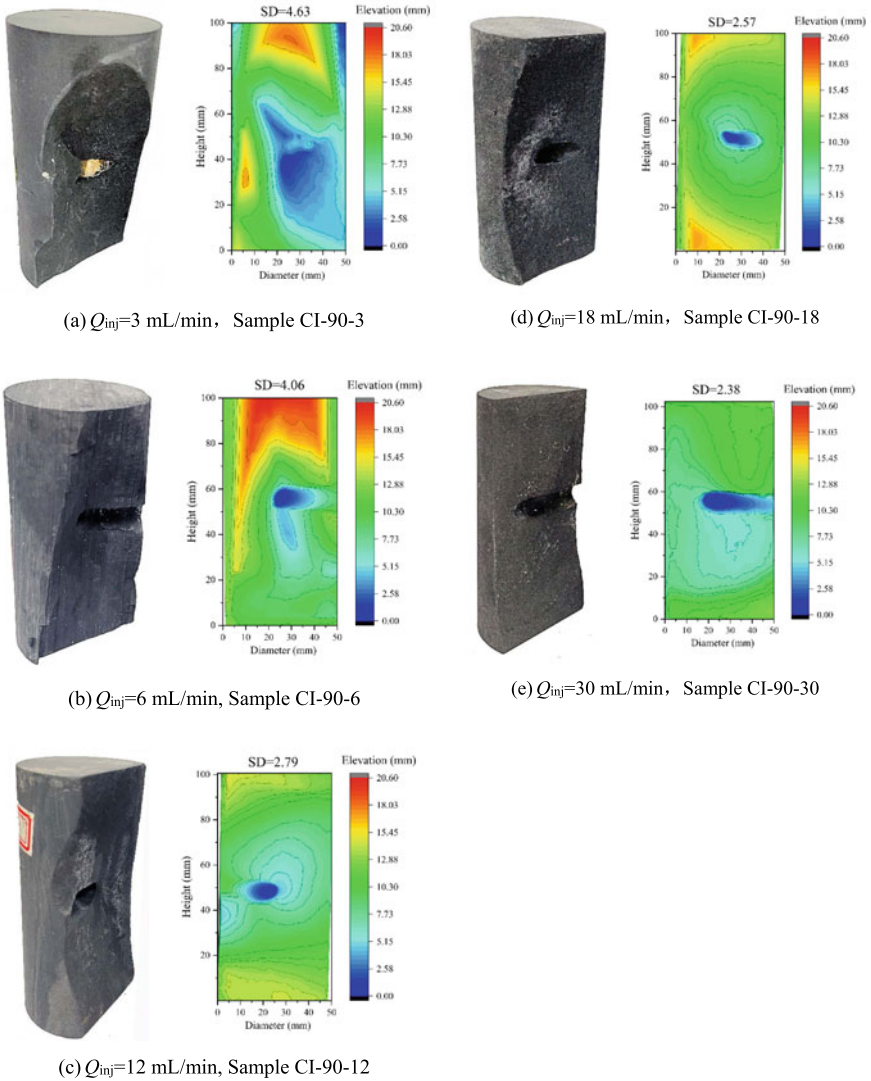
Fig. 4.18 Contour maps of vertical hydraulic fractures in shale samples under different injection rates

roughness coefficient of the fracture surface under different injection rates are calculated based on Eqs. (4.3) and (4.4). The results are summarized in Fig. 4.19. It should be noted that for sample CI-90-18 ($Q_{inj} = 18$ mL/min), the evolution trend of its three-dimensional average inclination angle and surface roughness coefficient presents completely opposite laws compared with its adjacent injection rate conditions. This phenomenon can be attributed to the difference in three-dimensional morphology of fracture surface caused by the heterogeneity of individual samples.
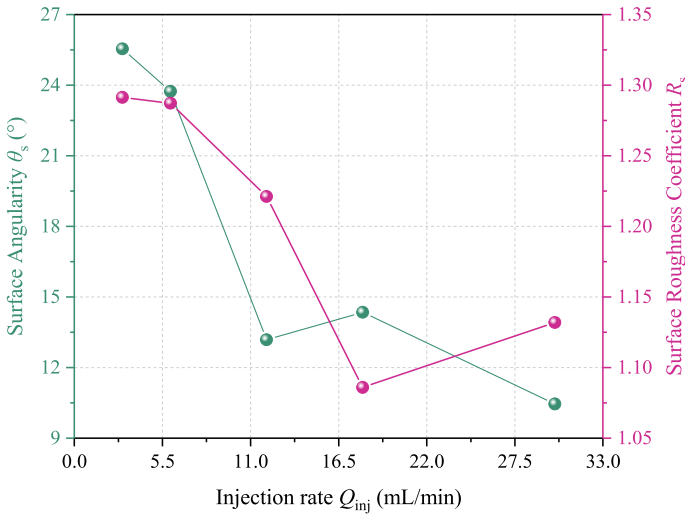
Fig. 4.19 Evolution of mean three-dimensional angle and roughness coefficient of hydraulic fracture surfaces under different injection rates

But overall, the three-dimensional average inclination and roughness coefficient of the fracture surface decreases with the injection rate, which further confirms the negative correlation and nonlinear correlation characteristics of the injection rate effect on the fracture surface morphology.

References

1. Zhuang L, Zang A (2021) Laboratory hydraulic fracturing experiments on crystalline rock for geothermal purposes[J]. Earth Sci Rev 1:103580
2. Lu GY, Gordeliy E, Prioul R, et al (2020) Time-dependent hydraulic fracture initiation [J]. J Geophys Res-Solid Earth 125(3)
3. Fallahzadeh SH, Shadizadeh SR, Pourafshary P (2010) Dealing with the challenges of hydraulic fracture initiation in deviated-cased perforated boreholes; proceedings of the Trinidad and Tobago energy resources conference, F, [C]. SPE-132797-MS
4. Wei M, Dai F, Ji Y, Wu W (2021) Effect of fluid pressure gradient on the factor of safety in rock stability analysis. Eng Geol. 294. https://doi.org/10.1016/j.enggeo.2021.106346
5. Lin C, He J, Li X, Wan X, Zheng B (2017) An experimental investigation into the effects of the anisotropy of shale on hydraulic fracture propagation. Rock Mech Rock Eng 50(3):543–554. https://doi.org/10.1007/s00603-016-1136-4
6. Jiang Z, Li Q, Hu Q, Liang Y, Xu Y, Liu L, Wu X, Li X, Wang X, Hu L, Ling F (2020) Acoustic emission characteristics in hydraulic fracturing of stratified rocks: a laboratory study. Powder Technol 371:267–276. https://doi.org/10.1016/j.powtec.2020.05.050
7. Baddari K, Frolov AD, Tourtchine V, Rahmoune F (2011) An integrated study of the dynamics of electromagnetic and acoustic regimes during failure of complex macrosystems using rock blocks. Rock Mech Rock Eng 44(3):269–280. https://doi.org/10.1007/s00603-010-0130-5

8. Hu X, Su G, Chen G, Mei S, Feng X, Mei G, Huang X (2019) Experiment on rock burst process of borehole and its acoustic emission characteristics. Rock Mech Rock Eng 52(3):783–802. https://doi.org/10.1007/s00603-018-1613-z

9. Li LR, Deng JH, Zheng L, Liu JF (2017) Dominant frequency characteristics of acoustic emissions in white marble during direct tensile tests. Rock Mech Rock Eng 50(5):1337–1346. https://doi.org/10.1007/s00603-016-1162-2

10. Jian-po L, Chang-yin Z, Ying-tao S, Ren W, Gang L, Shi-da X (2020) Temporal-spatial evolution of acoustic emission during progressive fracture processes around tunnel triggered by blast-induced disturbances under uniaxial and biaxial compression. Tunn Undergr Sp Technol. 96. https://doi.org/10.1016/j.tust.2019.103229

11. Wang C, Cao C, Liu Y, Li C, Li G, Lu H (2021) Experimental investigation on synergetic prediction of rock burst using the dominant-frequency entropy of acoustic emission. Nat Hazards 108(3):3253–3270 https://doi.org/10.1007/s11069-021-04822-6

12. Zang A, Wagner FC, Stanchits S, Dresen G, Andresen R, Haidekker MA (1998) Source analysis of acoustic emissions in Aue granite cores under symmetric and asymmetric compressive loads. Geophys J Int 135(3):1113–1130. https://doi.org/10.1046/j.1365-246X.1998.00706.x

13. Zhang ZH, Deng JH, Zhu JB, Li LR (2018) An experimental investigation of the failure mechanisms of jointed and intact marble under compression based on quantitative analysis of acoustic emission waveforms. Rock Mech Rock Eng 51(7):2299–2307. https://doi.org/10.1007/s00603-018-1484-3

14. Wang YS, Deng JH, Li LR, Zhang ZH (2019) Micro-failure analysis of direct and flat loading Brazilian tensile tests. Rock Mech Rock Eng 52(2). https://doi.org/10.1007/s00603-019-01877-7

15. Lei R, Zhang Z, Berto F, Ranjith PG, Liu L (2020) Cracking process and acoustic emission characteristics of sandstone with two parallel filled-flaws under biaxial compression. Eng Fract Mech. https://doi.org/10.1016/j.engfracmech.2020.107253

16. Ishida T, Aoyagi K, Niwa T, Chen Y, Murata S, Chen Q, Nakayama Y (2012) Acoustic emission monitoring of hydraulic fracturing laboratory experiment with supercritical and liquid CO_2. Geophys Res Lett https://doi.org/10.1029/2012GL052788

17. Hou P, Gao F, Gao Y, Yang Y, Cai C (2018) Changes in breakdown pressure and fracture morphology of sandstone induced by nitrogen gas fracturing with different pore pressure distributions. Int J Rock Mech Min Sci. https://doi.org/10.1016/j.ijrmms.2018.06.006

18. Rose W, Bruce WA (1949) Evaluation of capillary character in petroleum reservoir rock. J Pet Technol. https://doi.org/10.2118/949127-g

19. Guo P, Li X, Li S, Yang W, Wu Y, Li G (2021) Quantitative analysis of anisotropy effect on hydrofracturing efficiency and process in shale using x-ray computed tomography and acoustic emission. Rock Mech Rock Eng. https://doi.org/10.1007/s00603-021-02589-7

20. Ishibashi T, Fang Y, Elsworth D, Watanabe N, Asanuma H (2020) Hydromechanical properties of 3D printed fractures with controlled surface roughness: insights into shear-permeability coupling processes. Int J Rock Mech Min Sci. https://doi.org/10.1016/j.ijrmms.2020.104271

21. Belem T, Homand-Etienne F, Souley M (2000) Quantitative parameters for rock joint surface roughness. Rock Mech Rock Eng. https://doi.org/10.1007/s006030070001

22. El-Soudani SM (1978) Profilometric analysis of fractures. Metallography. https://doi.org/10.1016/0026-0800(78)90045-9

23. Chitrala Y, Moreno C, Sondergeld C, Rai C (2011) Microseismic and microscopic analysis of laboratory induced hydraulic fractures. In: Society of petroleum engineers—Canadian unconventional resources conference 2011, CURC 2011

24. Zeng Z, Roegiers JC (2002) Experimental observation of injection rate influence on the hydraulic fracturing behavior of a tight gas sandstone. In: Proceedings of the SPE/ISRM rock mechanics in petroleum engineering conference

25. Shao CY, Pan PZ, Zhao DC, Yao TB, Miao ST (2020) Effect of pumping rate on hydraulic fracturing breakdown pressure and pressurization rate. Rock Soil Mech 41(07):2411–2421+2484

26. Zhuang L, Kim KY, Jung SG, Diaz M, Min KB (2019) Effect of water infiltration, injection rate and anisotropy on hydraulic fracturing behavior of granite. Rock Mech Rock Eng. https://doi.org/10.1007/s00603-018-1431-3

27. Haimson BC (1968) Hydraulic fracturing in porous and nonporous rock and its potential for determining in-situ stresses at great depth. Doctoral thesis, University of Minnesota

28. Zoback MD, Rummel F, Jung R, Raleigh CB (1977) Laboratory hydraulic fracturing experiments in intact and pre-fractured rock. Int J Rock Mech Min Sci. https://doi.org/10.1016/0148-9062(77)90196-6

29. Solberg P, Lockner D, Byerlee J (1977) Shear and tension hydraulic fractures in low permeability rocks. Pure Appl Geophys PAGEOPH. https://doi.org/10.1007/BF01637103

30. Chitrala Y, Sondergeld C, Rai C (2012) Microseismic studies of hydraulic fracture evolution at different pumping rates. In: Society of petroleum engineers—SPE Americas unconventional resources conference 2012

31. AlTammar MJ, Sharma MM (2019) Effect of borehole pressurization scheme on breakdown pressure. Rock Mech Rock Eng. https://doi.org/10.1007/s00603-018-1731-7

32. Detournay E, Cheng A (1992) Influence of pressurization rate on the magnitude of the breakdown pressure. In: 33rd U.S. symposium on rock mechanics, USRMS 1992

33. Duan K, Kwok CY, Wu W, Jing L (2018) DEM modeling of hydraulic fracturing in permeable rock: influence of viscosity, injection rate and in situ states. Acta Geotech. https://doi.org/10.1007/s11440-018-0627-8

34. Li N, Zhang S, Zou Y, Ma X, Zhang Z, Li S, Chen M, Sun Y (2018) Acoustic emission response of laboratory hydraulic fracturing in layered shale. Rock Mech Rock Eng. https://doi.org/10.1007/s00603-018-1547-5

35. Zou YS, Zhang SC, Zhou T, Zhou X, Guo TK (2016) Experimental investigation into hydraulic fracture network propagation in gas shales using CT scanning technology. Rock Mech Rock Eng. https://doi.org/10.1007/s00603-015-0720-3

36. Zhao Z, Zhao Y, Jiang Z, Guo J, Zhang R (2021) Investigation of fracture intersection behaviors in three-dimensional space based on CT scanning experiments. Rock Mech Rock Eng. https://doi.org/10.1007/s00603-021-02587-9

Chapter 5
Constant Pressure Injection

5.1 Introduction

In practical hydraulic fracturing, limited by the operating power of the syringe pump and long transportation of pipelines, it is often difficult to maintain high pumping fluid pressure to crack the reservoir rock in deep formation. To overcome this difficulty, Ma et al. [1] and Zang et al. [2] tried to use "static fatigue" to break the reservoir rock by maintaining a constant fluid pressure on the rock for a long time, which has been proven to be able to reduce the breakdown pressure of the reservoir. The feasibility of this method has been verified in granite, limestone and sandstone reservoirs [3]. However, relevant technologies have not been applied to shale reservoirs, and the delayed fracturing process of shale lacks reliable laboratory evidence. In addition, few efforts focus on unraveling the mechanisms of fracturing reservoirs by constant pressure injection (delayed breakdown).

The delayed breakdown process of hydraulic fractures induced by constant pressure fluid is essentially the consequence of the long-term action of the extremely high fluid pressure, resulting in the initiation of hydraulic fractures due to fatigue damage. Different from the previous disturbance of pore pressure to the rock fracturing process, under the condition of constant pressure, hydraulic fracturing is dominated by fluid pressure. In terms of pore pressure disturbance, previous studies have focused on analyzing the effect of uniform pore pressure on rock fracture properties. Under the action of constant and uniform pore pressure, the damage to rock tends to be progressive and integral along the minimum principal stress. The nature of instability and damage caused by water inrush, collapse, slip, etc. [4, 5]. At present, there are few related studies on the effect of heterogeneous and asymmetric high pore pressure on the rock fracture process. Lu et al. [6] used the stress intensity factor at the crack tip and analyzed the deflection mechanism of hydraulic fracture propagation caused by non-uniform pore pressure, but failed to clarify the effect of local pore pressure on rock strength, deformation and fracture characteristics.

In this section, the constant pressure fracturing test is carried out based on previous research. The syringe pump is controlled by the constant pressure injection mode

using a feedback loop control. The constant pressure injection test scheme has been described in detail in Sect. 3.4.2. The following is an analysis of the delayed breakdown characteristics of hydraulic fractures based on the observation under constant pressure injection tests.

Note that the changes in pumping parameters (P_{inj} and V_{inj}) with time and fracture morphology under constant pressure and constant flow conditions were presented and compared, respectively. Specifically, to elaborate the characteristics of these pumping parameters during the fracturing process, four key parameters were defined: the maximum pump pressure (instantaneous or delayed breakdown pressure, P_{b}), the time (onset) of pressure declining (T_{pd}), the maximum injection rate ($\max V_{\text{inj}}$) and the time at which the injection rate reaches the maximum ($\max T_{\text{inj}}$).

5.2 Results and Analysis

5.2.1 Typical Curves of Pump Pressure and Injection Rate Versus Time

Unstable crack propagation leading to a macroscopic failure (a crack reaching the rock surface and splitting the specimen into two parts) is accompanied by a simultaneous drop of fluid pressure in the wellbore [7]. To quantitatively evaluate the relationship between fluid pressure and crack propagation, we introduced the pressure decay rate (v_{decay}) following Gehne et al. [8].

$$v_{\text{decay}} = \frac{P(t) - P(t + \Delta t)}{\Delta t} \tag{5.1}$$

where $P(t)$ is to the wellbore pressure at the time t, and Δt denotes an increment of time. According to Song et al. [9] and Hu et al. [10], when the friction flow of fracturing fluid inside the wellbore is neglected, the wellbore pressure ($P(t)$) can be considered the pumping pressure (P_{inj}) which is monitored in real-time by a pressure transducer near the injection hole. Thus, Eq. (5.1) can be rewritten as

$$v_{\text{decay}} = \frac{P_{\text{inj}}(t) - P_{\text{inj}}(t + \Delta t)}{\Delta t} \tag{5.2}$$

In the following part, we presented curves of pumping pressure and injection rate as a function of time under constant pressure injection conditions of $P_{\text{con}} = 17, 19$, and 21 MPa, respectively.

(1) Constant fluid pressure (specimen P-17)

Figure 5.1 depicts the curves of injection rate, pump pressure, and pressure decay rate with the increase of time for Specimen P-17. Overall, the pressurization of the

wellbore was steadily maintained at a pump pressure of 17 MPa with no fluid leak-off into the sample ($V_{inj} = 0$). Even after this state (constant pressure stage) lasted for nearly 370 min, the change in the curves was still hardly identified, indicating that there was probably no fluid exchange between the wellbore and the hydraulic fracturing system. Thus, the whole rock and fluid injection system were in static equilibrium, which means no fracture initiation or fluid infiltration occurred over the entire pressurization process. In this regard, the 17 MPa pump pressure is insufficient to break up the shale strength on the timeframe of 370 min. A much more extended period or higher pump pressure value is necessary to initiate a progressive (delayed) breakdown for fracture behavior evaluation.

Additionally, we outlined a local zoom of a time zone (Fig. 5.1b) when increasing the fluid pressure from zero to its target value ($P_{con} = 17$ MPa). The fluid injection rate and pressure decay rate were respectively recorded and calculated during the loading process, whose absolute values, unlike the increasing trend of pump pressure, increased first and then decreased to zero once the fluid pressure reached the preset pressure. Note that the minus sign of the pressure decay rate corresponds to the case that the fluid pressure is continuously increasing. Practically, the variations of injection rate and fluid pressure are associated with the initial fluid flow in the pipeline and wellbore, where the air is evacuated or compressed into smaller volumes with the accumulation of the injected fluid [11]. In this case, the initial variation of pumping parameters (fluid pressure or injection rate) may only reflect a primary change and adjustment in the stress state of the wellbore rather than a direct response of fracture behaviors. Therefore, this loading phase will not be analyzed when evaluating the relationship between fracture characteristics and pumping parameters in the following sections.

(2) Local pressure drop (specimen P-19)

The fracturing results for Specimen P-19 are presented in terms of pump pressure, injection rate, and pressure decay rate over time, as seen in Fig. 5.2. A similar constant change in pump pressure (constant pressure stage) is visible at $P_{con} = 19$ MPa compared with the sample pressurized at $P_{con} = 17$ MPa in Fig. 5.2a. We can see that within the first 400 min of hydrofracturing (excluding the initial loading stage), the pump pressure gradually stabilized at a level of 19 MPa, with the injection rate fluctuating around an average value of 0.1 mL/min. This fluctuation feature of the injection rate is different from the no fluid leakage phenomenon ($V_{inj} = 0$) under 17 MPa pump pressure, which implies that the static equilibrium previously observed at $P_{con} = 17$ MPa breaks as the pump pressure increases to 19 MPa. Instead, there is a stable leakage stage with constant pressure (19 MPa) and a roughly stable injection rate (0.1 mL/min), indicating that the sample-fluid (injection) system reaches a new dynamic equilibrium where a constant fluid leakage was maintained by the constant pump pressure (i.e., inflow equals outflow). This circumstance is possibly attributed to the occurrence of a local crack that connects the wellbore with the rock surface and provides a flow channel for the injected fluid, as later confirmed in Sect. 5.2.2. As a result, the internal fluid will continually spill out of the wellbore via an oriented crack channel, which further holds back the closure of the crack. Nevertheless, due
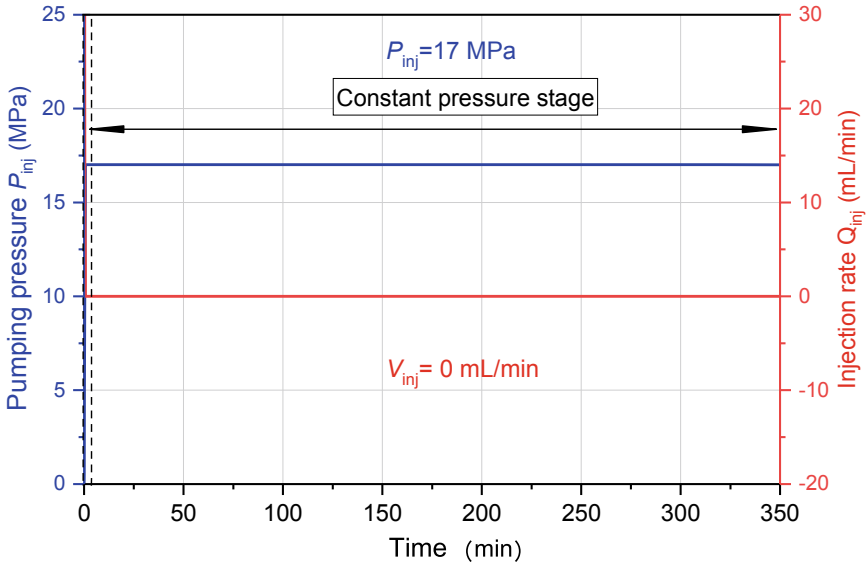
(a) Curves of the whole process
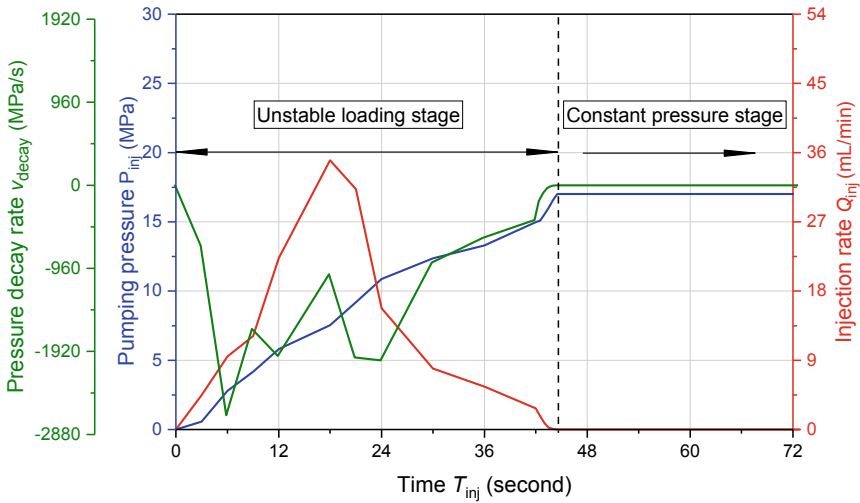

(b) Local zoom of unstable loading phase

Fig. 5.1 Curves of pump pressure and injection rate versus time for Specimen P-17 ($P_{con} = 17$ MPa)

to the actual compactivity of fracturing fluid, the outflow is not strictly stable, which appears to be an indirect reflection of the fluctuation of the injection flow [12]. On the other hand, these results indicate that the currently pumped 19 MPa fluid pressure can only initiate local cracks (or partly activated bedding planes) in the shale specimen with a constant aperture (opening) rather than further promote crack growth.

It is noteworthy that after $T_{inj} = 403$ min, the pump pressure started to decline, and the injection rate suddenly dropped to zero (Fig. 5.2a). These variations of the curves were caused by the stopping pumping operation when the fracturing fluid in the pump chamber was exhausted and the fluid injection was passively terminated, signifying the end of the hydraulic fracturing experiment.

In a partially enlarged view of the local cracking stage (Fig. 5.2b), a rapid change in fluid pressure was recorded, accompanied by an increase in the injection rate, which is consistent well with the previous reports [12–14]. By integrating the P_{inj} data, the pressure decay rate became evident, which helped classify the curves into three key stages. First, the constant pressure stage (1.5–120 s) was maintained at $v_{decay} = 0$ MPa/s and $V_{inj} = 0$ mL/min as the wellbore was subject to a constant pressure of 19 MPa. These variations of curves for Specimen P-19 look like those of Specimen P-17, demonstrating that Specimen P-19 is also in static equilibrium during this period. Afterward, the curves entered the second (typical) stage of local cracking at $T_{pd} = 120$ s, when the pump pressure started to decline. Shortly after a period of 15 s, the pump pressure dropped to the lowest (18.805 MPa) and then rebounded to an approximately stable level. This typical process was named P_{inj} oscillation, which was caused by the fracture tip locally outpacing the driving fluid and then catching up to further extend the crack, according to Gehne et al. [8].

During the P_{inj} oscillation, the pressure decay rate changed significantly in response to a slight drop-off in the pump pressure. Meanwhile, a noticeable change in the curve of injection rate was recorded with the maximum value (maxV_{inj}) of 0.82 mL/min at max$T_{inj} = 126$ s. Considering the fact that a slight decline in the pump pressure always coincides with a sharp increase in the injection rate, we may ulteriorly correlate the fluctuation of pressure decay rate with the evolution of the injection rate. The variation of the injection rate allows the wellbore to be compensated with an appropriate amount of fluid so as to maintain a constant pressure output ($P_{con} = 19$ MPa) under feedback loop control. Hence, the attenuation rate of wellbore pressure should correspond to the compensation rate of the injected fluid. The maximum v_{decay} (237.6 MPa/s) occurred at $T_{inj} = 125$ s, which is 1 s earlier than the maximum injection rate. This distinction illustrates that the variation of injection rate lags the fluid pressure decay rate. From this point of view, the fluctuating injection rate can be considered the result of fluid pressure oscillation in the wellbore under constant pressure output. As the fluid pressure gradually stabilized around 19 MPa ($v_{decay} \to 0$), the injection rate decreased accordingly, approximating a constant rate ($V_{inj} = 0.1$ mL/min), which heralds the beginning of the stable leakage stage. This stage is in dynamic equilibrium where fluid inflow is equal to fluid outflow, as expounded above. However, it is noteworthy that the pressure oscillation accompanied by flow compensation can still be observed, particularly during the preliminary leakage. Unlike the previous stage, curve oscillations during the leakage stage are
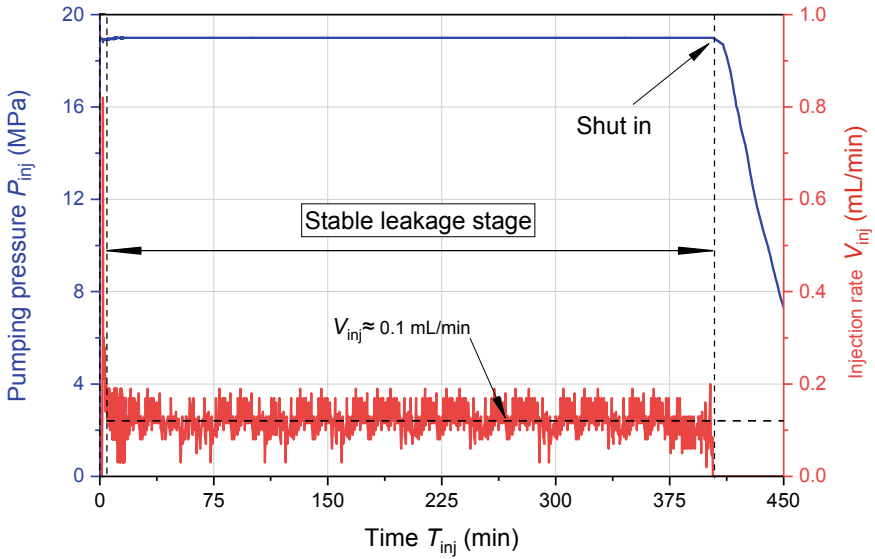
(a) Curves of the whole fracturing process
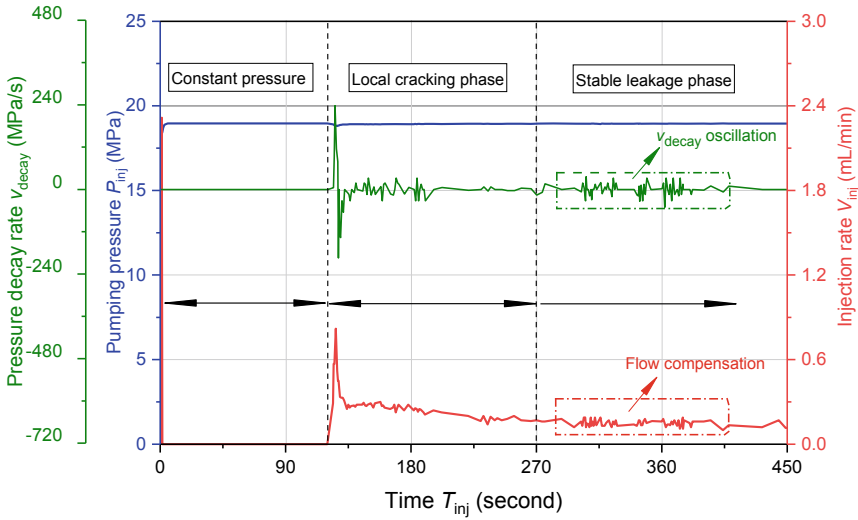
(b) Partially enlarged view of the local cracking stage

Fig. 5.2 Curves of pump pressure and injection rate as a function of time for Specimen P-19 (P_{con} = 19 MPa)

mainly reflected in the injection and pressure decay rates: each increase in pressure decay rate was associated with an increase in the injection rate. By contrast, the fluid pressure changes are almost indistinguishable. In this sense, the pressure decay rate (v_{decay}) behaves more sensitively to the changes in fracture initiation, which demonstrates the feasibility of employing this pressure gradient (v_{decay}) to evaluate fracture initiation.

(3)   Continuous pressure drop (specimen P-21)

Figure 5.3 shows the hydraulic fracturing data under the constant pressure of 21 MPa. Some characteristics of the curves for P-21 are similar to previous examples (P-17 and P-19): a constant pressure stage (7.5–1560 s) was first observed after the pump pressure reached its target value. Then, a local cracking stage emerged, followed by a more evident fluid pressure oscillation compared to the Specimen P-19. However, the pump pressure did not return to a constant value like recorded in Fig. 5.2. Instead, it remained an approximately steady downward trend accompanied by a uniformly varying injection rate (Fig. 5.3a). This process continued for 618 s until $T_{\text{inj}} = 2178$ s when significant changes in the pump pressure curve were observed alongside a stepwise increase of injection rate. These variations indicate that the curves stepped into a new stage (unstable cracking) completely different from other stages in previous examples. During this unstable cracking stage (Fig. 5.3a), the fluid pressure in the wellbore kept decreasing until encountering a transient plateau (2234–2429 s) after a sudden pressure reduction and recovery. Shortly afterward (57 s), the pressure dropped remarkably, with the injection rate rising to the maximum (max $V_{\text{inj}} = 106.62$ mL/min). This significant drop-off in fluid pressure means that the current stress conditions and the sample deformation are no longer sufficient to create an extra barrier to maintain the wellbore's constant pressurization for a long duration. Following these changes, yellow-green fracturing fluid was seen leaking from new cracks on the sample surface, which finally resulted in the loss of specimen integrity. The hydraulic fracturing pump was manually shut down as soon as the fluid pressure declined to zero for the sake of protecting the experimental setup from liquid shocks. This operation causes a plummet in injection rate at the end of the experiment ($T_{\text{inj}} = 2495$ s), as recorded in Fig. 5.3a.

   In order to elaborate the variation characteristics of the pump pressure and injection rate for Specimen P-21, the graphs of local cracking and unstable cracking stages were separately amplified in Fig. 5.3b and c. Similar to Specimen P-19, the pump pressure experienced a pressure (P_{inj}) oscillation ($v_{\text{decay}} = 170.18$ MPa/s) at the beginning of the local cracking stage and then jumped into a transient and stable leakage state with a constant injection rate of 0.12 mL/min from $T_{\text{inj}} = 1630$ to 1666 s as marked in grey shadow in Fig. 5.3b. These similarities suggest approximate fracture behavior of Specimen P-19 and Specimen P-21 during the initial fracturing process, where the inflowing fluid equally compensates the outflowing fluid. Within 303 s after the leakage state, P_{inj} decreased gradually and uniformly with the increase of V_{inj}. The fluctuation of the pressure decay rate also corresponds to the variation of the injection rate. Subsequently, the pump pressure met a new P_{inj} oscillation at $T_{\text{inj}} = 1976$ s with a pressure decay rate of 208.88 MPa/s. The new P_{inj} oscillation is

(a) Curves of the whole fracturing process
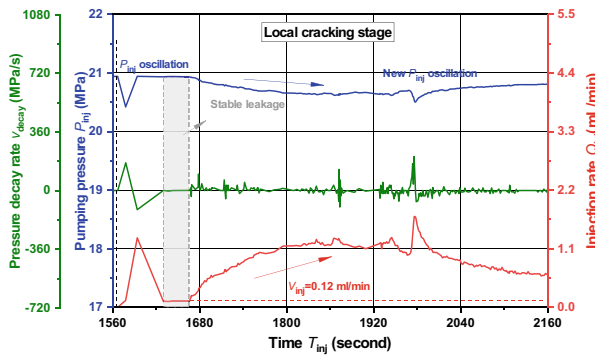
(b) Enlarged view of local cracking stage
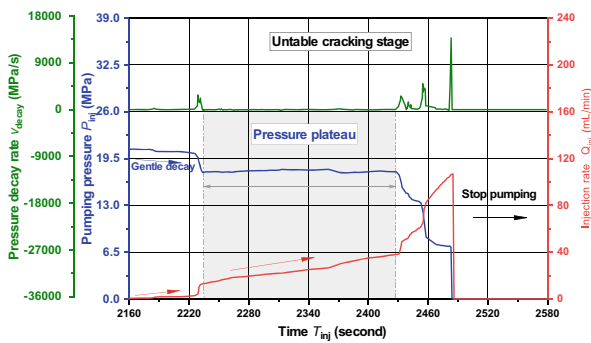
(c) Enlarged view of unstable cracking stage

Fig. 5.3 Curves of pump pressure and injection rate versus time for Specimen P-21 ($P_{con} = 21$ MPa)

relatively weaker than the previous oscillation at $T_{inj} = 1578$ s. In addition, a higher injection rate ($V_{inj} = 1.685$ mL/min) at $T_{inj} = 1979$s was observed in the second fluid oscillation compared to the maximum injection rate ($V_{inj} = 1.3$ mL/min) at $T_{inj} = 1583$ s in the first fluid oscillation.

By contrasting the pressure curve of carbonate rocks with AE events under constant pressure injection conditions, Lu et al. [14] reported that the precursor pressure oscillation was indicative of new fracture initiation and growth. This fracture initiation may provide more leakage paths for internal fluid. Thus, new fracture initiation or propagation could be responsible for the oscillation cases portrayed in Fig. 5.3b. On this basis, different oscillation degrees of the injection rate and the pressure decay rate should have a correlation with the fracture behavior and final morphology, which will be further analyzed and discussed in Sect. 5.2.2. It is also interesting to note that the changes in injection rate (V_{inj}) always lag the changes in pressure decay rate (v_{decay}) in the leakage stages of Specimen P-19 and Specimen P-21. Through comparison, we can speculate that this lag effect is caused by the pump's feedback control loop, which works by tracking pressure changes and adjusting the flow rate in an effort to regain constant pressure output. Under different pressure conditions, the lag time (hereafter refers to the time interval between the variations of v_{decay} and V_{inj} under the same P_{inj} oscillation) is different. For example, the lag time decreases from 5 s under $\Delta P_{inj} = 0.52$ MPa (first oscillation) to 3 s under $\Delta P_{inj} = 0.2$ MPa (new oscillation). For the P_{inj} oscillation of Specimen P-19 with $\Delta P_{inj} = 0.164$ MPa, the lag time becomes even shorter (1 s). These indicate that the lag time increases with the increase of the pump pressure decrement (ΔP_{inj}) at the oscillation point. More significant pressure decrements usually correspond to more extended fractures [15]. Therefore, the variation of lag time can reflect the cracking degree (fracture length and width) of hydraulic fractures in the specimen.

As Fig. 5.3c shows, the unstable cracking stage is relatively unique compared to the previously observed stages. A sudden pump pressure drop followed an initial gentle decay of pump pressure (2160–2223 s). Each decrease in pump pressure corresponds to the next jump of injection rate and a significant fluctuation of the pressure decay rate. Then, the pump pressure entered a plateau ($P_{inj} \approx 17.77$ MPa) when the injection rate still maintained a growing trend. Integrating the injection rate over time, we noted that the injected fluid volume is essentially equal to the sum of the leakage fluid amount and the crack volume inside the specimen. In the case of a constant leakage from a crack with a specified length (or width) at a certain P_{inj}, the increasing trend of injection rate broadly reflects the increase of the crack length (or width) per unit time inside the specimen. In this case, the sample was in the progressive failure stage, where crack opening and length increased gradually [16]. However, the continuously rising injection rate can only represent an increase in the fracture size (width and length) but cannot locate the specific crack coordinates. In other words, the increasing injection rate is a composite response of the crack volume change inside the rock, independent of crack location. At $T_{inj} = 2428$ s, the pump pressure started to drop rapidly. The maximum pressure decay rate (229.5 MPa/s) occurred at $T_{inj} = 2484$ s, and 1 s later, the injection rate reached its maximum $\max V_{inj} = 106.82$ mL/min. In addition, the period of rapid pressure decay suggests
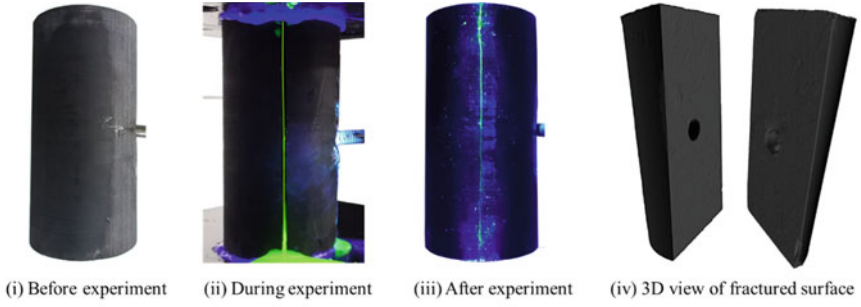
that the output of 21 MPa fluid pressure cannot consistently maintain a constant fluid leakage like observed in P-19. Instead, the 21 MPa fluid pressure will finally induce the initiation of new cracks.

In general, different pressure–time curves of the specimens (P-17, P-19, and P-21) have similar constant pressure stages. However, as the predetermined pump pressure increases, the shape of these curves becomes complicated, which indicates the increasing possibility of new fractures. In order to verify this conclusion, it is necessary to evaluate the hydraulic fracture behavior and morphology during the constant pressure fracturing process.
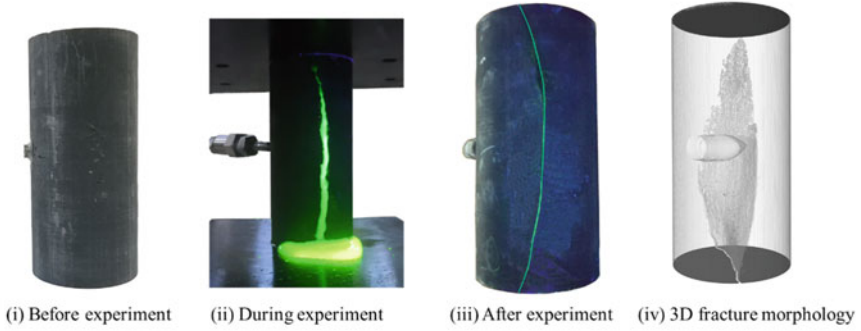
5.2.2   New Insights from Observing Hydraulic Fracture Morphology

The hydrofracturing characteristics of cylindrical specimens are conventionally described as a scenario that the fracture propagates radially via the shortest stress path, then, once the radial fracture reaches the edge of the sample, continuing vertically and rapidly [17, 18]. During this process, the injected fluid is maintained at a constant flow rate (constant flow injection mode), which continually provides an inner impetus for the extension of hydraulic fracture and finally contributes to sample failure. The hydraulic fracture mainly extended along a relatively straight and smooth path with few bifurcations both in the axial and radial directions. With the increase of the axial stress (V-25 in Fig. 5.4b), the fracture in Specimen V-25 ($V_{inj} = 12$ mL/min and $\sigma_v = 25$ MPa) became slightly twisted and bent in its strike (or radial) direction. Further, while the confinement of lateral pressure ($\sigma_c = 20$ MPa) was axisymmetrically applied on the cylindrical specimen surface in Fig. 5.4c, the fracture bifurcated and formed a more complex shape according to Lin et al. [18]. Knowing how the stress conditions affect the fracture morphology is out of the analytic scope of this study. Here we mainly presented the results to show the morphological similarity under constant flow injection conditions. Overall, the rupture of the shale specimen (bedding planes oriented parallel to the axial loading direction) under constant flow injection mode was either confined to or aligned with a single bedding plane so that the fracture can be preferably described as "simple" with relative homogeneous geometry.

However, when the sample is fractured by a series of constant pump pressures (17, 19, and 21 MPa) rather than a constant flow rate (e.g., 12 mL/min), some apparent distinctions can be discerned in terms of the fracture morphology. To present the hydraulic fracture geometry clearly, we carefully sketched the ultimate fracture path on the specimen surface through macroscopic observation, referring to Ishida et al. [19] and Hou et al. [20]. On this basis, a dimensionless parameter, tortuosity, was introduced to evaluate the hydraulic fracture morphology quantitatively, which can be expressed as [21]

(i) Before experiment   (ii) During experiment   (iii) After experiment   (iv) 3D view of fractured surface

(a) Specimen V-5 (V_{inj}=12 mL/min and σ_v=5 MPa)

(i) Before experiment   (ii) During experiment   (iii) After experiment   (iv) 3D fracture morphology

(b) Specimen V-25 (V_{inj}=12 mL/min and σ_v=25 MPa)

(c) (V_{inj}=12 mL/min, σ_v=25 MPa and σ_c=20 MPa) (after Lin et al. [38])

Fig. 5.4   Fracture morphology of Specimen V-5 and Specimen V-25 at different experimental stages

(a) Before experiment   (b) During experiment   (c) After experiment   (d) 3D reconstruction
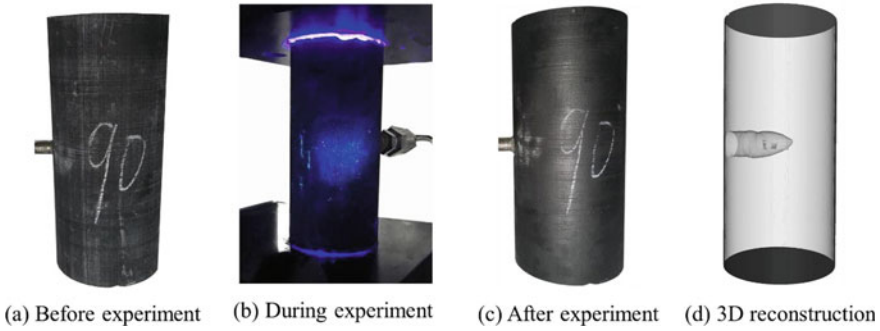
Fig. 5.5 Fracture morphology of Specimen P-17 at different experimental stages

$$\tau = \frac{L}{l} \tag{5.3}$$

where τ denotes the tortuosity, L is the actual length of the hydraulic fracture, l represents the distance between the two ends of the hydraulic fracture. It should be noted that only the tortuosity of the main hydraulic fractures was calculated based on Eq. (5.3).

As shown in Fig. 5.5, no fluid leakage or macroscopic fractures were observed in the shale Specimen P-17 over the entire fracturing process. Further, the smooth and intact 3D morphology of the Specimen P-17 reconstructed by CT scanning data demonstrates that no micro-crack was ever induced inside this sample. From another point of view, the sample remains in static equilibrium, which corresponds to the constant pressure stage as aforementioned in Sect. 5.1. This steady-state confirms that the applied fluid pressure (17 MPa) is insufficient to crack the shale on a time scale of 350 min.

Figure 5.6 shows the fracture morphology of Specimen P-19 at different experimental stages. A local crevice connecting the wellbore with the sample surface appeared about two minutes after the pump started. This result confirms the previous speculation about local leakage for the decrease in pump pressure and the increase in injection rate in Fig. 5.2b. Then, the phenomenon of fluid continuously spilling out of the local crevice was visible throughout the whole experiment (Fig. 5.6b), which corresponds to the stable leakage stage in Fig. 5.2a. The steady fluid leakage ($\approx$0.1 mL/min) inside the specimen reflects the equivalent fluid exchange process between the inflow and the outflow in the wellbore, indicating the local crevice's approximate stable state (i.e., a crack with roughly fixed length and width). In addition, macroscopic observation under ultraviolet light (Fig. 5.6c) and 3D reconstruction based on CT data (Fig. 5.6d) after the experiment further demonstrated that there was only one local crack generated near the wellbore. Thus, it is reasonable to correlate this local crack with pump pressure and injection rate variations. Comparing Fig. 5.2 with Fig. 5.6, we can conclude that the initiation of the local crack is characterized by the decline of fluid pressure and subsequent rise of injection rate. So, new
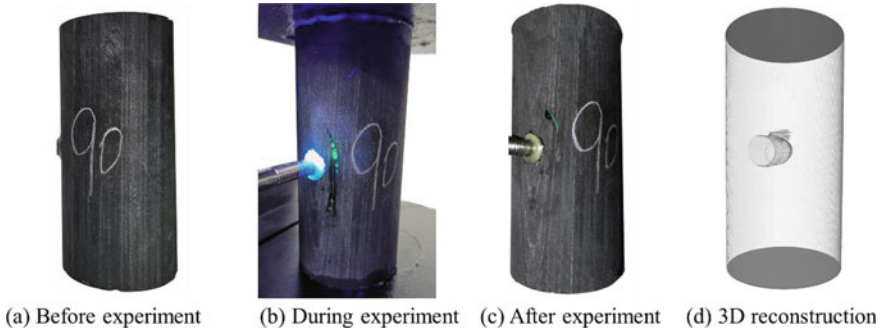
(a) Before experiment　(b) During experiment　(c) After experiment　(d) 3D reconstruction

Fig. 5.6 Fracture morphology of Specimen P-19 at different experimental stages

cracks should be the fundamental reason for changes in the pump pressure and injection rate curves. On the other hand, the rapid decay of pump pressure and the growth of injection rate serve as two indicators for predicting the initiation and propagation state of the tensile crack.

We then focus on the fracture morphology of Specimen P-19 after the fracturing process. The trajectory of the local crevice is outlined by combining the surface photograph and the CT scanning data, as shown in Fig. 5.6c and d. The local crevice is not strictly aligned with the direction of the bedding plane like those cracks induced by constant flow rate (V-5 and V-25), but across a vertical stratification group and restricted in vertical length. The deviation from the bedding direction could be attributed to the simultaneous initiation and the subsequent merge of multiple near-wellbore micro-cracks, eventually forming the visible local crack on the specimen surface. In this case, the macroscopic crack morphology will be dominated by the initial locations of the micro-crack initiation points around the wellbore and may not be consistent with the bedding planes. This phenomenon (i.e., crack initiation at multiple points) has a great propensity to occur when a constant fluid pressure (less than the instantaneous breakdown pressure) is maintained for a period to induce static fatigue damage inside the specimen in line with Bunger and Lu [22] and Zeng et al. [12]. In addition, although the local crack has not yet wholly fractured the rock matrix, some noticeable differences can still be identified in the fracture morphology between the two injection conditions. The local crack path is relatively tortuous ($\tau = 1.026$) compared to those fractures obtained under the constant flow injection mode ($\tau = 1.001$ for V-5 and $\tau = 1.024$ for V-25). This discrepancy is essentially due to different degrees of fluid diffusion in the rock matrix. Under the constant flow case, the wellbore is likely in a "fast" (nonfluid-penetrating) pressurization regime [7], while during the constant pressure fracturing (static fatigue) process, more fluid can permeate the rock, which effectively reduces rock breakdown pressure and forms complex and undulated fractures [23].

As the wellbore pressurization remains at 21 MPa, the hydraulic fracture appears to be somewhat more complex. Figure 5.7a shows the specimen observed before the experiment. The surface is relatively homogeneous, with notable bedding planes

parallel to the sample axis. During the experiment (Fig. 5.7b), the emergence of crack 1# was first recorded by photography at $T_{inj} = 27$ min. This crack caused the first P_{inj} oscillation in the local cracking stage of Fig. 5.3b. After about 7 min, another crack 2# appeared on the left side of the sample, which precisely corresponds to the new P_{inj} oscillation in the local cracking stage. The leaking fluorescent fracturing fluid perfectly exhibited the position and propagation state of the local cracks. As the experiment progressed, crack 1# started to propagate vertically, which should be related to the non-uniform decline in fluid pressure during the unstable cracking stage in Fig. 5.3c. The flow trajectory of the leaked yellow-green liquid roughly depicts the geometry of the hydraulic fractures. Figure 5.7c displays the resulting fracture morphology obtained by direct observation (under UV light), sketch, and 3D reconstruction after the experiment. The twisted and tortuous fractures indicate that both the tensile and shear stresses are responsible for crack propagation [24].

In terms of the quantitative results of tortuosity in Table 5.2, the crack morphology of Specimen P-21 appears to be most tortuous ($\tau = 1.078$) compared to Specimen P-19, V-5, and V-25. This result ulteriorly confirms that the constant pressure injection condition can make cracks more tortuous than the constant flow. To present the hydraulic fracture morphology in a micron-scale (500 µm), we additionally performed microscope observation based on two representative Specimen V-5 and P-21, respectively. As shown in Fig. 5.8, kinks, bends, fracture branches, diversions, and arrested fracture ends are all visible along the fracture path of Specimen P-21 (Fig. 5.8a), which differs remarkably from the "simple" type fracture geometry controlled by constant flow (V-5) in Fig. 5.8b. Therefore, it can be inferred that an undulated and complex hydraulic fracture is favored in the specimen with a relatively high constant pressure under static fatigue conditions. Many other factors such as fluid viscosity, injection rate, rock strength variability, and temperature also play an essential role in influencing fracture tortuosity. Detailed analysis of these factors is, therefore, recommended for further studies.

To establish a direct correlation between the crack behavior and pumping parameters (P_{inj}, v_{decay}, and V_{inj}), some abnormal variations of the fluid pressure in Specimen P-21 were elaborated. During the local cracking stage (Fig. 5.3b), Specimen P-21 experienced two evident P_{inj} oscillations, which correspond to the two cracks (1# and 2#) on the specimen surface, respectively. For the first P_{inj} oscillation, the maximum decrement of P_{inj}, v_{decay}, and V_{inj} during the oscillation is 0.52 MPa, 287.63 MPa/s, –1.3 mL/min, respectively, more significant than that ($\Delta P_{inj} = 0.2$ MPa, Δv_{decay} = 249.66 MPa/s, and ΔV_{inj} = –0.715 mL/min) of the second P_{inj} oscillation. The P_{inj} oscillation in Specimen P-19 shows that the decrements of these parameters are 0.16 MPa, 237.6 MPa/s, and 0.57 mL/min, respectively. Combining the fracture leakage situation that followed these P_{inj} oscillations in Figs. 5.6b and 5.7b, we can infer that higher pressure decrement (or injection rate increase) corresponds to more significant fluid leakage as well as more extended fractures. This phenomenon becomes particularly evident at the end of the unstable cracking stage (Fig. 5.3(c)), where a sudden drop of fluid pressure (7.17 MPa) accompanied by a relatively intact vertical hydraulic fracture (1#) emerged (Fig. 5.7b–iii), with the max$V$ = 106.82 mL/min and the maximum $v_{decay} = 13,770$ MPa/s. This result presents a

(a) Before experiment
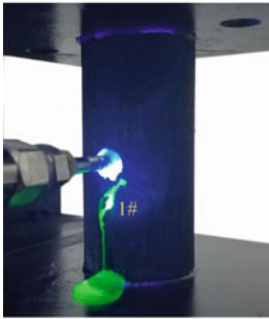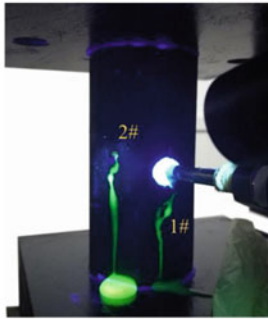
(i) T_{inj}=27 min   (ii) T_{inj}=34 min   (iii) T_{inj}=41 min
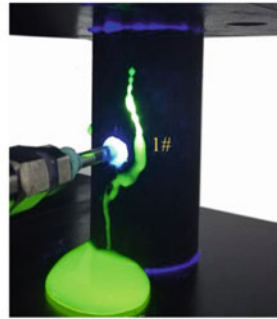
(b) During experiment

(i) Directly observed   (ii) Sketched view   (iii) 3D view

(c) After experiment

Fig. 5.7 Fracture morphology of Specimen P-21 at different experimental stages

(a)

(b)
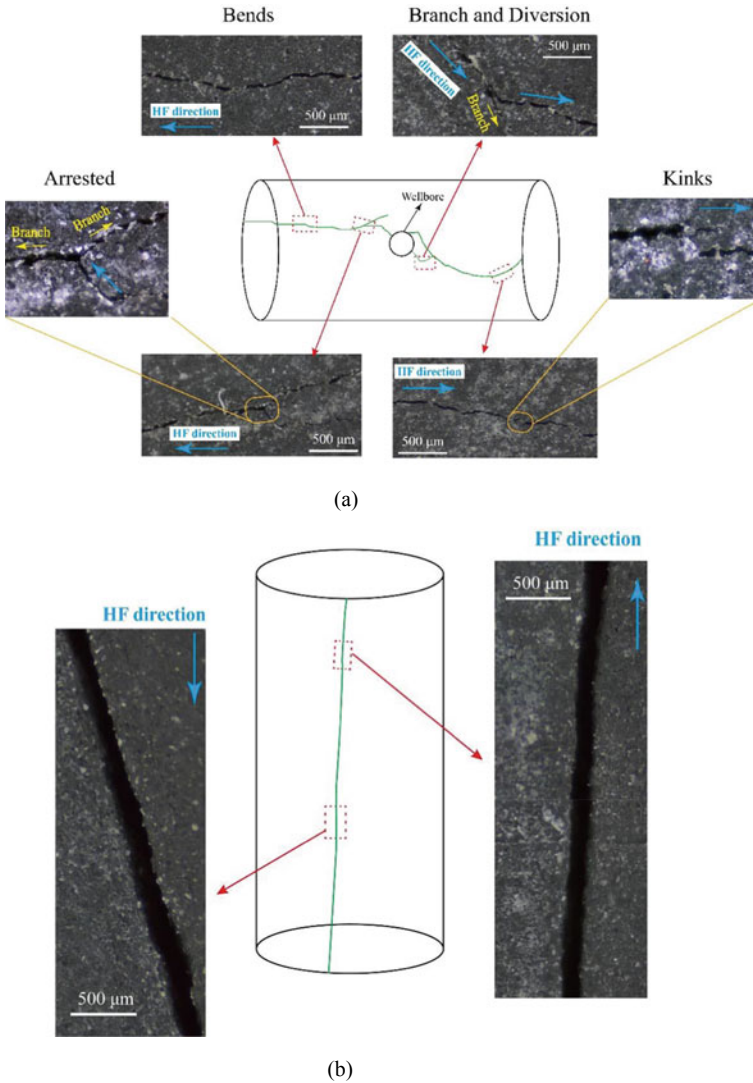
Fig. 5.8 Micrograph showing some details of the hydraulic fracture morphology: **a** Specimen P-21; **b** Specimen V-5

possible explanation for the (positive) correlation between the lag time and the pump pressure changes. It is likely to be the case that the relatively high P_{inj} oscillation promotes longer cracks such that more time is required for fluid injection to maintain a constant pressure.

After each P_{inj} oscillation, as observed in Figs. 5.2b and 5.3a, the pump pressure tends to return to a constant level and remain for a few minutes until the next pressure

drop-off. The injection rate is gradually leveling off amid this process. These observations are consistent with an interpretation that cracks can be arrested after their initial growth due to the interaction of the initiating fracture with the near-wellbore stress concentration, which has been theoretically verified by Detournay and Carbonell [7] and experimentally illustrated by Lu et al. [14]. Following such crack arrests, there is an unstable cracking stage (Fig. 5.3c) prior to the final loss of specimen integrity, in which a pressure plateau is visible accompanied by an approximately steady increase in the injection rate. Practically, to maintain the steadily increasing injection rate, the crack aperture and length should also change uniformly, which indicates that the pressure plateau corresponds to the stable propagation of hydraulic fractures. Other irregular fluctuations in the unstable cracking stage can be correlated to the process of unstable fracture propagation, which is influenced by the specimen geometry and imposed stress boundaries according to Gehne et al. [8] and Benshion et al. [25].

In summary, under constant pressure injection conditions, the fracture initiation and failure induced by static fatigue can exhibit a time-dependent progressive process like Specimen P-19 and P-21. In contrast to the smooth and straight fractures under constant flow tests, multiple fracture initiations may occur to form an undulated fracture deviating from the bedding direction. In addition, a more tortuous and complex hydraulic fracture is favored in the specimen as the constant output pressure is relatively high. In addition, the crack behaviors, such as initiation, arrest, stable and unstable propagation, are closely related to the relative variations of pump pressure, injection rate, and pressure decay rate. These findings provide a basis for possibly employing the curves of pump pressure and injection rate to predict and evaluate the extension range of hydraulic fracture in practical hydrofracturing engineering.

5.3   Correlation Between Fracture Behavior and Pumping Parameters Based on Engineering Parameters

Previous field tests can also verify the relationship between the crack behavior and the pumping parameters. Zorn et al. [26] analyzed the characteristics of the microseismic signals in the Marcellus shale formation (Pennsylvania, America) during the horizontal hydraulic fracturing process. Figure 5.9a displays the map view of passive microseismic monitoring results. The injection fluid was stably pumped by a flow rate ranging from 763 to 960 m^3 per hour for all treatments. Thus, the flow rate (or volume) controlled injection mode was practically achieved during hydrofracturing, although the injection rate did not remain constant. The b-value and D-value, as delineated in Fig. 5.9b, are indicators, which represent the fractal properties of microseismics. During hydrofracturing, the onset of seismic events fluid pressurization is correlated with the decrease of the pump pressure and injection rate (marked with red dotted boxes in Fig. 5.9b), which implies that the field hydrofracturing characteristics of shale formations can be reflected by the variation of pumping parameters (pump

pressure and slurry rate). These apparent correlations between changes in the micro-seismic events and pump pressure and rate perturbations reveal quantitatively that the fracture state and permeability of rock mass are continuously changing throughout hydraulic fracturing.

If combining the laboratory observations in Figs. 5.3 and 5.10, we can further conclude that whether under constant pressure or constant flow mode, the initiation of a new crack corresponds to the decline of the pump pressure. However, the fracturing mechanism under the two injection modes differs in the variation of the pump pressure. For the constant pressure mode, the injected fluid pressure remains constant, and only when the pressurization lasts for enough period can rupture occur. In this case, the constantly controlled pressure servers as the fundamental driving force for the rupture of the shale specimens and thus controls the whole fracturing process. As aforementioned in Sect. 5.2, the initiation of a new crack (crack 1# or crack 2# in Fig. 5.7) was followed by a first decay in fluid pressure and a subsequent increase in injection rate, which indicates a phenomenon that the variation of injection rate lags pump pressure for the constant pressure mode. In the constant flow mode, the increase of pump pressure is unceasingly sustained by the equal inflow of fracturing fluid, ultimately resulting in the breakdown of shale blocks. This rupture of the shale samples under this injection mode is usually characterized by the first increasing and then decreasing pump pressure and the invariable injection rate at the laboratory scale [18, 27]. However, during the field treatment, the stable injection of fracturing fluid can hardly be maintained due to the need to pump proppant materials (e.g., sand, ceramsite). An example illustrating the variation of fluid pressure and injection rate in the field setting can be found in the work of Vulgamore et al. [28], who applied fracture diagnostics in the Woodford shale. The overall variation trend of the treatment pump pressure is similar to the constant flow tests (V-5 and V-25) during the fracturing stage. However, before the pump pressure reached the breakdown value, the injection rate peaked at the time T_1. After the second shutdown of the pump, the decline of the pressure also lagged the injection rate. These results are contrary to the observation under constant pressure mode (i.e., V_{inj} lagging P_{inj}), indicating that the different injection modes will change the pump pressure and injection rate variation. In actuality, the different injection modes correspond to different cases of fluid diffusion in the rock matrix, which can change the effective stress around the wellbore and ultimately result in differences in specimen failure [29]. According to Vulgamore et al. [28], more microseismic events and more significant pressure fluctuation were found in the breakdown and sanding process, which ulteriorly demonstrates the correlation between the crack initiation and the variation of pump pressure.
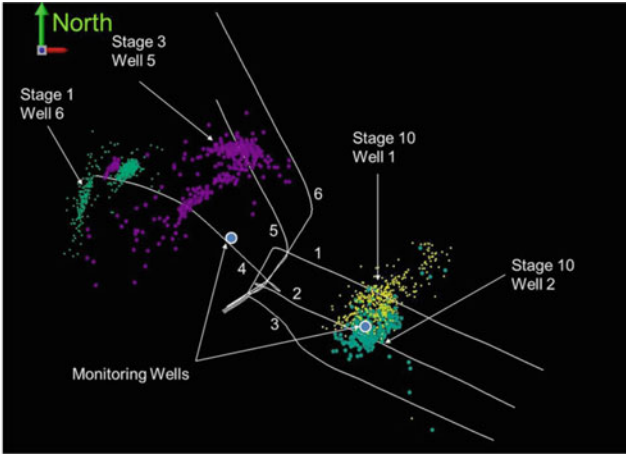
(a)
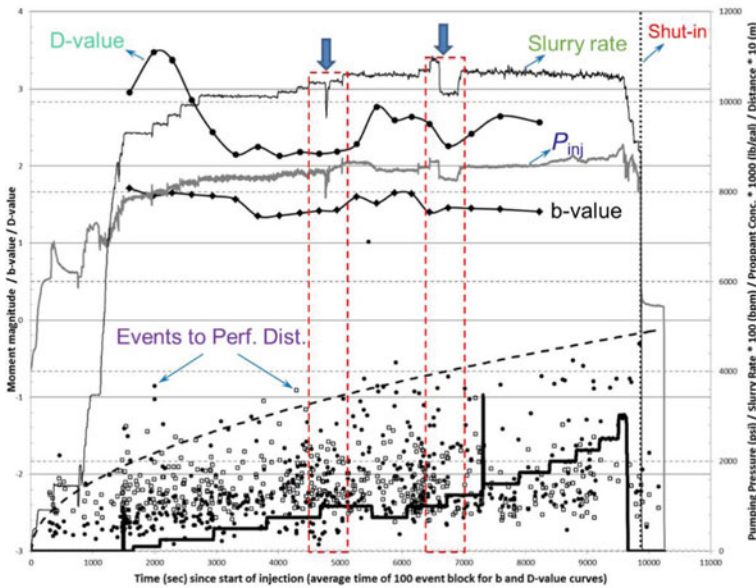
(b)

Fig. 5.9 Microseismic monitoring results during hydraulic fracturing operations in the Marcellus shale (after Zorn et al. [26]): **a** map view of microseismic monitoring results for Wells 1 ~ 6; **b** The recorded seismic and pumping variation in Stage 10 Well 1. Note that the b-value and D-value are indicators evaluating the fractal properties of microseismic according to Zorn et al. [26]
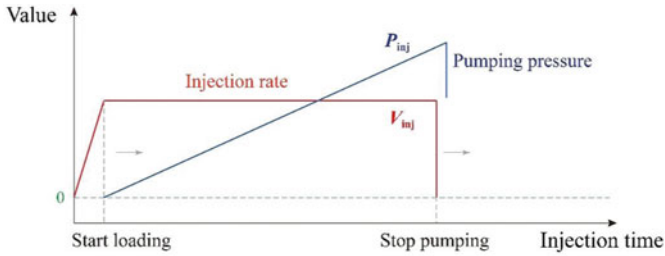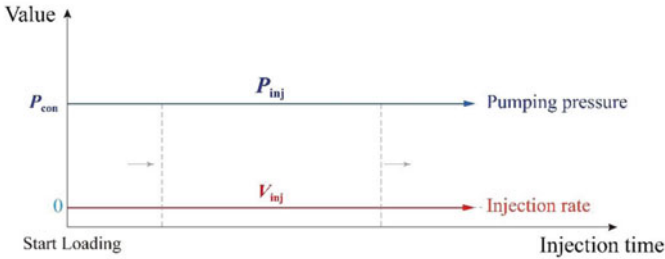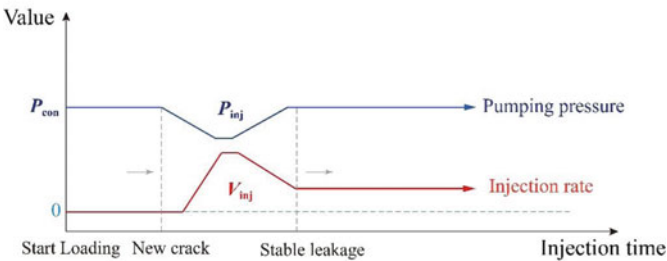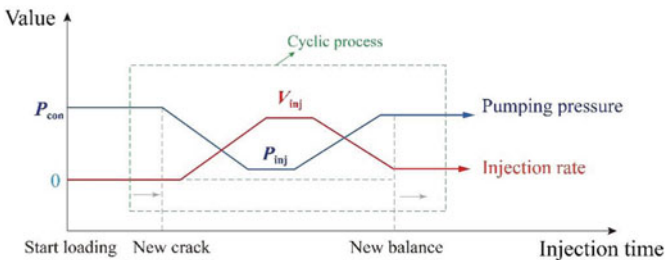
Fig. 5.10 Schematic diagram of variations of pumping parameters resulting from **a** constant flow condition, and **b–d** constant pressure condition: **a** instantaneous failure; **b** constant pressure (case (i)); **c** stable leakage (case (ii)); **d** continuous propagation process (case (iii))

5.4   Characterization of the Relationship Between Fracture Propagation and Pumping Parameters

The tensile hydraulic fracture is known to be induced via a complex crack-tip fracture process zone constituted by a zone of cohesive and high shear stress [30]. This zone is physically described as a lag with an unknown length between the fluid front and the fracture tip, full of the inviscid vapors from the fracturing fluid and the compressed air [31]. The presence of this crack-tip cavity, to a certain extent, removes the crack-tip singularity in the fluid pressure, according to Detournay [32]. In this case, the initiation of a new crack will merely require the fluid pressure to reach a critical value sufficient for overcoming the tensile strength of the rock matrix (or bedding planes). For the volume-controlled (or constant flow) tests, as mentioned in Sect. 5.2, the wellbore pressurization is probably in a fast nonfluid-penetrating regime, which results in a relatively high instantaneous breakdown pressure in line with Detournay and Carbonell [7]. Figure 5.10a roughly describes the pump pressure and injection rate variations during this instantaneous process. Under the constant pressure injection mode, a target pump pressure lower than the instantaneous breakdown pressure was applied and held constant for an extended period. Despite the low permeability of shale, constant pressurization and fluid diffusion can still be synchronously achieved as the loading duration is long enough. With the increase of this duration, the diffusion area of the pore pressure in the rock also increases, which significantly reduces the near-wellbore effective stress and increases the possibility of specimen failure.

Combining the experimental results (P-17, P-19, and P-21), we can see that there are three prominent failure cases under the constant pressure conditions: (i) If the target pressure is relatively low, no crack is induced inside the specimen, which corresponds to a long constant pressure stage as Fig. 5.10b depicts. Once a tensile notch appears, the constant pressure feedback loop control pushes excess fracturing fluid into the defects, resulting in a subsequent decrease in pump pressure and increased fluid flow (i.e., local cracking stage). The fluid is continuously injected into the specimen until a balance is reached between the notch space and fluid flow. (ii) If the fracture (notch) growth is arrested and the fracturing fluid can leak out via the notch, a stable leakage state (Fig. 5.10c) may be observed throughout the entire experiment, like Specimen P-19. (iii) Otherwise, a new crack near the notch appears accompanied by another decrease in fluid pressure and buildup in injection rate. Afterward, the pressure within the crack will be ramped up, followed by a decrease in the fluid flow, and then gradually approach a new balance between the power of the squeezed fluid and the strength of the shale block (or bedding planes). Another crack initiation near the last crack will break the new balance again and result in similar parameter changes. Therefore, the continuous propagation of hydraulic fractures is likely characterized by the cyclical variation of pumping parameters: the increases in injection rate and pump pressure occur alternately, as shown in Fig. 5.10d.

References

1. Ma L, Fauchille AL, Chandler MR, Dowey P, Taylor KG, Mecklenburgh J, Lee PD (2021) In-situ synchrotron characterisation of fracture initiation and propagation in shales during indentation. Energy 215. https://doi.org/10.1016/j.energy.2020.119161
2. Zang A, Zimmermann G, Hofmann H, Stephansson O, Min KB, Kim KY (2019) How to reduce fluid-injection-induced seismicity [J]. Rock Mech Rock Eng 52:475–493
3. Zeng B, Lu D, Zou Y, Zhou J, Li S, Li N, Cao Z (2020) Experimental study of the simultaneous initiation of multiple hydraulic fractures driven by static fatigue and pressure shock. Rock Mech Rock Eng 53(11):5051–5067. https://doi.org/10.1007/s00603-020-02190-4
4. Renshaw CE, Pollard DD (1994) Are large differential stresses required for straight fracture propagation paths? J Struct Geol. https://doi.org/10.1016/0191-8141(94)90147-3
5. Tang CA, Yang TH, Li LC, Liang Z, Tham LG, Lee KK, Tsui Y (2003) Numerical simulation to influence of pore pressure magnitude and gradient on fracture propagation in brittle heterogeneous rocks (S2):17–20
6. Lu YY, Jia YZ, Tang JR, Song CP (2016) Mechanism of hydrofracture propagation control by nonuniform pore pressure field. J Northeast Univ (Nat Sci) 37(07):1028–1033
7. Detournay E, Carbonell R (1997) Fracture-mechanics analysis of the breakdown process in minifracture or leakoff test. SPE Prod Facil. https://doi.org/10.2118/28076-PA
8. Gehne S, Benson PM, Koor N, Dobson KJ, Enfield M, Barber A (2019) Seismo-mechanical response of anisotropic rocks under hydraulic fracture conditions: new experimental insights. J Geophys Res Solid Earth. https://doi.org/10.1029/2019JB017342
9. Song C, Lu Y, Tang H, Jia Y (2016) A method for hydrofracture propagation control based on nonuniform pore pressure field. J Nat Gas Sci Eng. https://doi.org/10.1016/j.jngse.2016.05.029
10. Hu Q, Liu L, Li Q, Wu Y, Wang X, Jiang Z et al (2020) Experimental investigation on crack competitive extension during hydraulic fracturing in coal measures strata. Fuel. https://doi.org/10.1016/j.fuel.2019.117003
11. Ha SJ, Choo J, Yun TS (2018) Liquid CO_2 fracturing: effect of fluid permeation on the breakdown pressure and cracking behavior. Rock Mech Rock Eng. https://doi.org/10.1007/s00603-018-1542-x
12. Zeng B, Lu D, Zou Y, Zhou J, Li S, Li N et al (2020) Experimental study of the simultaneous initiation of multiple hydraulic fractures driven by static fatigue and pressure shock. Rock Mech Rock Eng. https://doi.org/10.1007/s00603-020-02190-4
13. Lu G, Gordeliy E, Prioul R, Aidagulov G, Uwaifo EC, Ou Q et al (2020) Time-dependent hydraulic fracture initiation. J Geophys Res Solid Earth. https://doi.org/10.1029/2019JB018797
14. Lu Q, Lu G, Prioul R, Aidagulov G, Bunger AP (2018) Impact of fluid acidity on the time-dependent initiation of hydraulic fractures in carbonate rocks. Rock Mech Rock Eng. https://doi.org/10.1007/s00603-018-1544-8
15. Liu L, Xu WY, Wang HL, Wang RB, Wang W (2016) Experimental studies on hydro-mechanical properties of metamorphic rock under hydraulic pressures. Eur J Environ Civ Eng. https://doi.org/10.1080/19648189.2015.1013638
16. Wang LZ, Jiang HY, Yang ZX, Xu YC, Zhu XB (2013) Development of discontinuous deformation analysis with displacement-dependent interface shear strength. Comput Geotech. https://doi.org/10.1016/j.compgeo.2012.06.006
17. Zhao Z, Li X, He J, Mao T, Li G, Zheng B (2018) Investigation of fracture propagation characteristics caused by hydraulic fracturing in naturally fractured continental shale. J Nat Gas Sci Eng. https://doi.org/10.1016/j.jngse.2018.02.022
18. Lin C, He J, Li X, Wan X, Zheng B (2017) An experimental investigation into the effects of the anisotropy of shale on hydraulic fracture propagation. Rock Mech Rock Eng. https://doi.org/10.1007/s00603-016-1136-4
19. Napier JAL, Detournay E (2019) Simulation of buoyancy-driven fracture propagation using the displacement discontinuity boundary element method [J]. Adv Eng Mater, Struct Syst: Innovations, Mech Appl 525–530

20. Khalil MA, Susi AO (2020) Hydraulic fracture geometry modeling techniques for extracting unconventional reservoirs [J]. J Eng Res Rep 5:1–5
21. Rose W, Bruce WA (1949) Evaluation of capillary character in petroleum reservoir rock. J Pet Technol. https://doi.org/10.2118/949127-g
22. Bunger AP, Gordeliy E, Detournay E (2013) Comparison between laboratory experiments and coupled simulations of saucer-shaped hydraulic fractures in homogeneous brittle-elastic solids. J Mech Phys Solids 61(7):1636–1654. https://doi.org/10.1016/j.jmps.2013.01.005
23. Haimson B, Fairhurst C (1976) Initiation and extension of hydraulic fractures in rocks [J]. Soc Petrol Eng J 7(03):310–318
24. Ning L, Shicheng Z, Yushi Z, Xinfang M, Shan W, Yinuo Z (2018) Experimental analysis of hydraulic fracture growth and acoustic emission response in a layered formation. Rock Mech Rock Eng. https://doi.org/10.1007/s00603-017-1383-z
25. Benson PM, Austria DC, Gehne S, Butcher E, Harnett CE, Fazio M et al (2020) Laboratory simulations of fluid-induced seismicity, hydraulic fracture, and fluid flow. Geomech Energy Environ. https://doi.org/10.1016/j.gete.2019.100169
26. Zorn EV, Hammack R, Harbert W (2014) Time dependent b and D-values, scalar hydraulic diffusivity, and seismic energy from microseismic analysis in the marcellus shale: connection to pumping behavior during hydraulic fracturing. In: Society petroleo engineering—SPE hydraulic fracturing technology conference 2014. https://doi.org/10.2118/168647-ms
27. Zhao Z, Li X, Wang Y, Zheng B, Zhang B (2016) A laboratory study of the effects of interbeds on hydraulic fracture propagation in shale formation. Energies. https://doi.org/10.3390/en9070556
28. Vulgamore T, Clawson T, Pope C, Wolhart S, Mayerhofer M, Machovoe S et al (2007) Applying hydraulic fracture diagnostics to optimize stimulations in the Woodford shale. https://doi.org/10.2523/110029-ms
29. AlTammar MJ, Gala DP, Sharma MM (2020) Application of different fluid injection methods to reduce breakdown pressure. Int Pet Technol Conf IPTC. https://doi.org/10.2523/iptc-19589-ms
30. Carrier B, Granet S (2012) Numerical modeling of hydraulic fracture problem in permeable medium using cohesive zone model. Eng Fract Mech. https://doi.org/10.1016/j.engfracmech.2011.11.012
31. Garagash DI, Detournay E (2005) Plane-strain propagation of a fluid-driven fracture: small toughness solution. J Appl Mech Trans ASME. https://doi.org/10.1115/1.2047596
32. Detournay E (2004) Propagation regimes of fluid-driven fractures in impermeable rocks. Int J Geomech. https://doi.org/10.1061/(asce)1532-3641(2004)4:1(35)

Part III
Theoretical Modelling Considering Non-uniform Fluid Pressure

Chapter 6
Fracture Initiation

6.1 Breakdown Process Under Constant Injection Flow

Field in-situ constant-flow hydraulic fracturing test is an important technique to determine the tectonic stress field. Classical hydraulic fracturing mechanics regards the maximum tensile stress criterion as the critical initiation condition, which assumes that the hydraulic fracture initiates and expands when the maximum effective tangential stress around the wellbore is larger than the tensile strength of the rock, resulting in tensile failure of the rock. Based on this condition, Hubbert and Willis [1] put forward a theoretical criterion for rock breakdown, which is also taken as synonymous with hydraulic fracture initiation,

$$P_b = 3\sigma_h - \sigma_H + \sigma_t - p \tag{6.1}$$

where σ_H and σ_h are the maximum and minimum principal stresses, respectively; σ_t is the tensile strength of rock; p virgin pore pressure in the formation. This criterion is suitable for the fast pressurization case where the fluid is not able to penetrate the near-wellbore region prior to breakdown (or impermeable rock medium).

Involving the effect of impermeability of rock matrix, Haimson and Fairhurst [2] refined the classical criterion of Hubbert and Willis, and proposed a linear elastic prediction model for breakdown pressure of porous rock,

$$P_b = \frac{3\sigma_h - \sigma_H + \sigma_t - 2\eta p}{2(1 - \eta)} \tag{6.2}$$

with η is a poroelastic constant and related to the Poisson's ratio v and Biot coefficient b as

$$\eta = \frac{\alpha(1 - 2v)}{2(1 - v)}, \quad (0 \leq \eta \leq 0.5) \tag{6.3}$$

The above two criteria indicate that the breakdown pressure mainly depends on the initial stress state (i.e., σ_H and σ_h). However, the above criteria failed to consider the impact of pressurization/injection rate on breakdown pressure. Moreover, current research tends to assume a linear relationship between fluid flow and pressurization rate, which is limited to reflect fluid compressibility and lag zone within the crack. When considering fluid compressibility and hysteresis, the hydraulic fracturing physical process can be schematically described by Fig. 6.1. In a closed space, the continuously injected fluid compresses the air into the defects around the wellbore. Part of the gas may penetrate into the pores of the rock matrix, and other part of the gas accumulates in front of the fracturing fluid, forming a fluid lag zone. With the continuous injection of fluid, the length of the fluid lag zone may decrease until a limit compression distance is reached. The higher injection rate results in higher fluid pressure in the wellbore per unit time, resulting in the corresponding increase amount of compression. When the fluid compression amount is close to the limit value, the pressurization rate begins to decrease. This section will model the relationship between the injection rate and breakdown pressure by using the quadratic nonlinear relation shown in Fig. 6.1. The detailed theoretical analysis process is as follows:

In line with Ito [3], three tangential stress components (σ_θ^1, σ_θ^2 and σ_θ^3) induced by far-field in-situ stress, net fluid pressure with the fracture and pore pressure gradient are considered around the wellbore σ_θ^1 is a function of far-field stress and polar coordinates (r, θ), which can be expressed by

$$\sigma_\theta^1 = \frac{\sigma_H + \sigma_h}{2}(1 + \frac{a^2}{r^2}) - \frac{\sigma_H - \sigma_h}{2}(1 + 3\frac{a^4}{r^4})\cos 2\theta + \frac{a^2}{r^2}p \qquad (6.4)$$

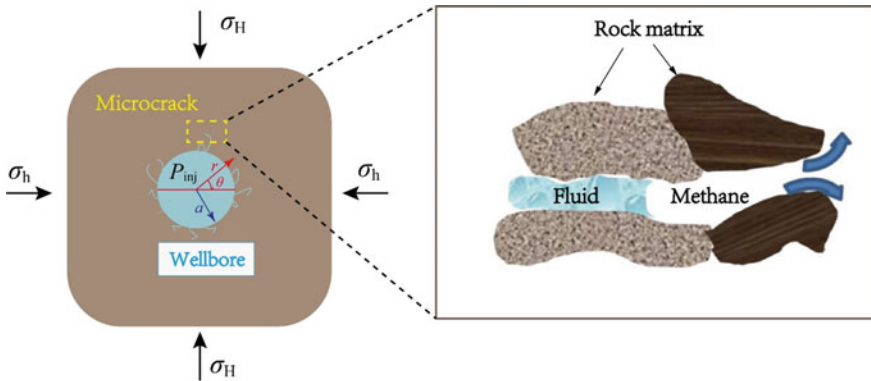σ_θ^2 is a near-wellbore stress component generated by fluid pressure increase

Fig. 6.1 Diagram of compressed air replaced by invaded water that causes pressure build-up during constant flow injection process

$$\sigma_\theta^2 = \frac{a^2}{r^2}(P_{inj} - p) \tag{6.5}$$

and σ_θ^3 is induced by fluid infiltration into rock matrix

$$\sigma_\theta^3 = \frac{1-2v}{1-v}\alpha\left\{\frac{1}{r^2}\int_a^r (P_{inj} - p)\rho d\rho - (P_{inj} - p)\right\} \tag{6.6}$$

where the wellbore pressure P_{inj} is a function of r and T_{in}, which can be calculated by

$$P_{inj} = \frac{dP_{inj}}{dT_{inj}}\int_0^{Teq} f(r, s)ds + p \tag{6.7}$$

with $f(r, t) = 1 + \frac{2}{\pi}\int_0^\infty \exp(-\frac{k}{\mu n\beta_w}u^2 T_{inj}) \times \left[\frac{J_0(ur)Y_0(ua) - Y_0(ur)J_0(ua)}{J_0^2(ua) + Y_0^2(ua)}\right]\frac{du}{u}$, k is the rock permeability, n is the rock porosity, μ is the fluid viscosity, β_w is the fluid compression coefficient, J_0 and Y_0 are the zero-order first and second Bessel functions.

The total tangential stress around the wellbore can be derived based on the principle of stress superposition.

$$\sigma_\theta^{\text{Total}} = \sigma_\theta^1 + \sigma_\theta^2 + \sigma_\theta^3 \tag{6.8}$$

Using the maximum tensile stress principle, we have

$$\sigma_\theta^{\text{Total}}(r = a) = \sigma_t - p \tag{6.9}$$

Considering the ultra-low permeability of the shale and assuming the initial pore pressure to be zero, the breakdown pressure under different injection rates can be calculated after substituting Eqs. (6.4) ~ (6.8) into Eq. (6.9). The related calculation parameters are shown in Table 6.1.

Figure 6.2 compares the theoretical calculation results of breakdown pressure with the experimental observations. It is easy to find that the theoretical prediction results are generally larger than the test breakdown pressure value. This may result from the preexistence of natural micro-cracks, holes, impurities and other defects near the wellbore, contrary to the isotropic and homogeneous assumption in the theoretical model. When the injection rate is high, the calculation and the test results are in good

Table 6.1 Parameters used for calculating breakdown pressure

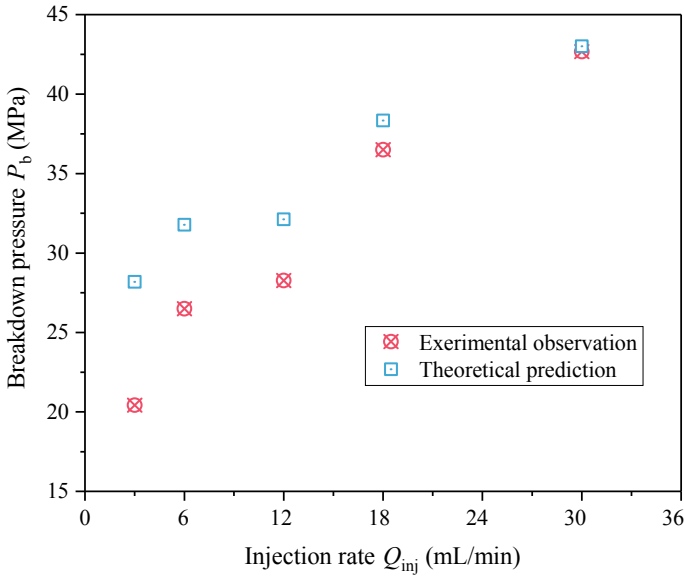| Rock type	σ_t	v	α	$k/10^{-22}$ m^2	$n/\%$
Longmaxi shale	5.03 ~ 8.27	0.119	0.9 [4]	1.76	2.39

Fig. 6.2 Comparison between theoretical and experimental results of rock breakdown pressure under different flow rates

agreement, and the deviation gradually increases with the decrease of the injection rate. We believe that this phenomenon is caused by the nonlinear relationship between the pressurization rate and the injection rate.

A larger flow rate leads to a greater pressurization rate and a shorter nonlinear change section of the pump pressure. The injection flow value based on the quadratic fitting can better reflect the change in the actual pressurization rate, resulting in a more consistent fitting effect at a high injection rate. This conclusion is consistent with the results of Shao et al. [5] who investigated the effects of pressurization rate on the breakdown pressure of limestone. Therefore, in summary, the predictions of the current model are consistent with the experimental observations, and the model can better explain the effect of the injection rate on the rock breakdown pressure.

6.2   Breakdown Process Under Constant Injection Pressure

To characterize the continuous propagation of hydraulic fractures (case (iii)), we additionally presented a conceptual model based on the wave-like theory of hydraulic fracture introduced by Jiang et al. [6]. As shown in Fig. 6.3a, for a wellbore uniformly pressurized by its internal fluid pressure (P_{inj}), the rock near the wellbore will suffer a gradual diffusion stress zone starting from the highest pressure area (blue area) to the second-highest pressure area (orange area). Due to the static fatigue (caused by fluid diffusion) inside the specimen, the rock in Circle 1 (called the first splitting ring)

will first reach the critical splitting condition (tensile failure), then the high-pressure water enters a fractured zone (orange area), where the natural beddings and induced fractures are interconnected. This process synchronously results in a decline in the pump pressure and an increase in the injection rate. Due to this pressure loss, the fluid pressure acting at the interface between the first split ring and the second split ring no longer satisfies the splitting condition. Thus, the rock beyond Circle 1 is temporarily free from hydraulic splitting failure. As the fluid pressure in the wellbore is built up by continuous injected fluid, the fluid pressure acting at the interface (Circle 1 in Fig. 6.3b–i) increases accordingly. Once the increased fluid pressure meets the splitting condition, a new hydraulic split ring (Circle 2) appears, which corresponds to a yellow-green area in Fig. 6.3b–ii. By analogy, it can be inferred that as the fluid pressure in the wellbore is repeatedly released, increased, and released, the third splitting ring (Circle 3) may be formed as outlined by the green area in Fig. 6.3b–iii. It is worth noting that once a new fracture is initiated, there would be very little fluid exchange between the fracture and the rock matrix due to its low permeability, which means that fluid migration will occur mainly within the crack [7]. The spreading of the hydraulic splitting rings is the so-called wave-like theory of hydraulic fracture in line with Jiang et al. [6]. This process is slowly extended, which agrees well with the variations of the pumping parameters. In addition, according to Jiang et al. [6], the most crucial feature of the splitting process is that there will be more than two wave peaks in the injection rate and fluid pressure curves with the continuous propagation of a hydraulic fracture. This feature can be identified by correlating the two P_{inj} oscillations during the fracturing process of Specimen P-21. The consistency further demonstrates the feasibility of employing this conceptual model to explain the constant pressure injection fracturing process.

The circulation of the parametric variations and the split rings can be alternatively repeated until the radial crack reaches the edge of the specimen surface. Then, the hydraulic fracture starts to propagate vertically, and the propagation state will primarily depend on the pump pressure. For a relatively small value of pump pressure (e.g., $P_{con} = 19$ MPa), an approximately constant fracturing aperture may be abidingly maintained to release the internal fluid, which corresponds to the stable leakage phase in the pump pressure curves. This inference was proved by the local leakage of the fracturing fluid observed during the experiment in Fig. 5.4b. Whereas in the case of a higher pump pressure (e.g., $P_{con} = 21$ MPa), through comparing the fluid leakage location and trajectory at a different time in Fig. 5.7b, we see that the leakage paths are gradually opened with an overall increase of the injection rate (Fig. 5.3a), corresponding to the subsequent local and unstable cracking stages during the fracturing process. Thus, the speculation for the conceptual model is reliable to elucidate the fracturing process under constant pressure injection conditions.

In summary, the pump's output modes (constant pressure or constant flow) have a pronounced influence on the morphology of the hydraulic fractures. Moreover, different stages of fluid pressure (or injection rate) curves are closely correlated with varying fracture behaviors in the fracture propagation process, which implies a potential for using the pumping parameter curves to predict the initiation and propagation of hydraulic fractures in actual engineering.
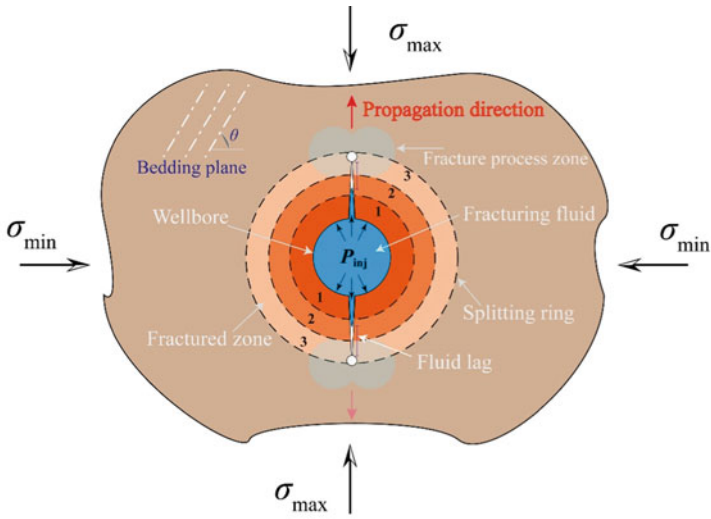
(a) Schematic diagram of the conceptual model

(i)   (ii)   (iii)
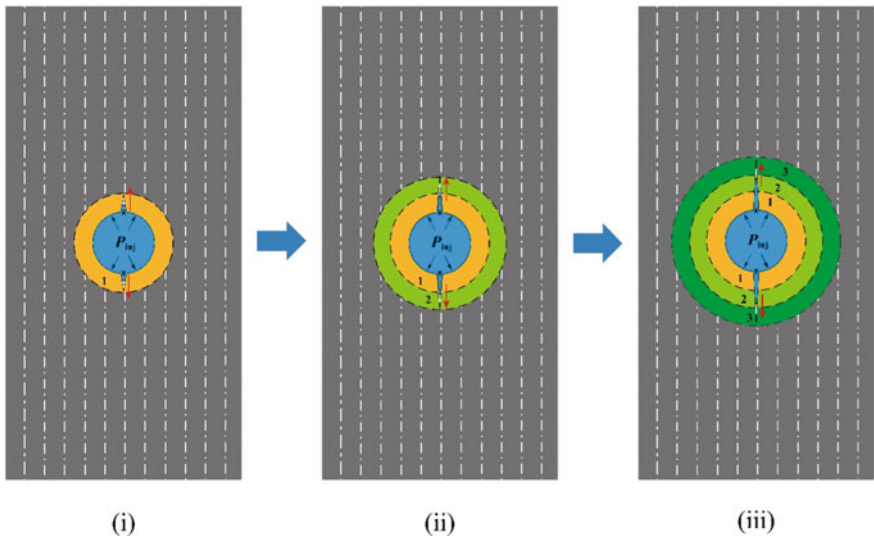
(b) Evolution of the splitting rings (θ=90°)

Fig. 6.3 Conceptual model of fractured zone propagation during hydraulic fracturing experiments

References

1. Hubbert M, Willis D (1957) Mechanics of hydraulic fracturing. Transp Soc Petrol Eng AIME 210:153–168
2. Haimson B, Fairhurst C (1976) Initiation and extension of hydraulic fractures in rocks. Soc Petrol Eng J 7(03):310–318
3. Ito T, Hayashi K (1991) Physical Background to the breakdown pressure in hydraulic fracturing tectonic stress measurements. Int J Rock Mech Min Sci Geomech Abs 28(4):285–293
4. Guo X, Li J, Liu G, Xi Y, Zeng Y, He M, Yan H (2019) Numerical simulation of casing deformation during volume fracturing of horizontal shale gas wells. J Petrol Sci Eng 172:731–742
5. Shao CY, Pan PZ, Zhao DC, Yao TB, Miao ST (2020) Effect of pumping rate on hydraulic fracturing breakdown pressure and pressurization rate. Rock Soil Mech 41(07):2411–2421+2484
6. Jiang Z, Fu S, Li S, Hu D, Feng S (2007) High pressure permeability test on hydraulic tunnel with steep obliquity faults under high pressure. Yanshilixue Yu Gongcheng Xuebao/Chinese J Rock Mech Eng
7. Gehne S, Benson PM, Koor N, Dobson KJ, Enfield M, Barber A (2019) Seismo-mechanical response of anisotropic rocks under hydraulic fracture conditions: new experimental insights. J Geophys Res Solid Earth. https://doi.org/10.1029/2019JB017342

Chapter 7
Fracture Propagation

7.1 Introduction

In previous theories regarding hydraulic fracture propagation, it is usually assumed the fluid pressure within the hydraulic fracture is constant in the calculation of the surrounding stress field. The actual fluid pressure during fracturing process, however, is often fluctuating, due to the disturbance of the irregular surface of rock fracture and the viscous flow of fracturing fluid. Considering the uneven distribution characteristics of fluid pressure inside a hydraulic fracture and investigating the propagation process of this hydraulic fracture is beneficial to reflecting the realistic dynamic propagation of hydraulic fractures and improving the theory of field hydraulic fracturing. Up to now, the specific form of fluid pressure inside the fracture remains unclear. The fluid pressure is not constant due to the flow and viscosity of the fluid inside the fracture. The fluid pressure can be any form, depending on the actual injection conditions (e.g., pulse hydraulic fracturing). Sneddon and Elliott [1] derived the theoretical solutions of the induced stress and displacement fields in response to the non-uniform pressure of internal fluid outside the crack, but merely obtained a form solution with an integral variable for the stress and displacement around the crack. The existence of the integral variable to a large extent complicates the state analysis near the crack and inhibits its potential application in investigating the fracturing process under non-uniform pressure.

Considering the nonuniform distribution of fluid pressure within the crack is beneficial to reflect the stress state around hydraulic fractures, refine the theory of hydraulic fracturing and provide support for the actual fracturing process. Though of apparent practical importance, the effect of nonuniform fluid pressure has not received due attention. In this chapter, the solution of Sneddon and Elliott [1] is reduced to a more simplified form and solved by means of the composite Simpson's rule to facilitate a stability analysis in the hydraulic fracturing process. It is theoretically feasible because the validity of this semianalytical solution can be guaranteed within a reasonable margin of error if the number of subintervals is sufficiently small. The applicability of the semianalytical solution is validated by comparing the

approximation results with those obtained from constant fluid pressure and laboratory experiments. The sensitivity of the initial pressure and crack length common in constant pressure and the perturbation of the number of subintervals and terms missed in constant pressure are also discussed to assess the solution's reliability.

7.2 Mathematical Formulation

Assume a $2a$-long Griffith crack nonuniformly pressured by internal fluid is propagating in an impermeable, homogeneous and linear elastic plane-strain medium (Fig. 7.1). As shown in Fig. 7.1, a rectangular coordinate system is established with the center of crack O as the origin and the crack extension direction as the y-axis. The fluid pressure within the crack is assumed to be $P'(x)$, a general polynomial function of the crack length and the position coordinate x ($x < a$), which implies that the nonuniform fluid pressure can be replaced by a dimensionless ratio of x coordinates to half of the total crack length a.

In order to ensure the applicability and validity of this model, the following assumptions are made:

(1) The rock medium is linear, elastic, homogeneous and impermeable.
(2) The crack is propagating in the plane strain plane, ignoring the change in the height of the crack (perpendicular to the plane).
(3) The fluid pressure in the hydraulic fracture is a function of the fracture length (a) and the transverse position (x), satisfying $x < a$.
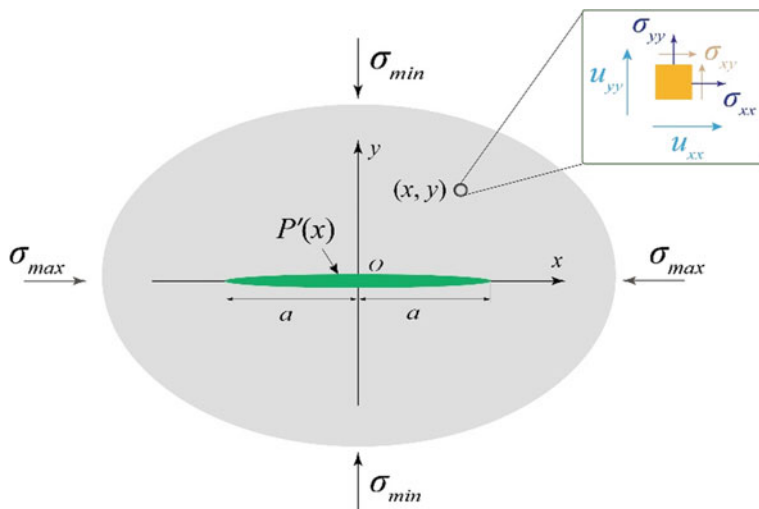

Fig. 7.1 Model for a Griffith crack non-uniformly pressurized by internal fluid
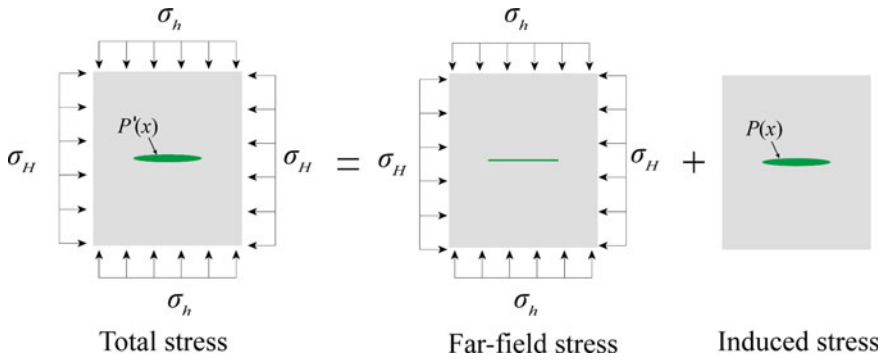
Fig. 7.2 Schematic of a Griffith crack stress decomposition (stress superposition principle)

(4) The hydraulic fracture is filled with fluid, ignoring the lag length between the fracture tip and the fluid front.

Based on the stress superposition principle delineated in Fig. 7.2, the total stress acting on the crack inner face can be decomposed into far-field in-situ stress and induced stress. The far-field stress remains uniform and is generated by in-situ stress, while the induced stress originates from the effective pressure within the crack and is controlled by injection pressure. Thus, we may solely consider the induced stress to analyze the fluid effect of nonuniform pressure in consideration of the case in which the variable fluid pressures at different x locations will greatly disturb the stress and displacement field around the crack.

7.2.1 Nonuniform Fluid Pressure Consideration

Due to variations in the fluid flow and viscosity inside the crack, the fluid pressure value cannot always remain constant. In contrast, the pressure may manifest as any form of function in terms of practical injection conditions. Taking this problem into consideration and using the superposition of far-field stress, the net fluid pressure acting on the crack is assumed to be a general polynomial.

$$P(x) = P'(x) - \sigma_h = P_0 \sum_{k=0}^{n} b_k \left(\frac{x}{a}\right)^k \ (x \leq a) \tag{7.1}$$

where $P'(x)$ is the injection pressure, σ_h represents the minimum horizontal in-situ stress, P_0 is defined as the initial fluid pressure (noting the fluid pressure mentioned here and after excluding the effect of far-field stress), k and n are both integers (≥ 0),

and b_k is a series of dimensionless real coefficient variables that varies with k. With the fitting properties of this polynomial, any form of fluid pressure distribution can be approximately expressed if the pressure of certain points within the crack can be determined.

According to [2], the integral transformation solution of the induced stress and displacement field can be expressed as (compression is considered to be negative)

$$
\begin{cases}
\sigma_{xx} = -\dfrac{2}{\pi} \displaystyle\int_0^{\infty} \xi^2 A(\xi)(1 - \xi y)e^{-\xi y} \cos(\xi x)d\xi \\[4mm]
\sigma_{yy} = -\dfrac{2}{\pi} \displaystyle\int_0^{\infty} \xi^2 A(\xi)(1 + \xi y)e^{-\xi y} \cos(\xi x)d\xi \\[4mm]
\sigma_{xy} = -\dfrac{2}{\pi} \displaystyle\int_0^{\infty} y\xi^3 A(\xi)e^{-\xi y} \sin(\xi x)d\xi
\end{cases}
\tag{7.2}
$$

The components of the displacement vector are similarly found to be

$$
\begin{cases}
u_x = -\dfrac{2(1 + v)}{\pi E} \displaystyle\int_0^{\infty} A(\xi)\xi[(1 - 2v) - \xi y]e^{-\xi y} \sin(\xi x)d\xi \\[4mm]
u_y = \dfrac{2(1 + v)}{\pi E} \displaystyle\int_0^{\infty} A(\xi)\xi[2(1 - v) + \xi y]e^{-\xi y} \cos(\xi x)d\xi
\end{cases}
\tag{7.3}
$$

As shown in Fig. 7.2, the following boundary conditions can be obtained (noting that only a quarter plane ($x \geq 0$, $y > 0$) is studied in consideration of the symmetry of the Griffith crack):

$$
\begin{cases}
x \text{ and } y \to \infty : \sigma_{xx} = \sigma_{yy} = \sigma_{xy} = 0 \\
y = 0, \quad 0 < x < \infty, \quad \sigma_{xy} = 0 \\
y = 0, \quad 0 < x < a, \quad \sigma_{yy} = P(x) \\
y = 0, \quad x > a, \quad u_y = 0
\end{cases}
\tag{7.4}
$$

Combining Eqs. (7.2) ~ (7.4), we can obtain

$$\begin{cases} -\frac{2}{\pi} \int\limits_0^\infty \xi^2 A(\xi) \cos(\xi x) d\xi = P(x), & 0 < x < a \\ \int\limits_0^\infty A(\xi) \xi \cos(\xi x) d\xi = 0, & x > a \end{cases} \tag{7.5}$$

The form of Eq. (7.5) can be transformed into a dual integral equation,

$$\begin{cases} \int\limits_0^\infty \eta f(\eta) J_{-1/2}(\eta\rho) d\eta = g(\rho), & 0 < \rho < 1 \\ \int\limits_0^\infty f(\eta) J_{-1/2}(\eta\rho) d\eta = 0, & \rho > 1 \end{cases} \tag{7.6}$$

where

$$x = \rho a, \ \eta = a\xi, \cos(\xi x) = (\frac{\pi \xi x}{2})^{\frac{1}{2}} J_{-1/2}(\xi x),$$

$$g(\rho) = a P_0 \sqrt{\frac{\pi a}{2}} \sum_{k=0}^n b_k(\rho)^k \rho^{-1/2}, \ A(\xi) \xi^{3/2} = f(\xi) = f(\eta) \tag{7.7}$$

The general form of a dual integral equation can be expressed as

$$\begin{cases} \int\limits_0^\infty \eta^\alpha f(\eta) J_v(\eta\rho) d\eta = g(\rho), & 0 < \rho < 1 \\ \int\limits_0^\infty f(\eta) J_v(\eta\rho) d\eta = 0, & \rho > 1 \end{cases} \tag{7.8}$$

whose solution is given by [5] in the form of

$$f(\eta) = \frac{(2\eta)^{1-\alpha/2}}{\Gamma(\alpha/2)} \int\limits_0^1 u^{1+\alpha/2} J_{v+\alpha/2}(u\eta) du \int\limits_0^1 g(\rho u)\rho^{v+1}(1-\rho^2)^{\alpha/2-1} d\rho \tag{7.9}$$

where α and v are the power of a power function (η^α) and the order of a Bessel function (J_v) both in Eqs. (7.8) and (7.9).

It is easy to find that Eq. (7.8) can be simplified to Eq. (7.6) in the case of $\alpha = 1, v = -\frac{1}{2}$. After substituting the determined $\alpha = 1$ and $v = -\frac{1}{2}$ into Eq. (7.9), the expression of $f(\eta)$ becomes

$$f(\eta) = \sqrt{\frac{2\eta}{\pi}} \int_0^1 u^{\frac{3}{2}} J_0(u\eta) \mathrm{d}u \int_0^1 g(\rho u)\rho^{\frac{1}{2}}(1-\rho^2)^{-\frac{1}{2}} \mathrm{d}\rho \qquad (7.10)$$

If the function of $g(\rho)$ in Eq. (7.7) is substituted into Eq. (7.10), we have

$$f(\eta) = a P_0 \sqrt{a\eta} \sum_{k=0}^n b_k \int_0^1 u^{k+1} J_0(u\eta) \mathrm{d}u \int_0^1 \rho^k (1-\rho^2)^{-\frac{1}{2}} \mathrm{d}\rho \qquad (7.11)$$

According to the Tables of Integrals [3], the definite integrals of power function and algebraic function can be found in the form of

$$\int_0^a x^\alpha (a^c - x^c)^\beta \mathrm{d}x = \frac{\Gamma(\frac{\alpha+1}{c})\Gamma(\beta+1)}{n\Gamma(\frac{\alpha+1}{c}+\beta+1)} a^{\alpha+c\beta+1} \qquad (7.12)$$

where c is a nonzero positive integer, and a, α and β are nonzero real numbers.

For the function of $\int_0^1 \rho^k (1-\rho^2)^{-\frac{1}{2}} \mathrm{d}\rho$ in Eq. (7.11), it is easy to find that $a = 1$, $x = \rho$, $c = 2$, $\alpha = k$ and $\beta = -\frac{1}{2}$. Thus, Eq. (7.11) has a more simplified form of

$$f(\eta) = f(\xi) = a P_0 \frac{\sqrt{a\xi\pi}}{2} \sum_{k=0}^n b_k \frac{\Gamma(\frac{k}{2}+\frac{1}{2})}{\Gamma(\frac{k}{2}+1)} \int_0^1 u^{k+1} J_0(u\xi) \mathrm{d}u \qquad (7.13)$$

Substituting Eq. (7.13) into Eq. (7.7), we can obtain

$$A(\xi) = \xi^{-\frac{3}{2}} f(\xi) = a P_0 \frac{\sqrt{a\pi}}{2\xi} \sum_{k=0}^n b_k \frac{\Gamma(\frac{k}{2}+\frac{1}{2})}{\Gamma(\frac{k}{2}+1)} \int_0^1 u^{k+1} J_0(u\xi) \mathrm{d}u \qquad (7.14)$$

Combining Eq. (7.2) and Eq. (7.14), the induced stress and displacement fields under nonuniform fluid pressure become

$$
\begin{cases}
\sigma_{xx} = -aP_0\dfrac{\sqrt{a}}{\sqrt{\pi}}\sum_{k=0}^{n}b_k\dfrac{\Gamma(\frac{k}{2}+\frac{1}{2})}{\Gamma(\frac{k}{2}+1)}\int_{0}^{1}u^{k+1} \\[4pt]
\qquad\int_{0}^{\infty}\xi J_0(u\xi)(1-\xi y)e^{-\xi y}\cos(\xi x)\mathrm{d}\xi\,\mathrm{d}u \\[10pt]
\sigma_{yy} = -aP_0\sqrt{\dfrac{a}{\pi}}\sum_{k=0}^{n}b_k\dfrac{\Gamma(\frac{k}{2}+\frac{1}{2})}{\Gamma(\frac{k}{2}+1)}\int_{0}^{1}u^{k+1} \\[4pt]
\qquad\int_{0}^{\infty}\xi J_0(u\xi)(1+\xi y)e^{-\xi y}\cos(\xi x)\mathrm{d}\xi\,\mathrm{d}u \\[10pt]
\sigma_{xy} = -aP_0\dfrac{\sqrt{a}}{\sqrt{\pi}}\sum_{k=0}^{n}b_k\dfrac{\Gamma(\frac{k}{2}+\frac{1}{2})}{\Gamma(\frac{k}{2}+1)}\int_{0}^{1}u^{k+1}\mathrm{d}u \\[4pt]
\qquad\int_{0}^{\infty}y\xi^{2}e^{-\xi y}J_0(u\xi)\sin(\xi x)\mathrm{d}\xi \\[10pt]
u_x = -\dfrac{aP_0(1+\nu)}{E}\sqrt{\dfrac{a}{\pi}}\sum_{k=0}^{n}b_k\dfrac{\Gamma(\frac{k}{2}+\frac{1}{2})}{\Gamma(\frac{k}{2}+1)}\int_{0}^{1}u^{k+1} \\[4pt]
\qquad\int_{0}^{\infty}J_0(u\xi)[(1-2\nu)-\xi y]e^{-\xi y}\sin(\xi x)\mathrm{d}\xi\,\mathrm{d}u \\[10pt]
u_y \doteq \dfrac{aP_0(1+\nu)}{E}\sqrt{\dfrac{a}{\pi}}\sum_{k=0}^{n}b_k\dfrac{\Gamma(\frac{k}{2}+\frac{1}{2})}{\Gamma(\frac{k}{2}+1)}\int_{0}^{1}u^{k+1} \\[4pt]
\qquad\int_{0}^{\infty}J_0(u\xi)[2(1-\nu)+\xi y]e^{-\xi y}\cos(\xi x)\mathrm{d}\xi\,\mathrm{d}u
\end{cases}
\tag{7.15}
$$

The pure analytical solution of Eq. (7.15) can be derived under the premise that the integrals about u and ξ are solved and integrated in the proper order. It is easy to see that the integrals about ξ in Eq. (7.15) (hereafter called ξ-integrals) primarily consist of Bessel, trigonometric, exponential and power functions, which can be unified into two general forms: $\int_0^\infty \xi^c e^{-\xi y}J_\nu(u\xi)\sin(\xi x)\mathrm{d}\xi$ $(c=0,1,2;\ \nu=0)$ and $\int_0^\infty \xi^d e^{-\xi y}J_\nu(u\xi)\cos(\xi x)\mathrm{d}\xi$ $(d=0,1,2;\ \nu=0)$. These ξ-integrals can all be deduced based on the recursion formula of the Bessel function and integration by parts (see Appendix 1 for details).

As c, d and ν all equal 0, the solution of ξ-integrals can be obtained referring to [3],

$$\int\limits_0^\infty e^{-\xi y} J_0(u\xi) \cos(\xi x)\mathrm{d}\xi = R^{-1} \cos\frac{1}{2}\varphi$$

$$\int\limits_0^\infty e^{-\xi y} J_0(u\xi) \sin(\xi x)\mathrm{d}\xi = -R^{-1} \sin\frac{1}{2}\varphi$$

(7.16)

where R and φ, hereafter, are both functions of the location coordinates and the integral variable u and can be expressed as $R^4 = (y^2 + u^2 - x^2)^2 + 4x^2y^2$ and $\varphi = \arg(y^2 + u^2 - x^2 - 2ixy)$, respectively.

In the case of $c = d = 1$ and $v = 0$, according to [3], the following solution of ξ-integrals can be provided:

$$\begin{cases} \int\limits_0^\infty \xi e^{-\xi y} J_0(u\xi) \cos(\xi x)d\xi = R^{-3}(y\cos\frac{3}{2}\varphi - x\sin\frac{3}{2}\varphi) \\ \int\limits_0^\infty \xi e^{-\xi y} J_0(u\xi) \sin(\xi x)d\xi = -R^{-3}(x\cos\frac{3}{2}\varphi + y\sin\frac{3}{2}\varphi) \end{cases} \quad (y > 0) \quad (7.17)$$

When both c and d equal 2 and $v = 0$, ξ-integrals become

$$\begin{cases} \int\limits_0^\infty \xi^2 e^{-\xi y} J_0(u\xi) \cos(\xi x)\mathrm{d}\xi = \frac{1}{u}\left[3uR^{-5}((y^2 - x^2)\cos\frac{5}{2}\varphi \right. \\ \left. \quad - 2xy\sin\frac{5}{2}\varphi) - uR^{-3}\cos\frac{3}{2}\varphi\right] \\ \int\limits_0^\infty \xi^2 e^{-\xi y} J_0(u\xi) \sin(\xi x)\mathrm{d}\xi = \frac{1}{u}\left[3uR^{-5}((x^2 - y^2)\sin\frac{5}{2}\varphi \right. \\ \left. \quad - 2xy\cos\frac{5}{2}\varphi + uR^{-3}\sin\frac{3}{2}\varphi\right] \end{cases}$$

(7.18)

Substituting Eqs. (7.16) ~ (7.18) into Eq. (7.15) and changing the order of integration allow one to specify the relation between the stress (or displacement) vector and the variable u in terms of a single integration. Simultaneously, the variable ξ in Eq. (7.15) can be eliminated by separating the variables and solving the definite integration on ξ. The new form of Eq. (7.1) is shown as follows:

$$
\left\{
\begin{aligned}
\sigma_{xx} &= -aP_0\frac{\sqrt{a}}{\sqrt{\pi}}\sum_{k=0}^{n}b_k\frac{\Gamma(\frac{k}{2}+\frac{1}{2})}{\Gamma(\frac{k}{2}+1)}\int_0^1 u^{k+1}[R^{-3}(y\cos\frac{3}{2}\varphi - x\sin\frac{3}{2}\varphi) \\
&\quad - (3R^{-5}((y^3-x^2y)\cos\frac{5}{2}\varphi - 2xy\sin\frac{5}{2}\varphi) - yR^{-3}\cos\frac{3}{2}\varphi)]du \\
\sigma_{yy} &= -aP_0\frac{\sqrt{a}}{\sqrt{\pi}}\sum_{k=0}^{n}b_k\frac{\Gamma(\frac{k}{2}+\frac{1}{2})}{\Gamma(\frac{k}{2}+1)}\int_0^1 u^{k+1}du[R^{-3}(y\cos\frac{3}{2}\varphi - x\sin\frac{3}{2}\varphi) \\
&\quad + (3R^{-5}((y^3-x^2y)\cos\frac{5}{2}\varphi - 2xy\sin\frac{5}{2}\varphi) - yR^{-3}\cos\frac{3}{2}\varphi)] \\
\sigma_{xy} &= -aP_0\sqrt{\frac{a}{\pi}}\sum_{k=0}^{n}b_k\frac{\Gamma(\frac{k}{2}+\frac{1}{2})}{\Gamma(\frac{k}{2}+1)}\int_0^1 u^{k+1}\left[15R^{-7}((x^3y-3xy^3)\cos\frac{7}{2}\varphi\right. \\
&\quad \left. - (y^4-3x^2y^2)\sin\frac{7}{2}\varphi) + 9R^{-5}(y^2\sin\frac{5}{2}\varphi + xy\cos\frac{5}{2}\varphi)\right]du \\
u_x &= aP_0\frac{\sqrt{a}(1+v)}{E\sqrt{\pi}}\sum_{k=0}^{n}b_k\frac{\Gamma(\frac{k}{2}+\frac{1}{2})}{\Gamma(\frac{k}{2}+1)}\int_0^1 u^{k+1}[(1-2v)R^{-1}\sin(-\frac{1}{2}\varphi)du \\
&\quad - y(R^{-3}(x\cos\frac{3}{2}\varphi + y\sin\frac{3}{2}\varphi))]du \\
u_y &= aP_0\frac{\sqrt{a}(1+v)}{E\sqrt{\pi}}\sum_{k=0}^{n}b_k\frac{\Gamma(\frac{k}{2}+\frac{1}{2})}{\Gamma(\frac{k}{2}+1)}\int_0^1 u^{k+1}[2(1-v)R^{-1}\cos(\frac{1}{2}\varphi) \\
&\quad + R^{-3}(y^2\cos\frac{3}{2}\varphi - xy\sin\frac{3}{2}\varphi)]du
\end{aligned}
\right.
$$

$$(7.19)$$

Since R and φ are implicit functions about the variable u, it becomes difficult to solve the integrals about u at the interval of [0, 1]. To solve this nested integral, a numerical approximation is suggested for calculating these integrals by discretizing the integral interval of [0, 1], which can facilitate to approach the real solution as long as the computational accuracy is high enough.

7.2.2 Semianalytical Solution

The composite Simpson's rule is an approximated method for numerical integration, which can reduce errors by quadratic interpolation. Suppose that the interval of u, [0, 1] is split up into m subintervals of equal length, with m as an even number. Then, the composite Simpson's rule is given by

$$\int_0^1 f(u)\mathrm{d}u = \frac{1}{6m}\left[f(0) + 4\sum_{i=0}^{m-1} f(u_{i+1/2}) + 2\sum_{i=1}^{m-1} f(u_i) + f(1) \right] \qquad (7.20)$$

Based on Eq. (7.20), the variable u can also be removed from the integrand in Eq. (7.19). Consequently, semianalytical and seminumerical solutions (called semianalytical solutions for short) of the stress and displacement field subjected to nonuniform fluid pressure can be completely derived.

To evaluate the applicability of the solution, let us consider a computational area for $-5 \le x \le 5$ and $-5 \le y \le 5$. Notably, the values of stress for the negative x- and y- axes are sketched by symmetric transformation considering the limitation of the positive coordinate position in Eq. (7.4). Adopting a set of rock and fluid properties [4], $E' = 30$ GPa, $v = 0.25$, and $P_0 = 7$ MPa, the total length of the Griffith crack is assumed to be $l = 2a = 2$ m, the real variable b_k remains constant at 1, and the number of term n is taken as 100 for the sake of reducing the computational load and facilitating the analysis. Figure 7.3 shows the regularity of the stress distribution of a Griffith crack induced by nonuniform fluid pressure. It is clear that the value of stress increasingly approaches infinity near the crack tip, which illustrates the existence of a tip-stress singularity. Another obvious feature is that the contour marked in red dotted boxes in Fig. 7.3a, b are caused by the precision of subinterval division as well as the error ($y = 0$), which violates the limitation of Eq. (7.17). To ensure the continuity of stress contours, the values of contours at $y = 0$ are assumed to equal those at $y = 1/m$. This assumption can be valid as the number of terms m is great enough.

7.2.3   Propagation Conditions Under Nonuniform Fluid Pressure

Considering nonuniform net fluid pressure in terms of a polynomial (Eq. 7.1) to simulate the arbitrary pressure distribution inside the crack, the assumed net fluid pressure at the inlet, crack tip and other places can be expressed piecewise as

$$P(x) = \begin{cases} P_0 b_0, & x = 0 \\ P_0 \sum_{k=0}^{n} b_k (\frac{x}{a})^k, & 0 < x < a \\ P_0 \sum_{k=0}^{n} b_k, & x = a \end{cases} \qquad (7.21)$$

For the existence of stress singularity as x equals a, the near-crack-tip behavior holds the key to fracture propagation conditions according to the linear fracture mechanics (LFEM). In LFEM, the stress intensity factor (SIF) is usually adopted to describe the stress state of the crack tip, which can be expressed in terms of the Bueckner–Rice

Fig. 7.3 Stress contours of σ_{xx} (**a**), σ_{yy} (**b**) and σ_{xy} (**c**) for a Griffith crack subjected to non-uniform fluid pressure ($m = 100$)
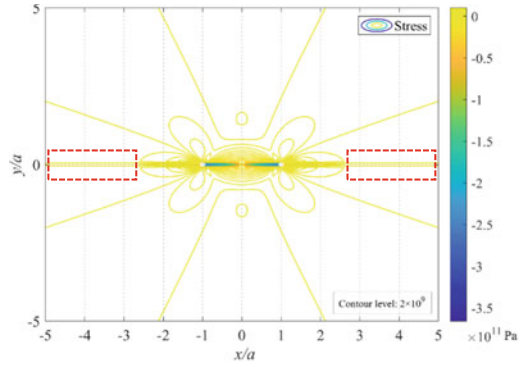
(a)
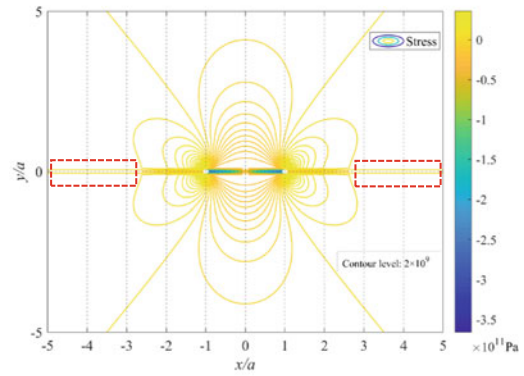
(b)

(c)

weight function [6]

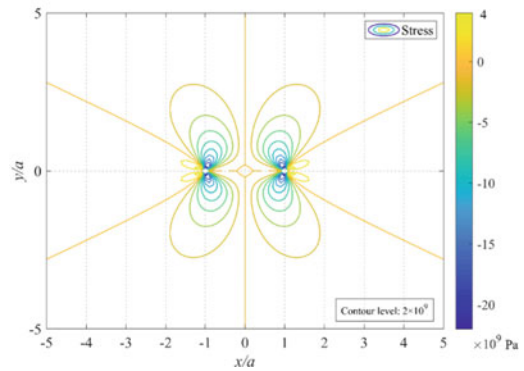$$K_I = \frac{2\sqrt{a}}{\sqrt{\pi}} \int\limits_0^a P(x) \frac{f(x/a)}{\sqrt{a^2 - x^2}} dx \qquad (7.22)$$

where f is a 'configurational' function modified by Nilson and Proffer (1984) and $f(x/a) \simeq 1$, in line with [7].

Integrating Eq. (7.22) by parts and after some simplification, we can obtain,

$$\frac{K_I}{\sqrt{\pi a}} = \int\limits_0^a F(\frac{x}{a}) \frac{dP(x)}{dx} dx + P_0 b_0 \qquad (7.23)$$

where

$$F(\frac{x}{a}) = \frac{2}{\pi} \int\limits_{x/a}^1 \frac{f(x/a)}{\sqrt{1 - (x/a)^2}} d(\frac{x}{a}) \qquad (7.24)$$

(The closed form for function $F(\xi)$ is given in Appendix 2).

In the case of a Griffith crack, [7] provided a more simplified form of Eq. (7.24)

$$F(\frac{x}{a}) = 1 - \frac{2}{\pi} \arcsin \frac{x}{a} \qquad (7.25)$$

Substituting $f(x/a) \simeq 1$ and Eq. (7.25) into Eq. (7.23), we can finally obtain

$$\frac{K_I}{\sqrt{\pi a}} = \int\limits_0^a (1 - \frac{2}{\pi} \arcsin \frac{x}{a}) \frac{dP(x)}{dx} dx + P_0 b_0 \qquad (7.26)$$

If Eq. (7.21) in the case of $x \to a$ is substituted into Eq. (7.26), the stress intensity under nonuniform fluid pressure becomes

$$K_I = P_0 \sqrt{\pi a} \sum_{k=0}^n \frac{k b_k}{a^k} \int\limits_0^a (1 - \frac{2}{\pi} \arcsin \frac{x}{a}) x^{k-1} dx + \sqrt{\pi a} P_0 b_0 \qquad (7.27)$$

Integrating Eq. (7.27) by parts and consulting the Tables of Integrals [3], we can get

$$K_I = P_0 \sqrt{a} \sum_{k=0}^n b_k \frac{\Gamma(\frac{k}{2} + \frac{1}{2})}{\Gamma(\frac{k}{2} + 1)} + \sqrt{\pi a} P_0 b_0 \qquad (7.28)$$

The stress intensity near the crack tip shows noticeable dependence on the number of polynomial terms, the crack length and the initial fluid pressure.

Based on LFEM theory, a Griffith crack starts to initiate and propagate in its favored direction when the SIF reaches its critical value, i.e., rock fracture toughness $K_I = K_{IC}^N$. Consequently, Eq. (7.28) can be expressed as

$$K_{IC}^N = P_0' \sqrt{a'} \sum_{k=0}^{n'} b_k \frac{\Gamma(\frac{k}{2} + \frac{1}{2})}{\Gamma(\frac{k}{2} + 1)} + \sqrt{\pi a'} P_0' b_0 \qquad (7.29)$$

7.3   Validation of the Semianalytical Solution

In the case of constant fluid pressure when the first item of Eq. (7.1) is considered for $n = 0$, $b_0 = 1$, [1] deduced the form of

$$A(\xi) = \xi^{-\frac{3}{2}} f(\xi) = \frac{\pi a P_0}{2} \xi^{-2} J_1(a\xi) \qquad (7.30)$$

To verify the validity of the semianalytical solution under nonuniform fluid pressure, we compare the derived stress and critical intensity factor with those under classic constant fluid pressure. All of the related parameters are selected the same as those assumed in Sect. 7.2.2.

7.3.1   Degradation from Nonuniform Pressure to Constant Pressure

In reality, the nonuniform pressure herein considered can be expressed in the form of constant pressure when the number of terms equals 0, as stated in Eq. (7.21). Nevertheless, whether it is feasible for the semianalytical solution to be degraded into the analytical solution of constant fluid pressure while simultaneously enabling reasonable accuracy still needs further verification. Consequently, we make a comparison between the two forms of the solutions by changing the number of subintervals m. The comparison aims to evaluate the approximation degree of the semianalytical solutions to the analytical solutions when the nonuniform pressure is degraded to be constant, by which the validity of the semianalytical solution is further validated.

Due to the symmetrical stress distribution of σ_{xx}, the tensile and compressive stresses on the positive y-axis are separately considered to analyze the difference, as shown in Fig. 7.4. Focusing on the same position on the line of $x = 5$ m, the semianalytical solution of stress under constant fluid pressure gradually approximates the real analytical solution with the increase in the number of subintervals m.

It seems that the discrepancy of the two solutions for both tensile stress and compressive stress can be roughly eliminated when m exceeds 30. This elimination makes it possible to supplant the analytical solution of constant pressure with the approximated semianalytical solution for unified analysis if the number of subintervals can ensure adequate calculation accuracy. In other words, the semianalytical solution is suitable for analyzing the stress induced by constant fluid pressure under the conditions in which a small reasonable error is accepted. This conclusion to some degree verifies the applicability of the semianalytical solution.

## 7.3.2   Stress Distribution

The approximate stress field induced by nonuniform fluid pressure has been analyzed in Sect. 7.2.2. Correspondingly, the stress distribution under constant fluid pressure is depicted in Fig. 7.5. Comparing Figs. 7.3 and 7.5, the induced stresses generated by constant fluid pressure and assumed nonuniform fluid pressure show similar stress distribution laws in contour shape. However, the magnitude of the stresses under the nonuniform fluid pressure is much greater than that induced by the constant fluid pressure amid the same conditions. Note that this result is concluded under the assumptions of $b_k = 1$ and $n = 100$ for the convenience of calculation. In fact, the difference will change as n and b_k vary. The influence of n will be further discussed in Sect. 4.3.

We may take the stress at $x = a$ or $y = 0.1$ as a separate example to evaluate the varying regularity of the normal and tangential stresses. On the line of $x = a$ shown in Fig. 7.6a–c, with the increase of the y coordinate, the stress variation influenced by constant pressure is nearly the same as that under nonuniform pressure. It is also of interest to find that as y tends to zero, regardless of different fluid pressure effects, σ_{xx} experiences the tension–compression stress transformation twice ($y/a = \pm 2.1$, $y = \pm 0.08$), σ_{yy} experiences it once ($y/a = \pm 0.8$), but σ_{xy} does not at all. These similarities partly illustrate the consistency of the stress distribution between constant fluid pressure and nonuniform fluid pressure.

A similarity ratio is introduced as the ratio of the stress components (σ_{xx}, σ_{yy} and σ_{xy}) under nonuniform fluid pressure to that under constant fluid pressure. As shown in Fig. 7.6d, the normal stresses (σ_{xx} and σ_{yy}) separately induced by constant pressure ($n = 0$, $b_0 = 1$) and nonuniform pressures ($n = 100$) present an obvious similarity, with average similarity ratios of 3500.57 and 3353.89 (neglecting the singular abrupt points), while the variation of the similarity ratio of tangential stress σ_{xy} mainly behaves as a fluctuation of a concave function. Moreover, two abrupt points on the curve of normal stresses are found symmetrically distributed on both sides of the crack tip ($y = 0$) in Fig. 7.6d. The emergence of these abrupt points marks the transition of tension–compression stress. For example, when a point moves from afar to $y = 0$, the normal stress σ_{xx} of this point changes from tension to compression (T $\rightarrow$ C) at $y/a = 2.1$, then returns to tension (C $\rightarrow$ T) at $y/a = 0.08$ and finally increases abruptly towards infinity at the crack tip. However, for the tangential stress
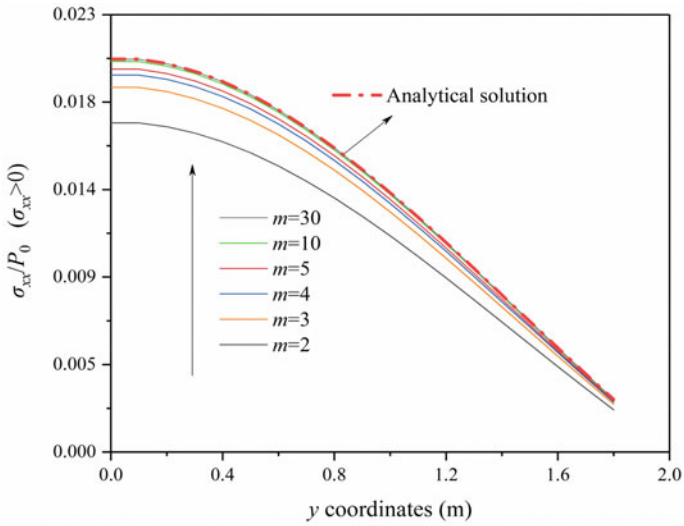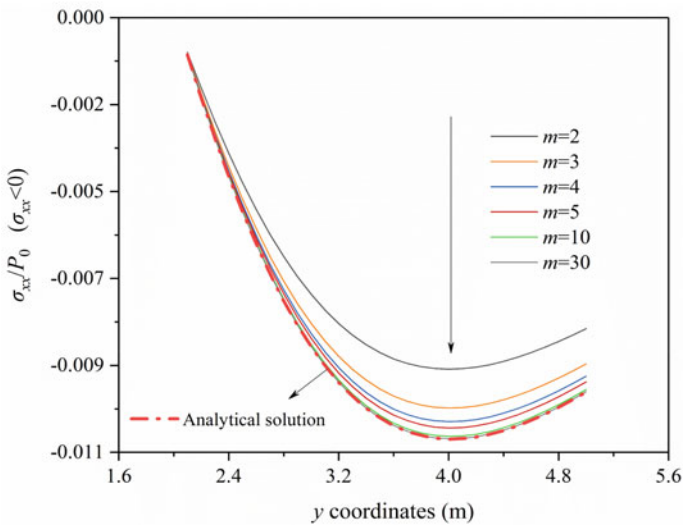
Fig. 7.4 Degradation from non-uniform pressure to constant pressure on the line of $x = 5$ m ($P_0 = 7$ MPa): **a** $\sigma_{xx} > 0$ (tension); **b** $\sigma_{xx} < 0$ (compression)

Fig. 7.5 Stress contours of
σ_{xx} (**a**), σ_{yy} (**b**) and σ_{xy}
(**c**) for a Griffith crack
subjected to constant fluid
pressure
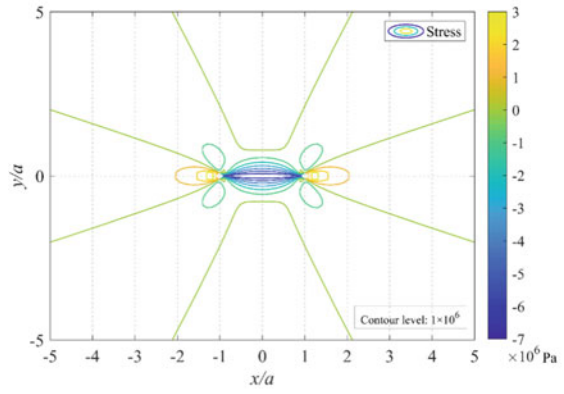
(a)
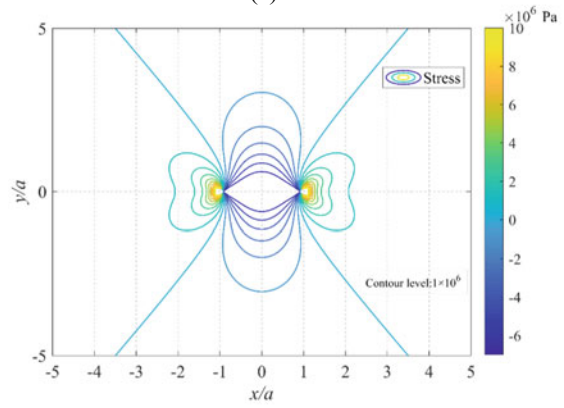
(b)
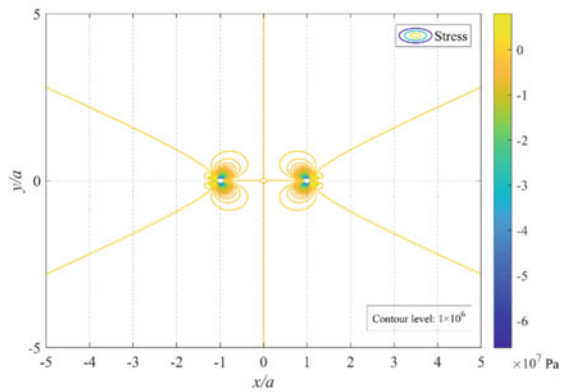
(c)

Fig. 7.6 Comparison of σ_{xx} (**a**), σ_{yy} (**b**), σ_{xy} (**c**) and similarity ratio (**d**) induced by non-uniform and constant pressure as $x = a$ (Unit: MPa)

(a)

(b)

(c)

(d)
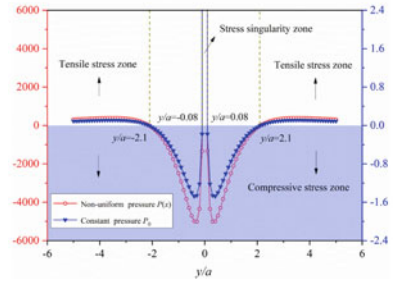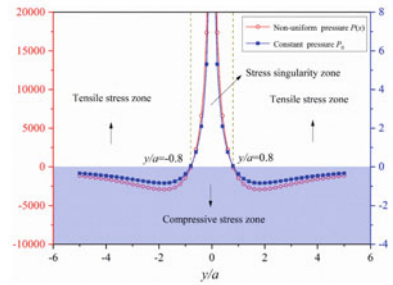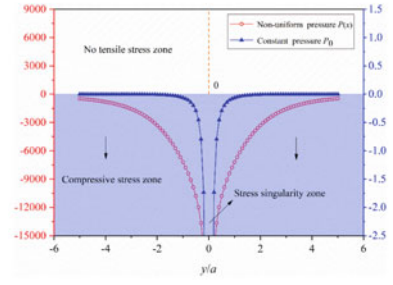
σ_{xy}, the similarity ratio remains symmetrically and uniformly distributed around the crack tip and progressively approaches infinity with the increase of the y coordin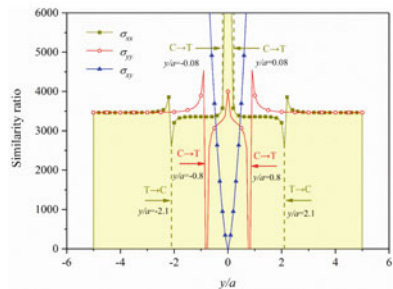ate. There is no abrupt point on the similarity curve of σ_{xy}, and correspondingly, there is no tension–compression transition, which precisely illustrates the correlation between the stress state and singularity ratio.

A similar variation of the induced stresses is found in Fig. 7.7 as y equals 0.1. The main stress discrepancy between Figs. 7.6 and 7.7 lies in the position change of the tension–compression transition point. Less influenced by tip singularity compared with $x = a$, which covers the singular point of $y = 0$ into the computational domain, the values of stress remain finite, and the tension–compression transitions all appear at the nearest point to the crack tip, $x/a = \pm 1$. Moreover, the tangential stress (σ_{xy}) starts to initially experience the tension–compression transition at $x/a = \pm 1$. These results differ from those in Fig. 7.6 and can be explained by the absence of stress singularity on the line of $y = 0.1$.

As evident from the two examples of $x = a$ and $y = 0.1$, nonuniform fluid pressure in the form of a polynomial ($n = 100$, $b_k = 1$) can produce a linear increasing effect on the normal stress, whereas a nonlinear effect is apparent on the tangential stress. This distinction implies that the stress state has a great correlation with the singularity ratio under the action of different fluid pressures and that the stress state can also be a reflection of stress singularity to a certain extent.

7.3.3   Critical Propagation Condition

The crack influenced by constant fluid pressure starts to move ahead as the magnitude of fluid pressure exceeds the critical value P_{hf}. According to [8] and [9], the SIF can be calculated using

$$K_{IC}^{C} = \sqrt{\pi a}(P_{hf} - \sigma_h) \tag{7.31}$$

Together with Eq. (7.29) which gives the expression of the critical SIF (fracture toughness) under nonuniform fluid pressure, the relationships and discrepancies of critical propagation conditions under different fluid pressures can be found by changing the parameters of $P0$, a and KIC as follows:

(i)   Regarding the same fracture geometry, rock medium and stress environment, the physical and mechanical properties of rock and in-situ stress are identical, which means that the critical propagation conditions of the crack for both constant and nonuniform pressures are the same. Thus, we can obtain

$$P_0'\sqrt{a} \sum_{k=0}^{100} b_k \frac{\Gamma(\frac{k}{2} + \frac{1}{2})}{\Gamma(\frac{k}{2} + 1)} + \sqrt{\pi a} P_0' b_0 = (P_{hf} - \sigma_h)\sqrt{\pi a} \tag{7.32}$$

Fig. 7.7 Comparison of σ_{xx}
(**a**), σ_{yy} (**b**), σ_{xy} (**c**) and
similarity ratio (**d**) induced
by non-uniform and constant
pressure as $y = 0.1$ (Unit:
MPa)

(a)

(b)

(c)

(d)
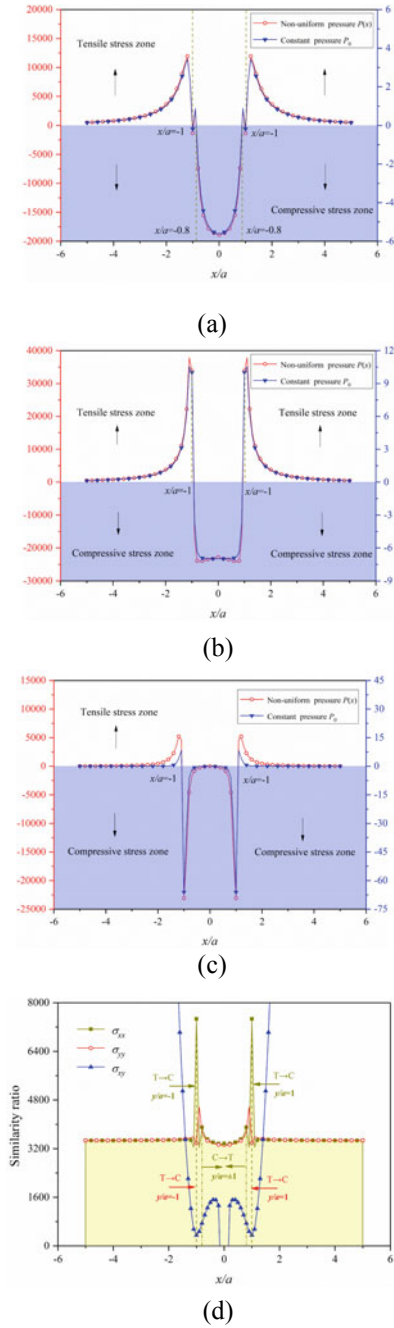
Assuming the coefficient variable and term number of the designated polynomial to be the same as before ($bk = 1$, $n = 100$), Eq. (7.32) can be simplified to

$$P_{hf} - \sigma_h = 15.401 P_0'$$ (7.33)

This expression exhibits a linear relationship between critical constant fluid pressure and critical nonuniform fluid pressure in an identical rock medium and stress environment. Additionally, the net fluid pressure under the effect of constant pressure $\left(P_{hf} - \sigma_h\right)$ is much greater than that of nonuniform fluid pressure at the injection point $\left(P_0'\right)$, which indicates that greater pump pressure is required to promote crack extension under constant fluid pressure than nonuniform fluid pressure.

(ii) In a two-dimensional horizontal plane, the magnitude of the in-situ stress is a direct reflection of the fracture geometry. Based on Eqs. (7.28) and (7.31), the relation of fracture length under different fluid pressures can be expressed by (Note that only a is changed for different fluid pressures and $bk = 1$, $n = 100$)

$$P_0'\sqrt{a^N} \sum_{k=0}^{100} b_k \frac{\Gamma(\frac{k}{2} + \frac{1}{2})}{\Gamma(\frac{k}{2} + 1)} + \sqrt{\pi a^N} P_0' b_0 = P_0'\sqrt{\pi a^C}$$ (7.34)

where aN and aC represent the critical fracture length at the beginning of fracture propagation under nonuniform and constant fluid pressure, respectively. After simplification, we obtain

$$269.112 a^N = a^C$$ (7.35)

From Eq. (7.35), it is easy to conclude that the critical fracture length, which is needed to maintain the continuous propagation of a hydraulic fracture under constant pressure, is much greater than that under nonuniform fluid pressure.

(iii) For the same initial net fluid pressure and fracture length, the SIF under different forms of critical fluid pressure can be expressed as

$$\begin{cases} K_I^C = \sqrt{a\pi}(P_{hf} - \sigma_h) = 1.772\sqrt{a} P_0 \\ K_I^N = 29.069\sqrt{a} P_0 \end{cases}$$ (7.36)

where K_I^N and K_I^C are the SIFs under critical nonuniform and constant fluid pressures, respectively.

Crack propagation occurs when the SIF reaches the critical value, rock fracture toughness KIC, i.e.,

$$K_I = K_{IC}$$ (7.37)

Considering the inequation of $K_I^N > K_I^C$, the SIF under nonuniform fluid pressure is more likely to reach or exceed the fracture toughness of rock formations than that under constant pressure.

Generally, this simplified nonuniform fluid pressure ($bk = 1$, $n = 100$) yields a higher SIF and requires lower pump pressure as well as a smaller fracture length to drive a crack forward than constant fluid pressure. Thus, it is reasonable to conclude that nonuniform fluid pressure is more likely to promote crack extension than constant pressure under this assumed form of fluid pressure ($bk = 1, n = 100$). This conclusion can be verified by field and experimental observations. For example, pulse hydraulic fracturing, which causes fluctuating variations in fluid pressure inside the hydraulic fracture, usually requires lower breakdown pressure and results in a more complicated fracture network than low-speed fluid fracturing operations [11, 12]. The fluid pressure acting on the crack's inner face is hard to remain constant in consideration of the pressure difference of fluid flow even during constant rate fracturing treatment [10]. Therefore, a nonuniform fluid pressure distribution is more realistic and applicable to reflect the crack propagation state in the field.

7.4 Parametric Sensitivity Analysis

It is notable that the semianalytical solution deduced herein is implemented for the analysis of the stress and displacement around a Griffith crack, different from the work conducted by Garagash and Detournay [13], which focused on the crack itself and the internal fluid pressure. The reliability and accuracy of this solution are determined by a series of parameters, such as the number of subintervals m, the crack length a, the initial fluid pressure P_0 and the number of terms n.

7.4.1 Reliability Analysis of the Numerical Solution (Perturbation of the Number of Subintervals m)

As mentioned above, the calculation accuracy of the derived semianalytical solution depends on the number of subintervals m in composite Simpson's rules. In theory, the greater the value of m is, the more accurate the solution becomes. However, a large m will conversely aggravate the computational load. In this regard, we tried to analyze the sensitivity of m to evaluate an appropriate value that can both ensure accuracy and reduce computational cost.

The function of Eq. (7.19) to be integrated can be uniformly expressed in the form of

$$P(k) \int_0^1 u^{k+1} F(u) \mathrm{d}u. \tag{7.38}$$

Table 7.1 Value of σ_{xx} for different numbers of subintervals m

$(x, y) = (a, 5)$		$(x, y) = (a, 0.1)$	
m_i	σ_{xx} (MPa)	m_i	σ_{xx} (MPa)
100	**309**.159876	100	$-$**1292**.262680
500	**309**.185738	500	$-$**1287**.527011
1000	**309**.198441	1000	$-$**1285**.296700
2000	**309.201**990	2000	$-$**1284**.002504
5000	**309.208**494	5000	$-$**1283**.578436
8000	**309.208**522	8000	-**1283**.241820

Thus, we may take Eq. (7.19) as an example (here we choose σ_{xx}) to elaborate the solution reliability resulted by m.

The difference of σ_{xx} under adjacent m must be below a certain small numerical tolerance, i.e., convergence is considered to be achieved if the following conditions are fulfilled:

$$\left| \sigma_{xx}^{m_{i+1}} - \sigma_{xx}^{m_i} \right| < \varepsilon \qquad (7.39)$$

where ε is the small numerical tolerance convergence, which can be $\leq 0.1\%$ according to [14].

When m increases from 100 to 8000 in Table 7.1, 6 significant figures (shown in bold) in the value of σ_{xx} are observed at $(a, 5)$, while only 4 significant figures are found at $(a, 0.1)$. This difference means that the convergence rate of the solution decreases at a closer distance to the crack tip, which can be ascribed to the influence of the tip-stress singularity. In other words, the results of this semianalytical solution can be reliable outside the zone of tip-stress singularity and are suitable for the calculation of the induced fields. However, the specific range of this singular zone still needs further study.

7.4.2   Sensitivity Analysis of the Initial Fluid Pressure P_0 and Crack Length a

Both P_0 and a are assumed to be initially constant in the calculation process of nonuniform fluid pressure. By means of the control variable method, we can analyze the sensitivity of the two parameters. Specifically, 3 groups of crack lengths ($a = 1$, 5 and 10 m) are initially considered, and P_0 was successively set to 7, 14, 21 and 28 MPa.

Figure 7.8a, b shows the distribution of σ_{xx} on the lines $x = a$ and $y = 0.1$ under different crack lengths. Obviously, the larger crack length value indicates the greater magnitude of σ_{xx} for the same position. The varying crack length will not change the tension and compression stress range divided by x coordinates, which implies that

an increase in crack length will result in a change in the stress value. To analyze the stress value variations at the same position, we extract three points on the line of $x = a$ ($y = 5$, 2.5 and 0.1 m). Another two cases of $a = 15$ m and $a = 20$ m are considered for better regularities of the curves. As shown in Fig. 7.8c, the values of σ_{xx} at the selected locations all exhibit increasing trends when the crack length changes from 1 to 20 m. So, the crack length has a nonlinear on the stress variation.

In addition, the distribution of σ_{xx} induced by nonuniform fluid pressure under different initial fluid pressures is depicted in Fig. 7.9. A similar increase of σ_{xx} is also found with the increase of P_0 in Fig. 7.9a, b. However, as shown in Fig. 7.9c, the stress value pressure exhibits linear growth with the increase of initial fluid P_0. As P_0 is changed from 7 MPa to 14, 21 and 28 MPa, the value of σ_{xx} at the point of (a, -0.1) will be accordingly expanded to 2, 3 and 4 times as much as its initial value ($P_0 = 7$ MPa). Similar outcomes can also be found at other positions on the line $x = a$, which means that a linear increment in the initial fluid pressure P_0 will lead to the same magnitude of stress increasing at different locations.

Based on Eq. (7.29), the critical intensity factor K_{IC}^N for a crack to propagate under nonuniform fluid pressure is a function of P_0 and a. If the number of terms n and the coefficient variable b_k are considered to remain invariable as before ($n = 100$, $b_k = 1$), the sensitivity of P_0 and a can be separately evaluated in Fig. 7.10. Similar to the variation of the stress value, the initial fluid pressure P_0 is linearly related to the critical intensity factor, while the crack length poses a nonlinear effect of a power function with a power of 1/2 on the critical propagation condition.

In summary, the varying initial fluid pressure P_0 shows a linear correlation with the stress value and the critical intensity factor. Meanwhile, with the increase of the crack length a, the magnitude of the induced stress near a Griffith crack and the critical intensity factor present a nonlinear increase, and the increase rate also increases.

### *7.4.3 Perturbation Analysis of the Number of Terms n*

In terms of fluid with power-law (non-Newtonian) rheology, the number of terms n in Eq. (7.1) represents the distribution form of fluid pressure inside the Griffith crack, which may fluctuate the surrounding stress state of certain locations. To explore the perturbation effect of different n, a series of numbers of terms ($n = 0, 1, 2, 3, 4, 5$) were considered when analyzing the variation of σ_{xx} on the line $x = 5$ m ($a = 1$ m). It is also important to mention that the number of subintervals m is chosen to be 1000 in consideration of the calculation accuracy.

As Fig. 7.11 shows, an equal increase in the number of terms n results in an incremental increase in stress value according to the peak line of σ_{xx} (the rate of increase becomes greater and greater). The demarcation between the compressive and tensile stress zones remains stable despite the varying number of terms n. It can be inferred that fluid with power-law rheology may merely influence the magnitude of the stress value instead of the form of stress distribution around the crack. Additionally, as a

Fig. 7.8 Distribution of σ_{xx} on the lines of $x = a$ (**a**) and $y = 0.1$ m (**b**) as well as the variation of stress value (**c**) under different crack lengths a
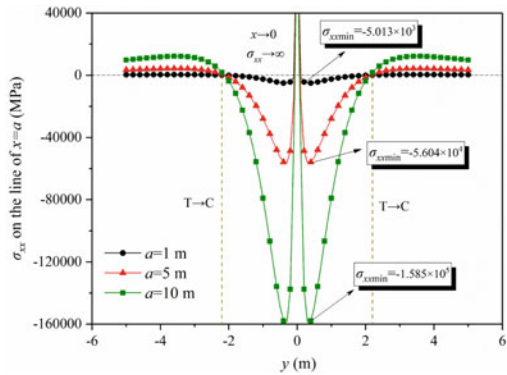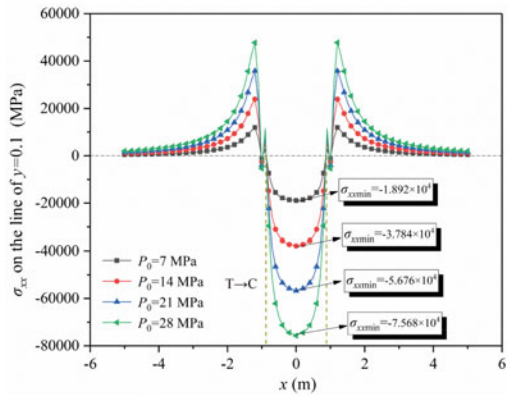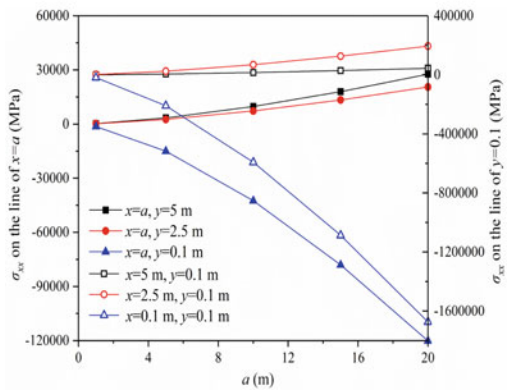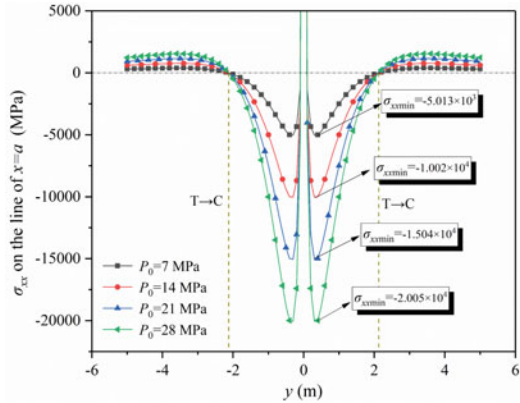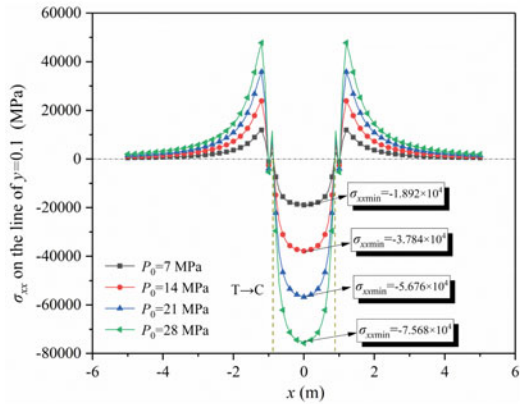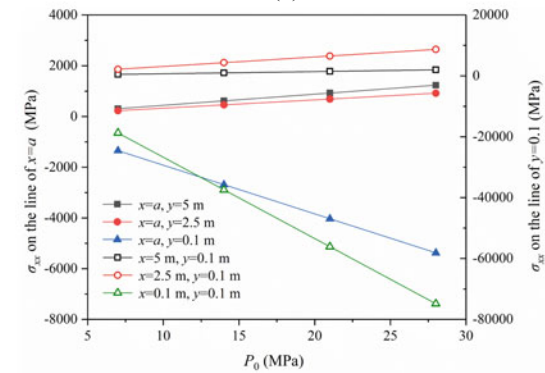
Fig. 7.9 Distribution of σ_{xx} on the lines of $x = a$ (**a**) and $y = 0.1$ m (**b**) as well as the variation of stress value (**c**) under different initial fluid pressures P_0
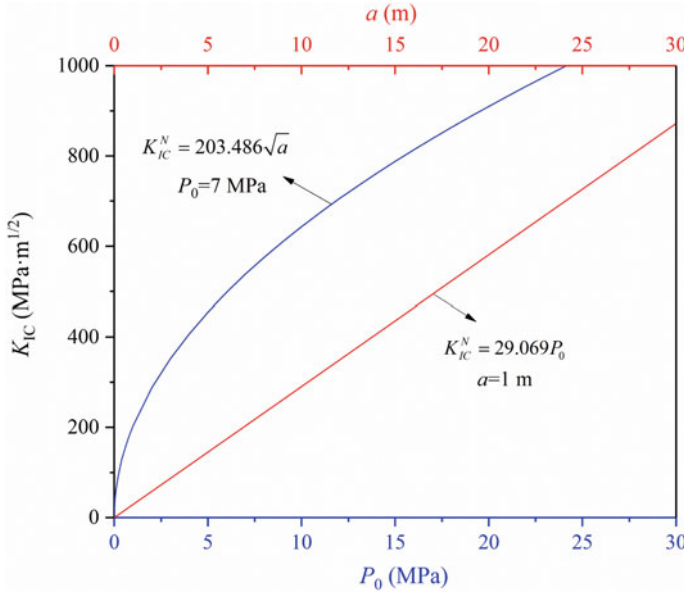

(a)

(b)

(c)

Fig. 7.10 Curves of critical stress intensity factor versus the crack length a and the initial fluid pressure P_0

point at line $x = 5$ m moves from $y = -5$ m to $y = 0$, the stress in the x-axial direction (σ_{xx}) decreases gradually and then increases until to the peak value. Symmetrical law is also observed on the positive y-axis. It seems that the closer a point is to $y = 0$, the greater the σ_{xx} becomes, which exactly reveals the effect of stress singularity near the crack tip.

The continuing crack propagation ($K_I \geq K_{IC}$) or arrest ($K_I < K_{IC}$) partly depends on the changing number of terms n. For the convenience of calculation, b_k is assumed to be the same as that in Sect. 7.2.2. According to Eq. (7.29), we can derive a dimensionless form of the critical intensity factor κ:

$$\kappa = \frac{K_{IC}^N}{P_0 \sqrt{\pi a}} = \frac{1}{\sqrt{\pi}} \sum_{k=0}^{n'} \frac{\Gamma(\frac{k}{2} + \frac{1}{2})}{\Gamma(\frac{k}{2} + 1)} + 1 \tag{7.40}$$

Figure 7.12 illustrates the relationship between the dimensionless critical intensity factor and the number of terms n. As n increases from 0 to 300, the dimensionless critical intensity factor exhibits an increasing trend, while its increase rate decreases gradually from 0.636 and tends to be constant at 0.051. Therefore, the accumulated number of terms of the polynomial form of fluid pressure ultimately possesses a linear effect on the critical propagation as n exceeds 200. The crack propagation behavior is related to the compound effect of injection fluid pressure and in-situ stress. Assuming b_k equals 1 is too simplified to reflect realistic and practical hydraulic fracturing.
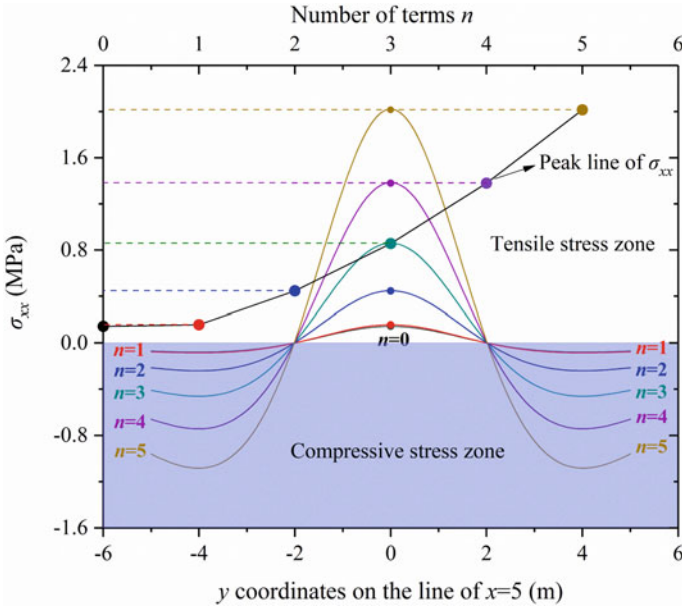
Fig. 7.11 Distribution of σ_{xx} on the line $x = 5$ m under different the number of terms n

Nonetheless, analyzing the variation of n can still help evaluate the perturbation of the fluid pressure form on the crack propagation conditions.

A mechanical model of a Griffith crack nonuniformly pressurized by interval fluid in a linear elastic and homogeneous plane is formulated. The initial state involving stress and displacement around the crack and the critical propagation condition of the crack are studied in detail. Based on Fourier transformation and the composite Simpson's rule, a semianalytical solution for a crack under nonuniform fluid pressure is obtained as a function of two numbers: the number of subintervals (m) and the number of terms (n).

$$\kappa = \frac{1}{\sqrt{\pi}} \sum_{k=0}^{n^*} \frac{\Gamma(\frac{k}{2} + \frac{1}{2})}{\Gamma(\frac{k}{2} + 1)} + 1$$

$\Delta\kappa/\Delta n = 0.051$

$n \geq 200$

$\Delta\kappa/\Delta n = 0.636$
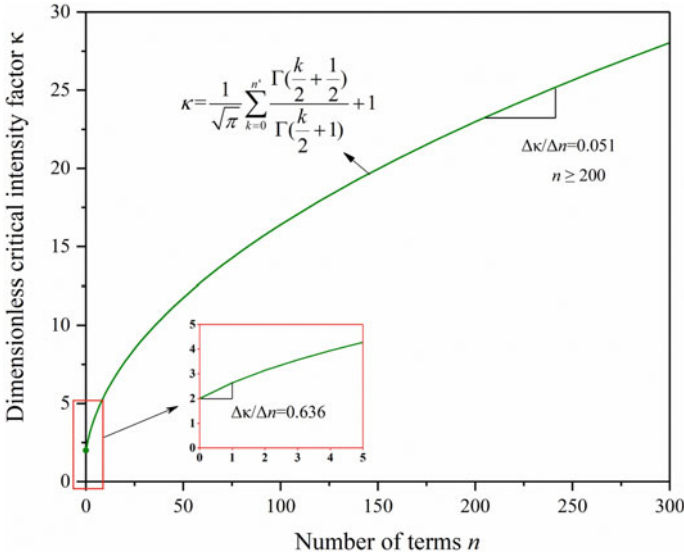
Fig. 7.12 Curves of dimensionless critical SIF κ versus the number of terms n

Appendix 1. ξ-Integrals Function

A pair of general form functions composed of Bessel, trigonometric, exponential and power functions (ξ-integrals) can be expressed as

$$\begin{cases} \int\limits_0^\infty \xi^d e^{-\xi y} J_v(u\xi) \cos(\xi x)\mathrm{d}\xi \\ \int\limits_0^\infty \xi^c e^{-\xi y} J_v(u\xi) \sin(\xi x)\mathrm{d}\xi \end{cases} \qquad (c = d = v, v+1, v+2, \ldots) \qquad (7.41)$$

where c, d and v are integers ranging from zero to infinity.

Gradshteyn and Ryzhik [3] also provided the following solution of ξ-integrals when c and d both equal $v + 1$:

$$
\begin{cases}
\displaystyle\int_0^\infty \xi^{v+1}e^{-\xi y}J_v(u\xi)\cos(\xi x)d\xi = \frac{2(2u)^v}{\sqrt{\pi}}\Gamma(v+\frac{3}{2})R^{-2v-3}[y\cos(v+\frac{3}{2})\varphi \\
\hspace{6cm} -x\sin(v+\frac{3}{2})\varphi] \\[4mm]
\displaystyle\int_0^\infty \xi^{v+1}e^{-\xi y}J_v(u\xi)\sin(\xi x)d\xi = -\frac{2(2u)^v}{\sqrt{\pi}}\Gamma(v+\frac{3}{2})R^{-2v-3}[x\cos(v+\frac{3}{2})\varphi \\
\hspace{6cm} +y\sin(v+\frac{3}{2})\varphi]
\end{cases}
$$

$$(y>0, v>-\frac{3}{2}) \hspace{6cm} (7.42)$$

A recursion formula of the Bessel function is given by

$$(x^v J_v(ax))' = a\cdot x^v J_{v-1}(ax) \hspace{4cm} (7.43)$$

Making v in Eq. (7.43) equal to $w+1$ (w is an integer greater than or equal to 0) and substituting this equation into the ξ-integrals, we obtain

$$\int_0^\infty \xi^{w+1}e^{-\xi y}J_w(u\xi)\cos(\xi x)d\xi = \frac{1}{u}\int_0^\infty (\xi^{w+1}J_{w+1}(u\xi))'e^{-\xi y}\cos(\xi x)d\xi$$

$$\int_0^\infty \xi^{w+1}e^{-\xi y}J_w(u\xi)\sin(\xi x)d\xi = \frac{1}{u}\int_0^\infty (\xi^{w+1}J_{w+1}(u\xi))'e^{-\xi y}\sin(\xi x)d\xi \hspace{1cm} (7.44)$$

Using integration by parts, Eq. (7.44) can be expressed as

$$\int_0^\infty \xi^{w+1}e^{-\xi y}J_w(u\xi)\cos(\xi x)d\xi = \frac{1}{u}[\xi^{w+1}J_{w+1}(u\xi)e^{-\xi y}\cos(\xi x)|_0^\infty$$

$$-\int_0^\infty \xi^{w+1}J_{w+1}(u\xi)(e^{-\xi y}\cos(\xi x))'d\xi]$$

$$\int_0^\infty \xi^{w+1}e^{-\xi y}J_w(u\xi)\sin(\xi x)d\xi = \frac{1}{u}[\xi^{w+1}J_{w+1}(u\xi)e^{-\xi y}\sin(\xi x)|_0^\infty$$

$$-\int_0^\infty \xi^{w+1}J_{w+1}(u\xi)(e^{-\xi y}\sin(\xi x))'d\xi] \hspace{1cm} (7.45)$$

After simplification, Eq. (7.45) becomes

$$\int_0^\infty \xi^{w+1} e^{-\xi y} J_w(u\xi)\cos(\xi x)d\xi = \frac{x}{u}\int_0^\infty \xi^{w+1} J_{w+1}(u\xi)e^{-\xi y}\sin(\xi x)d\xi$$

$$+ \frac{y}{u}\int_0^\infty \xi^{w+1} J_{w+1}(u\xi)e^{-\xi y}\cos(\xi x)d\xi$$

$$= \frac{x}{u}Y + \frac{y}{u}X = M_1$$

$$\int_0^\infty \xi^{w+1} e^{-\xi y} J_w(u\xi)\sin(\xi x)d\xi = -\frac{x}{u}\int_0^\infty \xi^{w+1} J_{w+1}(u\xi)e^{-\xi y}\cos(\xi x)d\xi$$

$$+ \frac{y}{u}\int_0^\infty \xi^{w+1} J_{w+1}(u\xi)e^{-\xi y}\sin(\xi x)d\xi$$

$$-\frac{x}{u}X + \frac{y}{u}Y = M_2 \tag{7.46}$$

In Eq. (7.46), two binary linear equations of $\int_0^\infty \xi^{w+1} e^{-\xi y} J_{w+1}(u\xi)\cos(\xi x)d\xi$ (X) and $\int_0^\infty \xi^{w+1} e^{-\xi y} J_{w+1}(u\xi)\sin(\xi x)d\xi$ (Y) can be solved using M_1 and M_2 derived by Eq. (7.42). Notably, these deductions, held as variables of c, d, v and w, are all integers ranging from zero to infinity. Thus, it is appropriate to replace variable w with v in X and Y for the sake of consistent expression with Eq. (7.45). Thus, the unknown functions X and Y are separately expressed as

$$\begin{cases} X = \int_0^\infty \xi^{v+1} J_{v+1}(u\xi)e^{-\xi y}\cos(\xi x)d\xi = \frac{(2u)^{v+1}}{\sqrt{\pi}}\Gamma(v+\frac{3}{2})R^{-2v-3}\cos(v+\frac{3}{2})\varphi \\[4mm] Y = \int_0^\infty \xi^{v+1} J_{v+1}(u\xi)e^{-\xi y}\sin(\xi x)d\xi = -\frac{(2u)^{v+1}}{\sqrt{\pi}}\Gamma(v+\frac{3}{2})R^{-2v-3}\sin(v+\frac{3}{2})\varphi \end{cases} \tag{7.47}$$

In the case of $c = d = v+2$, using the recurrence relation of Eq. (7.43), we can obtain

$$(x^{v+2} J_{v+1}(ax))' = a \cdot x^{v+2} J_v(ax) + x^{v+1} J_{v+1}(ax) \tag{7.48}$$

Then, this relation reduces to

$$x^{v+2} J_v(ax) = \frac{1}{a} \cdot [(x^{v+2} J_{v+1}(ax))' - x^{v+1} J_{v+1}(ax)] \tag{7.49}$$

Substituting Eq. (7.49) into ξ-integrals, we can obtain

$$\int_0^\infty \xi^{v+2} e^{-\xi y} J_v(u\xi) \cos(\xi x) \mathrm{d}\xi = \frac{1}{u} \int_0^\infty [(\xi^{v+2} J_{v+1}(u\xi))'$$

$$- x^{v+1} J_{v+1}(ux)] e^{-\xi y} \cos(\xi x) \mathrm{d}\xi$$

$$\int_0^\infty \xi^{v+2} e^{-\xi y} J_v(u\xi) \sin(\xi x) \mathrm{d}\xi = \frac{1}{u} \int_0^\infty [(\xi^{v+2} J_{v+1}(u\xi))'$$

$$- x^{v+1} J_{v+1}(ux)] e^{-\xi y} \sin(\xi x) \mathrm{d}\xi \qquad (7.50)$$

Based on integration by parts, Eq. (7.50) can be further simplified to

$$\int_0^\infty \xi^{v+2} e^{-\xi y} J_v(u\xi) \cos(\xi x) \mathrm{d}\xi = \frac{x}{u} \int_0^\infty \xi^{v+2} J_{v+1}(u\xi) e^{-\xi y} \sin(\xi x) \mathrm{d}\xi$$

$$+ \frac{y}{u} \int_0^\infty \xi^{v+2} J_{v+1}(u\xi) e^{-\xi y} \cos(\xi x) \mathrm{d}\xi$$

$$- \frac{1}{u} \int_0^\infty x^{v+1} J_{v+1}(ux) e^{-\xi y} \cos(\xi x) \mathrm{d}\xi$$

$$\int_0^\infty \xi^{v+2} e^{-\xi y} J_v(u\xi) \sin(\xi x) \mathrm{d}\xi = -\frac{x}{u} \int_0^\infty \xi^{v+2} J_{v+1}(u\xi) e^{-\xi y} \cos(\xi x) \mathrm{d}\xi$$

$$+ \frac{y}{u} \int_0^\infty \xi^{v+2} J_{v+1}(u\xi) e^{-\xi y} \sin(\xi x) \mathrm{d}\xi$$

$$- \frac{1}{u} \int_0^\infty x^{v+1} J_{v+1}(ux) e^{-\xi y} \sin(\xi x) \mathrm{d}\xi \qquad (7.51)$$

When v in Eq. (7.42) equals $v + 1$, it is easy to derive

$$\int_0^\infty \xi^{v+2} e^{-\xi y} J_{v+1}(u\xi) \cos(\xi x) \mathrm{d}\xi = \frac{2(2u)^{v+1}}{\sqrt{\pi}} \Gamma(v + \frac{5}{2}) R^{-2v-5} [y \cos(v + \frac{5}{2})\varphi$$

$$- x \sin(v + \frac{5}{2})\varphi]$$

$$\int_0^\infty \xi^{v+2} e^{-\xi y} J_{v+1}(u\xi) \sin(\xi x) \mathrm{d}\xi = -\frac{2(2u)^{v+1}}{\sqrt{\pi}} \Gamma(v + \frac{5}{2}) R^{-2v-5} [x \cos(v + \frac{5}{2})\varphi$$

$$+ y \sin(v + \frac{5}{2})\varphi] \tag{7.52}$$

Substituting Eqs. (7.47) and (7.52) into Eq. (7.51), ξ-integrals in the case of $c = d = v + 2$ are solved:

$$\begin{cases} \int\limits_0^\infty \xi^{v+2} e^{-\xi y} J_v(u\xi) \cos(\xi x) \mathrm{d}\xi = \frac{1}{u} \begin{bmatrix} \frac{2(2u)^{v+1}}{\sqrt{\pi}} \Gamma(v + \frac{5}{2}) R^{-2v-5}((y^2 - x^2) \\ \cos(v + \frac{5}{2})\varphi - 2xy \sin(v + \frac{5}{2})\varphi) \\ - \frac{(2a)^{v+1}}{\sqrt{\pi}} \Gamma(v + \frac{3}{2}) R^{-2v-3} \cos(v + \frac{3}{2})\varphi \end{bmatrix} \\ \int\limits_0^\infty \xi^{v+2} e^{-\xi y} J_v(u\xi) \sin(\xi x) \mathrm{d}\xi = \frac{1}{u} \begin{bmatrix} \frac{2(2u)^{v+1}}{\sqrt{\pi}} \Gamma(v + \frac{5}{2}) R^{-2v-5}((x^2 - y^2) \\ \sin(v + \frac{5}{2})\varphi - 2xy \cos(v + \frac{5}{2})\varphi) \\ + \frac{(2a)^{v+1}}{\sqrt{\pi}} \Gamma(v + \frac{3}{2}) R^{-2v-3} \sin(v + \frac{3}{2})\varphi \end{bmatrix} \end{cases} \tag{7.53}$$

Appendix 2. Closed—Form of $F(\xi)$

The function $F(\xi)$ in Eq. (7.24) can be expressed as

$$F(\xi) = \frac{2}{\pi} \int\limits_\xi^1 \frac{f(\xi)}{\sqrt{1 - \xi^2}} d\xi$$

$$= F_0 - \frac{2}{\pi}(\chi \arcsin \xi - (\chi - 1)\frac{\xi^{\alpha+1}}{\alpha + 1} {}_2F_1(\frac{\alpha + 1}{2}, \frac{1}{2}; \frac{\alpha + 3}{2}; \xi^2)) \tag{7.54}$$

where ${}_2F_1$ is a hypergeometric function.

References

1. Sneddon IN, Elliot HA (1946) The opening of a Griffith crack under internal pressure. Q Appl Math 4(3):262–267. https://doi.org/10.1090/qam/17161
2. Sneddon IN, Lowengrub M (1969) Crack problems in the classical theory of elasticity. Wiley, New York
3. Gradshteyn IS, Ryzhik IM (2007) Table of integrals, series and products. Academic Press, Boston
4. Cerasi P, Ladva HK, Bradbury AJ et al (2001) Measurement of the mechanical properties of filtercakes. In: Proceedings of the SPE European formation damage conference, The Hague, The Netherlands
5. Titchmarsh EC (1937) Introduction to the theory of Fourier intergals. Oxford University Press, Oxford
6. Rice JR (1968) Mathematical analysis in the mechanics of fracture. In: Liebowitz H (ed) Fracture, an advanced treatise, vol II. Academic Press, New York, pp 191–311

7. Garagash DI, Sarvaramini E (2012) Equilibrium of a pressurized plastic fluid in a wellbore crack. Int J Solids Struct 49(1):197–212. https://doi.org/10.1016/j.ijsolstr.2011.09.022

8. Hubbert M, Willis D (1957) Mechanics of hydraulic fracturing. Trans Soc Petrol Eng AIME 210:153–168

9. Yao, Y, Wang W, Keer LM (2017) An energy based analytical method to predict the influence of natural fractures on hydraulic fracture propagation. Eng Fracture Mech. https://doi.org/10.1016/j.engfracmech.2017.11.02

10. Lai J, Ioannides E, Wang J (2009) Fluid-crack interaction in lubricated rolling-sliding contact. In: Proceedings of the Stle/Asme international joint tribology conference 2008, 437–439. https://doi.org/10.1115/IJTC2008-71254

11. Jizhao X, Cheng Z, Lei Q (2017) Mechanism and application of pulse hydraulic fracturing in improving drainage of coalbed methane. J Natl Gas Sci Eng 40:79–90. https://doi.org/10.1016/j.jngse.2017.02.012

12. Wang C, Pan L, Zhao Y et al (2019) Analysis of the pressure-pulse propagation in rock: a new approach to simultaneously determine permeability, porosity, and adsorption capacity. Rock Mech Rock Eng. https://doi.org/10.1007/s00603-019-01874-w

13. Garagash DI, Detournay E (2002) Viscosity-dominated regime of a fluid-driven fracture in an elastic medium. In: Symposium on analytical and computational fracture mechanics of non-homogeneous materials, IUTAM pp 25–29. https://doi.org/10.1007/978-94-017-0081-8

14. Adachi JI (2001) Fluid-driven fracture in permeable rock. Ph.D. thesis, Minneapolis University of Minnesota

15. Zhou J, Chen M, Jin Y, Zhang GQ (2008) Analysis of fracture propagation behavior and fracture geometry using tri-axial fracturing system in naturally fractured reservoirs. Int J Rock Mech Mining Sci Geo-Mech Abstracts 45:1143–1152

Chapter 8
Fracture Interaction Behaviors

8.1 Introduction

Problems arising from hydraulic fracturing involve the nonlinear coupling of rock deformation and fluid flow, the nonlocal character of the fracture elastic response, the time dependence of fracture propagation and the interacting interference between the pre-existing and induced fractures. These problems will result in the offsetting of the fracture path and leak-off of fracturing fluid and then complicate the analysis of hydraulic fracturing [10]. Whereas the economic production from these reservoirs tends to depend on the efficiency of hydraulic fracturing stimulation treatment [26]. So fully modeling hydraulic fracturing is necessary and significant in optimizing the fracturing parameters and stimulating reservoir production.

Early research efforts concentrated on modeling the propagation of single planar hydraulic fracture (HF) in linear elastic, impermeable and homogeneous rock. As the horizontal in-situ stress in the overlying and underlying layers is much larger than that in the reservoir layer, the growth of HF height is expected to decline and ultimately stop, and therefore the phenomenon of constant fracture height appears [20, 30]. When the fracture length is sufficiently small compared to the fracture height, this hydraulic fracturing problem can be theoretically simplified to a plane-strain model, well-known as KGD and PKN models [11, 13, 18]. These models typically rely on the simplification of the fracturing problem either with respect to the fracture width profile or the fluid pressure distribution. However, the simple HF geometric assumption of a straight and bi-wing planar feature is untenable because of the pre-existing geological discontinuities including fissures, veins, joints, faults and bedding planes (assumed to be a natural fracture with a frictional interface and thereafter called NF) in naturally fractured formations [28]. The HF will inevitably intersect with multiple NFs and therefore result in complicated fracture networks [14]. Plenty of microseismic measurements and field observations [17, 9, 24] also suggest that the creation of complicated fracture networks is a common occurrence during the process of hydraulic fracturing treatments.
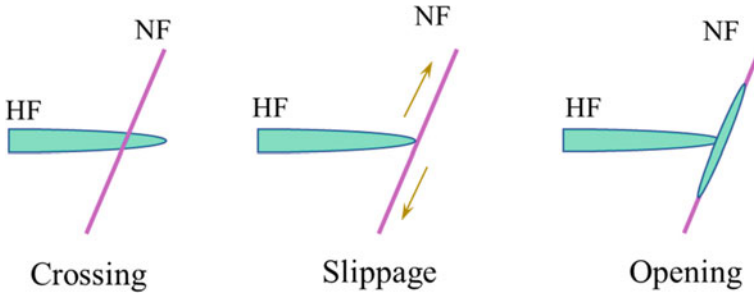
Fig. 8.1 Intersection modes between an HF and an NF [12]

Based on experiment and field analysis [4, 12, 33], three intersection modes (crossing, opening and slippage) were mainly observed when the HF propagated in naturally fractured formations as sketched in Fig. 8.1. The case of "Crossing", "Opening" and "Slippage" means that the HF crosses the NF, the NF slips upon contact with HF, and the HF propagates along the dilated NF, respectively. The occurrence of each intersection behavior depends on the stress conditions and material mechanic properties to a large extent [22]. In reality, the minimum horizontal stress contrast defines the lower limit for the propagation capacity of the HF where the pressure for initiating a fracture needs to exceed the sum of the minimum horizontal stress and the rock tensile strength.

In this chapter, the goal is to predict the intersection behaviors (including crossing, slippage and opening) between the HF and the NF based on known parametric conditions and assumed geometric models. We pay attention to presenting a composite criterion to predict subsequent behaviors based on stress conditions before the HF comes into contact with the NF. This criterion is validated by comparing the predicted results with previously published experimental observations and intersection criteria. Furthermore, this new criterion includes the sensitivity of the HF approaching distance missed in previous intersection models, with which the new criterion is discussed in detail.

8.2 Intersection Model Between Hydraulic Fracture and Natural Fracture

As shown in Fig. 8.2a, a plane-strain model is developed considering a finite-length HF uniformly pressurized by internal fluid which is approaching an unbounded frictional NF (red rough line) at an arbitrary angle β. The internal fluid inside the HF is incompressible and inviscid. The initial stress field equals the far-field in-situ stress components σ_H and σ_h which are parallel and perpendicular to the HF in the Oxy reference plane, respectively. The yellow arrow denotes the injection location and

injection rate Q_0. For convenience, a local coordinate system (O' βx βy) is established on the NF, where the βx axis is codirected with the NF in the direction of the approaching HF and intersects the βx axis at the NF midpoint (Fig. 8.2a).

During an HF approaching an NF, the stress components acting on the NF are influenced by the co-action of the fluid flow within the HF on both sides of the injection point and the far field in-situ stress. As the HF extends and moves closer to the NF, the stresses on NF increase and become closer to the critical failure thresholds (rock tensile strength or NF cohesion strength). Assuming a limit state where HF is infinitely close to but not in contact with the NF (Fig. 8.2b), the existing stress singularity near the HF tip will greatly influence the stress distribution on the NF, and certain points on the NF may have reached or even exceeded the critical failure limit. The possible behaviors of crossing, slippage and opening between the HF and the NF are assumed mutually independent. The mixed behaviors of opening after crossing and crossing after slippage are not considered.

8.2.1 Solution of Net Pressure Inside the Toughness-Dominated HF

Since the fracturing fluid is assumed to have zero viscidity, the propagation of HF can be identified be in the toughness-dominated regime [7]. The half-length of the HF is designated $l(t)$, the HF width is $w(x, t)$, P_{net} denotes the net pressure within the HF which only depends on the x coordinate (with origin at the injection point, O), and the fluid injection time is t.

According to [7], the unified form of theoretical solution to a single fracture is defined in a dimensionless form:

$$l(t) = L(t) \cdot \gamma[\rho(t)]$$
$$w(x, t) = \varepsilon(t) \cdot L(t) \cdot \Omega(\xi, t)$$
$$P_{net}(x, t) = \varepsilon(t) \cdot E' \cdot \Pi(\xi, t) \tag{8.1}$$

where $\xi = x/l(t)$ ($0 \leq \xi \leq 1$) refers to the scaled position which defines a moving system of coordinates (with respect to the fixed system of coordinates x); $\varepsilon(t)$ denotes a small dimensionless parameter that guarantees the variation range of Ω and Π from zero to infinity; L represents the length scale; γ, Ω, and Π are the dimensionless fracture half-length, opening and net pressure, respectively; and $\rho(t)$ is the dimensionless evolution parameter.

Based on the scaling of Eq. (8.1), the elasticity equation can be expressed as

$$\Omega = -\frac{4\gamma}{\pi} \int_0^1 \ln \left| \frac{\sqrt{1-\xi^2} + \sqrt{1-s^2}}{\sqrt{1-\xi^2} - \sqrt{1-s^2}} \right| \Pi(s, t) \mathrm{d}s \tag{8.2}$$
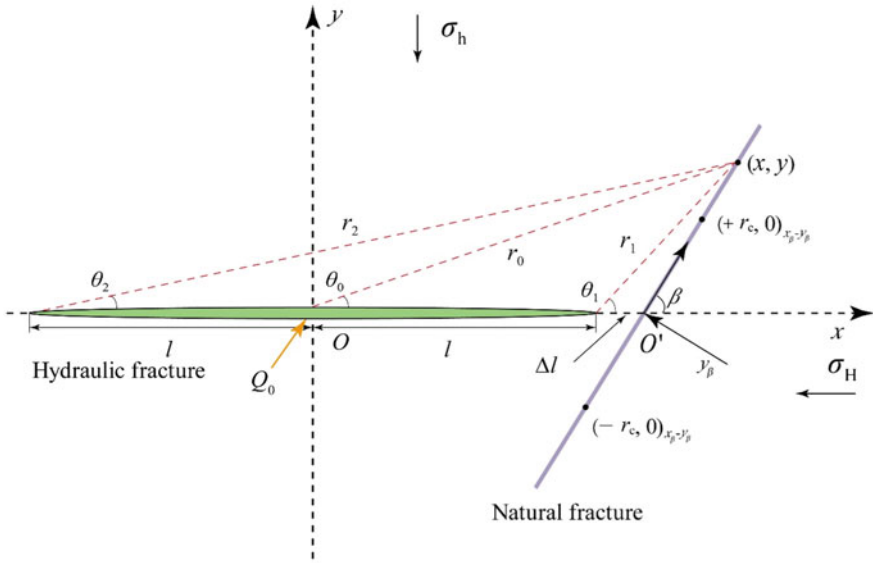
(a) Geometry of the intersection model
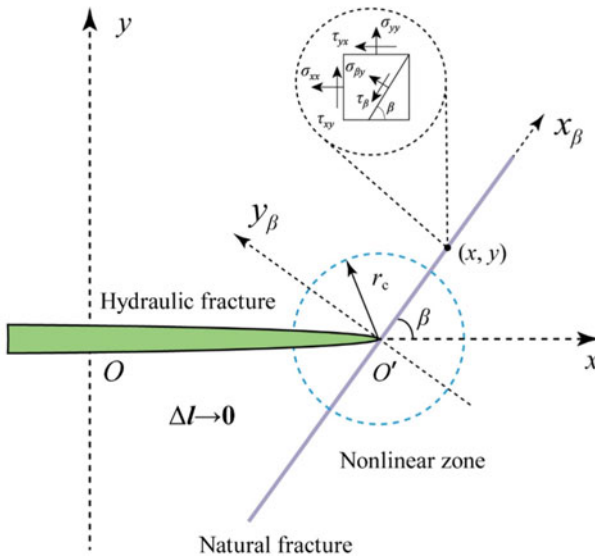
(b) Limit state for $\Delta l \rightarrow 0$

Fig. 8.2 Schematic diagram of a hydraulic fracture approaching a natural fracture

The fluid lubrication equation can be written as

$$\left(\frac{\dot{\varepsilon}t}{\varepsilon} + \frac{\dot{L}t}{L}\right)\Omega - \frac{\dot{L}t}{L}\xi\frac{\partial\Omega}{\partial\xi} + \dot{\rho}t\left(\frac{\partial\Omega}{\partial\rho} - \frac{\xi}{\gamma}\frac{d\gamma}{d\rho}\frac{\partial\Omega}{\partial\xi}\right) = \frac{1}{G_m\gamma^2}\frac{\partial}{\partial\xi}\left(\Omega^3\frac{\partial\Pi}{\partial\xi}\right) \quad (8.3)$$

The fluid mass balance is

$$2\gamma\int_0^1 \Omega d\xi = G_v \quad (8.4)$$

The HF propagation condition $(K_I = K_{IC})$ is

$$\Omega = G_k\gamma^{1/2}(1 - \xi)^{1/2}, \, 1 - \xi << 1 \quad (8.5)$$

In the toughness-dominated regime, the dimensionless groups of G_v and G_k both equal 1, and G_m is a function expression about the known parameters ($G_m = \frac{\mu'}{\varepsilon^3 E't}$, μ' represents the magnitude of fluid viscosity) according to [1]. The classic zero-viscosity solution of a toughness-dominated fracture is derived by Garagash [10], and the related dimensionless parameters are expressed as follows:

$$K' = \frac{8}{\sqrt{2\pi}} \cdot K_{IC}, \, E' = \frac{E}{1 - v^2} \quad (8.6)$$

$$\varepsilon(t) = \left(\frac{K'^4}{E'^4 Q_0 t}\right)^{1/3}, \, L(t) = \frac{E' Q_0 t^{2/3}}{K'} \quad (8.7)$$

$$\gamma = \frac{2}{\pi^{2/3}}, \, \Omega(\xi) = \pi^{-1/3} \cdot (1 - \xi^2)^{1/2}, \, \Pi = \frac{\pi^{1/3}}{8} \quad (8.8)$$

where E' is defined as plane-strain elastic modulus, v denotes Poisson's ratio, K_{IC} is the rock fracture toughness and Q_0 represents the injection rate.

Finally, the hydraulic fracturing solution of a single HF is obtained by combining Eqs. (8.1) and (8.6) ~ (8.8):

$$l(t) = \gamma \cdot \left(\frac{E'}{K'}\right)^{2/3} \cdot (Q_0 t)^{2/3} \quad (8.9)$$

$$w(\xi, t) = \Omega(\xi) \cdot \left(\frac{K'}{E'}\right)^{2/3} \cdot (Q_0 t)^{1/3} \quad (8.10)$$

$$P_{net}(\xi, t) = E' \cdot \Pi(\xi) \cdot \left(\frac{K'}{E'}\right)^{4/3} \cdot (Q_0 t)^{-1/3} \quad (8.11)$$

8.2.2 Slippage Condition for the NF

The HF propagates is subject to the combined action of far-field in-situ stress (σ_H and σ_h) and inner fluid pressure (P_f). According to the stress superposition principle [23], the total stress on the NF interface should be equivalent to the superposition of the far field stress and the induced stress. The far field stress keeps uniform and is generated by in-situ stress, while the induced stress originates from the net pressure (P_{net}) within the HF and is generated by internal fluid flow.

According to Westergaard's analysis [27], the induced stress field produced by the net fluid pressure within the HF in Oxy reference plane is

$$
\begin{cases}
\sigma_{xx} = P_{net}\left[\dfrac{r_0}{2r^*}\right] \times \begin{bmatrix} 2\cos(\theta^* - \theta_0) + 2\sin\theta_0\sin\theta^* - \sin\theta_1 \times \\ \sin(\theta^* + \theta_1 - \theta_0) - \sin\theta_2\sin(\theta^* + \theta_2 - \theta_0) \end{bmatrix} - P_{net} \\[4mm]
\sigma_{yy} = P_{net}\left[\dfrac{r_0}{2r^*}\right] \times \begin{bmatrix} 2\cos(\theta^* - \theta_0) - 2\sin\theta_0\sin\theta^* + \sin\theta_1 \times \\ \sin(\theta^* + \theta_1 - \theta_0) + \sin\theta_2\sin(\theta^* + \theta_2 - \theta_0) \end{bmatrix} \\[4mm]
\tau_{xy} = P_{net}\left[\dfrac{r_0}{2r^*}\right] \times \left[\sin\theta_1\cos(\theta^* + \theta_1 - \theta_0) - \sin\theta_2\cos(\theta^* + \theta_2 - \theta_0)\right]
\end{cases}
\tag{8.12}
$$

where

$$
\begin{aligned}
&-\pi \le \{\theta_0, \theta_1, \theta_2, \theta^*\} \le \pi, \\
&r^* = \sqrt{r_1 r_2}, && \theta^* = \tfrac{1}{2}(\theta_1 + \theta_2), \\
&r_0 = \sqrt{x^2 + y^2}, && \theta_0 = \tan^{-1}(\tfrac{y}{x}), \\
&r_1 = \sqrt{(x-l)^2 + y^2}, && \theta_1 = \tan^{-1}(\tfrac{y}{x-l}), \\
&r_2 = \sqrt{(x+l)^2 + y^2}, && \theta_2 = \tan^{-1}(\tfrac{y}{x+l}),
\end{aligned}
$$

The stress components of the HF-induced stress applied to the NF, inclined by the angle β with respect to the direction of σ_{xx}, are expressed as follows:

$$
\begin{cases}
\sigma_{P_{net}, \beta x} = \dfrac{\sigma_{xx} + \sigma_{yy}}{2} + \dfrac{\sigma_{xx} - \sigma_{yy}}{2}\cos(2\beta) + \tau_{xy}\sin(2\beta); \\[3mm]
\sigma_{P_{net}, \beta y} = \dfrac{\sigma_{xx} + \sigma_{yy}}{2} - \dfrac{\sigma_{xx} - \sigma_{yy}}{2}\cos(2\beta) - \tau_{xy}\sin(2\beta); \\[3mm]
\tau_{P_{net}, \beta} = -\dfrac{\sigma_{xx} - \sigma_{yy}}{2}\sin(2\beta) + \tau_{xy}\cos(2\beta);
\end{cases}
\tag{8.13}
$$

The stress components projected on NF (inclined at angle β) from far-field stresses σ_H and σ_h are given by

$$
\begin{cases}
\sigma_{\gamma, \beta x} = \frac{\sigma_H + \sigma_h}{2} + \frac{\sigma_H - \sigma_h}{2}\cos 2\beta \\
\sigma_{\gamma, \beta y} = \frac{\sigma_H + \sigma_h}{2} - \frac{\sigma_H - \sigma_h}{2}\cos 2\beta \\
\tau_{\gamma, \beta} = -\frac{\sigma_H - \sigma_h}{2}\sin 2\beta
\end{cases}
\tag{8.14}
$$

The total normal and shear stress of the combined stress field can be obtained by superposing Eqs. (8.5) and (8.6):

$$
\begin{cases}
\sigma_{\beta y} = \sigma_{P_{\text{net}}, \beta y} + \sigma_{\gamma, \beta y} \\
\tau_{\beta xy} = \tau_{P_{\text{net}}, \beta} + \tau_{\gamma, \beta}
\end{cases}
\tag{8.15}
$$

When the normal stress on the NF is compressive, the failure of the interface can be judged by Mohr–Coulomb criterion (supposing compressive stress to be negative):

$$
\left| \tau_{\beta xy} \right| \geq c - \mu \sigma_{\beta y}
\tag{8.16}
$$

where μ is the friction coefficient, c denotes the cohesion of the NF, $\sigma_{\beta y}$ and τ_β are the total normal and shear stresses on the NF interface, respectively.

The onset of slip is analytically estimated using the geometric model illustrated in Fig. 8.1b. If Eq. (8.16) holds, the NF may undergo shear failure at different degrees such that the growth of the HF will probably get arrested by the NF. Once the HF is arrested by NF, the pre-existing stress singularity at HF tip will diminish, and the stress field in the vicinity of the HF tip will differ significantly.

8.2.2.1 Opening Criterion for the NF

The critical fluid pressure required to open the NF and sustain the HF propagation [29] is

$$
P_{\text{NF}} = \sigma_{\beta y} + \frac{K_{\text{IC}}}{\sqrt{\pi l}} \sqrt{\eta}
\tag{8.17}
$$

$$
P_{\text{NF}} \leq P_{\text{HF}}
\tag{8.18}
$$

where $\eta = \gamma_{\text{NF}}/\gamma_{\text{Rock}}$, γ_{NF} and γ_{Rock} are the surface energy of the NF and the intact rock matrix, respectively.

The NF will be probably opened by the fracturing fluid inside the HF under the opening condition (Eq. 8.18) which defines the upper limit of the NF opening in combined stress field. Once the HF encounters the NF, the penetrating fracturing fluid may flow along either side of the NF midpoint, which highly depends on the intersection angle [21].

8.2.2.2 Crack Initiation Condition

According to the linear elastic fracture mechanics, the stress field near the fracture tip is approximated as

$$\begin{cases} \sigma_x = \sigma_H + \dfrac{K_I}{\sqrt{2\pi r}} \cos\dfrac{\theta}{2}(1 - \sin\dfrac{\theta}{2}\sin\dfrac{3\theta}{2}) \\[2mm] \sigma_y = \sigma_h + \dfrac{K_I}{\sqrt{2\pi r}} \cos\dfrac{\theta}{2}(1 + \sin\dfrac{\theta}{2}\sin\dfrac{3\theta}{2}) \\[2mm] \tau_{xy} = \dfrac{K_I}{\sqrt{2\pi r}} \sin\dfrac{\theta}{2}\cos\dfrac{\theta}{2}\cos\dfrac{3\theta}{2} \end{cases} \tag{8.19}$$

where K_I is the stress intensity factor, r and θ are the polar coordinates with the origin at HF tip, and $\theta = \beta$ (or $\beta-\pi$).

As the HF tip approaches the NF, the stress projected on the NF is increased such that the inelastic deformation is produced within a certain range of the HF tip, which implies the existence of a nonlinear region adjacent the approaching intersection point in limit state (Fig. 8.1b). Within the nonlinear region, the rock may stay in elastoplastic or plastic state and the highly accumulated elastic strain energy near the HF tip has been dissipated to some extent in the form of heat and surface energy, which makes the linear elastic fracture mechanics invalid for distances less than the critical radius (r_c) to the HF tip. Therefore, the effective stresses within nonlinear region is always assumed to be equal to or less than the stresses at r_c [2, 8, 12].

Similar to the notion of [12], which considered the inelastic behavior of the HF tip prior to contacting with the NF, the mechanical condition for a new fracture initiation on the opposite side of the NF interface is to achieve equilibrium between the maximum principle tensile stress and the rock tensile strength T_0. Hence the critical initiating condition is given by

$$\sigma_1 = \frac{\sigma_x + \sigma_y}{2} + \sqrt{\left(\frac{\sigma_x - \sigma_y}{2}\right)^2 + \tau_{xy}^2} = T_0 \tag{8.20}$$

With known T_0 and K_{IC} (critical stress intensity factor), the nonlinear region critical radius r_c is derived by combining Eqs. (8.19) and (8.20).

Thus, the initiation position can be determined by checking the stress acting on the NF starting from the distance of r_c away from the NF midpoint. It follows then that crossing will occur if the stresses of certain points outside the nonlinear region ($r \geq r_c$) dissatisfy the shear failure condition (Eq. 8.16) and the opening condition (Eq. 8.18):

$$\left|\tau_{\beta xy}\right| < c - \mu\sigma_{\beta y}; \quad P_{NF} > P_{HF} \tag{8.21}$$

Many researchers [5, 25] have demonstrated that the in-situ stress difference and intersection angle were the predominant factors to be considered in the analysis of HF-NF intersection mechanism. Thus, we pay attention to the sensitivity of the stress difference of far-field maximum and minimum horizontal stresses and the intersection angle on the condition that other related parameters including fracture toughness, friction coefficient and initial fracture length remain constant.
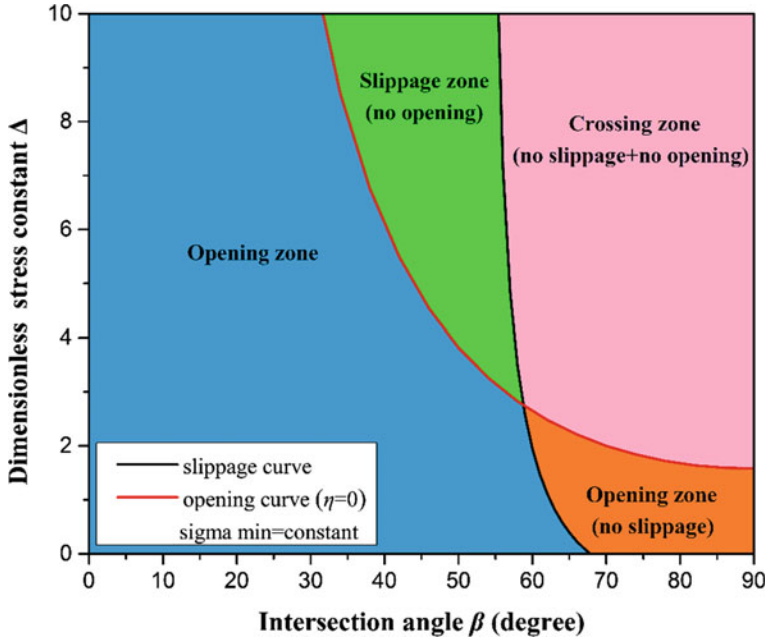
Fig. 8.3 Diagram of different intersection modes based on composite criterion where the dimensionless stress constant $\Delta = (\sigma_H - \sigma_h)/\sigma_h$

Combining the slippage, opening and initiation conditions expressed in Eqs. (8.16), (8.18) and (8.21), the possible intersection behaviors can be predicted mathematically with coded computational program, and the corresponding critical slippage as well as the opening curves can also be drawn out. As delineated in Fig. 8.3, the division of these zones is directly related to the critical shear failure condition and the critical opening condition of the NF. Therefore, the scope of each zone will also be directly related to the mechanical parameters of the two critical conditions.

8.3 Validation of Composite Criterion

8.3.1 Comparison with Previous Intersection Criteria

Previous research effort has concentrated on establishing effective predicting criterion for the HF-NF intersection behavior through theoretical and numerical analysis [4, 6, 15, 16, 25, 29]. To explore the discrepancy and advantage between the proposed criterion and previous criteria, we conduct a comparison using Blanton's criterion, Gu and Weng criterion and Yao criteria under the same parametric conditions.

Figure 8.4 shows the boundary of different areas of the predicting intersection behavior corresponding to different analytical criteria in the parameter space of the intersection angles β and the horizontal in-situ stress difference. The initial material parameters are selected from Blanton experiments, where Devonian shale is chosen as the rock sample with tensile strength T_0 of 5.67 MPa (823 psi), fracture toughness K_{IC} of 1.59 MPa m$^{1/2}$, Young modulus E of 10 GPa and Poisson ratio v of 0.22, NF cohesion c of 0 MPa, NF friction efficient μ of 0.75, minimum horizontal in-situ stress σ_h of 5 MPa (725 psi), initial HF length l of 0.06 m, and injection rate Q of 0.82e^{-6} m^3/s.

(1) Blanton's criterion

In Blanton's experiments and analysis of HF-NF intersection [3] an intersection criterion was developed and validated through dynamic triaxial fracturing tests. The crossing will occur and the initiation of a new fracture can initiate provided that the treating pressure within the HF exceeds the superposition of the rock tensile strength and the stress acting parallel to the NF. After mathematical simplification, the final form of the crossing criterion is introduced by the following:

$$\sigma_H - \sigma_h > \frac{-T_0}{\cos 2\beta - b \sin 2\beta} \tag{8.22}$$

where $b = 0.2$ as an asymptote for an unbounded interface at the NF.

As shown in Fig. 8.4a (red dash line), the lower and upper branches of Blanton curve are almost parallel to the bottom segment of slippage curve and the top part of opening curve, respectively. This result implies that the two criteria have approximately identical predicting results for a relatively large and small intersection angle. However, based on the initial assumptions and mechanical conditions, the subsequent behavior predicted by Blanton criterion is either crossing or opening, but the case of slippage and the effect of induced stress field is not taken into consideration, which results in the criterion merely relating to three parameters (stress difference, intersection angle and b). Hence Blanton criterion is to some extent insufficient for predicting all of the intersection behaviors.

(2) Gu and Weng criterion (Gu and Weng criterion)

Gu et al. [12] considered an HF approaching a frictional interface prior to contact at non-orthogonal angles and proposed a crossing criterion based on linear elastic stress analysis near the fracture tip. This criterion can be applied to determine the occurrence of crossing provided that the accumulated fluid pressure is sufficient to initiate a new crack on the opposite side of the NF before the superposition stress consisting of the remote in-situ stress and the HF-tip stress field along the interface reaches the critical shear resistance. As shown in Fig. 8.4a (black dash-dot line), Gu and Weng criterion was plotted as the boundary between the area of crossing and no-crossing. And the crossing area is relatively reduced compared with the crossing region separated by the two critical curves of the composite criterion. As the intersection angle exceeds 67.5°, the lower branch of Gu & Weng crossing curve becomes closer to the x-axial
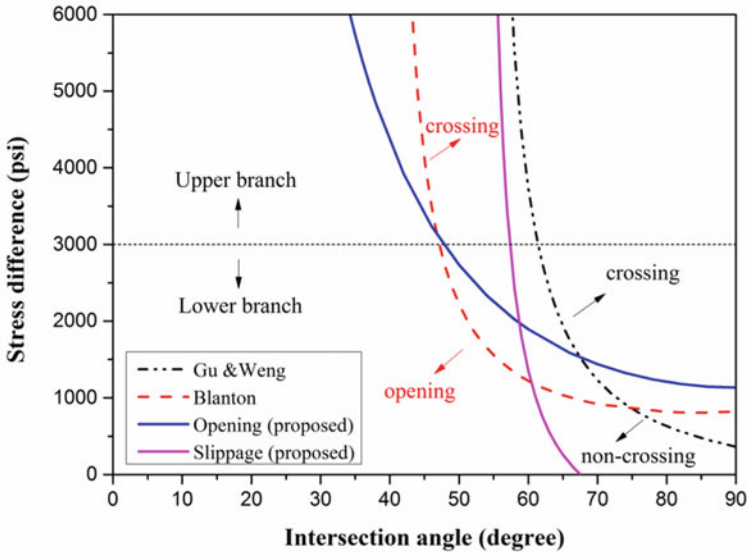
(a) Compared to Blanton and Gu & Weng criteria
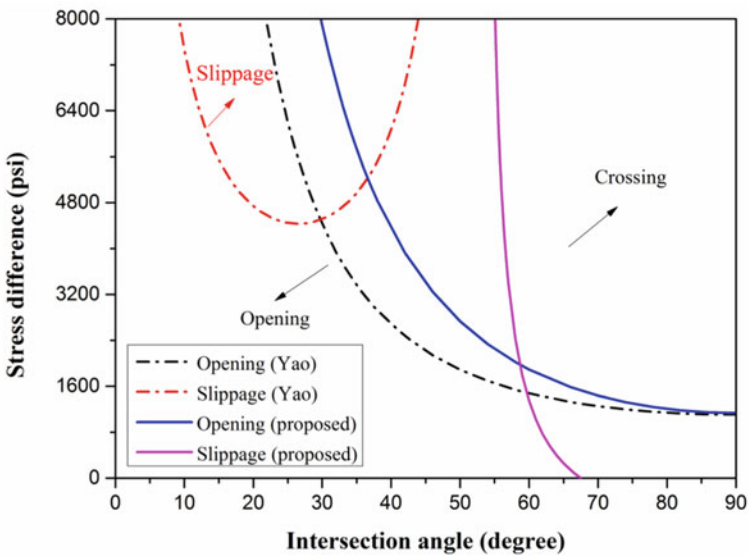
(b) Compared to Yao criteria

Fig. 8.4 HF-NF criteria plotted as the boundary of the intersection areas

than that of the proposed opening curve but farther from the *x*-axial than that of the proposed slippage curve. These distinctions are attributable to the neglected effect of the inner fluid pressure inside the HF in Gu and Weng criterion.

Moreover, field and laboratory observations have demonstrated that opening is a common occurrence when investigating the intersection between the HF and NF [3, 5, 33]. The opening zone (no slippage) depicted in orange color in Fig. 8.3 also designates that the NF may also be dilated in the case of no slippage occurring, which will subsequently impede the HF propagation to penetrate across the NF.

(3) Yao criteria

In Yao's work [29], it is assumed that an HF gets blunted upon contacting an NF and will temporarily stay in the NF for a while and then breakout to propagate in a mechanically favorable direction depending on the orientation of natural fracture relative to the stress field. On basis of energy conservation and slip stability analysis, the opening and slippage criterion in terms of stress difference is derived and correspondingly expressed as:

$$\sigma_H - \sigma_h > \frac{K_{IC}(1 - \sqrt{\eta})}{\sqrt{\pi l}\sin^2\beta} \tag{8.23}$$

$$\sigma_H - \sigma_h > \frac{c - \mu K_{IC}/\sqrt{\pi l}}{\sin\beta(\cos\beta - \mu\sin\beta)} \tag{8.24}$$

Yao criterion is delineated in Fig. 8.4b compared with the presented composite criterion. It can be seen that Yao' slippage curve is approximately manifested in the regulation of quadratic function, which means that the difficulty for slippage to occur decreases initially and then increases progressively with the increase of intersection angle. This significantly differs from the monotonically steep decrease of the slippage curve proposed herein. Furthermore, the opening curve of Yao outlines a larger crossing area than that of the composite criterion as the intersection angle decreases away from 90°.

8.3.2 Comparison with Laboratory Experiments

To validate the applicability of the composite prediction, the intersection behaviors predicted by current analytical model are compared to three independent laboratory experiments: Blanton experiments, Zhou experiments and Gu experiments [3, 4, 12, 33]. It should be noted that the value of η in Eq. (8.17) is assumed to be zero for the surface energy of NF is infinitely small compared with that of rock.

(1) Blanton experiments

Blanton [3] preformed the fracture intersection experiments using hydrostone blocks which were fractured by a pre-existing surface under different angles of approach
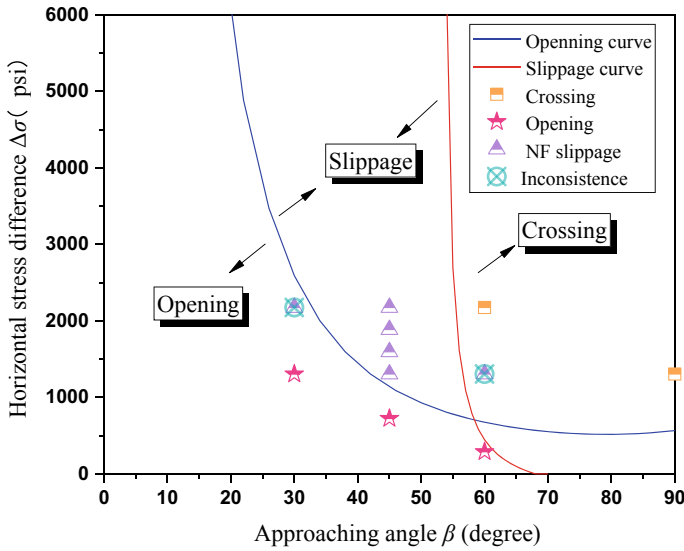
Fig. 8.5 Comparison between Blanton's experimental results and predictions of the proposed composite criteria

(30°, 45°, 60° and 90°) and stress states ($-\sigma_h = 5$ or10 MPa and the principal differential stresses varied from 2 to 15 MPa). The pre-fractured surface was frictional and cohesively with a friction coefficient of 0.75. The tensile strength of hydrostone was 3.1 MPa. And the Mode I fracture toughness was 0.176 MPa m$^{1/2}$. The fracturing fluid was injected at a constant flow rate of 0.82 cm^3/s through a wellbore simulated by a steel pipe. In addition, the half-length of the HF was equal to 0.06 m. The fluid viscosity is assumed to be sufficiently small in a toughness-dominated HF, so its effect becomes negligible. Figure 8.5 summarizes the results of Blanton experiments and the corresponding calculation outcomes from the new criterion.

(2) Zhou experiments

Zhou et al. [33] reported similar experiments about the HF-NF intersection on cement-sand model blocks with scaled proportion to real rock in triaxial compressive stress state. The pre-fractures were created by 3 types of paper with cohesion of 3.2 MPa and friction coefficient of 0.38, 0.89 and 1.21, respectively. The interaction angles in each block between the HF and NF were varied systematically of 30°, 60° and 90°. The Mode I fracture toughness of model blocks is 0.59 MPa m$^{1/2}$, and the half-length of HF was designed as 0.06 m. The vertical stress remains invariable at 20 MPa, meanwhile, the horizontal stress difference was changed from 3 to 10 MPa. The comparison is shown in Fig. 8.6.
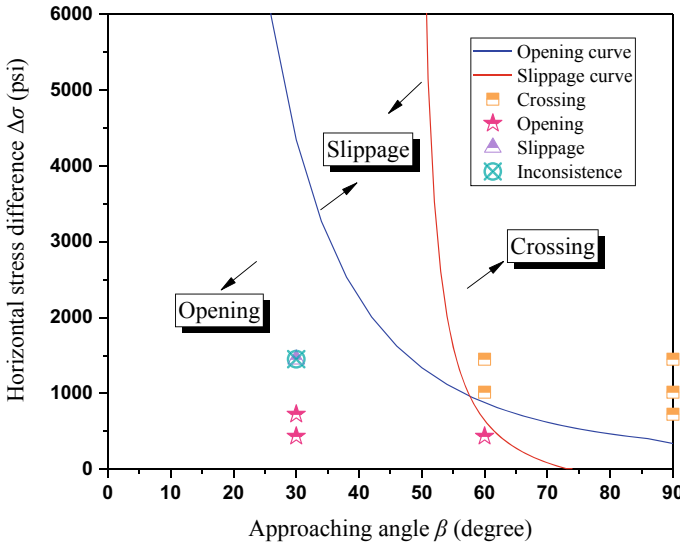
Fig. 8.6 Comparison between Zhou et al.'s experimental results and predictions of the proposed composite criteria

(3)   Gu experiments

In recent experiments conducted by [12], Calton sandstone ($T_0 = 4.054$ MPa, K_{IC} = 1.6 MPa m$^{1/2}$) was cut into rectangle blocks and prepared for the intersection test at true triaxial-stress condition. A discontinuity interface characterized by friction efficient of 0.615 and negligible cohesion was prefabricated in the blocks at specified angles ranging from 45° to 90°. Silicone oil (viscosity of 1 Pa s) was injected at a constant rate of 0.5 cm^3/s. The vertical stress remains invariable at 27.58 MPa, meanwhile, the horizontal stress difference was changed from 0.69 to 10.35 MPa with unchangeable minimum horizontal stress of 6.89 MPa. And the initial half-length of HF was 0.076 m. The prediction results are depicted in Fig. 8.7.

In general, the comparison results in Figs. 8.5–8.7 indicate that the calculation outcomes obtained from the composite criterion show good agreement with the experimental results except for several particular cases. The disagreement between the experimental and predicted results arises from the inappropriate range of the nonlinear zone which implies that the actual nonlinear region at the crack tip is relatively larger. A possible explanation for this change is the co-action of stress singularity and plastic zone ahead of the HF tip which can enlarge the radius of the nonlinear zone. In this case, the initially calculated points at r_c no longer follow the linear elastic mechanics, resulting in inapplicable cases.
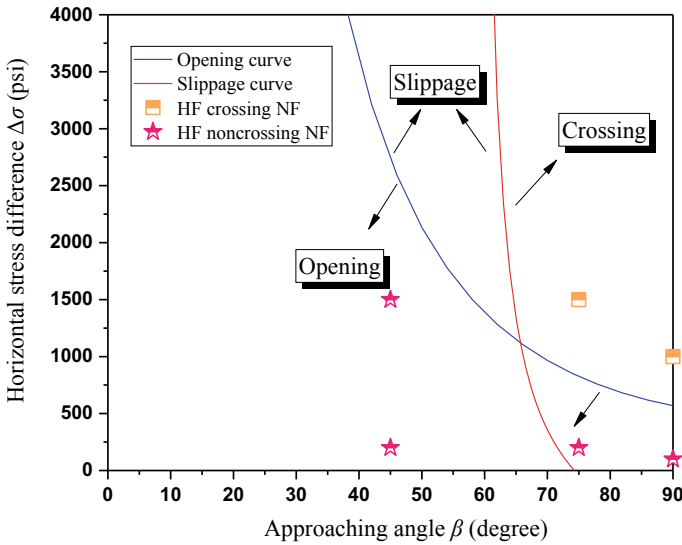
Fig. 8.7 Comparison between Gu et al.'s experimental results and predictions of the proposed composite criteria

8.4 Composite Criterion Considering Nonuniform Fluid Pressure

8.4.1 Nonuniform Form of Fluid Pressure

The intersection between a hydraulic fracture and a natural discontinuity is ubiquitous during hydraulic fracturing treatment. For better prediction of the fracture intersection, Zhao et al. [31, 32] proposed a composite criterion that synchronously considered three possible intersection modes (opening, crossing and arrested) and the coupling effects between fluid flow and solid elastic deformation. Nevertheless, the fluid effect in Zhao et al. [31, 32] is confined to a uniform pressure distribution at the limit intersection point where the hydraulic fracture is infinitely close to but does not intersect with the discontinuity. In this section, we aim to use the newly derived semianalytical solutions for the stress field induced by nonuniform fluid pressure and replace the induced stress field with that of constant fluid pressure. Subsequently, the induced stress is superimposed with far-field in-situ stress, and then the total stress field around the hydraulic fracture and possible fracture intersection can be evaluated. Meanwhile, we can compare the laboratory experimental observations of fracture intersection [25, 33] with the corresponding intersection results predicted by the semianalytical solution of nonuniform pressure, through which the validity and applicability of the presented semianalytical solution can be further demonstrated.

The specific polynomial form (Eq. (8.1)) was determined by fitting the analytical relationship of the nonuniform fluid pressure distribution along the crack referring to the first-order approximation of large toughness solutions in [7]. As depicted in Fig. 8.8, with the increase of the polynomial degree, the fitting precision (*R*-square) increases while the enlarged precision range decreases. Specifically, as the degree equals 7, it is easy to find that the continuous increase of the polynomial degree will only yield less than a 0.5% difference in accuracy. For convenience of calculation, we set the degree of fitting polynomial to 7. Then, referring to [1], the form of net fluid pressure inside the hydraulic fracture can be expressed as

$$P(x) = P_0 \Pi = P_0 \begin{pmatrix} -137.128\xi^7 + 445.392\xi^6 - 567.697\xi^5 + 358.686\xi^4 - \\ 116.684\xi^3 + 18.261\xi^2 - 1.249\xi + 0.373 \end{pmatrix}$$

(8.38)

where

$$P_0 = (\frac{K'^4}{E'Qt})^{1/3}, \quad \xi = x/a$$

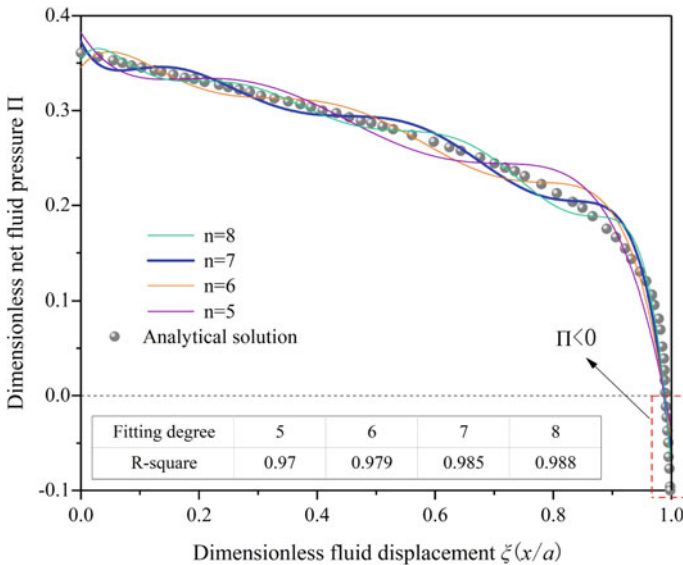$$K' = \frac{8}{\sqrt{2\pi}} \cdot K_{IC}, \quad E' = \frac{E}{1 - v^2}$$

Fig. 8.8 Fitting curves of the non-uniform fluid pressure within a toughness-dominated crack based on [7]

It should also be noted that the net fluid pressure inside the crack is assumed to be always positive, but the abnormal negative Π marked in the red box near the region of $\xi = 1$ is attributed to the existence of stress singularity of the crack tip.

8.4.2   Comparison with Laboratory Experiments

Using this fitted pressure distribution as well as the critical conditions of the composite criterion presented by Zhao et al. [32], possible behaviors influenced by nonuniform fluid pressure under different in-situ stresses and approaching angles can be obtained. Meanwhile, the predicted results are also compared to previous conclusions, which neglected the effect of nonuniform fluid pressure in Zhao et al. [32].

Table 8.6 lists the results of Warpinski experiments [25], the corresponding calculation outcomes from the composite criterion of Zhao et al. [32] and the results predicted by the semianalytical solution for nonuniform fluid pressure. Note that the notation β refers to the intersection angle ($\leq 90°$) between the hydraulic fracture and the natural discontinuity. The Warpinski experiment was deployed using Coconino sandstone (Young's modulus of 34.5 GPa, Poisson's ratio of 0.24, fracture toughness of 1.59 MPa m$^{1/2}$) that was processed into prismatic blocks and prepared for the intersection test under true triaxial stress conditions. A discontinuity interface characterized by a friction efficient (μ) of 0.68 and cohesion of 0.1 MPa was prefabricated at specified angles (β) ranging from 30° to 90°. Fracturing fluid was injected into the wellbore at a constant rate of 0.1 cm^3/s. The vertical stress was maintained at an invariable level for all tests, while the maximum horizontal in-situ stress (σ_H) changed from 6.89 to 13.79 MPa with an unchangeable minimum horizontal in-situ stress of 3.45 MPa. The initial half-length of HF was 0.06 m. In addition, the notation r_c denotes the critical radius of the plastic zone ahead of the fracture tip, and its corresponding calculation formula can be found in [19].

Table 8.7 shows the comparison of intersection results newly predicted by nonuniform fluid pressure with the Zhou experiment and the predicted outcomes of Zhao et al. [32]. In line with the experiment of Zhou [33], the model blocks were prepared from a mixture of No. 325 Chinese cement and fine sand with a tensile strength of 3.2 MPa, Young's modulus of 8.402 GPa and a Poisson's ratio of 0.23. Furthermore, a discontinuity interface characterized by three types of friction coefficients (0.38, 0.89, 1.21) and cohesion of 3.2 MPa was prefabricated in the blocks at specified angles (β) ranging systematically from 30° to 90°. The Mode I fracture toughness of the model blocks is 0.59 MPa m$^{1/2}$, and the half-length of hydraulic fracture was designated as 0.06 m. The injecting fluid is assumed to be incompressible, with a viscosity of 0.135 Pa s and an injection rate of 4.2×10^{-9} m^3/s. The vertical stress remains invariable, and the maximum and minimum horizontal in-situ stress difference was changed from 3 to 10 MPa.

Tables 8.6 and 8.7 suggest that both constant and nonuniform fluid pressure can properly predict fracture intersection within a reasonable range of accuracy. However,

Table. 8.6 Comparison with Warpinski experiment and Zhao predicted results

β (°)	σ_H (MPa)	σ_h (MPa)	r_c (m)	μ	Experimental results	Constant predicted	Nonuniform predicted
30	6.89	3.45	0.0068	0.68	Opening	Opening	Opening
30	10.34	3.45	0.0067	0.68	Opening	Opening	Opening
30	13.79	3.45	0.0066	0.68	Arrested	Arrested	Arrested
60	6.89	3.45	0.0083	0.68	Opening	**Arrested**	Opening
60	10.34	3.45	0.0083	0.68	Crossing	**Arrested**	**Crossing**
60	13.79	3.45	0.0083	0.68	Crossing	Crossing	Crossing
90	6.89	3.45	0.0066	0.68	Opening	**Crossing**	Opening
90	10.34	3.45	0.0063	0.68	Crossing	Crossing	Crossing
90	13.79	3.45	0.0062	0.68	Crossing	Crossing	Crossing

Table. 8.7 Comparison with Zhou experiment and Zhao predicted results

β (°)	σ_H (MPa)	σ_h (MPa)	r_c (m)	μ	Experimental results	Constant predicted	Nonuniform predicted
90°	−8	−3	0.0020	0.38	Crossing	Crossing	Crossing
90°	−8	−5	0.0012	0.38	Crossing	Crossing	Crossing
60°	−10	−3	0.0026	0.38	Crossing	Crossing	Crossing
60°	−8	−3	0.0026	0.38	Opening	**Crossing**	**Crossing**
30°	−10	−3	0.0021	0.38	Arrested	Arrested	Arrested
30°	−8	−3	0.0021	0.38	Opening	Opening	Opening
90°	−10	−5	0.0011	0.89	Crossing	Crossing	Crossing
90°	−10	−3	0.0019	0.89	Crossing	Crossing	Crossing
60°	−10	−3	0.0026	0.89	Crossing	Crossing	Crossing
60°	−13	−3	0.0026	0.89	Crossing	Crossing	Crossing
60°	−8	−5	0.0026	0.89	Opening	Opening	Opening
30°	−10	−5	0.0012	0.89	Opening	Opening	Opening
30°	−8	−5	0.0012	0.89	Opening	**Arrested**	Opening
30°	−13	−3	0.0021	0.89	Arrested	**Opening**	**Opening**
90°	−8	−3	0.0020	1.21	Opening	**Crossing**	**Crossing**
90°	−13	−3	0.0019	1.21	Crossing	Crossing	Crossing
60°	−13	−3	0.0026	1.21	Opening	**Crossing**	**Crossing**
60°	−10	−3	0.0026	1.21	Opening	**Crossing**	**Crossing**
30°	−13	−3	0.0021	1.21	Opening	Opening	Opening
30°	−8	−3	0.0021	1.21	Opening	Opening	Opening

the difference is that the results using the semianalytical solution of nonuniform fluid pressure exhibited better agreement with the experimental observations than those predicted by Zhao et al. [32]. This distinction can be attributed to the variable fluid pressure inside the crack, which demonstrates the necessity to consider nonuniform fluid pressure. Furthermore, the fine matching between the experiments and the predicted results from nonuniform pressure further reveals the applicability of the presented semianalytical solutions for hydraulic fracturing analysis.

8.5 Perturbation Analysis of Key Parameters

The composite criterion is a function of horizontal in-situ stress, initial fracture length, intersection angle, fracture toughness and approaching distance. As mentioned above, the composite criterion curves of the stress difference versus the intersection angle were drawn and delineated at constant minimum horizontal stress and fracture toughness, and infinitesimally small approaching distance, which initially and geometrically restrict the composite criterion curve to be explored in depth. For further understanding fracture behavior at different parameters, it's necessary to conduct parametric sensitivity analysis considering minimum horizontal in-situ stress, fracture toughness and approaching distance, and conduct stress field analysis adjacent to the intersection. For convenience, a slip function f is introduced based on the slippage condition, which is expressed as:

$$f = \left| \tau_{\beta xy} \right| - c + \mu \sigma_{\beta y}, \quad (\sigma_{\beta y} < 0) \tag{8.25}$$

Note that the increase of slip function means its absolute value decreases and the possibility of the NF slippage increases.

8.5.1 Impact of Initial Horizontal In-Situ Stress

The critical curves of the composite criterion considering the influence of varying the minimum horizontal stress at constant maximum horizontal stress and varying the maximum horizontal stress at constant minimum horizontal stress are depicted in Fig. 8.9a. To facilitate the contrast analysis, the critical curves of stress difference versus intersection angle at fixed minimum horizontal stress ($\sigma_h = -5$ MPa) are delineated in Fig. 8.9b. It should be specified that the critical curves in Fig. 8.9 are calculated and plotted at identical parametric conditions aside from initial valve of the horizontal stress.

By comparison, it can be seen that as the variation of horizontal stress changes from decreasing σ_H to increasing σ_H, the slippage curve deflects symmetrically along the line $\beta = 60°$ while the opening curve hardly exhibits significant changes in shape. On the other hand, there is an evident discrepancy in the curvature of opening curves in
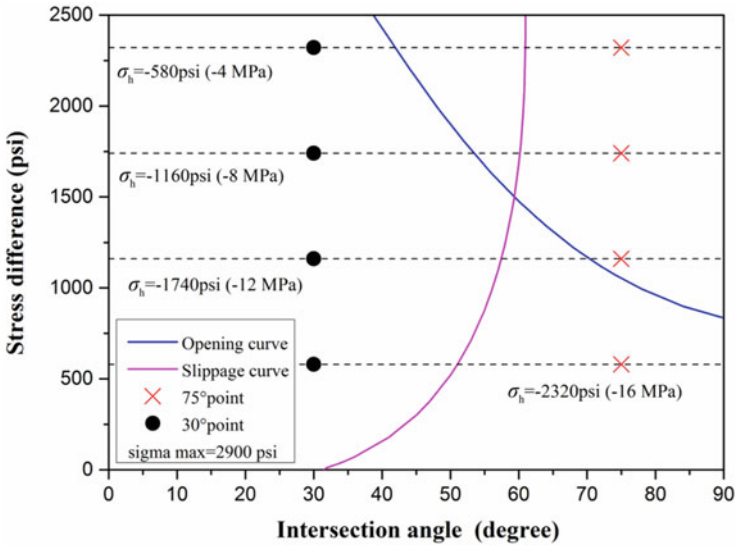
(a) Composite criterion at constant maximum horizontal stress
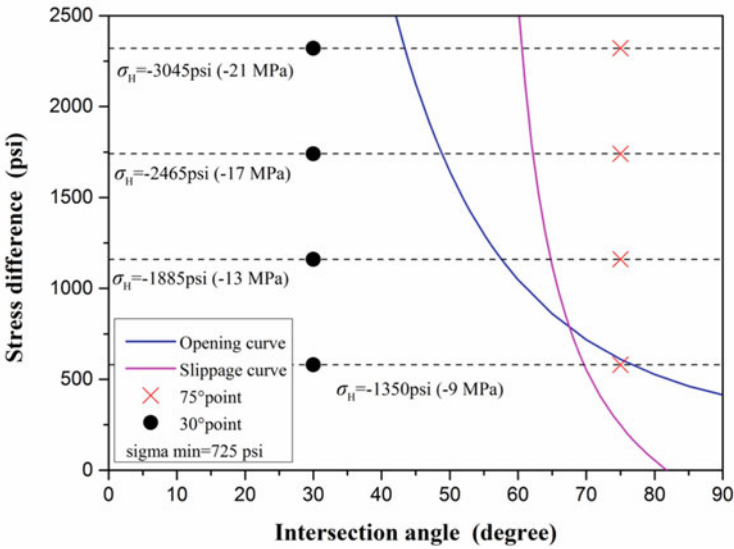
(b) Composite criterion at constant minimum horizontal stress

Fig. 8.9 Influence of horizontal stress difference: **a** varying σ_h with fixed $\sigma_H = -20$ MPa (-2900 psi); **b** varying σ_H with fixed $\sigma_h = -5$ MPa (-725 psi)

Fig. 8.9a compared with Fig. 8.9b. The discrepancy mainly embodies in the decreased opening tendency and subsequently imposes greater difficulty for opening to occur. In addition, it's also easy to find that slippage becomes easier as the intersection angle β decreases from 90° according to Fig. 8.9a, which is opposite to the slipping tendency in Fig. 8.9b.

The slippage analysis of certain points at the intersection angle $\beta = 30°$ (solid black dots) and $\beta = 75°$ (red forks) with the stress difference of 4, 8, 12, 16 MPa are also respectively shown in Fig. 8.9. For further analysis of the NF stability, we solely concentrate on the slippage curves. We can predict that the solid black dots will probably slip whereas the red forks can remain stable regardless of the stress difference and initial horizontal stress value in line with their relative position to the slippage curves. This indicates that varying the minimum horizontal stress does not affect the final predicted intersection results at some intersection angles, thus it is feasible for the composite criterion to be used for the verification of the laboratory experiments as the minimum horizontal stress varies.

Figure 8.10 presents the slip function distribution on the NF interface when the HF approaches the NF at the angle of 30° (b) and 75° (c). Due to the existence of the stress singularity at the intersection, the starting points for calculation are determined by the radius of nonlinear region $\pm r_c$ and sixty points are symmetrically extracted from the natural frictional interface on both sides of the intersection in βx-βy coordinate system. The slip functions under different stress conditions share similar distribution characteristics of steep convex profile, which is manifested as the larger values of slip function for the closer distance to the intersection. And the slip function values of the calculation points on the negative NF interface ($\beta x < 0$) are less than those on positive NF interface ($\beta x > 0$). This difference means slippage is probably to occur on the positive NF rather than on the negative NF interface.

In addition, the values of slip function partially or entirely exceed zero for $\beta = 30°$ in Fig. 8.10a, b, which implies the tangential stress applied along the NF is greater than the shear resistance and therefore further substantiates the slippage occurrence. As for $\beta = 75°$, the values of slip function all stay below zero in spite of the initial horizontal stress (Fig. 8.10c, d). This result ensures sufficient stability to inhibit slippage on the NF interface. For clarity, the zero value of the slip function is marked out with dash lines shown in these figures.

### 8.5.2 Impact of Fracture Toughness

The opening and slippage curves of the composite criterion with fracture toughness of 0.59, 1.09, 1.59 and 2.09 MPa/m$^{1/2}$ are plotted in Fig. 8.11. A small contrast in fracture toughness makes significant changes in the slippage curves whereas a relatively slight effect on the opening curve. Specifically, as the fracture toughness increases, the scope of crossing zone increases especially at low stress differences, while the slippage zone decreases despite the intersection angle and the stress difference. This
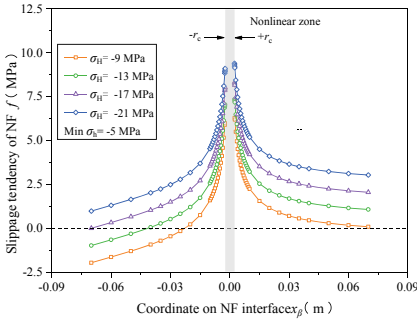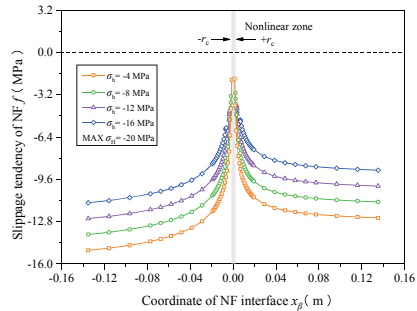
(a) Fixed σ_H and increasing σ_H (β=30°)
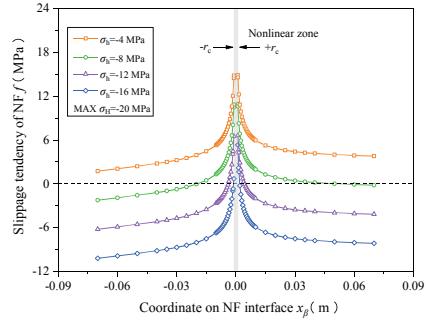
(b) Fixed σ_H and increasing σ_h (β=30°)
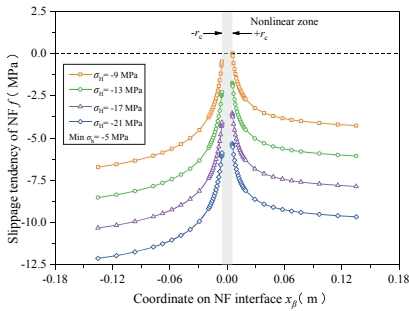
(c) Fixed σ_h and increasing σ_H (β=75°)

(d) Fixed σ_H and increasing σ_h (β=75°)

Fig. 8.10 Distribution of slippage tendency function f on the natural fracture interface

discrepancy signifies that the occurrence of crossing becomes easier at larger values of fracture toughness.

Furthermore, the opening curves have two-stage variation with the increase of fracture toughness: (i) distinguishable changes of the opening curves in the action of different fracture toughness are found in the angle range of 26–54° (shadow area); (ii) the opening curves tend to coincide as the intersection angle increases from 54°. This allows us reach a conclusion that the effect of fracture toughness on the open curve is limited in a certain range of the intersection angle.

Figure 8.12 shows the slippage stability and stress distribution of the analyzed point. For different fracture toughness, the values of slip function of the analyzed point increase progressively as the calculated points move closer to the HF tip and finally presents a steep increase at the intersection. By comparison, the slip function on the positive βx axis is greater than that on the negative βx axis, indicating that the incipient slippage probably takes place on the right side of the NF rather than on the left. In general, the slip function increase with the increase of fracture toughness, which is contrary to the various laws in the coordinate interval of (−0.14 m, -0.08 m)
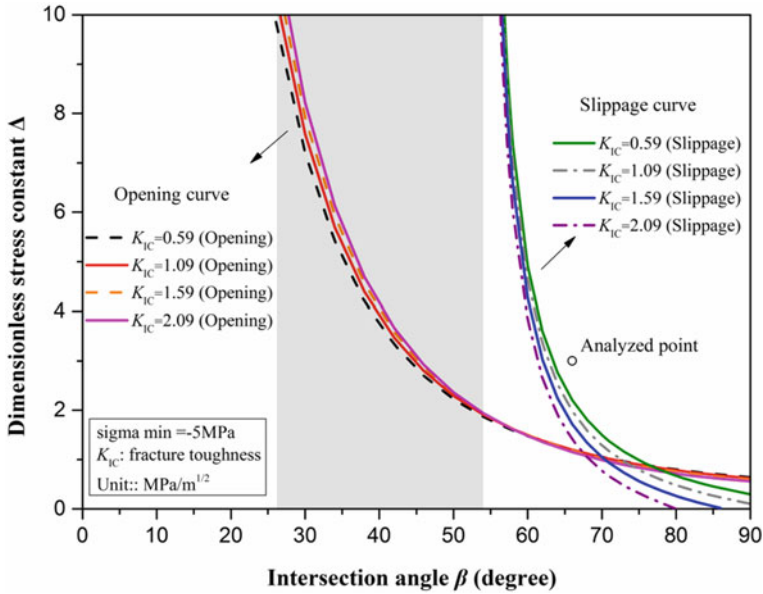
Fig. 8.11 Composite criteria considering the variation of rock fracture toughness

on the NF interface. Thus, the fracture toughness has a nonlinear effect on the slip function as the coordinate of the NF varies.

Moreover, the variation in the total normal stress with the increase of the fracture toughness on both sides of $\beta x = -0.02$ m is entirely contrary. The higher the fracture toughness gets, the smaller the total normal stress on the left side of $\beta x = -0.02$ m is, whereas the greater the normal stress on the right of $\beta x = -0.02$ m becomes. However, the contrast of the normal stress on the right of $\beta x = -0.02$ m is lower than that on the right side under different fracture toughness. A reasonable explanation for this result is that the calculated points at the positive βx axis are far from the HF, where the net pressure within the HF has an inappreciable stress component on the positive NF interface. As shown in Fig. 8.12c, the total shear stress appears approximately symmetrical distribution on both sides of the NF midpoint and has a positive correlation with fracture toughness. Hence the slippage stability of NF is mainly dominated by the total normal stress.
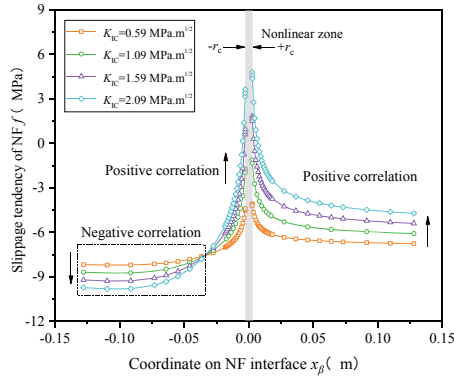
(a) Distribution of slippage tendency function on the natural fracture interface

under different fracture toughness
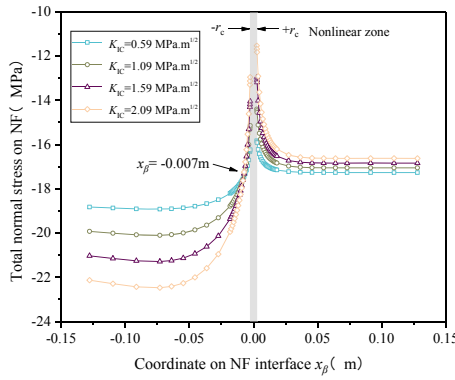
(b) Total normal stress
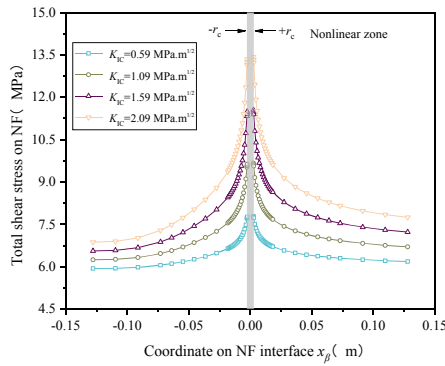
(c) Total shear stress

Fig. 8.12 Slippage stability and stress distribution on the NF interface at analyzed point for intersection angle $\beta = 66°$, $\sigma_H = -20$ MPa and $\sigma_h = -5$ MPa

### 8.5.3 Impact of Approaching Distance

The approaching distance is introduced as a small perturbation between the right tip of HF and the intersection point, which aims to investigate whether the slippage will occur before the HF tip intersects with the NF. The magnitude of the approaching distance reflects the degree of HF tip close to the intersection. For the convenience of comparison, the HF half-length is assumed to be 6 m, and four sets of approaching distances (0, 0.03, 0.07, 0.22, and 1.5 m) are taken into account.

Figure 8.13 displays the critical opening and slippage curves under different approaching distances. With increasing approaching distance, the critical opening curves (Fig. 8.13a) are close to the coordinate axis, and the angle interval, within which the occurrence of the opening is more prone even at a relatively small stress difference, is surely reduced. Thus, it might become more difficult for the NF opening, especially at greater intersection angles. The opening can occur only under the prerequisite of the HF contacting HF. But here we merely concentrate on possible behaviors before the intersection. Thus, the opening curves are delineated by comparing the fluid pressure (P_{HF}) inside the HF with the total normal stress ($\sigma_{\beta y}$) acting perpendicularly to the NF, which defines the upper limit for opening to occur. In Fig. 8.13b, the larger value of approaching distance indicates the more symmetrical shape of the slippage curves. The form of asymmetrical curves for $\Delta l = 0.03$ m can be attributed to the combined action of fluid pressure and far-field in-situ stress. And as the approaching distance increases, the HF goes far away from the NF. So, the influence of fluid pressure diminished gradually and the remote in-situ stress starts to exert a dominating effect on the slippage.

The slip function curves in Fig. 8.14 show different tendencies under various intersection angles. In detail, the slip function curves are symmetrically distributed on both sides of the NF midpoint for $\beta = 90°$. While β equals 60°, 30° and 10, the values of slip function on the left side are greater than that on the right. This discrepancy is because the left side (negative βx axis) is closer to the HF than the right side, leading to a higher influence degree, which appears a larger variation magnitude of the slip function on the left.

In summary, the chance of slippage of the NF increases gradually during the approaching process. When the intersection angle increases from 30° to 90°, the slip function value decreases. And the natural fracture becomes less likely to slip, which indicates that the crossing behavior may more easily occur.
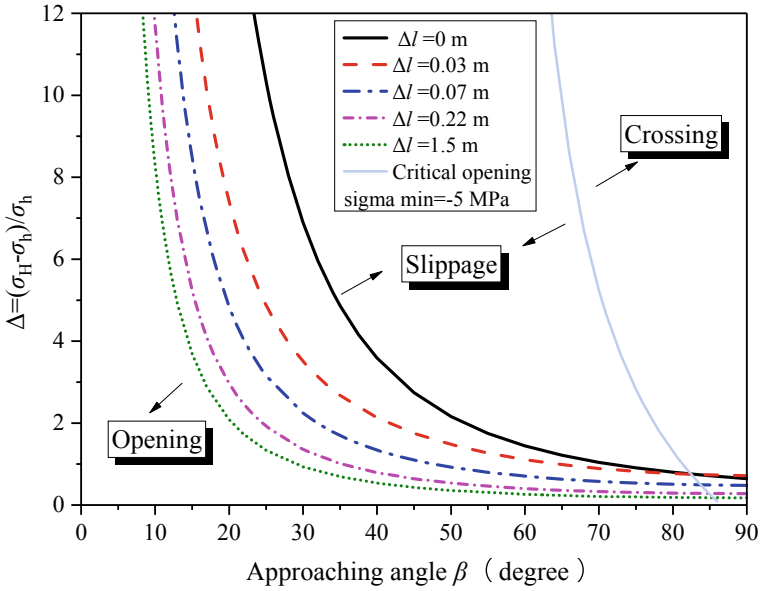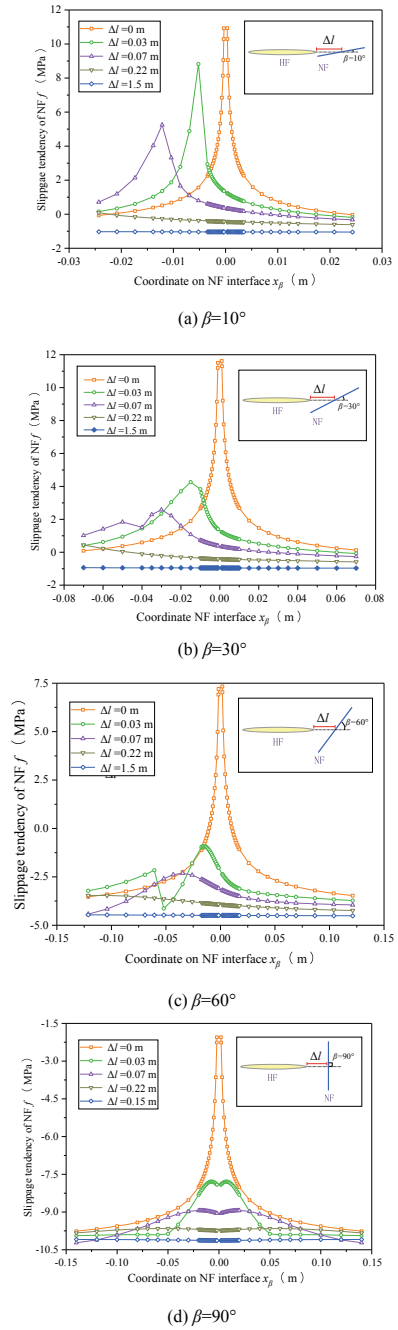
(a)
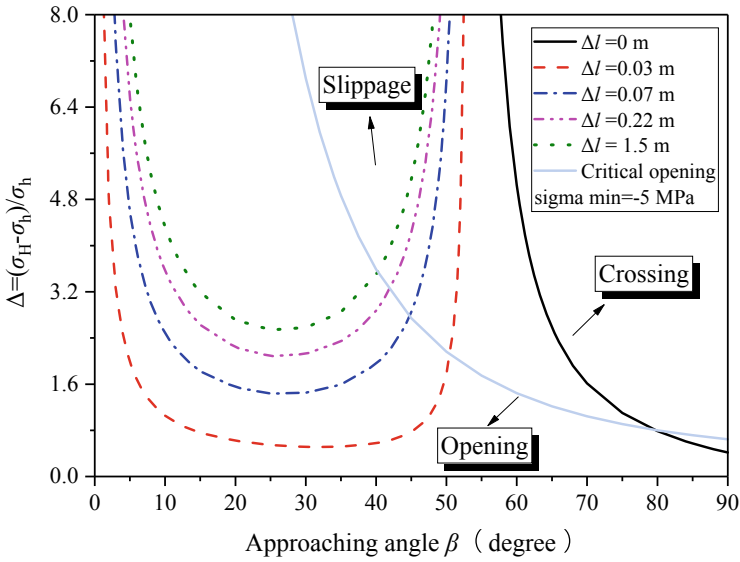
(b)

Fig. 8.13 The critical opening **a** and slippage **b** curves under different approaching distances (σ_h = −5 MPa)

Fig. 8.14 The slippage
tendency (slip function)
under different approaching
distances for different
intersection angles

(a) β=10°

(b) β=30°

(c) β=60°

(d) β=90°

References

1. Adachi JI (2001) Fluid-driven fracture in permeable rock. PhD thesis, Minneapolis University of Minnesota
2. Barenblatt GI (1962) The mathematical theory of equilibrium cracks in brittle fracture. Adv Appl Mech 7:55–129
3. Blanton TL (1982) An experimental study of interaction between hydraulically induced and pre-existing fractures. In: Society of petroleum engineers unconventional gas technology symposium, Pittsburgh. https://doi.org/10.2523/10847-ms
4. Blanton (1986) Propagation of hydraulically and dynamically induced fractures in naturally fractured reservoirs. In: SPE unconventional gas recovery symposium, society of petroleum engineers
5. Chuprakov D, Melchaeva O, Prioul R (2014) Injection-sensitive mechanics of hydraulic fracture interaction with discontinuities. Rock Mech Rock Eng 47(5):1625–1640
6. Dahi A, Olson JE (2011) Numerical modeling of multistranded-hydraulic-fracture propagation: accounting for the interaction between induced and natural fractures. Soc Petrol Eng 16:575–581. https://doi.org/10.2118/124884-pa
7. Detournay E (2004) Propagation regimes of fluid-driven fractures in impermeable rocks. Int J Geomech 4(1):35–45. https://doi.org/10.1061/(asce)1532-3641(2004)4:1(35)
8. Dugdale DS (1960) Yielding of steel sheets containing slits. J Mech Phys Solids 8(2):100–104
9. Fisher MK, Davidson BM, Goodwin AK, Fielder EO, Buckler WS, Steinberger NP (2002) Integrating fracture mapping technologies to optimize stimulations in the barnett shale. In: Paper SPE 77411, SPE annual technical conference and exhibition, San Antonio, Texas, USA. https://doi.org/10.2118/77441-ms
10. Garagash (2000) Hydraulic fracture propagation in elastic rock with large toughness. In: Proceedings of 4th North American rock mechanics symposium, the Netherlands, 221–228
11. de Geertsma K (1969) A rapid method of predicting width and extent of hydraulic induced fractures. J Petrol Technol 21(12):1571–1581
12. Gu H, Weng X, Lund J, Mack M, Suarez-Rivera R (2011) Hydraulic fracture crossing natural fracture at non-orthogonal angles: a criterion and its validation. In: SPE hydraulic fracturing technology conference, society of petroleum engineers. https://doi.org/10.2118/139984-pa
13. Khristianovic SA, Zheltov YP (1955) Formation of vertical fractures by means of highly viscous liquid. In: Proceedings of the fourth world petroleum congress, Rome, 579–586
14. Kresse O, Weng X, Wu R, Gu H. Numerical modeling of hydraulic fractures intersection in complex naturally fractured formations. Am Rock Soc Assoc. 2012. https://doi.org/10.1007/s00603-018-1539-5
15. Li ZC, Li LC, Li M et al (2018) A numerical investigation on the effects of rock brittleness on the hydraulic fractures in the shale reservoir[J]. J Natl Gas Sci Eng 50:22–32. https://doi.org/10.1016/j.jngse.2017.09.013
16. Liu HL, Li LC, Li ZC et al (2017) Numerical modelling of mining-induced inrushes from subjacent water conducting karst collapse columns in northern China[J]. Mine Water Environ. https://doi.org/10.1007/s10230-017-0503-z
17. Maxwell SC, Urbancic TI, Steinsberger NP, Zinno R (2002) Microseismic imaging of hydraulic fracture complexity in the Barnett shale. In: Paper SPE 77440, SPE annual technical conference and exhibition, San Antonio, Texas. https://doi.org/10.2523/77440-ms
18. Perkins T, Kern L (1961) Widths of hydraulic fractures. J Pet Tech Trans AIME 222:937–949
19. Renshaw CE, Pollard DD (1995) An experimentally verified criterion for propagation across unbounded frictional interfaces in brittle, linear elastic-materials. Int J Rock Mech Mining Sci Geo-Mech Abstracts 32(3):237–249
20. Sarmadivaleh M, Rasouli V (2013) Modified Renshaw and Pollard criteria for a non-orthogonal cohesive natural interface intersected by an induced fracture. Rock Mech Rock Eng 47(6):2107–2115
21. Song CP, Yiyu LU, Xia BW et al (2014) Effect of natural fractures on hydraulic fracture propagation in coal seam. J Northeastern Univ (Natl Sci) 35(5):756–760

22. Taleghani AD, Olson JE (2013) How natural fractures could affect hydraulic-fracture geometry. SPE J 19(1):161–171. https://doi.org/10.2118/167608-pa
23. Valko P, Economides MJ (1995) Hydraulic fracture mechanics. Wiley, Chichester
24. Warpinski NR, Kramm RC, Heinze JR, Waltman CK (2005) Comparison of single- and dual-array microseismic mapping techniques in the Barnett shale. In: Paper SPE 95568, SPE annual technical conference and exhibition, Dallas, Texas. https://doi.org/10.2523/95568-ms
25. Warpinski NR, Teufel LW (1987) Influence of geologic discontinuities on hydraulic fracture propagation. J Petrol Technol 39:209–220. https://doi.org/10.2118/13224-Pa
26. Xiaowei W (2015) Modeling of complex hydraulic fractures in naturally fractured formation. J Unconventional Oil Gas Resour 9:114–135
27. Westgaard HM (1939) Bearing pressures and crack. J Appl Math Mech 6:A49–A53
28. Wu R, Kresse O, Weng X, Cohen C-E, Gu H (2012) Modeling of intersection of hydraulic fractures in complex fracture networks. In: SPE hydraulic fracturing technology conference, Society of Petroleum Engineers. https://doi.org/10.2118/152052-ms
29. Yao, Y, Wang W, Keer LM. An energy based analytical method to predict the influence of natural fractures on hydraulic fracture propagation, Engineering Fracture Mechanics; 2017. https://doi.org/10.1016/j.engfracmech.2017.11.020.
30. Yew CH, Weng X (2014) Mechanics of hydraulic fracturing. Gulf Professional Publishing, Houston
31. Zhao Y, He PF, Zhang YF, Wang L (2019) A new criterion for a toughness-dominated hydraulic fracture crossing a natural frictional interface. Rock Mech Rock Eng 52:2617–2629. https://doi.org/10.1007/s00603-018-1683-y
32. Zhao Y, Yongfa Z, Pengfei H (2019) A composite criterion to predict subsequent intersection behavior between a hydraulic fracture and a natural fracture. Eng Fract Mech 209:61–78. https://doi.org/10.1016/j.engfracmech.2019.01.015
33. Zhou J, Chen M, Jin Y, Zhang GQ (2008) Analysis of fracture propagation behavior and fracture geometry using tri-axial fracturing system in naturally fractured reservoirs. Int J Rock Mech Mining Sci Geo-Mech Abstracts 45:1143–1152

Part IV
Field Implication

Chapter 9
Formation of Complex Networks

9.1 Introduction

When a hydraulic fracture interacts with multiple natural fractures (such as bedding planes, faults, weak interlayers, and formation interfaces) in the formation, arrests, bifurcations, crossings, and openings may occur, contributing to forming a complex fracture network (referred as CFN). Shale differs from other types of rocks due to its apparent bedding anisotropy, making it easier to form complex fracture networks during hydraulic fracturing. A mass of field hydraulic fracturing data and laboratory studies have confirmed that the hydraulic fractures generated in shale reservoirs are not bi-wing planar fractures in homogeneous media, but multi-dimensional, asymmetric, and non-planar complex hydraulic fractures (as shown in Fig. 9.1) [1–3].

Although many scholars have investigated hydraulic fracture propagation and evaluated its spatial geometry through field and laboratory tests, most of the problems related to the control and reconstruction of hydraulic fracture networks are still empirical. Since there is no reliable standards to evaluate hydraulic fracturing effectiveness, it is difficult to adjust parameter settings and guide the construction process according to the hydraulic fracture network. Using a conventional hydraulic fracture model to simulate and guide fracturing design may lead to poor fracturing effectiveness or even the failure of fracturing. To qualitatively assess the hydraulic fracturing effectiveness, previous scholars have mainly divided the morphologies of hydraulic fracture into the following categories [4, 5]: (a) single transverse hydraulic fracture; (b) main Arc fracture; (c) fishbone-like complex fracture; (d) complex fracture network (see Fig. 9.2).

Research on the formation mechanism of complex fracture networks and effective fracture network reconstruction (number and connectivity of HF) have a pronounced impact on enhancing fluid infiltration and improving the extraction rate of shale gas [6]. However, technically limited by hydraulic fracturing (e.g., working pressure and flow), the recovery rate of shale reservoirs fluctuates from 5 to 60%), and the initial recovery rate is quite low (5–15%). The core reason is the stress shadow effect between different hydraulic fractures, which makes it fail to form a fracture network

Fig. 9.1 Hydraulic fracture morphology retained by injecting fluid into the particulate material matrix
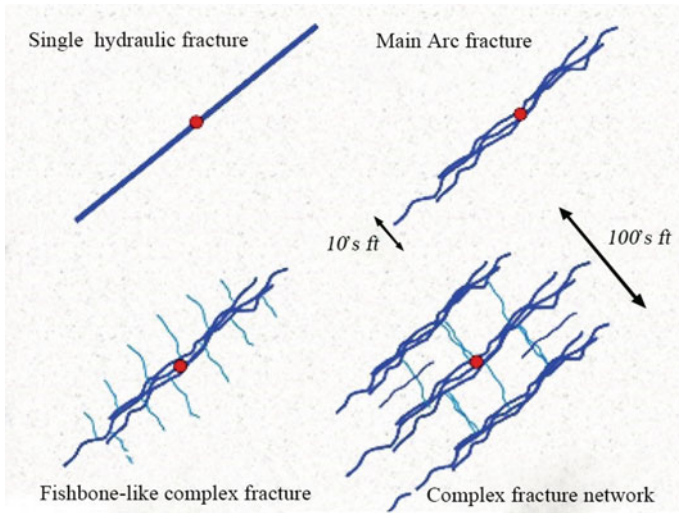

Fig. 9.2 Different types of hydraulic fracture morphology

in which multiple fractures simultaneously propagate. Effective fracture networks are fundamental to maximizing the production of shale gas [7, 8]. In addition, high-pressure injection during hydraulic fracturing reduces the effective stress of the local formation, which may induce fault activation and seismic slip [9]. The infiltration of fracturing fluid via secondary fractures can also deteriorate the pollution of groundwater. Therefore, it is particularly important to understand the formation mechanism of the complex fracture networks.

Based on experimental set-ups used for uniaxial and true triaxial hydraulic fracturing described in Chap. 2, this chapter investigated the deformation and hydraulic fracture propagation in different types of shales (Longmaxi shale and Lushan shale), bedding inclinations ($\beta = 0°$, $45°$ and $90°$) and stress levels (uniaxial stress state ($\sigma_H > \sigma_v = \sigma_H = 0$), normal-faulting stress regime ($\sigma_v > \sigma_H > \sigma_h$), strike-slip faulting stress regime ($\sigma_H > \sigma_v > \sigma_h$) and reverse faulting stress regime ($\sigma_H > \sigma_h > \sigma_v$), and qualified the formation mechanism of the complex fracture networks. The results can provide experimental references for hydraulic fracturing design and optimization of the fracturing parameters to obtain the optimal fracturing effectiveness, so as to enhance reservoir permeability and improve reservoir recovery.

9.2 Effect of Bedding Anisotropy on Hydraulic Fracturing

Shales are intrinsically anisotropic and heterogeneous sedimentary rocks due to the preexisting bedding planes and microfractures. Bedding anisotropy directly affects hydraulic fracture behaviors. Available data indicate that the propagation of hydraulic fractures perpendicular to the bedding plane requires higher injection pressure than that parallel to the bedding plane [10]. The change of bedding inclination will disturb the propagation pattern of hydraulic fractures, resulting in crossing, sliding, arresting and even opening at the intersection. Lin et al. [11] explored the effect of shale anisotropy on the propagation of hydraulic fractures using Longmaxi shale samples. They found that when the bedding inclination is greater than $60°$, hydraulic fractures would propagate along the bedding plane, while when the bedding inclination is small, the hydraulic fractures will deflect into the bedding direction. Guo et al. [10] performed triaxial hydraulic fracturing tests with anisotropy Longmaxi shale. The results demonstrate that the breakdown pressure of rock decreases with increasing bedding inclination, and the complex hydraulic fracture networks are prone to be created at the bedding inclination of $0–30°$. Wang et al. [12] quantitatively analyzed the hydraulic fracturing characteristics of anisotropic shale based on the fractal dimension and the equivalent fracture width. They found that with the increase of bedding inclination, the fractal dimension and equivalent fracture width showed an "S" shape (i.e. decrease-increase-decrease). However, previous studies do not reveal the relationship between shale anisotropy and acoustic emission evolution during hydraulic fracturing. In addition, limited by sample size (100–300 mm), current observation and description of fracture morphology mostly focus on the main hydraulic fracture. In fact, there are many micro-cracks around hydraulic fractures,

so it is necessary to carry out micro-scale observation of fractured shale samples to deepen our understanding of the influence mechanism of anisotropic bedding planes.

In this section, the acoustic emission technique is used to monitor fracturing characteristics of anisotropic shales ($\beta = 0°$, $45°$ and $90°$) in real time. Meanwhile, microscopic observations of hydraulic fractures are conducted on a stereomicroscope. Moreover, the hydraulic fracturing results of the Longmaxi shale and the Lushan shale are compared to clarify the impact of bedding anisotropy and rock heterogeneity on the hydraulic fracturing characteristics of shale.

### 9.2.1 Pump Pressure and Deformation

The evolution of shale hydraulic fractures is a complicated three-dimensional process. When pump pressure exceeds the bearing capacity of the surrounding rock, hydraulic fractures initiate. To gain an in-depth understanding of hydraulic fracture initiation and propagation, axial and circumferential strain gauges were used to measure the deformation in the process of hydraulic fracturing. Taking the results under an injection rate of 12 mL/min as an example, the effects of bedding anisotropy and matrix heterogeneity on the hydraulic fracturing fracture process are analyzed in the following part.

Figure 9.3 shows the evolution of pump pressure, deformation and acoustic emission of the Longmaxi shales and the Lushan shales with different bedding inclinations during hydraulic fracturing. It can be seen from Fig. 6.3 that as the bedding inclination increases from 0° to 90°, the breakdown pressure and instantaneous deformation (including circumferential (ΔD_c) and axial (ΔD_a)) of the two kinds of shale show a first increasing and then decreasing trend, which reaches the maximum at 45° bedding. This tendency agrees with the conclusions of Chong et al. [13] and Zhao et al. [14], who stated that the relationship between breakdown pressure and anisotropic angle approximately was characterized by a quadratic polynomial. Thus, we can conclude that the variation of shale anisotropy could mainly affect the breakdown pressure and instantaneous deformation during hydraulic fracturing.

Matrix heterogeneity would seriously complicate the effect of bedding anisotropy on the deformation and breakdown process. Comparing Fig. 9.3a–c and d–f, it can be found that in Longmaxi shale with good homogeneity, the hydraulic fracture initiation and propagation state can be identified according to the variation of AE cumulative energy. The fracture initiation and propagation pressures (15.10 MPa and 20.59 MPa) of the 0° sample are higher than those of 90° sample (11.67 MPa and 18.10 MPa). This can be attributed to the case that the 0° bedding is perpendicular to the axial stress. Initiation of micro-cracks induced by fluid injection must overcome axial stress limitation, so higher injection pressure is required. However, in the Lushan shale reservoirs with poor homogeneity, the AE count rate and cumulative energy increase steeply when the fluid pressure reaches the breakdown value. There is no microfracture initiation and propagation phenomenon before the injection pressure reaches the breakdown pressure, indicating that the Lushan shale matrix shows
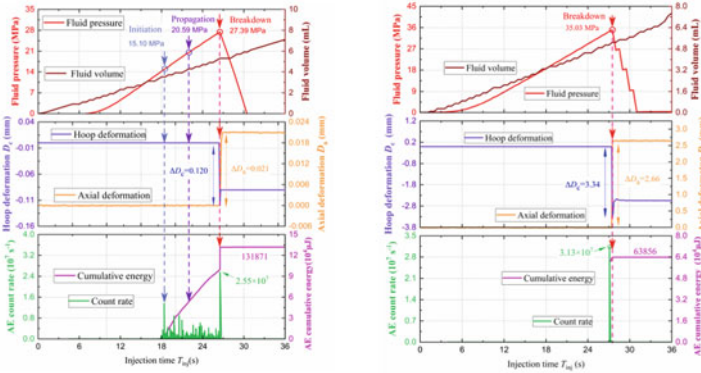
(a) Longmaxi sample CV-0-12(β=0°)   (b) Longmaxi sample CV-45-12(β=45°)
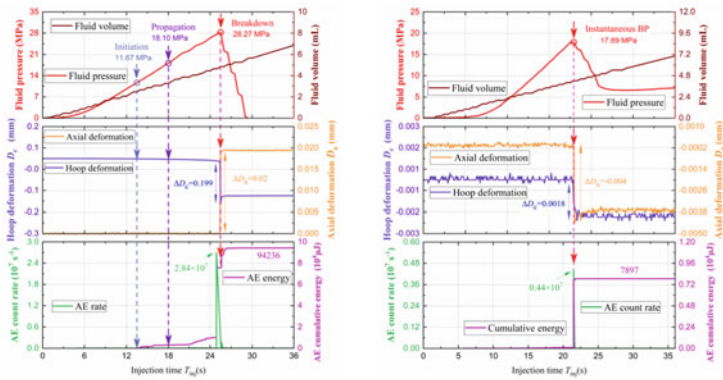
(c) Longmaxi sample CV-90-12 (β=90°)   (d) Lushan sample LV-0-12 (β=0°)
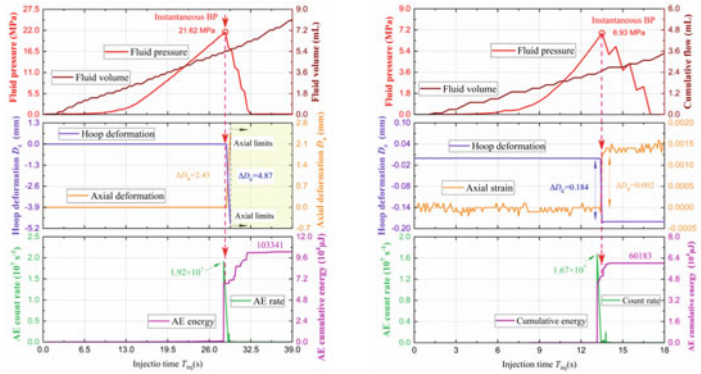
(e) Lushan sample LV-45-12 (β=45°)   (f) Lushan sample LV-90-12 (β=90°)

**Fig. 9.3** Fracturing results of anisotropic shale samples

typically brittle characteristics. Concerning the AE count rate and the cumulative energy, for the Longmaxi shale, when the bedding inclination increases from 0° to 90°, the AE peak count rate always keeps increasing, which is 2.55×107 s^{-1}, 3.13×107 s^{-1} and 5.4×107 s^{-1}, respectively, while the cumulative energy of AE first decreases and then increases. However, for the Lushan shale, with the increase of bedding inclination, AE peak count rate and AE cumulative energy increased first and then decreased. Du et al. [15] show that the AE counting rate reflects the initiation and propagation behavior of microcracks in the sample, and the AE cumulative energy reflects the energy consumption and fracturing degree of the sample. Therefore, it can be inferred that rock heterogeneity could suppress the effect of bedding anisotropy and make it mainly reflect in the initiation and evolution state of microfractures and the final rupture degree of the sample.

### 9.2.2 Acoustic Emission Response of Microfracture

As described in Sect. 4.2 of Chap. 4, the evolution characteristics of the dominant frequency band of the acoustic emission waveform can reflect the microfracture mechanism inside the rock. Specifically, the low-frequency signal corresponds to the tensile fracture, the medium-frequency signal reflects the tension-shear mixed fracture, and the high-frequency signal reflects the shear fracture. Figure 9.4 shows the time-varying frequency domain evolution curve of acoustic emission during hydraulic fracturing of anisotropic shale. Comparing Fig. 9.4a–c (or d–f), the evolution law of the induced microfractures is closely related to the bedding inclination during fluid injection. The proportion of low-frequency bands in anisotropic shales is generally more significant than the sum of the medium and high-frequency bands, indicating that tensile micro-fractures are mainly produced in the entire hydraulic fracturing process. Taking Longmaxi shale as an example, when the bedding inclination (β) is 0°, the proportions of low and high dominant frequency bands are 55.9% and 43.7%, respectively; When β is 45°, the low and high dominant frequency bands account for 80.59% and 17.3%, respectively; When β is 90°, the proportions of low and high dominant frequency bands are 87.5% and 2.5%, respectively. These phenomena indicate that with the increase of bedding inclination, the proportion of tensile micro-fractures increases, whereas the proportion of shear micro-fractures decreases. This is because under the action of the initial axial stress (without confining pressure), hydraulic fractures mainly initiate and propagate along the axial direction (i.e., the direction of the maximum principal stress). For samples with 0° bedding, hydraulic fractures will frequently intersect with beddings in their propagation path. More shear fractures are prone to be produced in the branching, initiation, and re-propagation at the intersection. For the samples with a bedding inclination of 90°, since the propagation direction of hydraulic fractures is consistent with the direction of the bedding plane, the tensile fractures are mainly generated in the 90° samples. In addition, in the time-varying frequency domain of acoustic emission of 45° samples, there is no stable propagation stage (III) of low-frequency and low-amplitude signals,

indicating that the samples with 45° bedding are entirely fractured, and no closed crack reopening or new cracks initiation can occur.

Comparing Fig. 9.4a–c and d–f), the difference in shale heterogeneity not only affects the evolution characteristics of mixed tension-shear micro-fractures, but also changes the relative size of each dominant frequency band. Specifically, for the homogeneous Longmaxi shale, the proportion of medium frequency band signals and the amplitude of each frequency band keep increasing with the increase of bedding
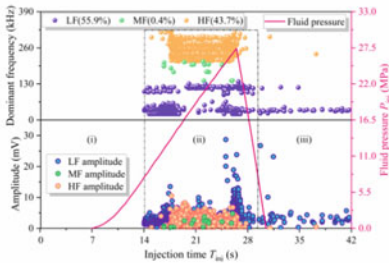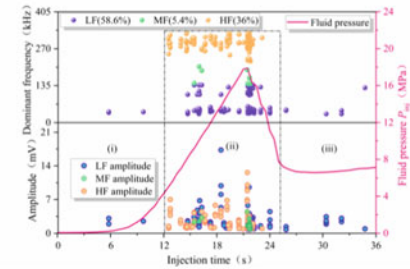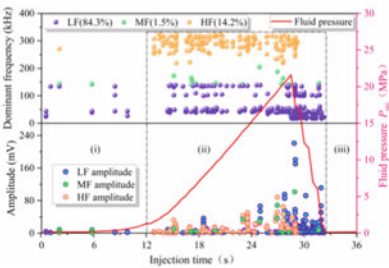

(a)Longmaxi sample CV-0-12(β=0°)   (b)Longmaxi sample CV-45-12(β=45°)
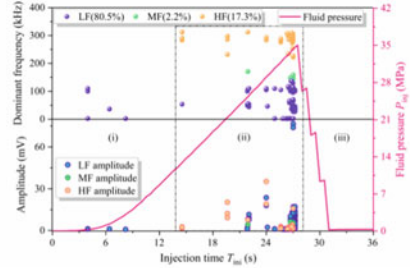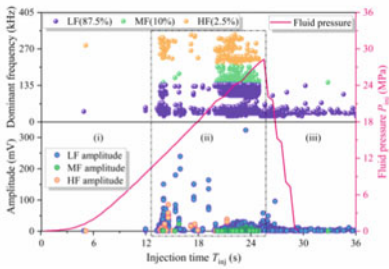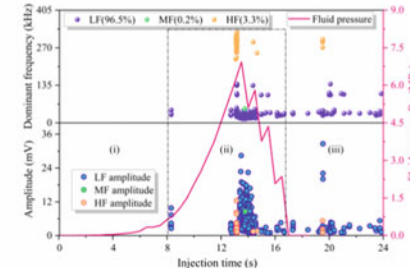
(c)Longmaxi sample CV-90-12(β=90°)   (d)Lushan sample LV-0-12(β=0°)

(e)Lushan sample LV-45-12(β=45°)   (f)Lushan sample LV-90-12(β=90°)

Fig. 9.4 Time-varying features of AE frequency domain of anisotropic shale samples during the fluid injection process

inclination. However, for the heterogeneous Lushan shale, the proportion of the medium frequency band decreases with the increase of the bedding angle, and the low-medium- and high-frequency amplitudes show a trend of increasing first and then decreasing. In addition, the influence of matrix heterogeneity can also be reflected by the time-domain distribution difference of frequency band signals. For example, the dominant frequency and amplitude detected in the Longmaxi shale concentrate mainly before the fluid pressure reaches the breakdown pressure. But in the Lushan shales with 0° and 45°, although the dominant frequency and amplitude have the same distribution trend as those of the Longmaxi shales when the bedding of Lushan shale is 90°, accumulation of dominant main signals are not visible before the injection pressure reaches the breakdown pressure. The reason for this phenomenon may be that the injected fluid directly activated the micro-cracks in the case of 90° bedding so no obvious signals appeared before the injection pressure reached the breakdown pressure.

9.2.3   Hydraulic Fracture Morphology

The anisotropic bedding plane of shale has a great impact on the hydraulic fracture propagation behavior. Figure 9.5 shows the macroscopic fracture propagation morphology on the sample surface after hydraulic fracturing. By exposing the sample to ultraviolet light, the fluorescent fracture path can be discerned. Overall, the hydraulic fracture propagation behavior is significantly different under different bedding inclinations. For the samples with a bedding inclination of 90°, the hydraulic fractures mainly spread along the bedding direction, resulting in vertical failure perpendicular to the fluid-injection direction. The propagation of the hydraulic fracture with a 45° bedding finally deflects toward the bedding plane. In the two types of shale, it can be observed that the hydraulic fractures are both 45° inclined to the horizontal plane. When the bedding plane of the sample is 0°, there are two propagation patterns. One is that hydraulic fractures propagate vertically and intersect with the bedding planes (Fig. 9.5a); The other is that the hydraulic fracture spread horizontally along the bedding plane (Fig. 9.5b).

Comparing Fig. 9.5a and b, it can be seen that the hydraulic fractures in Lushan shale are basically along the bedding plane regardless of varying bedding inclinations. By contrast, the fracture morphology in Longmaxi shale is relatively complex. Specifically, the hydraulic fracture of 90° Longmaxi shale bends to the direction perpendicular to the shale bedding, which is different from fractures parallel to bedding orientation in the 90° Lushan shale. For 45 shale, the hydraulic fracture oblique to the bedding finally deflects towards the axial direction. When the bedding inclination is 0°, the hydraulic fracture crosses the bedding and further extends vertically to the bedding plane. These differences can be attributed to the abundant and randomly-distributed microcracks and defects in Lushan shale (see Sect. 3.2 for microscopic observation). Initiation of hydraulic fractures will promote the rupture, coalescence and overlapping of these defects, forming a preferable way for hydraulic

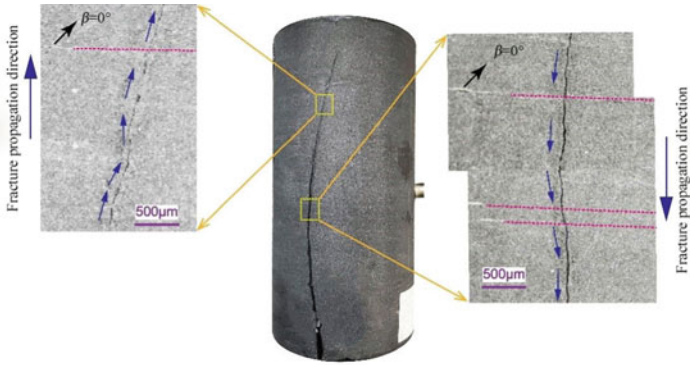**Fig. 9.5** Morphology of hydraulic fracture on sample surface
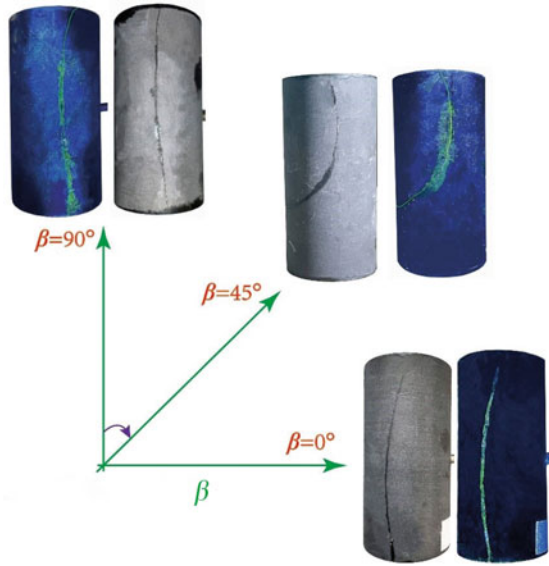
(a) Longmaxi shale
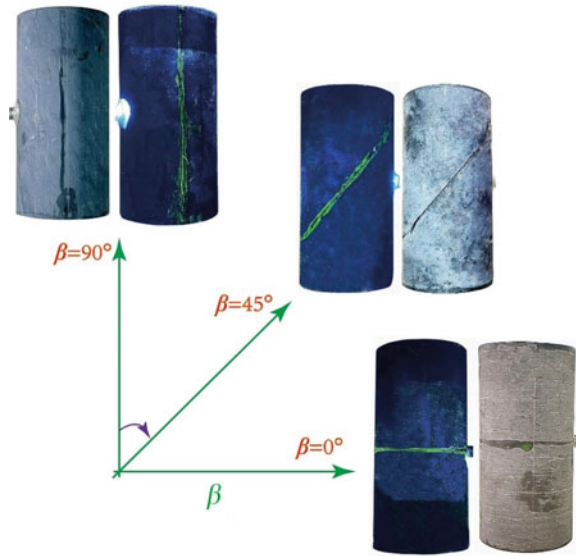
(b) Lushan shale

fracture to propagate in the bedding direction. On the contrary, Longmaxi shale a relatively homogeneous and bedding plane is not developed. Thus, hydraulic fractures are confined to grow along the mechanically preferential way, which results in axially growing hydraulic fractures.

To further analyze the influence of bedding anisotropy and matrix heterogeneity on hydraulic fracture propagation, the microscopic morphology of hydraulic fracture was observed by a stereomicroscope (500 μm). The results are shown in Figs. 9.6 and 9.7. Compared with 0° and 90°, 45° shale has the most twisted fracture path, and the fracture opening is the largest. Since these tests are carried out without confining pressure, the propagation of hydraulic fractures is mainly affected by the bedding planes, matrix homogeneity and axial stress. When the main hydraulic fracture spreads along the bedding, there will also be associated micro-fractures extending in the longitudinal direction. This conclusion can be verified by observing the fractures in Fig. 9.6c and 9.7b. In addition, whether the hydraulic fracture is parallel to or perpendicular to the bedding direction, the fracture opening varies slightly (Fig. 9.6b), indicating that the changes in fracture opening are probably dominated by the difference of individual samples rather than the bedding plane.

From Figs. 9.6 and 9.7, it can be found that the presence of defects in Lushan shale causes hydraulic fractures to propagate along the boundary of matrix defects (Fig. 9.7a) or through the shale matrix (Fig. 9.7c), and then the hydraulic fractures are slipped, branched or diverted. Especially, when the bedding inclination is 45°, an obvious shear spall zone appears near the main hydraulic fracture. The hydraulic fractures neat the matrix defects show "discontinuous and intermittent" on a microscopic scale (Fig. 9.7c). The hydraulic fractures in the discontinuous part are mainly connected with the shear dislocation zone (marked with red ovals in Fig. 9.7), forming complex hydraulic fractures.

Figure 9.8 summarizes the roughness parameters of the anisotropic shale fracture surface: (see Sect. 3.2.1 in Chap. 3 for definitions of these parameters). It is easy to find that with the increase of bedding inclination, the standard deviation (SD) of fracture surface elevation and the three-dimensional average inclination angle (θ_s) both show a first increasing and then decreasing trend. When the hydraulic fractures are inclined to the bedding planes ($\beta = 45°$), a relatively rough fracture surface is created. By contrast, the fracture surfaces generated by the propagation of hydraulic fractures perpendicular to the bedding planes ($\beta = 0°$) are rougher than those along the bedding planes ($\beta = 90°$). In addition, the surface roughness of Longmaxi shale is generally larger than that of Lushan shale. Due to the difference in matrix properties, the hydraulic fracture in Lushan shale propagates primarily along the bedding direction, while the fracture in Longmaxi shale mostly grows vertically confined by the axial stress. These two different propagation patterns lead to differences in the roughness of the fracture surface. From another point of view, this phenomenon also shows that the surface roughness of hydraulic fractures will decrease when they propagate along the bedding, while the propagation through the bedding is more conducive to the formation of rough and complex hydraulic fracture morphology. Therefore, in the actual fracturing operation, the induced hydraulic fractures should be designed to cross the shale beddings as much as possible to promote the formation of complex

(a)Longmaxi sample CV-0-12(β=0°)
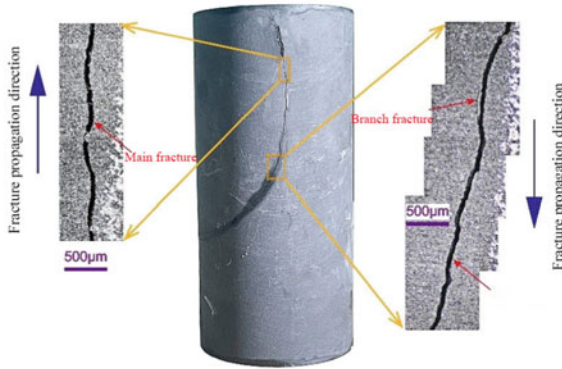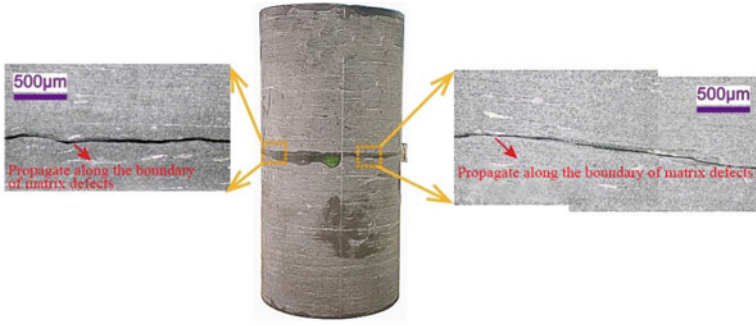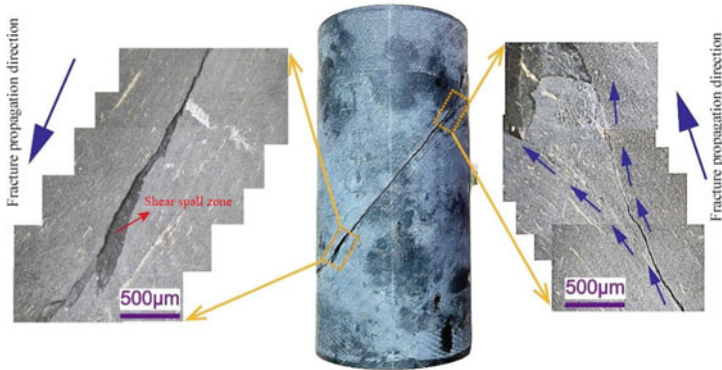

(b)Longmaxi sample CV-45-12(β=45°)
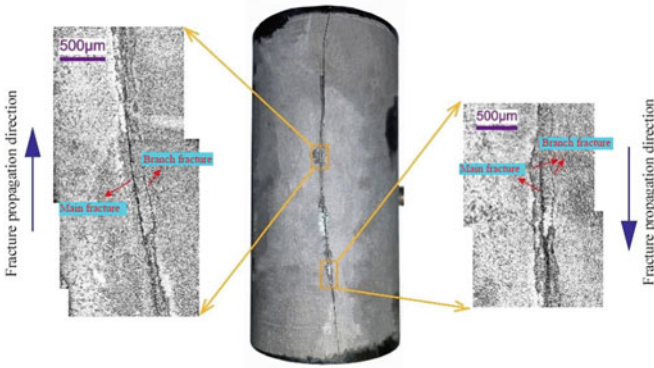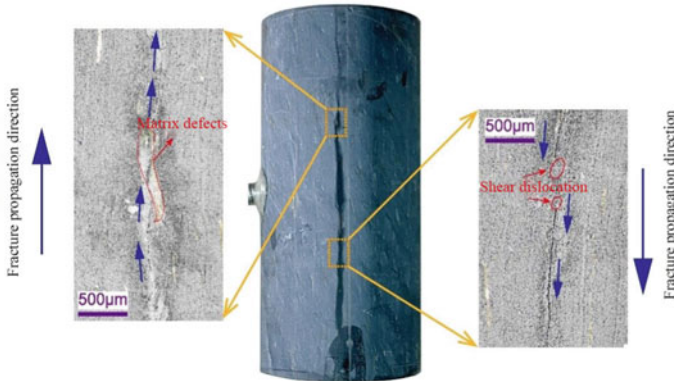

(c)Longmaxi sample CV-90-12(β=90°)

Fig. 9.6 Surface morphology of hydraulic fracture of anisotropic Longmaxi shale samples

(a)Lushan sample CL-0-12(β=0°)

(b)Lushan sample CL-45-12(β=45°)

(c)Lushan sample CL-90-12(β=90°)

Fig. 9.7 Surface morphology of hydraulic fracture of anisotropic Lushan shale samples

fracturing fracture networks with larger fracture surfaces, so as to provide a good channel for the effective migration of natural gas and improve the permeability and production of shale reservoirs.

9.3   Effect of Different In-Situ Stress States and Wellbore Orientations on the Formation Mechanism of Complex Fracture Networks

The true triaxial hydraulic fracturing tests can restore the three-dimensional stress state of reservoir rock, and more truly simulate the process of initiation and propagation of hydraulic fractures and the formation of fracture networks in shale-gas reservoirs. During the tests, the in-situ stress state (magnitude and direction) has an important influence on the formation of the fracture networks. The current hydraulic fracturing tests mainly focus on the effect of the in-situ stress magnitude (difference) on the propagation law and the complexity of fracture networks. Based on the true triaxial hydraulic fracturing tests, the research results of Ma et al. [16], Guo [17] and Zeng et al. [18] show that with the increase of the in-situ stress difference, the hydraulic fractures change from vertical fractures to horizontal fractures, and mainly propagate along the weak beddings to form a relatively simple hydraulic fracture morphology. In fact, when the magnitudes of the three principal in-situ stresses are the same, there are three stress states, as shown in Fig. 9.9, due to the different in-situ stress directions: normal faulting stress state ($\sigma_v > \sigma_H > \sigma_h$), strike-slip faulting stress state ($\sigma_H > \sigma_v > \sigma_h$) and reverse faulting stress state ($\sigma_H > \sigma_h > \sigma_v$). However, there are relatively few studies on the fracture network formation process in the context of the anisotropic stress state of the reservoirs. Zhou et al. [19] discussed the influence of the normal faulting stress state and strike-slip faulting stress state on hydraulic fracture morphology based on true triaxial hydraulic fracturing tests. The results show that under the normal faulting stress state, the hydraulic fractures mainly expand vertically with more branches along the way, while under the slip faulting stress state, the hydraulic fractures are tortuous and have fewer branches. However, Guo et al. [20] insisted that horizontal beddings are easier to be activated under a strike-slip faulting stress state, resulting in more branched hydraulic fractures. By analyzing the field data, Salvage and Eaton [21] found that the field hydraulic fracturing operations may change the direction of the principal stress of the formations, resulting in the stress state of the deep formations changing from the stress state of strike-slip faulting to the stress state of reverse faulting. Therefore, it is necessary to further analyze the influence of reverse faulting stress state on hydraulic fracture propagation and fracture network formation.

The wellbore orientation also plays a key role in the propagation of hydraulic fractures. Guo et al. [10] compared the effect of wellbore orientations including horizontal and vertical wellbores on fracture propagation law and found that the breakdown pressure of horizontal wellbore fracturing was lower than that of vertical
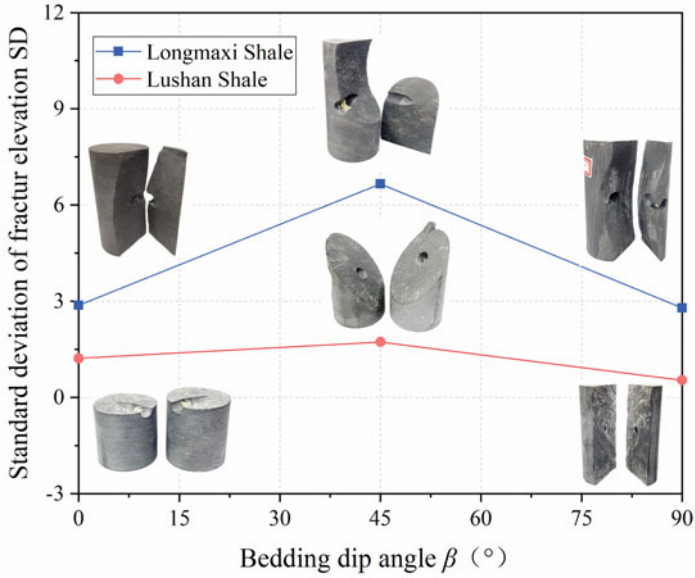
(a) Standard deviation of fracture surface elevation (SD)
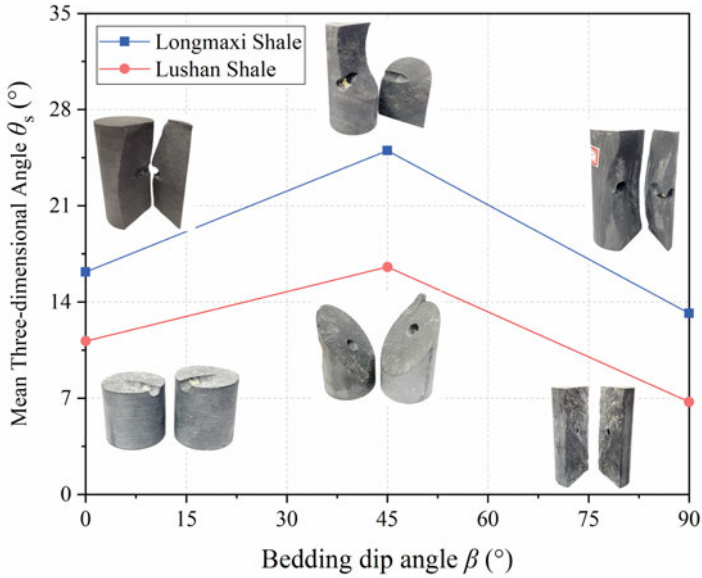
(b) Three-dimensional average inclination angle of fracture surface θ_s

Fig. 9.8 Evolution of fracture toughness parameters of anisotropic shale samples
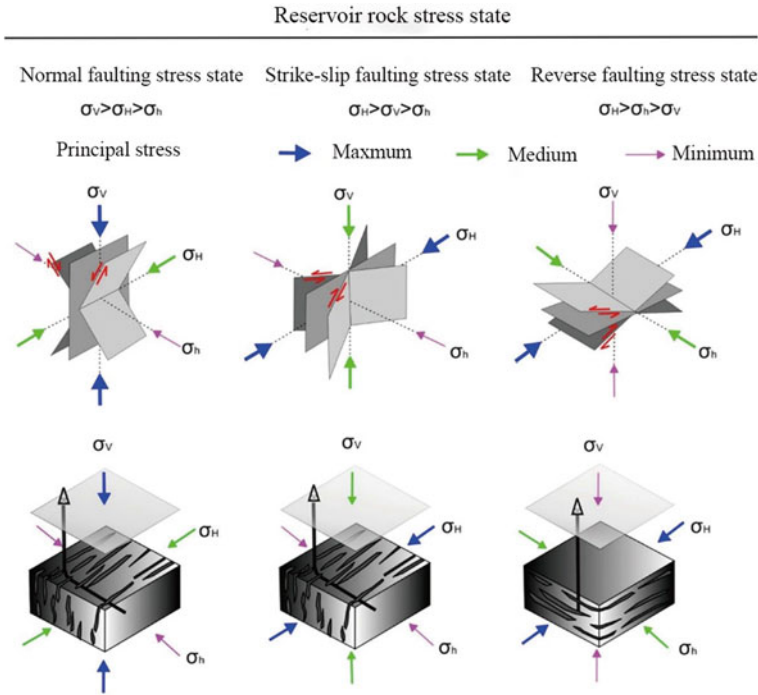
Fig. 9.9 Anisotropy of in-situ stress regime in shale reservoirs (revised from [22, 23])

wellbore fracturing, and horizontal wells mainly produce horizontal transverse fractures while vertical wells mainly produce vertical fractures. These phenomena are obvious at small bedding inclinations. However, the tests of Guo et al. [10] were carried out on cylindrical samples, so the fracture propagation is limited by the length in the radial direction of the samples. In this section, based on previous studies, the differences in bedding inclinations, in-situ stress states and well orientations were taken into account to more truly simulate the fracturing process in shale reservoirs. By analyzing the results of the true triaxial hydraulic fracturing test and quantitatively characterizing the shape and complexity of the fracture network with the help of statistical methods, the formation mechanism of the complex hydraulic fracture network in reservoir rock shale is revealed.

The results of the true triaxial hydraulic fracturing test are summarized in Table 9.1. By comparing samples #1 and #2, we can get the effect of the normal-faulting stress state and strike-slip faulting stress state on hydraulic fracturing results, as shown in Fig. 9.10a and b. The effect of the normal faulting stress state and reverse faulting stress state on hydraulic fracturing can be studied by comparing samples #3 and #4, as shown in Fig. 9.10a and b. samples #5 and #6 are used for hydraulic fracturing of horizontal wells under the assumption that the vertical stress is applied along the Z-axis, as shown in Fig. 9.10e and f.

Table 9.1 Hydraulic fracturing schemes and observation of experimental results

| No.	In-situ state	Injection rate (mL min^{-1})	Breakdown pressure (MPa)	Fracture morphology
#1	$\sigma_v > \sigma_H > \sigma_h$	20	27.27	Multiple HFs (M-III)
#2	$\sigma_H > \sigma_v > \sigma_h$	20	25.85	Multiple HFs (M-IV)
#3	$\sigma_v > \sigma_H > \sigma_h$	20	21.42	Single bi-wing HF (M-I)
#4	$\sigma_H > \sigma_h > \sigma_v$	20	19.19	Multiple HFs (M-II)
#5	$\sigma_v > \sigma_H > \sigma_h$	20	17.69	Multiple HFs (M-IV)
#6	$\sigma_H > \sigma_v > \sigma_h$	20	22.36	Single bi-wing HF (M-I)

9.3.1 Characteristics of Fluid Pressure and Deformation

(1) Fluid Pressure Response

The fluid pressure curves under various conditions can be described by four typical stages, which are the slow pressurization stage (stage I), rapid pressurization stage (stage II), pressure releasing stage (stage III), and pressure stabilization stage (stage IV), respectively (see Sect. 3.5.3 for details). However, there are still significant differences in injection pressure curves under different conditions, mainly reflected in stages II and IV. According to the division criteria of each stage of the injection pressure curve in Chapter II, stage II corresponds to the process of injection pressure increasing rapidly until reaching the breakdown pressure, and stage IV corresponds to the process of injection pressure stably fluctuating. We considered two in-situ stress states (normal faulting and strike-slip faulting) when investigating the hydraulic fracturing effectiveness of vertical wells (samples #1 and #2) whose wellbore is perpendicular to the bedding plane. In stage IV, there are two stages of pressure drop, pressure stability and pressure rise in sample #1, which may be caused by the pressure holding, re-initiation, and arrest of hydraulic fractures.

Compared with the injection pressure curve of sample #1, the injection pressure of sample #2 appears at an approximate climbing stage before reaching the breakdown pressure ($P_b = 25.85$ MPa), and the time for sample #3 to reach the stabilized pressure is 55 s longer than that of sample #1. The reason for the above phenomenon of sample #2 may be that the fluid pressurization causes the local cracking of the sample, resulting in the leakage of fluid through the crack, which eventually leads to the slow process of pressurization and pressure stabilization. Similarly, the injection pressure of sample #3 with an angle of 45° between the wellbore and bedding plane shows a phenomenon of slow decline and fluctuating rise before reaching the breakdown pressure, which can also be explained by the local cracking of the sample. The

Fig. 9.10 Curves of pump pressure and sample displacement with time under different beddings and true triaxial stress conditions
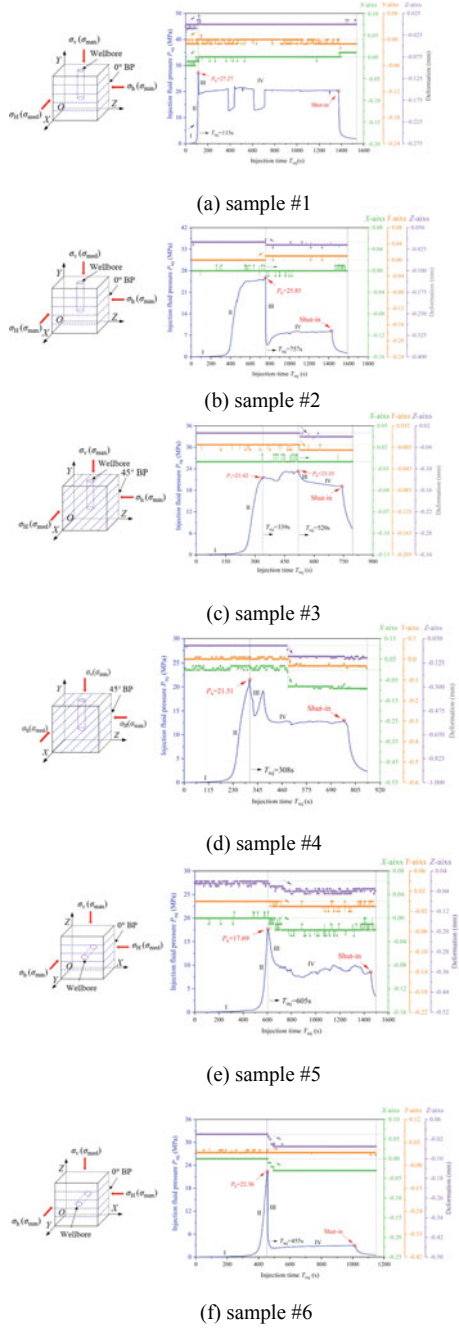
(a) sample #1

(b) sample #2

(c) sample #3

(d) sample #4

(e) sample #5

(f) sample #6

difference between the injection pressure changes of samples #2 and #3 in stage II can be attributed to the relative time difference between fluid pressure release and pressure holding caused by different crack cracking degrees. The difference between the injection pressure changes of samples #2 and #3 in stage II can be attributed to the difference in the relative time difference between fluid pressure release and pressure holding, which is caused by the difference in the crack cracking degree of samples #2 and #3. For sample #4 with 45° bedding, under the reverse faulting stress state, the injection pressure appears at the second peak which is defined as the secondary breakdown pressure ($P_b = 19.19$ MPa) after the breakdown pressure ($P_b = 21.51$ MPa), which reflects that the sample is not fully fractured at 21.51 MPa, and the subsequent injection can continue to hold pressure. When the injection pressure reaches 19.19 MPa, sample #4 is fully fractured, and then the pump pressure remains stable. Further, when the wellbore is parallel to the bedding plane (horizontal well fracturing), the evolution trend of the pump pressure evolution curve of the two samples (sample #5 is in normal faulting stress, and sample #6 is in tectonic stress state) is similar. The injection pressure curves of samples #5 and #6 maintain the characteristics of the above four stages, but there are still differences in breakdown pressure and pressure stabilization time due to different in-situ stress directions. These phenomena show that the stress mechanism will directly affect the variation trend of injection pressure by disturbing the crack initiation process. The deformation along the direction of the minimum principal stress is less than those along the directions of the middle and maximum principal stress.

(2) **Deformation Response**

It can be seen from Fig. 9.10 that the sample deformation caused by pumping is abrupt, which mainly occurs at the moment of fracturing ($P_{inj} = P_b$). Under different stress conditions, the deformation characteristics of samples induced by pumping are different. When the wellbore is perpendicular to the bedding, under the normal faulting stress state (Sample #1), the deformations in X-, Y- and Z-directions increase at the moment of breakdown, while under the strike-slip faulting stress state (Sample #2), at the moment of breakdown, the deformation in the X-direction is basically unchanged, the deformation in the Y-direction increases, and the deformation in the Z-direction decreases. When the wellbore is 45° with the bedding, at the moment of breakdown, sample #3 has no deformation in the X-direction, while the deformations in the Y- and Z-directions decrease. For sample #4 whose wellbore direction is consistent with the direction of the minimum principal stress, the deformations of sample #4 in three directions did not change when the injection pressure reached the breakdown pressure but began to decrease synchronously after 170 s from the breakdown point. When the wellbore is parallel to the bedding, the deformations of samples #5 and 6# in X-, Y- and Z-directions show a decreasing trend at the moment of sample breakdown. Therefore, different stress conditions significantly affect the deformation caused by injection pressure. On the one hand, in the process of constant flow pressurization, the fluid pressure acting on the wellbore is non-uniform distribution, which leads to a different release of injection pressure in different directions at the moment of breakdown, and eventually leads to uneven deformation of the

wellbore. On the other hand, due to the heterogeneity caused by the micro-cracks, beddings and other defects distributed in the shale, it is difficult to unify the initiation direction of hydraulic fractures at the moment of fracturing, which directly affects the propagation of subsequent fractures, and then affects the deformations of samples.
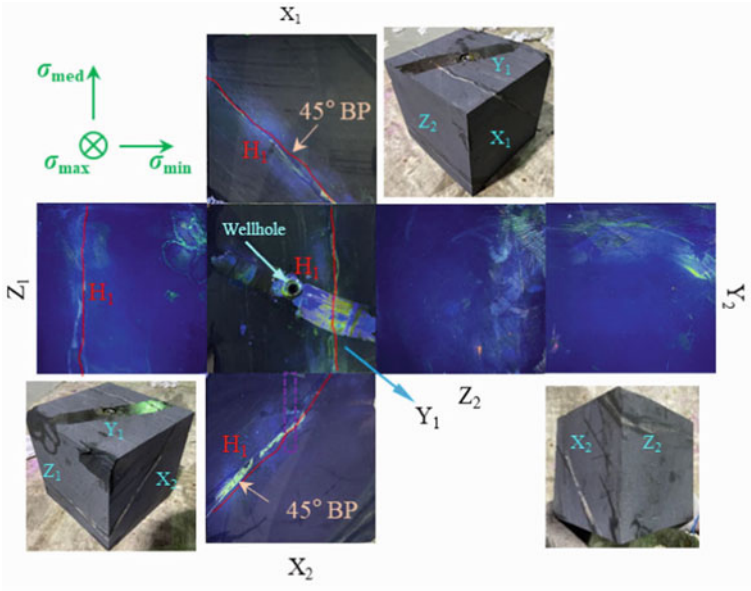
9.3.2 Hydraulic Fracture Propagation Modes

As summarized in Table 9.1, the morphology of hydraulic fractures can be mainly classified into four types in terms of different causes: (i) a single bi-wing hydraulic fracture (samples #3 and #6) generated by opening a weak bedding plane, which is called M-I; (ii) the multiple hydraulic fractures formed by cracking shale matrix and then coalescing with bedding planes, called M-II (e.g., sample #4); (iii) the multiple hydraulic fractures formed by activating natural fractures and then coalescing with bedding planes, which are called M-III (e.g., sample #1); (iv) the multiple hydraulic fractures formed by first cracking shale matrix and activating natural fractures and then coalescing with the bedding planes, called M-IV (e.g., samples #2 and #5). These experimental results are consistent with the observations of Warpinski et al. [24], Hou et al. [25], and Jiang et al. [26], who also conducted hydraulic fracturing experiments using similar anisotropic shale blocks.

For the convenience of analyzing, we introduced several symbols to characterize and distinguish the type of fractures induced by hydrofracturing. Fractures formed by cracking the shale matrix are defined as the main fractures M_i. Note that i hereafter refers to the fracture number of the specified fracture type ($0 \leq i \leq N$, N is the total number of fractures). The bedding planes opened by fracturing fluid are denoted as BP, the hydraulic fractures are represented by H_i, and the natural fractures activated by fluid injection are denoted as N_i.

Figure 9.11 shows the typical unfolded surface morphology of type M-I hydraulic fractures in the X–Z plane. The induced hydraulic fractures in samples #3 and #6 propagated along the direction of the bedding plane. The difference in bonding properties between beddings can cause the twisting of induced fractures, while the main fracture propagation direction did not turn and branch. Possible reasons for forming M-I type hydraulic fractures can be summarized as follows: (i) there is a fully developed bedding plane near the open hole section of the wellbore; (ii) no pre-existing natural fractures, joints and other weak bedding planes are distributed along the trajectory of induced hydraulic fracture; (iii) the tensile strength of shale matrix and the cohesion strength of other bedding planes are higher than the activated bedding plane.

Figure 9.12 depicts the unfolded surfaces of M-II multiple fractures by taking sample #4 as an example. Under the confinement of the maximum in-situ stress (σ_{max}), two main fractures (M_1 and M_2), parallel to the direction of the maximum in-situ stress, were formed in the shale matrix. The fluid pressure opened a bedding plane (45° BP) near the open hole section of the wellbore and formed a hydraulic fracture H_1. In the propagation process of fractures M_1 and M_2, the fluid pressure

(a) sample #3(with β=45° and $\sigma_v>\sigma_H>\sigma_h$)
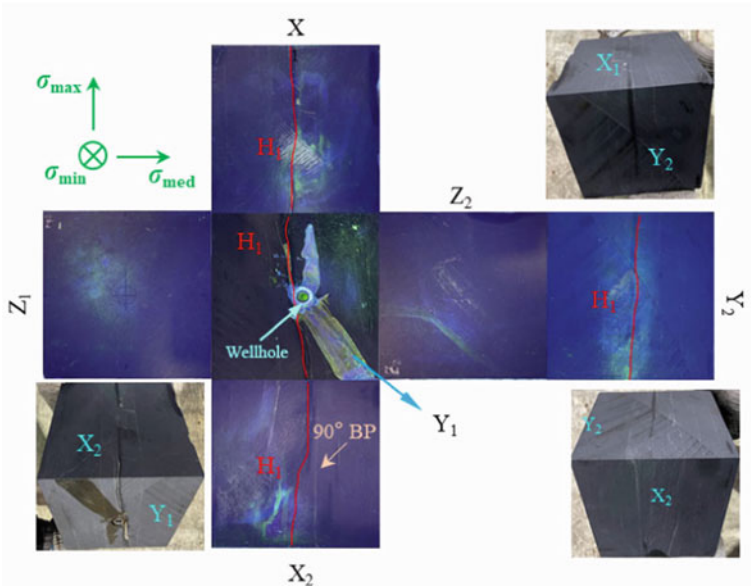
(b)sample #6(horizontal well and $\sigma_H>\sigma_v>\sigma_h$)

Fig. 9.11 Unfolded surface morphology of hydraulic fractures that belong to type M-I

successively opened two bedding planes, forming hydraulic fractures H_2 and H_3. The propagation path of the M-II type main fracture is relatively short, and the main fracture produces branches with the same propagation direction at the bedding. As shown in Fig. 9.12, the main fractures M_1 and M_2 only appear on the surface of X_2 of sample #4. When hydraulic fractures (M_1 and M_2) intersect with bedding planes, two fracturing effectiveness will occur: (1) hydraulic fractures are arrested by the bedding plane and open the bedding plane (H_3); (2) hydraulic fractures cross directly bedding planes and open bedding planes (H_1 and H_2). The activation of bedding will divert the fluid in the matrix fracture. Because the fluid is divided at H_1 and H_2, the fluid pressure is insufficient to make the matrix fractures (M_1 and M_2) cross the bedding plane when matrix fractures propagate to H_3, resulting in more fluid flowing into the bedding (H_3) and promote H_3 to propagate to other surfaces of sample #4. The main causes for this kind of hydraulic fracture (M-II) are as follows: (i) microcracks are highly developed in the rock matrix near the open hole section of the wellbore; (ii) the direction of the maximum in-situ stress is not parallel to the bedding plane but at an inclination angle of $\theta = 45°$; (iii) the initiation pressure of microcracks in the rock matrix is less than the cohesion strength of the bedding planes, so that the hydraulic fractures propagate along the direction of the maximum in-situ stress in the matrix before propagating along the bedding; (iv) the cohesion strength of the bedding planes is lower than the tensile strength of the rock matrix, which causes the matrix fractures M_1 and M_2 to cross and open the bedding planes (H_1, H_2, and H_3).
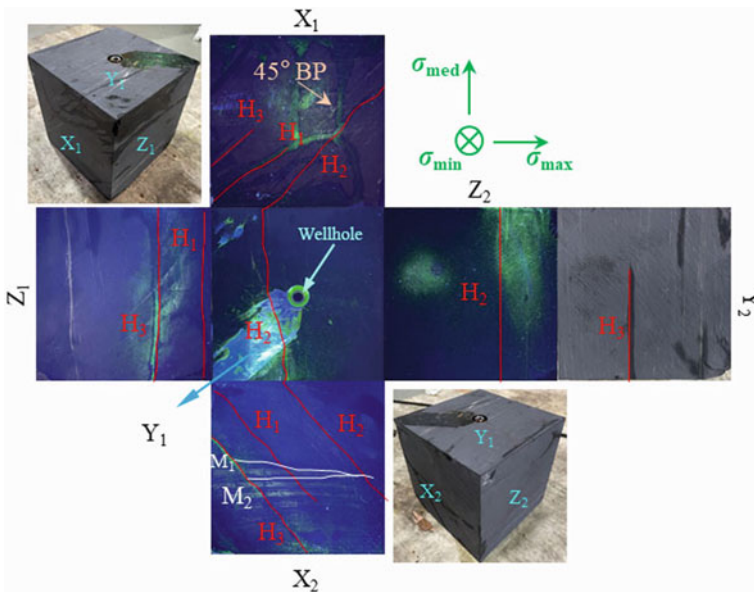

Fig. 9.12 Unfolded surface morphology of hydraulic fractures that belong to type M-II (Sample #4, $\beta = 45°$ and $\sigma_H > \sigma_h > \sigma_v$)

The M-III fracture morphology represented by sample #1 is displayed in Fig. 9.13. The cyan dotted line on the Z_2 surface in Fig. 9.13 is the location of the wellbore. It can be seen that hydraulic fractures (H_1, H_2, H_3, and H_4) are formed by the activation of bedding planes located in the open hole section of the wellbore due to fluid injection pressurization. It should be noted that the direction of the maximum principal stress is perpendicular to the direction of the bedding plane, and the hydraulic fractures propagating along the bedding plane first need to overcome the limitation of the maximum principal stress. Under the limit of the maximum principal stress, the range of each hydraulic fracture propagating along the bedding plane is small. For example, H_2 only propagates to the Z_2 surface, H_1 and H_3 only appear on the X_1 and Z_2 surfaces, and although H_4 appears on the four surfaces (X_1, X_2, Z_1, and Z_2), its propagation path does not completely connect the bedding planes where it is located. In addition, an obliquely propagating natural fracture N_1 is generated near the open hole section of the wellbore. The natural fracture is mainly distributed on the surfaces of X_2, Z_2, and Y_2, and is a branch of H_4 after the termination of its propagation at a 0° bedding, whose propagation direction is determined by the interaction of the maximum principal stress and the fluid pressure. The causes of M-III type fractures are as follows: (i) the fluid pressure first opens the bedding plane in the open hole section of the wellbore; (ii) the natural fracture in the open hole section of the wellbore is activated; (iii) when the fracturing fluid encounters a bedding plane in the activation process of a natural fracture, fluid pressure will directly open the bedding plane.
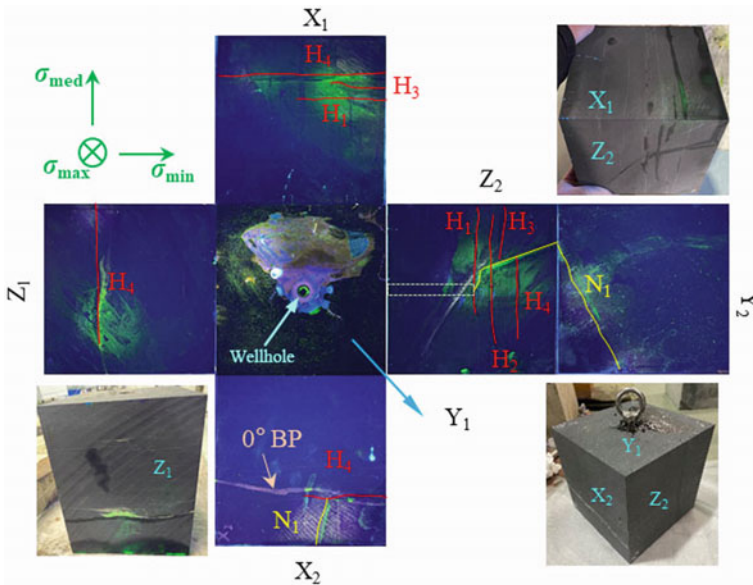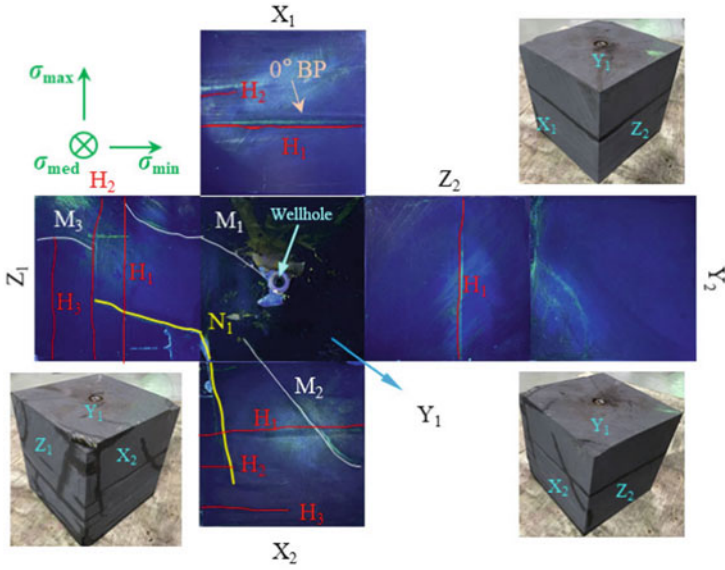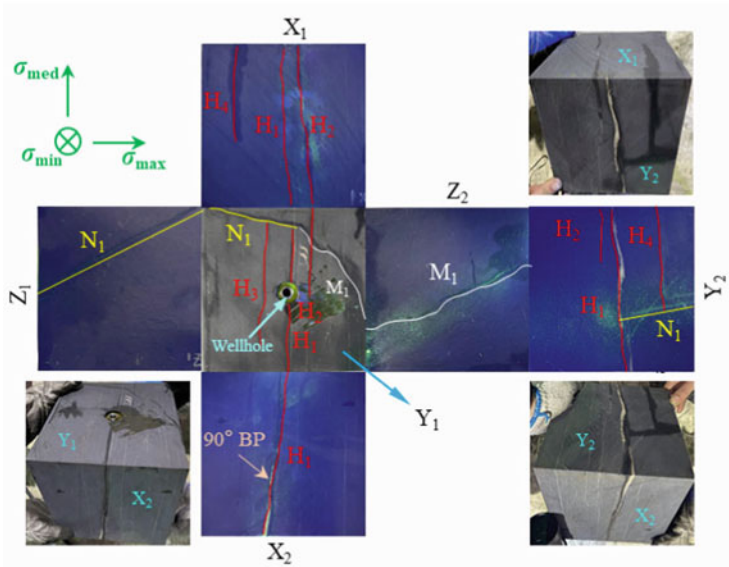

Fig. 9.13 Unfolded surface morphology of hydraulic fractures that belong to type M-III

Unfolded surfaces of M-IV type hydraulic fracture morphology after fracturing is shown in Fig. 9.14. This type of hydraulic fracture includes cracked shale matrix, opened bedding planes, and activated natural fractures. The hydraulic fractures are connected and overlapped with each other to form a complex fracture network. The formation process and network morphology of hydraulic fractures significantly differ under different matrix and bedding structures. For example, there are three matrix fractures M_1, M_2, and M_3 propagating obliquely in sample #2. From the perspective of fracture penetration on the surface, M_1 is directly overlapped with the wellbore and mainly appears on Y_1 and Z_1 surfaces, M_2 appears on Y_1 and X_2 surfaces, and M_3 only appears on Z_1 surface. The matrix fractures appear intermittently and are mainly connected with the bedding plane (H_1 and H_2) and the natural fracture (N_1). When there are hydraulic fractures formed by opening bedding and hydraulic fractures formed by cracking the matrix at the same time near the wellbore, the tensile strength of the matrix is generally higher than the cohesion strength of the bedding, so the former usually give priority to cracking. It can be inferred that for this type of hydraulic fracture, the natural fracture (N_1) is activated in the process of hydraulic fracture propagating along the bedding, and finally, the hydraulic fracture extends along the matrix. Due to the different degrees of disturbance by opening bedding, the hydraulic fractures formed by cracking the matrix are not continuous. Similarly, in sample #5, the hydraulic fractures (H_1, H_2 and H_3) propagating along beddings near the wellbore activate the natural fracture (N_1) during their propagation process and induce the matrix to crack, forming a main fracture (M_1). The reason for M-IV type hydraulic fractures are as follows: (i) the bedding planes with similar cohesion strength near the wellbore are fully developed, resulting in multiple bedding planes being opened; (ii) natural fractures exist in the rock matrix, which is the key to the evaluation of the propagation behavior of the main fractures and the formation of complex fracture networks.

In summary, hydraulic fractures in shale reservoirs primarily propagate along the bedding plane. However, due to different in-situ stress states and the distribution of natural fractures, hydraulic fractures may have different propagation modes, forming different fracture network morphology. Based on the initiation and propagation mode of hydraulic fractures in anisotropic shale reservoirs, hydraulic fracture morphology could be divided into four categories in detail: (1) a single bending hydraulic fracture formed by propagating along the bedding (Fig. 9.15a); (2) fishbone-like hydraulic fractures formed by hydraulic fractures crossing the beddings (Fig. 9.15b); (3) dendritic fractures formed by hydraulic fractures first propagating along the beddings and then activating natural fracture (Fig. 9.15c); and (4) a complex fracture network formed by hydraulic fractures opening and crossing the beddings and activating natural fractures (Fig. 9.15d).

(a)Sample #2(Vertical well and $\sigma_H > \sigma_v > \sigma_h$)

(b)Sample #5(Horizontal well and $\sigma_v > \sigma_H > \sigma_h$)

Fig. 9.14 Unfolded surface morphology of hydraulic fractures that belong to type M-IV
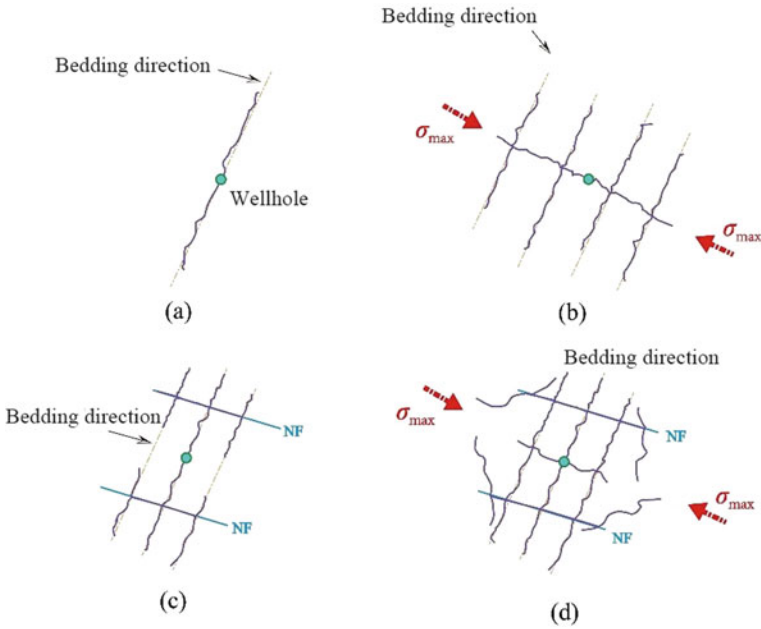
Fig. 9.15 Classification of fracture networks after hydrofracturing in anisotropic shale reservoirs

9.3.3 Quantitative Evaluation of Fracture Morphology

To quantitatively evaluate the morphological characteristics of the hydraulic fracture network under various working conditions, the three-dimensional hydraulic fracturing effectiveness is quantitatively evaluated by counting the induced fracture occurrence and stimulated rock area (SRA) [25].

(1) **Induced Fracture Occurrence**

In order to better display the distribution of hydraulic fractures in the fractured samples with three bedding inclination angles, a polar coordinate axis is established with the wellbore center as the origin as shown in Fig. 9.16. The distribution angle between the induced fracture and horizontal bedding plane is defined as β. When the fracture is parallel to the horizontal bedding plane, β is 0°, and the sign of β is assumed to be positive in the clockwise direction.

The statistical results of the induced fractures for each sample were quantitatively presented in the form of a rose diagram (Fig. 9.17) in accordance with the method suggested by Taleghani and Olson [27] and Ezati et al. [28]. It is easy to see that the main reasons for the formation of multiple hydraulic fractures (M-II, M-III and M-IV) are the simultaneous initiation of multiple bedding planes in the open hole section of the wellbore and the generation of main fractures propagating along the shale matrix. The reason for the formation of a single bending fracture (M-I) is
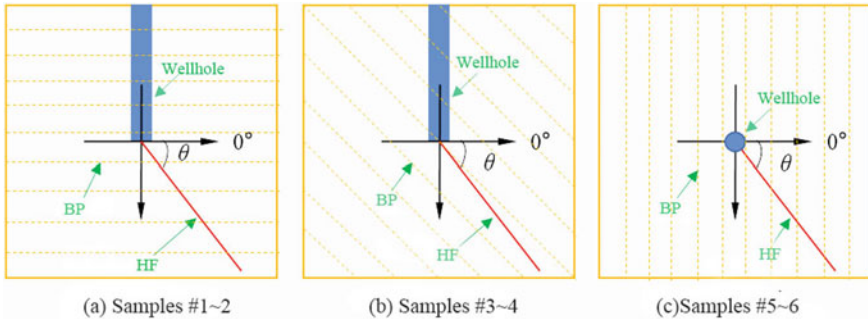
(a) Samples #1~2   (b) Samples #3~4   (c)Samples #5~6

Fig. 9.16 Schematic diagram of hydraulic fracture statistical method

that there is only one hydraulic fracture propagating along a bedding plane near the wellbore. In addition, it can be found that the number of hydraulic fractures in the sample with activated natural fractures is more than that in the sample without activated natural fractures, which indicates that the activation of natural fractures leads to more branches and more complex fracture networks.

(2)   **Stimulated Rock Area**

The fracture network generated by hydraulic fracturing of shale samples is composed of one or more combinations of the main fractures, the activated natural fractures
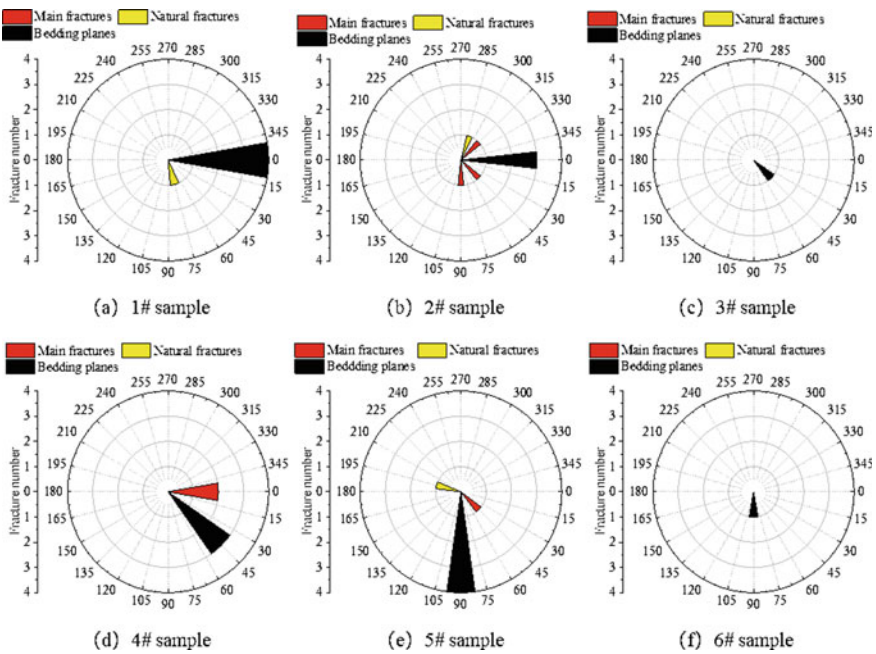

(a) 1# sample   (b) 2# sample   (c) 3# sample

(d) 4# sample   (e) 5# sample   (f) 6# sample

Fig. 9.17 Rose diagram of hydraulic fractures occurrence in each sample

(turning, opening or crossing), and the opened bedding planes. Since the hydraulic fracture morphology of the sample is the observation result under the condition of three-dimensional complete unloading, the traditional method of calculating the stimulated reservoir volume [29] is no longer applicable, so the "stimulated reservoir area (SRA)" proposed by Hou et al. [30] is used to evaluate the hydraulic fracturing effectiveness. According to Hou et al., the SRA was the total area of the main fractures, the opened bedding planes and the activated natural fractures, which were divided into four grades based on the fracture area: 1.0 (approximately 200 mm × 200 mm), 0.75 (approximately 150 mm × 150 mm), 0.5 (approximately 100 mm × 100 mm), and 0.25 (approximately 50 mm × 50 mm). Moreover, larger SRA resulted in a larger fracture area in the reservoir, which was conducive for complex fracture formation and gas migration. Using identical method, we analyzed the shale fracturing effectiveness under different conditions.

The SRA of various types of fractures calculated by fracturing samples is shown in Fig. 9.18. The SRA actually reflects the extent of fracture propagation, while the counted number of hydraulic fractures represents the complexity of fractures. On the whole, the SRA of four types of hydraulic fracture (M-I, M-II, M-III and M-IV) in Sect. 9.3.2 increases successively, and the complexity of the four types of hydraulic fracture also increases correspondingly. The M-IV type fractures (samples #2 and #5) with activated natural fractures and opened bedding planes have the best effectiveness in increasing and stabilizing production. There is an overall good correspondence between the SRA value and the counted number of hydraulic fractures. However, it is insufficient to evaluate the hydraulic fracturing effectiveness only by SRA value or the counted number of hydraulic fractures. For example, the SRA values of samples #2 and #4 are 0.5, but the number of the main fractures is 3 and 2, respectively (Fig. 9.18a). In opened bedding planes, the SRA of samples #1 and #2 are 1.25 and 1.5, whereas the number of (activated) bedding planes is 4 and 3 (Fig. 9.18b). Although samples #1, #2, and #4 have the same counted number of natural fractures, their SRA values are different (Fig. 9.18c). These differences may be related to the limitation of the sample size. Although a large-scale shale sample with a side length of 200 mm has been used in the tests, such a sample size is still insufficient to reflect the state of reservoir rocks. Therefore, in the process of hydraulic fracturing tests, once hydraulic fractures propagate to the surface of the sample, the fracturing fluid is likely to leak directly through the induced fractures, resulting in the instantaneous reduction of fluid pressure, which cannot drive other fractures to continue to propagate. In other words, the SRA value is essentially related to the time when the hydraulic fracture propagates to the surface of the sample. The larger the sample size is, the larger the SRA value of each type of hydraulic fracture will be. Therefore, the SRA value and the counted number of hydraulic fractures are synchronously adopted as the quantitative evaluation indexes to evaluate the hydraulic fracturing effectiveness.
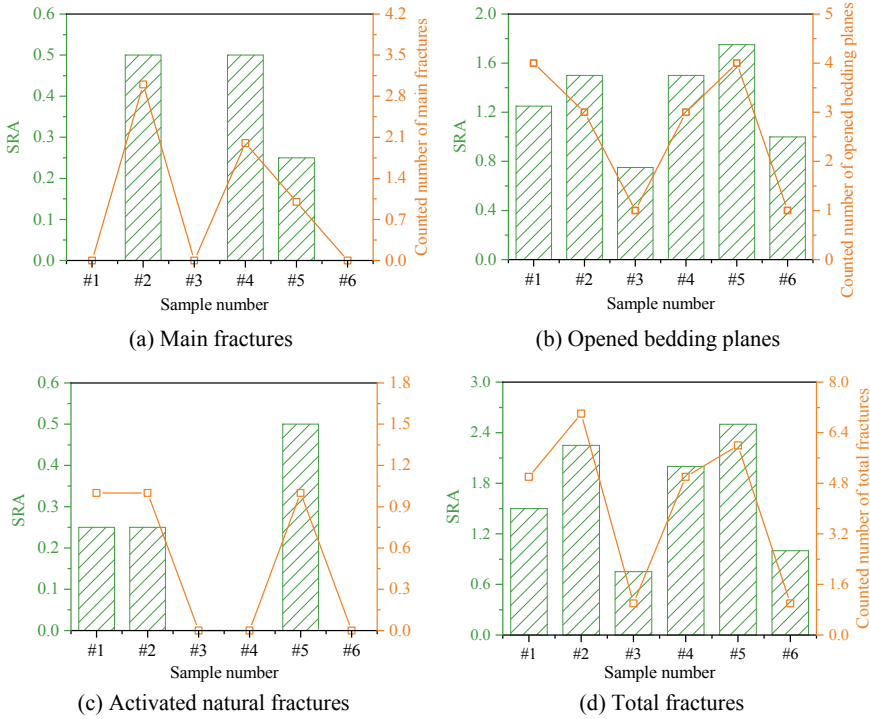
Fig. 9.18   SRA and fracture number distribution of the fractured shale samples

9.3.4   *Effects of Bedding Planes*

By comparing the fracture morphology of sample #1 (the bedding is orthogonal to the wellbore), sample #3 (the bedding is oblique to the wellbore (45°)), and sample #5 (the bedding is parallel to the wellbore), the influence of anisotropic bedding on the fracture network morphology is analyzed. It can be seen from Table 6.1 that samples #1, #3 and #5 are in a normal faulting stress state.

When the bedding is vertical to the wellbore, the fracture network of sample #1 belongs to dendritic hydraulic fractures (M-III type) that propagate along the beddings and activate natural fractures. We found five hydraulic fractures in sample #1, four of which (H_1, H_2, H_3, and H_4) propagate along the 0° bedding planes, and one of which (N_1) is an activated natural fracture. The calculated SRA of all fractures in sample #1 is 1.5 in line with Fig. 9.18. However, under the same stress state, when the angle between the bedding and the wellbore is 45°, only a single hydraulic fracture (M-I) is produced in sample #3, and the calculated SRA is 0.75, which is 50% lower than that of the sample #1. When the bedding is parallel to the wellbore, the hydraulic fracture morphology of sample #5 is M-IV complex fracture network morphology,

and compared with samples #1 and #3, sample #5 has the largest SRA value and the counted number of hydraulic fractures, which are 2.5 and 6 respectively.

Comparing the SRA values of samples #1, #3, and #5, it can be found that the hydraulic fracturing effectiveness is the smallest when the bedding inclination is 45°, which seems to be in contradiction with Sect. 9.2 of this chapter. However, it should be noted that the sample size used in the true triaxial fracturing tests is larger than that used in the uniaxial tests. During the sampling process, it is inevitable to produce differences in individual properties, resulting in the fracture morphology of sample #3, not in line with expectations. Therefore, the difference between the bedding and fracture morphology of shale before and after the test is compared to explain the cause of this phenomenon. As shown in Fig. 9.19a, comparing the photos before and after the test of sample #1, it can be found that although the beddings of sample #1 propagate horizontally as a whole, the propagation track is not straight, and the spacing and distribution of beddings are also extremely uneven. The beddings on the Z_1 surface do not appear in the X_1 surface, indicating that the beddings on the Z_1 surface are not fully developed. For these reasons, after multiple beddings are opened instantaneously to form hydraulic fractures, they will not always propagate along the bedding of Z_1 surface, but will deflect or terminate under the disturbance of the maximum principal stress. The actual propagation morphology of sample #1 (Fig. 9.13) also confirms this conclusion. However, it can be seen from Fig. 9.19b that there is obvious bedding that completely extends to the surface of sample #3, resulting in the tendency of the sample to slip along 45° during the loading process of three-dimensional stress. In addition, during the fluid injection process, new cracks initiate near the weak bedding, and the fracturing fluid flows into the bedding plane, further reducing the effective stress of the bedding. Once the sample breaks slightly along the bedding plane, the fluid pressure is released instantly and drives the hydraulic fracture to propagate along the bedding plane, forming a single hydraulic fracture propagating along the 45° direction. In Fig. 9.19c, the local details of sample #5 whose bedding is parallel to the wellbore before and after fracturing are compared. It is easy to find that there is no obvious weak bedding before the test in the sample #5, and beddings with the same width are densely distributed near the wellbore. Shale with this structure is prone to crack at many places during hydraulic fracturing to form multiple hydraulic fractures propagating along beddings. In addition, there is no obvious weak bedding in sample #5, which ensures that the hydraulic fractures can propagate along their mechanical optimal direction and the bedding direction. This process may lead to the initiation of fracture matrix, activation of natural fractures, and forming an M-IV type of complex fracture network. It should be noted that since the wellbore of sample #5 is arranged horizontally, in addition to the bedding plane, the wellbore orientation may also be a factor in the generation of the M-IV fracture network, which will be discussed in Sect. 9.3.6.

In conclusion, hydraulic fractures in anisotropic reservoirs mainly initiate and propagate along the bedding plane. The complexity of the hydraulic fracture network depends on the distribution of beddings and the difference in bedding strength and is less affected by the change of bedding inclination angle. When a bedding plane is developed, a hydraulic fracture directly penetrates the bedding to form a single
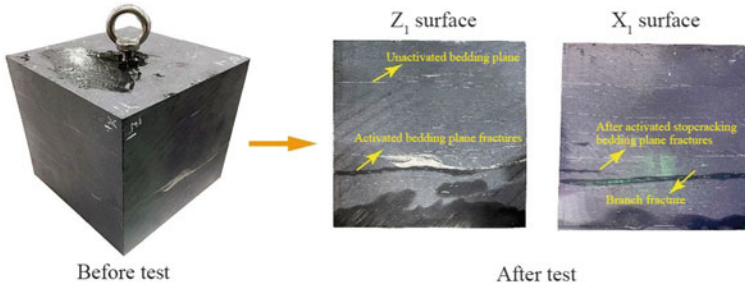
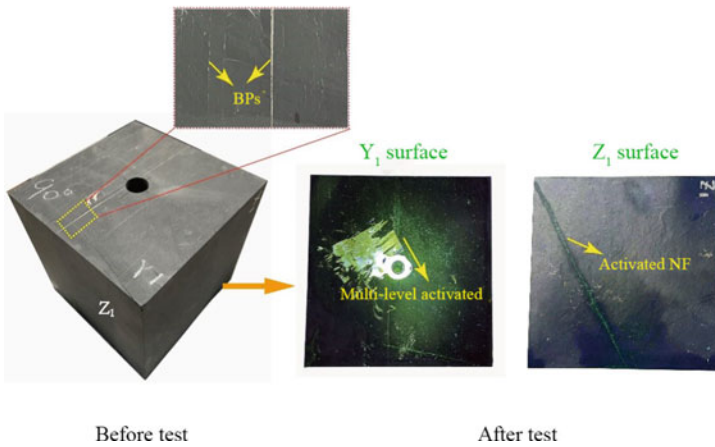(a)Sample #1(The bedding is 90° orthogonal to the wellbore)
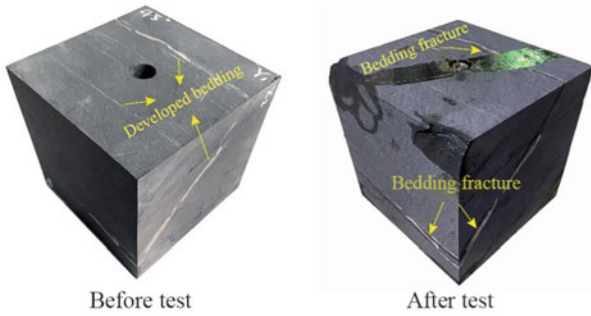
(b)Sample #3(The bedding is 45° orthogonal to the wellbore)

(c)Sample #5(The bedding is parallel to the wellbore at 0°)

Fig. 9.19 Effect of bedding on hydraulic fracture networks

hydraulic fracture, while when the bedding planes are uniformly distributed or locally developed, it is easier to form a relatively complex fracture network. In the actual fracturing, to prevent fluid leak-off into the beddings near the wellbore, the plugging agents are widely used, and the fracturing parameters (injection rate, injection pressure, fluid viscosity) can be adjusted to make fracture reorientation.

9.3.5 Effects of In-Situ Stress

Under a normal faulting stress state ($\sigma_V > \sigma_H > \sigma_h$), the dendritic hydraulic fractures (M-III) formed by activating natural fractures and then coalescing with bedding planes are generated in sample #1. The SRA value and the counted number of hydraulic fractures of sample #1 are 1.5 and 5, respectively. However, under the strike-slip faulting stress state, a complex fracture network (M-IV) with activated natural fractures and open bedding planes is generated in sample #2. The SRA value and the total number of fractures are 2.25 and 7, respectively. In comparison, the fracture area and fracture complexity of sample #2 are higher than those of sample #1, which indicates that it is easier to form tortuous and complex hydraulic fracture morphology under the strike-slip faulting stress state. The bedding inclination angle and in-situ stress difference of samples #1 and #2 are the same, but the direction of the maximum in-situ stress is different. Concretely, the direction of the maximum principal stress of sample #1 is perpendicular to the bedding plane, while the direction of the maximum principal stress of sample #2 is parallel to the bedding plane. In the process of hydraulic fracturing, the maximum principal stress in the normal faulting stress state inhibits the initiation and propagation of hydraulic fractures along the 0° bedding, while the maximum principal stress in the strike-slip faulting stress state is easier to make hydraulic fractures propagate horizontally along the bedding plane. Therefore, under the strike-slip faulting stress state, the resistance of hydraulic fracture propagating along 0°bedding is small, and more fractures propagating along bedding may be generated. When the beddings of shale are not developed, under the combined action of fluid pressure and maximum principal stress, multiple bedding planes may occur, resulting in multiple hydraulic fractures propagating along the bedding inclination. During the propagation of hydraulic fractures along the bedding plane, fluid activates natural fractures and even induces the cracking of the shale matrix. Therefore, under the strike-slip faulting stress state, the morphology of hydraulic fracture is more complex. This conclusion is consistent with the indoor true triaxial test observations by Guo et al. [20], Zhou et al. [19], and Hou et al. [31].

In the case of horizontal well fracturing, the fracture patterns under the normal faulting and strike-slip faulting stress are also compared. The M-IV complex fracture network is produced in sample #5 under the normal faulting state, while a single hydraulic fracture is generated in sample #6 under the strike-slip faulting stress state. This is because there is a well-developed bedding plane in sample #6 (Fig. 9.20),

which leads to the fact that in the process of hydraulic fracturing, a hydraulic fracture directly cracks and propagates along this bedding plane without multiple fractures forming complex fractures. However, under the strike-slip faulting stress state, the propagation path of the main fracture of sample #6 is tortuous (as shown in Fig. 9.11b), and its tortuosity is higher than that of the main fracture of sample #5 (Fig. 9.14b), which is consistent with the conclusion that the sample in the stress state of strike-slip faulting is more likely to produce tortuous hydraulic fracture.

When the bedding inclination angle is 45°, the influence of the normal faulting stress state and reverse faulting stress state on the morphology of hydraulic fracture can be analyzed by comparing those of samples #3 and #4. It can be seen from Sect. 9.3.2 of this chapter that sample #3 has a single hydraulic fracture (M-I), under a normal faulting stress state. Because there is obvious bedding in sample #3 (Fig. 9.19b), under the action of the maximum vertical principal stress and fluid pressure, the hydraulic fracture mainly initiates and propagates along the bedding, forming a single hydraulic fracture. However, under the reverse faulting stress state ($\sigma_H > \sigma_h > \sigma_V$), the maximum principal stress is arranged along the horizontal direction, while the vertical in-situ stress is the minimum principal stress. Under the reverse faulting stress state, hydraulic fractures of sample #4 propagate along bedding planes and induce the activation of natural fractures to form dendritic hydraulic fractures (M-II). The SRA value and the counted number of hydraulic fractures are 2 and 5 respectively, which are higher than those of sample #3 (0.75 and 1 respectively) under a normal faulting stress state, indicating that the fracture morphology of sample #4 is more complex and the fracturing effectiveness of sample #4 is better. This phenomenon also shows that compared with the normal faulting stress state, the reverse faulting stress state is also conducive to the formation of complex hydraulic fractures in shale reservoirs. In addition, since the vertical stress has the least restriction on the sample, the shale matrix in sample #4 is cracked along the direction of the maximum principal stress, and two main fractures connecting the parallel bedding planes are generated (M_1 and M_2 in Fig. 9.12), forming dendritic hydraulic fractures.
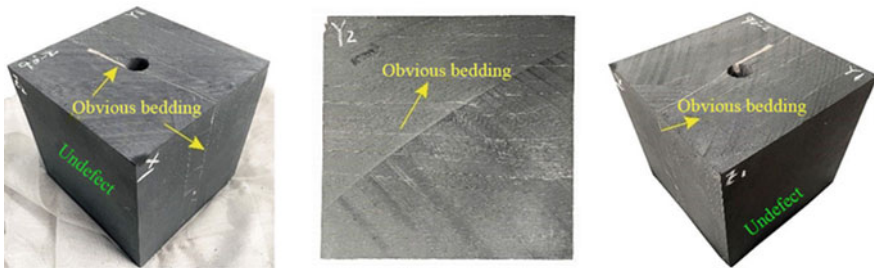

Fig. 9.20 Bedding distribution of end faces of Sample 6# before fracturing tests

9.3.6 Effects of Wellbore Orientations

It can be seen from Table 6.1 that samples #1 and #5 simulate the hydraulic fracturing of vertical and horizontal wells, respectively, under a normal faulting stress state, while samples #2 and #6 simulate the hydraulic fracturing of vertical and horizontal wells, respectively, under a reverse faulting stress state. In addition, the breakdown pressures of vertical well hydraulic fracturing are higher than those of horizontal well hydraulic fracturing, which accords with the experimental observations of triaxial hydraulic fracturing in shale performed by Guo et al. [10].

However, due to the pre-existing obvious bedding planes and natural fractures in sample #6, it becomes inappropriate to use sample #6 for comparison. Therefore, we compared sample #1 to sample #5 to investigate the effects of wellbore orientations on hydraulic fracture morphology.

The SRA value and the total number of fractures of the vertical well (sample #1) are 1.5 and 5, respectively. The SRA value and the total number of fractures of the horizontal well (sample #5) are 2.5 and 6, which increased by 66.7% and 20% compared with the fracturing of vertical wells. Since the wellbore direction is vertical to the bedding plane direction, hydraulic fracturing of vertical wells often produces fractures propagating vertically or horizontally along the bedding [32]. Since the maximum principal stress acts vertically on the wellbore, when the fractures around the wellbore crack, under the limitation of the maximum principal stress, the hydraulic fractures will propagate perpendicular to the bedding, resulting in main fractures (such as M_1 in sample #5). This process is conducive to the formation of a complex fracture network.

References

1. Liu Z, Wang T, Gao Y, Zeng Q, Zhuang Z, Huang KC (2016) The key mechanical problems on hydraulic fracture in shale. Guti Lixue Xuebao/Acta Mech Solida Sin 37(1):34–49
2. Xiao H (2014) Research of hydraulic fracturing dynamic propagation in fractured reservoirs. Ph.D. thesis, Southwest Petroleum University Chendu
3. Guo JY, Wang Y (2016) Mechanism of natural fracture activation and propagation by hydraulic fracture. J Eng Geol 26(06):118–128
4. Ning WX, He B, Li FX, Xie LZ, Shi AP, He Q (2021) Experimental study on fractures morphology of hydraulic fracturing in continental shale oil reservoir. Sci Technol Eng 21(18):7505–7512
5. Dou FK (2020) Influences of shale meso-mechanical properties on hydraulic fracture propagation and its quantitative evaluation. Ph.D. thesis, China University of Mining and Technology Xuzhou
6. Zhang Y, Long A, Zhao Y, Zang A, Wang C (2023) Mutual impact of true triaxial stress, borehole orientation and bedding inclination on laboratory hydraulic fracturing of Lushan shale. Journal of Rock Mechanics and Geotechnical Engineering. https://doi.org/10.1016/j.jrmge.2023.02.015
7. Zhang D, Yang T (2013) An overview of shale-gas production. Shiyou Xuebao/Acta Pet Sin
8. Lee KS, Kim TH (2016) Integrative understanding of shale gas reservoirs. Springer, Heidelberg

9. Gan Q, Elsworth D (2014) Analysis of fluid injection-induced fault reactivation and seismic slip in geothermal reservoirs. J Geophys Res Solid Earth. https://doi.org/10.1002/2013JB010679

10. Guo P, Li X, Li S, Yang W, Wu Y, Li G (2021) Quantitative analysis of anisotropy effect on hydrofracturing efficiency and process in shale using X-ray computed tomography and acoustic emission. Rock Mech Rock Eng. https://doi.org/10.1007/s00603-021-02589-7

11. Lin C, He J, Li X, Wan X, Zheng B (2017) An experimental investigation into the effects of the anisotropy of shale on hydraulic fracture propagation. Rock Mech Rock Eng 50(3):543–554. https://doi.org/10.1007/s00603-016-1136-4

12. Wang J, Xie H, Li C (2021) Anisotropic failure behavior and breakdown pressure interpretation of hydraulic fracturing experiments on shale. Int J Rock Mech Min Sci. https://doi.org/10.1016/j.ijrmms.2021.104748

13. Chong Z, Yao Q, Li X (2019) Experimental investigation of fracture propagation behavior induced by hydraulic fracturing in anisotropic shale cores. Energies 12(976):1–16. https://doi.org/10.3390/en12060976

14. Li A, Ding WL, Zhang GL, Zhang MG, Zhang ZX, Yan BZ, Zhou CX, Chen ZZ, Bai P (2016) Reservoir characteristics of marine shale in the Malong block of eastern Yunnan Province and comparison analysis. Earth Sci Front 23(02):176–189

15. Du K, Li X, Wang S, Tao M, Li G, Wang S (2021) Compression-shear failure properties and acoustic emission (AE) characteristics of rocks in variable angle shear and direct shear tests. Meas J Int Meas Confed. https://doi.org/10.1016/j.measurement.2021.109814

16. Ma G, Zhang F, Liu X, Feng D, Zhang PW (2016) Experimental study of impact of crustal stress on fracture pressure and hydraulic fracture. Rock Soil Mech 37(S2):216–222

17. Guo YT, Yang CH, Jia CG, Xu JB, Wang L, Li D (2014) Research on hydraulic fracturing physical simulation shale and fracture characterization methods. Chin J Rock Mech Eng 33(01):52–59

18. Zeng YJ, Zhou J, Wang HT, Zuo L, Jiang TX, Zhong GY, Guo YT, Chang X, Wang L, Yang CH (2019) Research on true triaxial hydraulic fracturing in deep shale with varying pumping rates. Chin J Rock Mechan Eng 38(09):1758–1766

19. Zhou J, Chen M, Jin Y, Zhang G-q (2008) Analysis of fracture propagation behavior and fracture geometry using a tri-axial fracturing system in naturally fractured reservoirs. Int J Rock Mech Min Sci. https://doi.org/10.1016/j.ijrmms.2008.01.001

20. Guo T, Zhang S, Qu Z, Zhou T, Xiao Y, Gao J (2014) Experimental study of hydraulic fracturing for shale by stimulated reservoir volume. Fuel 128:373–380. https://doi.org/10.1016/j.fuel.2014.03.029

21. Salvage RO, Eaton DW (2021) How is induced seismicity affected by transitional stress regimes? In: 55th U.S. rock mechanics/geomechanics symposium 2021

22. Moska R, Labus K, Kasza P (2021) Hydraulic fracturing in enhanced geothermal systems—field, tectonic and rock mechanics conditions—a review. Energies 14(18):5725. https://doi.org/10.3390/en14185725

23. Zimmermann G, Moeck I, Blöcher G (2010) Cyclic waterfrac stimulation to develop an Enhanced Geothermal System (EGS)—conceptual design and experimental results. Geothermics 39(1):59–69. https://doi.org/10.1016/j.geothermics.2009.10.003

24. Warpinski NR, Mayerhofer MJ, Vincent MC, Cipolla CL, Lolon ER (2009) Stimulating unconventional reservoirs: maximizing network growth while optimizing fracture conductivity. J Can Pet Technol 48(10):39–51. https://doi.org/10.2118/114173-PA

25. Hou B, Chen M, Cheng W, Tan P (2014) Fracturing mechanism of shale gas reservoir with variable pump rates. Chin J Geotech Eng 36(11):2149–2152

26. Jiang C, Niu B, Yin G, Zhang D, Yu T, Wang P (2019) CT-based 3D reconstruction of the geometry and propagation of hydraulic fracturing in shale. J Pet Sci Eng 179:899–911. https://doi.org/10.1016/j.petrol.2019.04.103

27. Taleghani AD, Olson JE (2014) How natural fractures could affect hydraulic-fracture geometry. SPE J. https://doi.org/10.2118/167608-pa

28. Ezati M, Azizzadeh M, Riahi M A, Fattahpour V, Honarmand D (2020). Evaluation of faults reactivation tenacity in one of the low-pressure SW Iranian carbonate reservoirs: an IOR viewpoint. J Pet Sci Technol 10(1):20–29. https://doi.org/10.22078/JPST.2020.3825.1605

29. Umar IA, Negash BM, Quainoo AK, Ayoub MA (2021) An outlook into recent advances on estimation of effective stimulated reservoir volume. J Nat Gas Sci Eng 88(3):103822. https://doi.org/10.1016/j.jngse.2021.103822

30. Hou B, Zhang R, Zeng Y, Fu W, Muhadasi Y, Chen M (2018) Analysis of hydraulic fracture initiation and propagation in deep shale formation with high horizontal stress difference. J Pet Sci Eng. https://doi.org/10.1016/j.petrol.2018.06.060

31. Hou B, Chen M, Li Z, Wang Y, Diao C (2014) Propagation area evaluation of hydraulic fracture networks in shale gas reservoirs. Pet Explor Dev. https://doi.org/10.1016/S1876-3804(14)60101-4

32. Liu YW, Gao DP, Li Q et al (2019) Mechanical frontiers in shale-gas development. Adv Mech 49(00):1–236

Epilogue

Main Insights

Comparing the mechanism of fracturing with a constant injection rate and fracturing with constant pressure injection, and characterizing the relationship between the behaviors of fracture initiation, arrest, stable and unstable propagation and pumping parameters (injection rate and injection pressure), the time-delayed initiation mechanism of hydraulic fractures fatigue induced by constant pressure injection is revealed.

By considering that the fluid pressure in the fracture is in the form of non-uniform distribution, this breaks through the limitations of existing studies that less consider the effect of non-uniform fluid pressure distribution in the fracture. The model equation of hydraulic fracture whose fluid pressure changes with the position in the fracture is constructed to determine the distribution law of the stress field and displacement field near the hydraulic fracture under non-uniform pressure and to predict the propagation trajectory of hydraulic fracture.

A composite criterion based on the critical intersection process of a hydraulic fracture and a natural fracture is established to predict the subsequent intersection behavior and to systematically analyze the effects of singularity at the tip of hydraulic fracture, approach distance and fracture toughness on the intersection behaviors.

Considering the disturbance effect of wellbore orientations (vertical well or horizontal well) and in-situ stress states (normal faulting, strike-slip faulting and reverse faulting) on the morphology of hydraulic fracture network, the anisotropic fracturing characteristics of shale are evaluated, and the formation mechanism of complex fracture network is revealed.

Implications for Future Study

The hydraulic fracture behaviors of shale are studied through laboratory tests and theoretical analysis, and some meaningful conclusions are obtained. The following research work will be carried out from the following aspects:

(1) Based on the uniaxial stress state, the hydraulic fracturing tests with constant injection rate and constant pressure are studied. There is little research on the deformation, breakdown pressure, acoustic emission signal evolution and fracture morphology characteristics of samples of hydraulic fracturing tests with constant injection rate and constant pressure under triaxial and true triaxial stress, which still needs further research.

(2) Both the model and the composite intersection criterion of non-uniform pressure hydraulic fracture are two-dimensional models are two-dimensional. In the actual three-dimensional fracturing, affected by the vertical stress, their applicability and reliability need to be further verified.

(3) The effects of bedding inclination angle, in-situ stress state and wellbore orientation on the morphology of complex fracturing network and fracturing effectiveness are analyzed, but the relative disturbance of different parameters on the fracture network morphology has not been deeply explored. Fracturing parameters need to be further refined, so as to further clarify the influence of these parameters on fracture behaviors and fracture network morphology can be more clear, which will be further explored in the future.